Photoemission Spectroscopy for the Electronic Structure Determination of Energy Materials

Roxy Lee

University College London

Primary Supervisor: Prof. Robert G. Palgrave

Secondary Supervisor: Prof. David O. Scanlon

A thesis submitted in partial fulfilment of the requirements for the degree of Doctor of Engineering at University College London

December 27, 2023

Declaration

I, *Roxanna Lilian Lee*, confirm that the work presented in this thesis is my own. Where information has been derived from other sources, I confirm that this has been indicated in the thesis.

Roxanna Lilian Lee

December 27, 2023

University College London

Abstract

Accurate surface characterisation is essential for the research and development of new energy materials and technologies, which are required to transition the current energy system to a low carbon energy mix. For many functional materials, their application is dominated by processes occurring at the surface, thus a major challenge lies in the characterisation of the surface structure. X-ray photoemission spectroscopy (XPS) is a powerful tool to analyse the top ~ 5 nm of a sample, providing elemental quantification and chemical state information. In XPS measurements, core and valence electrons are ejected from the sample surface, giving rise to core-level and valence band (VB) spectra, respectively. Analysis of core-level spectra to determine peak positions and intensities is the basis of most routine XPS characterization. However, VB spectra have complex spectral features that arise from the overlap of several orbital contributions from different atoms, which makes analysis more challenging.

Whilst centred around XPS, a major theme in this thesis is the integration of other scientific practices with the technique, thus emulating the interdisciplinary nature of materials science. The aim is to extend the conventional applications of XPS and develop new methods in materials analysis and can be divided into four main parts. Firstly, this work combines XPS with theoretical photoemission spectra simulated within the framework of density functional theory (DFT) to develop a refinement method, offering new insights into VB electronic structure and complex spectral features in metals and vacancy-ordered double perovskites, Cs_2TeX_6 (X = Cl, Br, I). This refinement method is then used in the second part to probe the vibrational broadening in materials with a range of conductivities, including photocatalysts bismuth oxyhalides, semiconductors Nb-doped strontium titanate and alkali halides. In the third part, a joint theoretical/experimental VB mapping method is developed and combined with photocatalytic activity mapping, to quantify phases in heterogeneous surfaces, applied to mixed-phase TiO_2. Lastly, electrochemical

measurements are performed in tandem with XPS data collection during the operando monitoring of Na ion behaviour and ionic liquids electrolytes in a 3-electrode electrochemical cell.

Impact Statement

Enormous changes to the current energy system are required, not only to fulfil greenhouse gas emissions targets, but to create a fairer world, and ultimately to avoid a climate apocalypse. Fundamental materials research, including the synthesis, characterisation, and theoretical understanding of functional materials for energy applications will play a vital role in these efforts. This thesis investigates the electronic structure and properties of a range of materials with energy and environmental applications, including photocatalytic materials – mixed-phase TiO_2 and bismuth oxyhalides, which have applications in photovoltaics, water splitting technologies, photoreduction of CO_2 and the purification of air and water borne pollutants. Ionic liquids are also investigated, which can be utilised as electrolytes for energy conversion and storage, as solvents/catalysts for CO_2 conversion or capture, and in non-volatile, green synthesis. Finally, the behaviour of Na ions in battery applications is probed under operando conditions, in the interest of Na battery research, which are promising contenders for future grid-scale energy applications.

Increasingly, researchers are turning to simulation methods to understand experimental photoemission spectra. This work is expected to aid future comparisons between DFT-simulated and VB XPS spectra, leading to a more thorough understanding of the electronic structure of materials. This is vital for the design and characterization of energy materials. Interdisciplinary studies are also crucial to further scientific advancements, and progress made in this work is expected to aid further work in the scientific community where XPS is integrated with the methods utilised herein. Namely, the refinement of DFT-simulated photoemissions spectra to probe vibrational broadening at variable temperatures, the phase

quantification of photocatalytic heterogenous surfaces and the correlation with experimentally determined photocatalytic activity, and the integration of electrochemistry and XPS to perform operando measurements on electrochemical cells. Together with the power of policy makers, governments and international cooperation, the research and development of materials with energy and environmental applications will hopefully bring positive changes to our world. This research has been disseminated through research publications and conference presentations.

Acknowledgements

UCL Research Paper Declaration Form
referencing the doctoral candidate's own published work(s)

Please use this form to declare if parts of your thesis are already available in another format, e.g. if data, text, or figures:

- *have been uploaded to a preprint server*
- *are in submission to a peer-reviewed publication*
- *have been published in a peer-reviewed publication, e.g. journal, textbook.*

This form should be completed as many times as necessary. For instance, if you have seven thesis chapters, two of which containing material that has already been published, you would complete this form twice.

1. **For a research manuscript that has already been published** (if not yet published, please skip to section 2)

   a) **What is the title of the manuscript?**

   Phase Quantification of Heterogeneous Surfaces Using DFT-Simulated Valence Band Photoemission Spectra

   b) **Please include a link to or doi for the work**

   https://doi.org/10.1021/acsami.3c06638

   c) **Where was the work published?**

   ACS Applied Materials & Interfaces

   d) **Who published the work?** (e.g. OUP)

   American Chemical Society (ACS)

   e) **When was the work published?**

   August 8, 2023

   f) **List the manuscript's authors in the order they appear on the publication**

   Lee, Roxy; Quesada-Cabrera, Raul; Willis, Joe; Iqbal, Asif; Parkin, Ivan P.; Scanlon, David O.; Palgrave, Robert G.

   g) **Was the work peer reviewed?**

   Yes

   h) **Have you retained the copyright?**

   Yes

   i) **Was an earlier form of the manuscript uploaded to a preprint server?** (e.g. medRxiv). If 'Yes', please give a link or doi)

   https://chemrxiv.org/engage/api-gateway/chemrxiv/assets/orp/resource/item/64134c4e2bfb3dc251dff09e/original/phase-quantification-of-heterogeneous-surfaces-using-dft-simulated-valence-band-photoemission-spectra.pdf

If 'No', please seek permission from the relevant publisher and check the box next to the below statement:

☐

*I acknowledge permission of the publisher named under **1d** to include in this thesis portions of the publication named as included in **1c**.*

2. **For a research manuscript prepared for publication but that has not yet been published** (if already published, please skip to section 3)

3. **For multi-authored work, please give a statement of contribution covering all authors** (if single-author, please skip to section 4)

   Manuscript preparation, XPS analysis and VB fitting method by Roxy Lee under the supervision of Robert Palgrave. Photocatalysis measurements and analysis by Roxy Lee and Raul Quesada-Cabrera. DFT calculations by Roxy Lee under the supervision of Joe Willis and David Scanlon. Sample synthesis by Raul Quesada-Cabrera under the supervision of Ivan Parkin. MATLAB code for RGB analysis written by Asif Iqbal.

4. **In which chapter(s) of your thesis can this material be found?**

   Chapter 4 - Valence Band Analysis of Heterogeneous Systems

5. **e-Signatures confirming that the information above is accurate** (this form should be co-signed by the supervisor/ senior author unless this is not appropriate, e.g. if the paper was a single-author work)

   Candidate
   Roxy Lee
   Date:
   22/12/23

   Supervisor
   Robert Palgrave
   Date
   22/12/23

Table of Contents

xi

Publications

related to thesis work:

Phase Quantification of Heterogeneous Surfaces using DFT Simulated Valence Band Photoemission Spectra.[1] **Roxy Lee**, Raul Quesada-Cabrera, Joe Willis, Asif Iqbal, Ivan P. Parkin, David O. Scanlon and Robert. G. Palgrave, *ACS Applied Materials & Interfaces*, 2023, **15**, 39956-39965

Advanced XPS characterization: XPS-based multi-technique analyses for comprehensive understanding of functional materials.[2] Mark A. Isaacs, Josh Davies-Jones, Philip R. Davies, Shaoliang Guan, **Roxy Lee**, David J. Morgan and Robert Palgrave, *Materials Chemistry Frontiers*, 2021, **5**, 7931-7963.

unrelated to thesis work:

XPS surface analysis of ceria-based materials: Experimental methods and considerations.[3] Mark A. Isaacs, Charalampos Drivas, **Roxy Lee**, Robert Palgrave, Chris M. A. Parlett and David J. Morgan, *Applied Surface Science Advances*, 2023, **18**, 100469.

Faraday Discussions – photoelectron spectroscopy and the future of surface analysis.[4] R. Arrigo, L. Ban, T. Bartels-Rausch, P. R. Davies, S. Eyley, W. Flavell, G. Galli, S. Guan, S. Hall, G. Held, J. Kahk, **R. Lee**, R. Lindsay, J. Lischner, K. Lovelock, A. Nilsson, D. Payne, O. Renault, A. Shard and S. Suzer, *Faraday Discussions*, 2022, **236**, 412-428.

Ultrasensitive and miniaturised ion sensors using ionically imprinted nanostructured films.[5] Antonio Ruiz-Gonzalez, Jingle L. Huang, Cao Xun, Roohi Chhabra, **Roxy Lee**, Huang Yizhong, Andrew Davenport, Bing Li, Robert Palgrave and Kwang Leong Choy, *Applied Materials Today*, 2022, **29**, 101600.

in preparation:

Vibrational Broadening in Photoemission Spectra Investigated via DFT and Variable Temperature XPS. **Roxy Lee**, Mark Isaacs, Robert Palgrave

Monitoring the Behaviour of Na Ions at the Surface of an Electrode Using Operando Electrochemical XPS. **Roxy Lee**, Tim S Nunney, Mark Isaacs, Robert Palgrave, Avishek Dey

Conference Contributions

Oral Presentations:

Phase quantification of heterogeneous surfaces using DFT simulated valence band photoemission spectra, (Invited) Thermo Fisher XPS User Meeting, Karlsruhe, Germany (June 2023)

Operando Electrochemical XPS at the Electrode-Electrolyte Interface, MRS Spring, San Francisco, USA (April 2023)

Thermal broadening in core level and valence band XPS, SPIE Photonex, Birmingham, UK (December 2022)

TiO_2 valence band phase mapping via a joint study of simulated and experimental photoemission spectra, SPIE Photonex, Glasgow, UK (September 2021)

Poster Presentations:

Vibrational broadening in Nb-doped STO investigated by variable temperature XPS, SSCG Christmas Meeting, Edinburgh, UK (December 2023)

A New Method of Mapping Heterogeneous Mixed-Phase Photocatalytic Surfaces, IUMRS-ICYRAM, Fukuoka, Japan (August 2022)

Acronyms

AdC adventitious carbon

AIMD ab initio molecular dynamics

AP ambient pressure

BLB blacklight-bulb

BE binding energy

BCC body centred cubic

BO Born-Oppenheimer

CA chronoamperometry

CCD charge-coupled device

CCP cubic close packed

CE counter electrode

CEI cathode electrolyte interface

CV cyclic voltammetry

DFT density functional theory

DOS density of states

DSSC dye-sensitised solar cell

EDL electric double layer

ESCA electron spectroscopy for chemical analysis

fcc face centred cubic

FG flood gun

FWHM full width at half maximum

GC glassy carbon

GGA generalised gradient approximation

HAXPES hard x-ray photoelectron spectroscopy

HEC hydroxy ethyl-cellulose

HOMO highest occupied molecular orbital

HF Hartree-Fock

HSE Heyd–Scuseria–Ernzerhof (exchange-correlation functional)

ICSD inorganic crystal structure database

IMFP inelastic mean free path

IP ionization potential

IUPAC international union of pure and applied chemistry

LDA local density approximation

LEIS low energy ion scattering

LUMO lowest unoccupied molecular orbital

MA moving average

MAE mean absolute error

MO molecular orbital

NAP near-ambient pressure

PBE Perdew-Burke-Ernzerhof (GGA functional)

pDOS partial/projected density of states

PEEK poly-ether-ether-ketone

PXRD powder x-ray diffraction

QM quantum mechanics

RAPW relativistic augmented plane wave

RE reference electrode

RGB red green blue

RSS residual sum of squares

RT room temperature

SA surface area

SED sacrificial electron donor

SEI solid electrolyte interface

SSP single side polished

tDOS total density of states

UHV ultra-high vacuum

UPS ultraviolet photoelectron spectroscopy

UV ultraviolet

VASP Vienna ab initio simulations package

vdW van der Waals

VB valence band

VBM valence band maximum

WE working electrode

XPS x-ray photoelectron spectroscopy

XRD x-ray diffraction

Part I - Introduction

1.1 Thesis Outline

This work explores the electronic structure and properties of several groups of materials with energy and environmental applications. This is achieved using both experimental and theoretical photoemission spectroscopy, integrated with other scientific techniques. X-ray photoelectron spectroscopy (XPS) and density functional theory (DFT) are utilised to determine the electronic structure via experimental and theoretical approaches, respectively. The introduction provides a background of both XPS and DFT methods, followed by short overviews of supporting techniques, which together form **Part I** of this thesis. The investigations presented in this work can then be divided into four main parts, named **Part II-V**.

Part II evaluates the use of valence band (VB) photoemission spectra simulated within the framework of DFT for two classes of materials – metals and semiconductors. This is applied to the Group 11 coinage metals and vacancy-ordered double halide perovskites. Different simulation methods are compared, including different DFT functionals, and different spectral broadening and photoionization cross-section correction methods. In **Part III,** the vibrational broadening in core and VB XPS is explored, by fitting temperature-dependent XPS spectra with broadened DFT-derived theoretical ground state spectra. This is applied to three series of materials with a range of different conductivities, namely alkali halides, bismuth oxyhalides and Nb-doped strontium titanate single crystals.

In **Part IV**, a method of mixed-phase quantification is developed, involving the simulation and fitting of DFT-derived spectra to mixed-phase XPS data. This is applied to mixed phase anatase/rutile thin films and compared to an empirical fitting method. The photocatalytic activity of the thin films is discussed in terms of the XPS/DFT-determined phase-fraction and both methods are applied to large scale mapping of thin film surfaces. **Part V** explores XPS of ionic liquids (ILs) and *operando* XPS. First, XPS studies of

ILs and charging effects induced by measurement conditions are investigated. Next, an *operando* electrochemical XPS cell is designed, and then applied to study Na ion chemistry, with the view to further Na ion battery research. Finally, **Part VI** presents a summary of the current work and outlook for further research.

1.2 Experimental Techniques

The main experimental technique utilised throughout this work is x-ray photoemission spectroscopy (XPS). A more detailed introduction to the XPS method is given first, followed by shorter overviews of supporting characterization techniques.

1.2.1 X-ray Photoelectron Spectroscopy

XPS has a long history, encompassing the discovery of the photoelectric effect by Hertz in 1887 and subsequent investigations of many others into this phenomenon,[6, 7] which was ultimately quantified by Einstein in 1905.[8] The development of XPS as an analytical tool won Siegbahn the Nobel Prize in physics in 1981, although he preferred the term electron spectroscopy for chemical analysis (ESCA), which was how it was referred to in his group's early work.[9-13] Use of the acronym ESCA is attributed to the fact that XPS is sensitive to the chemical environment of atoms, making it a powerful tool in materials chemistry analysis. The following basic principles are well documented and more thoroughly explained in several dedicated textbooks,[14-16] review articles,[17-19] and practical guides.[20-22]

1.2.1.1 The Photoemission Process

In x-ray photoemission the electrons in a solid are excited by high energy photons, which must have enough energy to allow the electrons to leave the solid so that they can then be detected by an electron spectrometer. The photoemission process and associated energy level diagram are illustrated schematically in **Figure 1.1**.
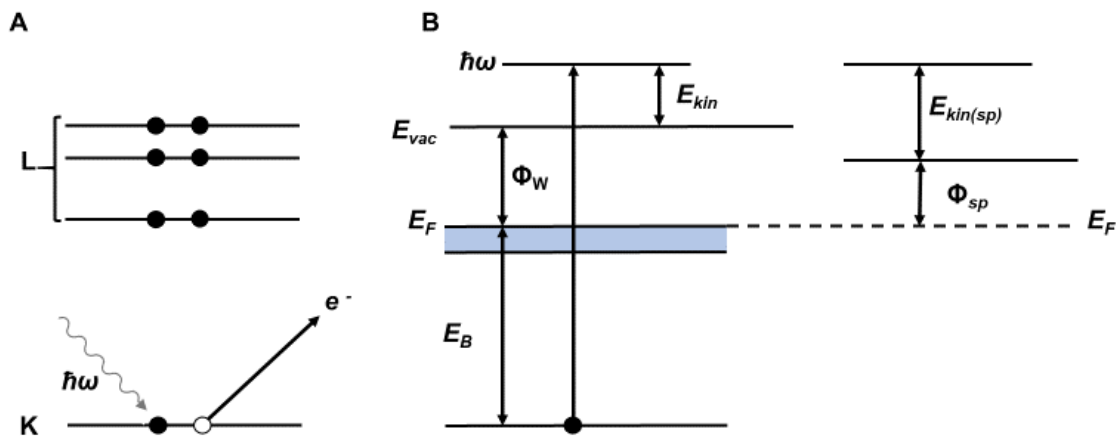
Figure 1.1a) The process of photoemission and **b)** the associated energy level diagram for the emission process into the spectrometer or vacuum. Φ_{sp}, Φ_W are the work functions with respect to the spectrometer and with respect to the vacuum level, E_{vac}, respectively, $\hbar\omega$ is the energy of the incoming photon, E_B is the binding energy of the photoelectron and E_{kin} is the kinetic energy of the emitted electron. K and L indicate subshells with principal quantum numbers 1 and 2, respectively. The blue region indicates the valence band, or filled states, in the simplified band structure depiction of a metal.

The kinetic energy of the emitted electron is directly analysed, and its value can be calculated by:

$$E_{kin(sp)} = \hbar\omega - \left[E_B + \Phi_{sp}\right] \qquad\text{(Eq.1.1)}$$

where E_{kin} is the kinetic energy of the emitted electron, $\hbar\omega$ is the energy of the incoming photon, E_B is the binding energy of the electron and Φ_{sp} is the work function with respect to the spectrometer level. Because Φ_{sp} is a spectrometer constant, it must be calibrated with well-known elements such as Au and Cu.

1.2.1.2 Chemical Environment

In XPS, core and valence electrons are ejected from the surface of a sample, giving rise to what can be considered two distinct types of spectra, although there is no sharp boundary between the two. Photoemission from core levels produces photoelectron peaks at characteristic binding energies, which are subject to chemical shifts depending on the local chemical environment.

Figure 1.2a) displays the characteristic survey spectrum collected for anatase TiO_2. Survey spectra are typically collected for basic elemental

4

identification and to evaluate sample purity by the presence/absence of contaminant signals. The core level signals have been labelled with the orbitals from which they originated, e.g. Ti $2p$. The spectrum also contains features due to *Auger* electrons, which is a secondary emission process that occurs due to the creation of core holes by the primary emission process. The excited ionised state relaxes by filling the core hole with a valence electron, releasing energy in the process. This released energy may then 'kick out' a second electron that will also reach the detector, thus contributing to the collected data. The notation used to describe *Auger* transitions follows K, L, M nomenclature (i.e. K for *s* orbitals, etc.) and is explained here for the oxygen O_{KLL} signal seen in **Figure 1.2a**: the first electron was ejected from a K orbital, creating a core hole that was filled by an electron from an L orbital, and the ejected *Auger* electron also originated from an L orbital.

To obtain chemical state information, high resolution scans are collected spanning the region in which the signals are expected to appear. A high-resolution scan of the Ti $2p$ region is shown in **Figure 1.2b**, recorded on the same anatase TiO_2 sample as the survey scan. An important feature of XPS core level spectra is illustrated in this case: all signals except those arising from *s* orbitals appear as doublets due to spin-orbit coupling. The intensity ratios of the doublet peaks are defined by the **j** quantum number, which appears as a subscript in conventional core level notation, for example Ti $2p_{3/2}$ and Ti $2p_{1/2}$ in this case. The relative areas are determined by $(2\mathbf{j} + 1)$ for each peak, i.e. 2:1 for Ti $2p_{3/2}$: Ti $2p_{1/2}$. Additionally, in most cases, the full width at half maximum (FWHM) would be equal for the two doublet peaks. However, in this example, the $2p_{1/2}$ peak is wider due to a Coster-Kronig transition, which is a special case of an *Auger* process.
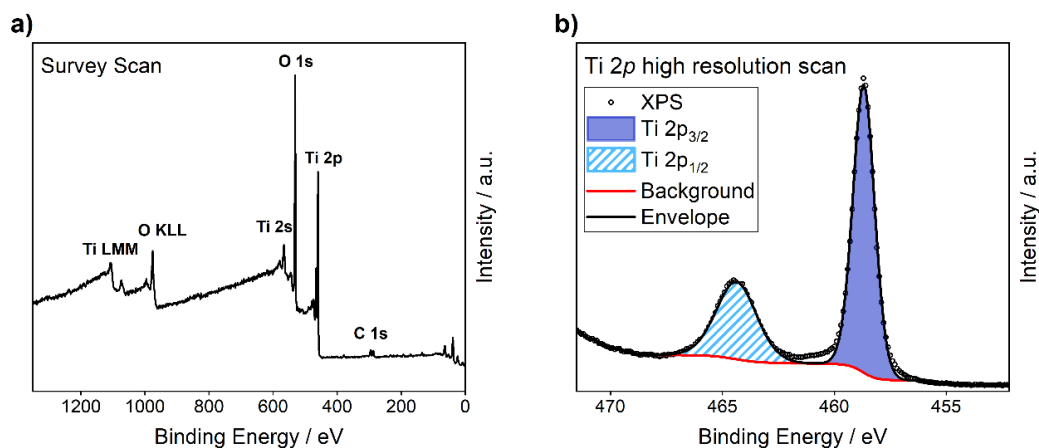
Figure 1.2a) An XPS survey spectrum recorded on anatase TiO_2, and **b)** the corresponding high-resolution scan of the Ti $2p$ region. The labels are explained in the text.

Determining the positions and intensities of these core lines is the basis of most routine materials analysis by XPS, which allows us to quantify not only the atomic species present, but also their chemical bonding environments within a sample. The binding energy of the Ti $2p_{3/2}$ peak in **Figure 1.2b** is 458.7 eV, which is characteristic of Ti (IV) species and indicative of the oxidation state of Ti in TiO_2. Emission from core orbitals can be modelled using simple line shapes, commonly by a convolution of 70 % Gaussian and 30 % Lorentzian functions for semi-conductors like TiO_2, to model instrumental and lifetime broadening, respectively. Whilst final state effects can cause difficulties, usually straightforward modelling and interpretation of core level spectra is possible. Emission from valence states is less straightforward and will be discussed later in **Section 1.2.1.6**.

1.2.1.3 Surface Sensitivity

Whilst the incoming x-rays penetrate quite deeply within a sample (on the order of a few µm), any electrons generated at this depth will undergo many inelastic collisions, eventually losing too much energy to escape the sample. Electrons that are excited closer to the surface may escape after several random inelastic collisions. These electrons have a lower kinetic energy than those described by **Eq.1.1**, due to the loss of energy during collisions, and thus contribute to the inelastic background of the XPS spectrum. Only

6

electrons that are scattered elastically (i.e. leave the surface with no collisions) form the main characteristic peaks of the XPS spectrum.

The information depth that can be probed by XPS is controlled by several factors, including the inelastic mean free path (IMFP). The IMFP of electrons is the average distance travelled by an electron through a solid before it is inelastically scattered, which depends on both the nature of the solid and the initial kinetic energy of the electron but can roughly be described by a universal curve that is the same for all materials.[23] In addition to the IMFP, the attenuation length also plays a role, which also factors in elastic scattering. Ultimately, the probability of escape decays very rapidly with increasing distance and so only electrons from the top 1-10 nm of the material that are excited by the incoming x-rays will escape (typically the top ~ 5 nm in lab-based sources). XPS is therefore a highly surface sensitive technique, which must be accommodated by the instrument design.

1.2.1.4 XPS Instrumentation

X-ray radiation in XPS spectrometers is produced by bombarding a metallic anode with high-energy electrons. The spectrometers used in this work were equipped with an aluminium anode in conjunction with a quartz crystal monochromator, which produces a beam of Al K_α x-rays (**Figure 1.3**). In addition to filtering out other Al x-ray lines and Bremsstrahlung radiation, the crystal focusses the x-ray beam onto the surface of the sample, with a spot size typically between $50 - 400$ µm. This illumination causes ejection of electrons with a range of energies and directions. In most XPS instruments, the analyser is positioned to collect photoelectrons that originate from the surface of the sample with a trajectory in line with the surface normal, known as *normal emission*. This can be described in terms of the take-off angle, θ, which is the angle between the trajectory of the electron and the local or average surface plane. In *normal emission*, which was employed throughout this work, $\theta = 90°$.
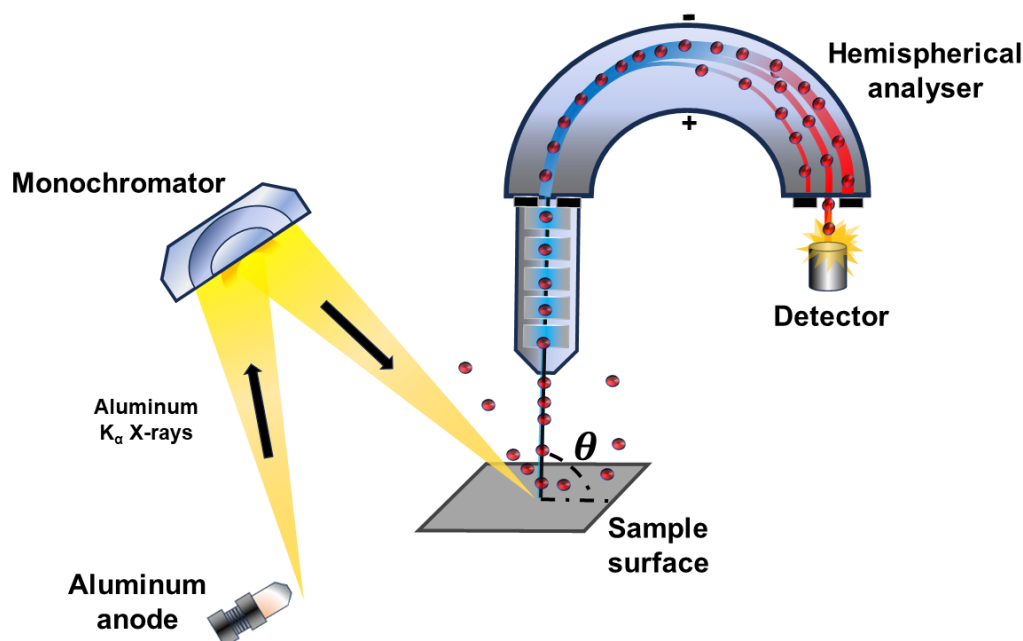
Figure 1.3. The main components of an XPS spectrometer commonly include an Al anode produces Al K$_\alpha$ radiation, which is monochromated and focused by a quartz crystal onto a sample surface, causing the ejection of electrons. The take-off angle, θ, is the angle between the trajectory of the electron as it leaves the surface and the local or average surface plane. Normal emission, as depicted here, refers to the case when $\theta = 90°$. Photoelectrons generated in this manner will pass through a hemispherical analyser and be collected by the detector.

Photoelectrons pass through a set of lenses and a hemispherical analyser, which retards their kinetic energy to only allow electrons of a given energy, the so-called pass energy, to reach the detector. Any collisions with air molecules would impede their pathway and reduce the signal intensity, therefore ultra-high vacuum (UHV) conditions are employed in the analysis chamber, (pressures below $\sim 10^{-9}$ mbar). A further reason for the UHV environment is the surface sensitivity of the technique – any contamination on the surface greatly influences the quality and appearance of collected data. UHV ensures a minimum contamination on the surface of measured samples. Additionally, the extremely high voltages required in the instrumentation, e.g. 10 – 20 kV for an x-ray gun applied over several mm, require UHV to support high electric field strengths without arcing (electrical breakdown of gas molecules).

8

1.2.1.5 Charge Correction

During the photoemission process, electrons are removed from the surface of the sample, creating a positively charged surface. For metallic and conducting materials, these electrons removed by photoemission can be replaced if the sample is grounded to the spectrometer. However, for semi-conducting and insulating samples, the positive charge build-up can result in BE shifts and peak distortion. In such cases, the use of a charge neutraliser can greatly improve the situation, by the flow of low energy electrons or ions. Even with the use of charge compensation methods, the measured BE may not represent the 'true' value, and thus a post-measurement processing step is often introduced, known as charge correction.

Charge correction, also known as charge calibration, is a means to calibrate the BE scale with respect to a reference peak. The most common method of charge correction was introduced by Siegbahn et al. during the early days of the XPS technique.[12] This approach relies on the layer of adventitious carbon (AdC) that is present on essentially every sample after exposure to air. The alkyl carbon (C-H, C-C) component of the AdC C 1s spectrum is assumed to have a binding energy in the range of 284.6-285.0 eV, and any difference between the measured value and this reference value is used to apply a constant shift to all other spectra measured at the same analysis point.

The validity and reliability of the AdC reference has been heavily debated for a long time. Early work by Swift highlighted the range of contemporary AdC C 1s binding energies and stressed that *'adventitious carbon is not the panacea for energy referencing'*.[24] Recently, extensive analysis of XPS literature by Greczynski et al. has revealed an increasing spread of reported AdC C 1s values.[25] This report also draws attention to the changeable nature of the AdC layer, which can have varying chemical identity depending on many factors such as the length of time and nature of the

exposure environment, the thickness of the AdC layer, the substrate material and charging in the sample and/or the AdC layer.

Alternative methods for charge correction include noble metal decoration, where a small amount of a noble metal (often gold) is deposited *in situ* onto the sample.[26] The binding energies measured on the Au deposits can be compared to Au in contact with the spectrometer to monitor charging in the sample. This method, however, relies on deposition sources and suffers from sample signal attenuation. A variation on this method is to implant noble gas atoms into the sample.[27] This method does not have the drawback of sample signal attenuation, but it may damage the sample and has been shown to suffer from unstable binding energies in some cases.[28] A further method is internal referencing, where enough information is known about the nature of one component of the sample to set it to a value that is well recorded in the literature. For example, catalysts commonly involve well documented materials, such as TiO_2, and in some such cases, with careful analysis of the peak shape, the Ti $2p_{3/2}$ peak could be used as an internal reference.[29]

Despite the concerns for the reliability of the AdC C 1s referencing, in the absence of alternative charge correction options, it can still provide a very useful method if utilised with proper caution.[25, 29] A recent (2022) study by Biesinger into 1237 samples submitted to a multi-user facility over five years investigated the effectiveness of the AdC charge referencing method in insulating samples.[30] For 117 samples that also contained an alternative charge referencing possibility, an average AdC C 1s binding energy of 284.91 eV (Std. Dev. 0.25 eV) was found. Through thorough assessment of the 522 samples where AdC charge referencing was employed, it was found that this method provided meaningful and satisfactory results for 95 % of cases.

1.2.1.6 Valence Band Spectra

Valence band (VB) spectra arise from the photoemission of electrons from the valence orbitals of a material, which results in significantly different spectra compared to core-level photoemission. By their nature, valence orbitals interact with neighbouring atoms; they can no longer be assumed to be unaltered atomic orbitals. VB spectra thus contain contributions from several elements and orbitals, and often show complex shapes influenced by the structure of the sample, making analysis more challenging than core line analysis. The VB spectrum of anatase TiO_2 (**Figure 1.4**) illustrates the increased complexity of this region. This data was recorded on the same sample as the survey and high-resolution scans described earlier (**Figure 1.2**).
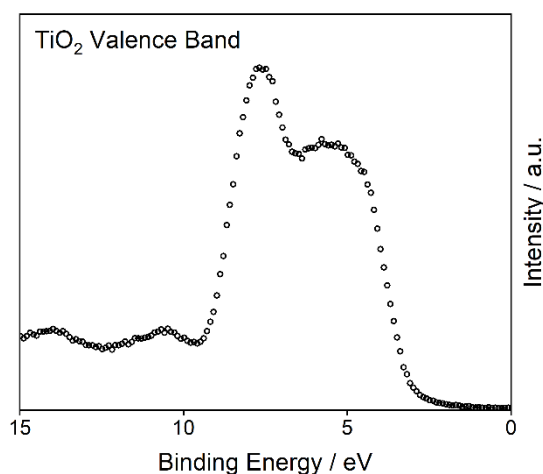
Figure 1.4. The VB XPS spectrum of anatase TiO_2.

To interpret this region, it is instructive to consider the valence electronic structure in terms of band theory. The electronic structure of solids can be described by considering the overlap of atomic orbitals throughout the entire structure as forming continuous 'bands' of energy, which is the basis of band theory. This concept is similar to molecular orbital theory, where the atomic orbitals from adjacent atoms overlap to from molecular orbitals (MOs). The electrons from the constituent atoms occupy these MOs, and their distribution is governed by the molecule as a whole.

As in small molecules, the valence orbitals in a solid can overlap, generating a set of molecular orbitals that extend through the solid. The lowest energy MO consists of all bonding interactions and the highest energy MO is completely antibonding. As the number of atomic orbitals increases, the separation between energy levels becomes so small that they effectively form a continuous band of allowed energy levels. This is summarised diagrammatically in **Figure 1.5**, where the number of atomic orbitals is increasing A<B<C<D.
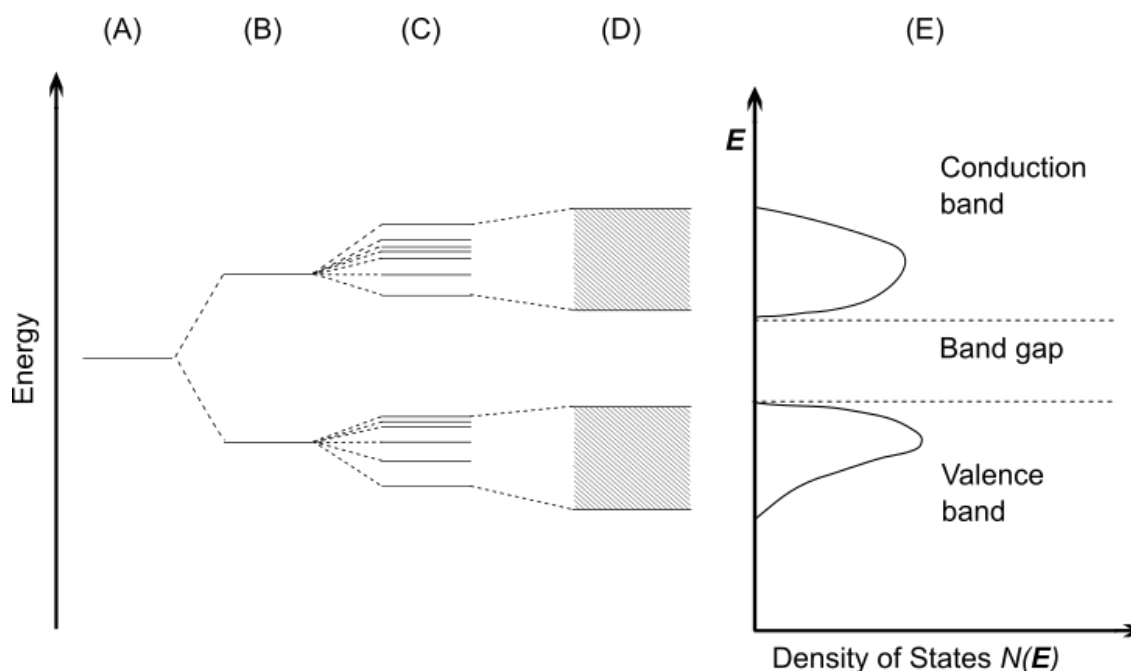
Figure 1.5. A depiction of how energy bands are formed from the overlap of atomic orbitals in solids, adapted from Cox.[31] As the number of atomic orbitals increases A<B<C<D, the separation between adjacent energy levels decreases, so that the allowed energy levels essentially form a continuous band (E). The valence band is the top filled band, and the conduction band is the bottom empty band, separated in energy by the band gap. The distribution of energies within these bands leads to the concept of the density of states, N(E), which is zero in the band gap.

Within the bands, the orbitals are not distributed evenly but are concentrated together at certain energies, which leads to the concept of the density of states (DOS), N(E), defined as:[31]

$N(E)$ dE is the number of allowed energy levels per unit volume of the solid, in the energy range E to E + dE.

N(*E*), or the DOS, is zero in the forbidden band gaps. The top filled band is known as the VB, and the bottom empty band is known as the conduction band (CB). The difference in energy of the valence and conduction bands (the band gap) in a solid determine the electrical conductivity, which is commonly divided into three classifications: metals, semiconductors, and insulators. The top filled level in a metal lies within a band and therefore there is no band gap associated with the excitation of electrons into the next lowest molecular orbitals, resulting in high electrical conductivity. In insulators the band gap is so large that there is little or no electrical conductivity. In semiconductors the energy gap is small enough that thermal or other excitations can allow movement of electrons from the valence band to the conduction band.

The DOS therefore contains valuable information on the properties and electronic structure of solids, which is probed experimentally in this work using VB XPS. To aid with the interpretation of the inherently complex features observed in VB spectra, theoretical DOS calculations are employed. Density functional theory (DFT) is a suitable framework for calculating ground state DOS and is introduced in more detail in **Section 1.3.1**.

1.2.1.7 VBM Measurement

There are several methods to determine the position of the valence band maximum (VBM) from a valence band XPS spectrum. The linear extrapolation method involves fitting straight lines to the leading edge of the VB spectrum and the baseline at the low binding energy side. These two straight lines are then extrapolated, and the point of intersection is taken as the VBM. The linear extrapolation method is widespread in the literature and has several uses.[32-36] For example, it has been used to locate a reference point for core levels in valence band XPS studies on diamond, graphite and glassy carbon.[34]

Alternatively, one can use a hybrid theoretical-experimental approach where the VBM is determined by fitting the experimental spectrum with

broadened theoretical DOS, as described by Kraut et al.[37, 38] This procedure has been used to investigate the effect of polarity and surface states on the Fermi level of GaN and AlN surfaces.[39] The fitted VBM position relative to core lines can also be used to determine the valence band offsets of different materials (i.e. A and B), following:[37, 38]

$$\Delta E_v = (E_{cl}^A - E_{cl}^B)_{\frac{A}{B}} - [(E_{cl} - E_v)_A - (E_{cl} - E_v)_B] \qquad \textbf{Eq.1.2}$$

where ΔE_v is the valence band offset, E_{cl} is the BE of a core line, and E_v is the position of the VBM.

This method has been used to measure the valence band offset in strained Si/Ge (100) heterojunctions,[40] and to study the valence band structure and band alignment at the ZrO/Si interface.[41] Different results may be obtained depending on the method of VBM determination used. For example, VBM values used in band alignments of bulk molybdenum dichalcogenides (MoS_2, $MoSe_2$ and $MoTe_2$) were found to vary in some cases between the extrapolation method and the fitted DOS method.[42] However, there was close (+/- 0.1 eV) or exact agreement in most cases. The authors describe the difficulty in the linear extrapolation method arising from the sensitivity to where the extrapolation is fitted.

Chambers et al. review several cases comparing the two methods, and present results for $SrTiO_3$ (001).[43] The linear extrapolation method applied to Ge,[44] GaAs[44] and Si[45] is in excellent agreement with broadened DOS fitted to the experimental VB of Ge and III-V semiconductors.[46] In contrast, Chambers et al. find that in the case of $SrTiO_3$ (001) and several other oxides the linear extrapolation method is in substantial disagreement with broadened DOS calculated within the LDA or GGA.[43] However, fitting with broadened DOS calculated at a higher level of theory (*GW* approximation) gave results in excellent agreement with the extrapolated VBM.

Further work by Chambers et al. into *n*-$SrTiO_3$, *n*-TiO_2 *anatase* and SrO epitaxial films and their band offsets with SrO provides more evidence that

the fitted DOS method fails in some cases.[47] They conclude that the extrapolation method gives more physically reasonable results than fitting with broadened DOS calculated by DFT, because the theory predicts too sharp a rise in the leading edge, thus locating the VBM at a higher binding energy. High resolution UPS data was also used to locate the VBM, by determining the energy at which the intensity of the leading edge goes to zero, which was in excellent agreement with the XPS linear extrapolation method. It is suggested that for the extrapolation method to give meaningful results, the region of the leading edge used to fit the extrapolation line must be truly linear. In addition, the experimental resolution of the spectrometer should be less than the region of the leading edge, in order to accurately capture its shape, and to remove the resolution induced tail by extrapolating the leading edge to the baseline.

Materials that have a low DOS near the VBM are difficult to fit accurately with the linear extrapolation method. Endres et al. introduced a new method for such cases, exemplified by their work on metal halide perovskites.[48] These materials exhibit soft VBM onsets with non-linear leading edges, therefore the standard linear extrapolation misses the VBM. They largely correct this problem by plotting the XPS data on a logarithmic scale, resulting in more reliable VBM determination. This method was later adopted by Philippe et al. investigating valence level character in mixed perovskites, who also find the logarithmic extrapolation gives more reliable results than the traditional linear method.[49]

1.2.2 Raman Spectroscopy

Raman spectroscopy is a technique to determine the vibrational modes of molecules and is commonly used in chemistry to identify molecules by a structural fingerprint. Typically, measurement involves illuminating a sample with a laser beam (**Figure 1.6**), where the wavelength is selected depending on the material, to minimise fluorescence. The light is scattered by the sample, following the polarization of the molecular electron cloud. Raman scattering is the inelastic scattering of the incident light, resulting in scattered light of a different wavelength. The difference between the incident and scattered light is known as the Raman shift. The scattered light is focused, filtered, and passed through a spectrometer to a charge-coupled device (CCD) detector, producing a spectrum according to the Raman shift.
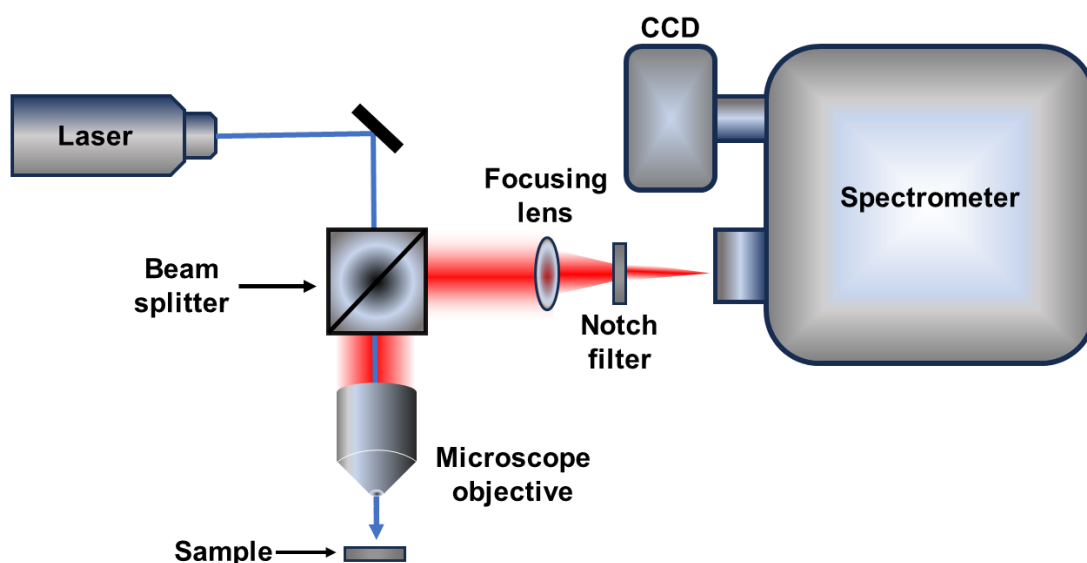

Figure 1.6. A schematic of a Raman spectrometer. This set-up focusses laser light (coloured blue) onto the sample. The Raman-shifted light (coloured red) is filtered out from the laser light by the beam splitter, which is then focussed and passed through a notch filter to remove interfering signals before reaching the spectrometer and the CCD detector.

1.3 Computational Methods

In computational chemistry, computer simulations are utilised to aid in solving complex chemical problems. The range of applications is vast, where theoretical chemistry is combined with efficient computer programs, for example, to calculate structures, properties, and interactions of molecules and materials. In this thesis, computational methods are used to calculate the electronic structure of materials using the theory of quantum mechanics (QM). The main aim of QM methods utilised in theoretical chemistry is to solve the time-independent Schrödinger equation (TISE):[50]

$$\widehat{H}\Psi = E\Psi \qquad\qquad \textbf{Eq.1.3}$$

where $\widehat{H}$ is the Hamiltonian operator corresponding to the total energy of a system, E is the energy eigenvalues, and Ψ is the wavefunction describing a system comprising N electrons and M nuclei. Ψ depends on $3N$ spatial coordinates $\mathbf{r}_i$ and N spin coordinates $\mathbf{s}_i$, collectively forming $\boldsymbol{x}_i$ coordinates of the electrons, and $3M$ spatial coordinates of the nuclei $\boldsymbol{R}_I$:

$$\Psi = \Psi(\boldsymbol{x}_1, \boldsymbol{x}_2 .. \boldsymbol{x}_N,, \boldsymbol{R}_1, \boldsymbol{R}_2 .. \boldsymbol{R}_M) \qquad\qquad \textbf{Eq.1.4}$$

The Hamiltonian is equal to the sum of the kinetic ($\widehat{T}$) and potential ($\widehat{V}$) energy contributions, and in its full form is given by:

$$\widehat{H} = -\frac{1}{2}\sum_{i=1}^{N}\nabla_i^2 - \frac{1}{2}\sum_{A=1}^{M}\frac{1}{M_A}\nabla_A^2 - \sum_{i=1}^{N}\sum_{A=1}^{M}\frac{Z_A}{r_{iA}} + \sum_{i=1}^{N}\sum_{j>i}^{N}\frac{1}{r_{ij}} + \sum_{A=1}^{M}\sum_{B>A}^{M}\frac{Z_A Z_B}{R_{AB}}$$

$$\textbf{Eq.1.5}$$

where ∇_i^2 is the Laplacian operator, indices i through j run though N electrons, indices A and B run through M nuclei, M_A is the nuclear mass, Z is the nuclear charge, $\boldsymbol{r_{iA}}$ is the distance between particles i and A, $\boldsymbol{r_{ij}}$ is the distance between particles i and j and $\boldsymbol{r_{AB}}$ is the distance between particles A and B. The equations are given in atomic units. The terms in the equation, in order of appearance, represent the kinetic energy of the electrons, $\widehat{T}_e$ the kinetic energy of the nuclei, $\widehat{T}_N$, the nuclear-electron attraction term, $\widehat{V}_{eN}$,

the electron-electron repulsion term, $\hat{V}_{ee}$ and the nuclear-nuclear interaction term, $\hat{V}_{NN}$. **Eq.1.5** can therefore be written as:

$$\hat{H} = \hat{T}_e + \hat{T}_N + \hat{V}_{eN} + \hat{V}_{ee} + \hat{V}_{NN} \qquad \textbf{Eq.1.6}$$

An exact solution of the TISE would give the exact ground state energy, however, a solution is only possible for a system with one nucleus and one electron, i.e., the hydrogen atom. As more nuclei and electrons are added to the system, the terms become extremely complex to solve, and the problem becomes computationally intractable. Therefore, approximations are necessary to make any calculations possible.

The first approximation used is the Born-Oppenheimer (BO) approximation, which considers the movement of nuclei to be stationary with respect to the electrons. This is generally a safe approximation, given that the mass of a neutron is ~ 2000 times that of an electron. We therefore ignore the kinetic energy of the nuclei, yielding:

$$\hat{H} = \hat{T}_e + \hat{V}_{eN} + \hat{V}_{ee} + \hat{V}_{NN} \qquad \textbf{Eq.1.7}$$

where the potential energy of nuclear interactions, $\hat{V}_{NN}$, will be constant for a given set or atomic coordinates. It is relatively simple to calculate $\hat{T}_e$ and $\hat{V}_{eN}$, however, the potential energy due to the energy of interaction between the electrons ($\hat{V}_{ee}$) is virtually impossible to solve directly, due to the *many body problem*. The *many body problem* refers to the increased complexity of any system containing more than two bodies that makes exact calculations practically impossible to calculate.

To obtain numerical solutions to the Schrödinger equation, the *variational principle* is employed. This *variational principle* states that for any trial wavefunction (Ψ_T), the calculated expectation value (E_T) of the Hamiltonian will always exceed the true ground state energy (E_0) of the true wavefunction (Ψ_0):

$$\langle \Psi_T | \hat{H} | \Psi_T \rangle = E_T \geq E_0 = \langle \Psi_0 | \hat{H} | \Psi_0 \rangle \qquad \textbf{Eq.1.8}$$

Using this principle, convergence towards an accurate energy can be achieved by using an increasing number of trial wavefunctions, to minimise E_T.

1.3.1 Density Functional Theory

1.3.1.1 Background

In this thesis, photoemission spectra are simulated using theoretical ground state density of states (DOS). Density function theory (DFT) is a suitable framework in which to calculate the ground state DOS of a material and has been used extensively in this work. DFT offers an alternative approach to solve the TISE (**Eq.1.5**) One of the advantages of DFT is that it greatly reduces the computational cost of solving the TISE by reducing the *many body problem* to a simplified version in which the ground state energy of a system depends solely on the electron density.[51]

In 1964, Hohenberg and Kohn demonstrated that the ground state energy of a system can be defined in terms of the electron density, $\rho(\boldsymbol{r})$.[52] This is different to Hartree-Fock theory, for which the wavefunction must be solved for a large number of non-interacting particles. DFT aims to solve the TISE in terms of $\rho(\boldsymbol{r})$, offering an enormous reduction of the number of variables to be solved, from $3N$ (where N is the number of electrons) to just 3 (*x, y,* and *z* coordinates). DFT makes use of the *variational principle* (**Eq.1.8**) in that the total energy calculated from the trial electron density will always be larger than the true ground state energy (arising from the true electron density).

In 1965, Kohn and Sham developed the electron density model further, by introducing the following approximation: a system of many *interacting* electrons moving in an external potential may be simplified to a system of many *non-interacting* electrons moving in an external field.[53] Using this approximation, a set of self-consistent single particle equations (the Kohn-Sham equations) were derived:

$$[T + V_{ei}(\boldsymbol{r}) + V_H(\boldsymbol{r}) + V_{xc}(\boldsymbol{r})]\varphi_i(\boldsymbol{r}) = \epsilon_i\varphi_i(\boldsymbol{r})$$

<div align="right">**Eq.1.9**</div>

where T is the single electron kinetic energy, V_{ei} is the electron-ion Coulomb potential, V_H is the Hartree potential, V_{xc} is the exchange-correlation potential, φ_i represents the single electron Kohn-Sham orbitals, and ϵ_i represents the corresponding Kohn-Sham eigenvalues. The density can then be found by summing over all occupied orbitals:

$$\rho(\boldsymbol{r}) = \sum_{occu.} \varphi_i^*(\boldsymbol{r})\varphi_i(\boldsymbol{r})$$

<div align="right">**Eq.1.10**</div>

The terms V_H (the Hartree potential) and V_{xc} (the exchange-correlation potential) depend on the electron density:

$$V_H(\boldsymbol{r}) = e^2 \int d^3\boldsymbol{r}' \frac{\rho(\boldsymbol{r}')}{|\boldsymbol{r}'-\boldsymbol{r}|'} , \qquad \text{**Eq.1.11**}$$

$$V_{xc}(\boldsymbol{r}) = \frac{\delta E_{xc}(\rho)}{\delta\rho} \qquad \text{**Eq.1.12**}$$

making it possible to solve this set of equations self-consistently. In this process, an initial guess is made for $\rho(\boldsymbol{r})$, then **Eq.1.9** is solved for the Kohn-Sham orbitals, $\varphi_i(\boldsymbol{r})$. This is inserted into **Eq.1.10** to obtain a new density. If the initial and new densities are different, they are mixed together, and the process is repeated until they become self-consistent (i.e. the same). Although the theory is exact, the form of the exchange-correlation functional, $E_{xc}(\rho)$, is not actually known. This is where practical application of DFT relies on the development of accurate approximations to $E_{xc}(\rho)$, which is discussed in the next section.

1.3.1.2 Level of Theory – different density functionals

To investigate the effect of the level of theory on theoretical XPS spectra, this work utilised two different density functionals, which implement different approximation to the exchange-correlation functional. The first is the Perdew-Burke-Ernzehof (PBE)[54] functional, which is a non-empirical

functional that implements the generalised gradient approximation (GGA). In GGA, the non-homogeneity of the true electron density is taken into account. GGA level of theory is a popular choice, due to its reasonable computational cost and accuracy for a large range of systems.[55] A version of the PBE functional that was adapted toward the description of solid state systems, PBEsol,[56] is used in this work.

The hybrid functional of Heyd, Scuseria and Ernzehof (HSE06)[57] was also employed, which uses 25 % exact Hartree-Fock (HF) exchange together with 75 % exchange and 100 % of the correlation energies from PBE. The HSE06 functional avoids the slow convergence of the exchange energy over distance, by only calculating the short-range exchange with HF, and the remainder using PBE. Both PBEsol and HSE06 functionals are used in this work and, in some cases, compared.

1.3.1.3 Dispersion Corrections

Two types of materials investigated in this work have structures that exhibit dispersive van der Waals (vdW) forces: vacancy-ordered double perovskites and bismuth oxy halides. As most functionals do not account for vdW forces, an additional correction term is added. This work implements the DFT-D3 approach, which was suggested by Grimme et al.[58]

Part II - DFT-simulated Valence Band Photoemission Spectra

An experimental XPS spectrum gives us information on the DOS within a sample and is thus comparable to theoretically determined DOS from DFT. Such a comparison requires several corrections to both experimental and theoretical DOS, as discussed below. Any comparison should be approached with caution due to the fundamental differences between a theoretical ground state spectrum, and an experimental XPS spectrum, which contains several important contributions other than loss-free electron ionization, as pointed out by Bagheri et al.[59] Nonetheless, a simulated DFT spectrum, produced from a DOS suitably broadened and weighted with photoionization cross-sections, can match very closely to experimental XPS VB spectra.[59-69]

Comparison of experimental and simulated valence band spectra has been used, for example, to investigate energy dependent VB spectra for several oxides,[59] and carbides,[70] to determine the VBM in metal halide perovskites,[48, 71, 72] and metal nitrides,[73] to probe the valence states in cerium vanadate–based materials,[68] to identify the electronic structure origins of poor performance in tin monosulfide (SnS) solar cells,[60] to understand changes to the VB spectrum seen on varying incident photon energy,[59] to explore the effect of polymorphism on the electronic structure of Ga_2O_3 phases,[62] and to study lifetime and satellite effects in tungsten metal.[66]

The current chapter (**Part II**) looks at the simulation of VB XPS spectra for two groups of materials: i) the Group 11 metals (coinage metals Cu, Ag, Au) and ii) a series of vacancy-ordered double perovskite semiconductors Cs_2TeX_6 series, X = Cl, Br, I. The first section provides an overview of simulation methods utilised in the literature, focussing on spectral broadening and photoionization cross-section correction methods, followed by an explanation of the techniques utilised in this study for simulating and fitting theoretical spectra to VB XPS. The subsequent sections will focus on

the two distinct material groups, which is followed by some final conclusions for **Part II**.

2.1 Introduction to Valence Band Simulation and Fitting Methods

There are several stages to simulate VB XPS spectra from the DFT calculated partial density of states (pDOS). Firstly, each orbital contribution must be weighted by energy dependent photoionization cross-section values, to simulate the probability of photoionization from different elements and orbitals by incoming radiation of a specific energy. Secondly, spectral broadening must be applied to simulate the XPS line shape. Finally, an offset must be applied to align the XPS binding energy and DFT energy scales. Although the latter correction is straightforward, the first two parameters require some attention and there is no consistent approach taken in the literature. This section reviews the different approaches taken, firstly, to spectral broadening, and secondly to the weighting of the pDOS. Lastly, the methodologies utilised in this thesis for VB simulation and least squares fitting are presented. There are also corrections required to the XPS spectrum, such as background subtraction, which is detailed later in **Section 2.2.1**.

2.1.1 Review: Simulating XPS Spectra – Photoionization Cross-section Weightings and Spectral Broadening

To simulate the line shape seen in photoemission spectra, spectral broadening is applied to the calculated DOS. This is universally carried out by convolution of Lorentzian functions to simulate lifetime effects and Gaussian functions to simulate spectrometer resolution, X-ray linewidth and vibrational broadening.[62, 68, 74-77] Regarding the application method, two distinct approaches can be identified: the first involves broadening based on the instrumental resolution, which can be determined by the FWHM of a core line of a standard sample (e.g. Ag metal), or by fitting the Fermi edge of a metal. The second is an empirical approach, in which the optimum broadening is determined by fitting with experimental spectra.

An example of the former case is some early work by Wolfram and Ellialtioglu,[78] who used the spectrometer resolution to broaden the DOS of some oxide perovskites, and more recently Parvizian *et al.* similarly broadened their calculated DOS of Cu_3N.[73] In both these cases, the width of the calculated spectrum is considerably narrower than the experimental spectrum. Further examples where this is the case include VB studies into the electronic structure of CdO, ZnO and MgO by King et al.,[64] and investigations into the valence band orbital character of CdO by Mudd et al.[65]

Strict use of spectrometer energy resolution is an attractive approach but has some difficulties. The Lorentzian portion is estimated or empirically fitted in many cases, for example using the range of lifetime broadenings suggested by Fadley and Shirley (0.1-1.0 eV).[79] Some researchers have applied a varying Lorentzian component, to simulate the changing lifetime across the VB region.[68, 80] The use of purely empirical broadening is exemplified by Bagheri and Blaha, who apply a fixed Lorentzian contribution of 0.1 eV, but vary the Gaussian contribution between 0.36 and 1.05 eV, to fit the VB spectra of a range of oxides.[59] Empirically determined broadening has produced simulated spectra in good agreement with the experimental VB in many cases and often requires application of a Gaussian of larger width than the experimental resolution.[43, 72, 78, 81, 82]

Turning to the process of weighting the pDOS by energy dependent cross-section values, this process is not straightforward as there are different tabulated values available for a photon energy of 1486.6 eV (the monochromatic K-Alpha x-ray radiation used in this work), such as those of Scofield,[83] and Yeh and Lindau (referred to herein as YL).[84] In addition, there are no values available for levels that are unoccupied in the neutral atomic species, which is often the case for the valence band region. This requires some cross-section values to be estimated. The approach taken by Mudd et al. when estimating the unoccupied Cd 5*p* orbital contribution in CdO was to apply the In 5*p*/In 5*s* ratio to the Cd 5*s* cross-section value, as In

is the next heaviest element with an occupied $5p$ orbital.[65] Bagheri and Blaha extrapolated the cross-section values for neighbouring atoms to obtain estimates for empty sub-shell cross-section values.[59] In the case of PbO_2, they estimated the $6d$ cross-section parameter by extrapolating values from neighbouring elements that contain occupied $6d$ states in the free atom (Ac, Th, Pa), and in the case of ZnO they extrapolate the $4p$ value from Ga and Ge. An alternative method is to use tabulated values for filled states and to estimate the contribution from empty states empirically by fitting the model to experimental data.[66, 85] This approach has been used by Kalha *et al.* to simulate the VB spectrum of tungsten metal with an optimised weighting for W $6p$, with a reasonable fit also obtained from the tabulated cross-section for W $5p$.[66]

The suitability of photoionization cross-sections for VB simulation remains a point of contention within the field. The correction of pDOS using YL tabulated cross-sections was described as 'essential' in an experimental and theoretical investigation of the electronic structure of CdO by Dou *et al.*[86] In contrast, King *et al.* found good agreement between experimental spectra and DOS calculations for CdO, ZnO and MgO and state that there is no need for cross-section correction as the anion p and cation s cross-sections are similar.[64] Walsh *et al.* also reported that the experimental curve for α-Bi_2O_3 is well represented by the DOS and conclude that the cross-sections for O $2p$, Bi $6s$ and Bi $6p$ are very similar,[87] which is not in accordance with the YL tabulated values. A study on the electronic structure of lanthanide scandates by Mizzi *et al.* reported that tabulated cross-section values are unreliable for the valence band, therefore they use the literature values as starting points and then vary them.[88] Similarly, a study on rutile TiO_2 by Woicik *et al.* approximated the Ti $4p$ cross-section as equal to that of Ti $4s$ states, and then adjusted all pDoS weightings to obtain good agreement with site-specific VB XPS spectra.[89] Clearly, the process of pDOS weighting should be approached with some caution.

2.1.2 Current Study: Photoionization Cross-section Weightings

In this work, the values reported by Yeh and Lindau (YL),[84] and a second set of values modified from the original YL values, denoted modified YL (YL*), are investigated. The reason for trialling two different sets of values is due to the varied success of other researchers discussed above. Although YL values have been successful in some cases, others report worse agreement with experimental data and express caution since some YL values are for orbitals with binding energies much higher than the valence region, for example by around ~ 70 eV. Herein, modified YL* values are constructed using original values for some orbitals, and then some values obtained using a 'ratio' method that aims to estimate cross-section values for those where the YL value is deemed inappropriate, i.e. with BEs not within the VB region (c.a. ~0 − 10 eV). This is not always a straightforward evaluation, since DFT does not give any information on the principal quantum number n, only on the subshell l that describes the shape of the orbital (e.g. s, p, d, f). To judge the applicability of the YL values, the tabulated experimental BEs of the orbitals from Trzhaskovskaya and Yarzhemsky (TY) were used.[90] If the TY BE was in the region of ~0 − 10 eV, the YL value was used, as this is applicable to the VB region. Otherwise, a value was estimated using the 'ratio' method, as detailed below.

The 'ratio' method draws on methods reported by other researchers to estimate cross-section values for valence orbitals.[65] This involves taking the ratio of photoionization cross section values for two orbitals of a heavier element than that of interest. This ratio, together with a value from the element of interest are used to estimate the unknown value. This is explained by way of example in the following: for the element Au, the tabulated YL values refer to the 6s, 5p and 5d orbitals.[84] However, the experimental BE of the Au 5p orbital is around 60 eV below the Fermi level,[90] and thus not an appropriate orbital to use. An estimated value for the Au 6p level is obtained by multiplying the YL 6p/6s ratio of a heavier element by the YL Au 6s value. The chosen element is the next heaviest

where it is possible to obtain the $6p/6s$ ratio from the YL dataset, in this case Tl. The details for all values used and obtained in the 'ratio' method for all materials studied are summarised in the appropriate 'Computational Methodology' sections throughout this work.

2.1.3 Current Study: Least Squares Fitting Method

A least-squares refinement method was implemented to fit the XPS spectra with DFT simulated spectra, whereby optimal parameters were obtained by minimising the residual sum of squares (RSS) between the observed and calculated spectra:

$$RSS = \sum_i (I_i^{obs} - I_i^{calc})^2$$
<div align="right">**Eq.1.13**</div>

where I_i^{obs} and I_i^{calc} are the intensities observed and calculated in the spectra, respectively.

There are several stages to fitting the theoretical and experimental spectra. To begin with, there is some spectral processing required on the experimental side. The inelastic background is modelled and subtracted to facilitate comparison with the calculated DOS, which does not contain an inelastic background. The method used here is Shirley background subtraction. Additionally, the data here are smoothed because the theoretical and experimental spectra are aligned using the normalised spectral maximum, which may be affected by any noise in the data. This was performed using a moving average (MA) filter, typically with a width of $3-5$ data points. The energy scales are also aligned to overlap the experimental and calculated curves, which is done in two stages. In the first step, the XPS VBM is aligned to 0 eV because this is the default VBM position in the calculated DOS. The position is then optimised by fitting the two spectra together to minimise the RSS.

The least squares fitting method (i.e. minimising the RSS) in this work utilises the Solver function in Excel. This method of least squares refinement was demonstrated by Evans et al. in their showcase of Rietveld

refinement in Excel.[91] In addition to the energy scale alignment, the evaluation of different photoionization cross-section parameters and the optimisation of spectral broadening, as discussed earlier, were also performed in this manner. When optimising the spectral broadening, a small fixed Lorentzian contribution of 0.1 eV was applied to all theoretical spectra to simulate lifetime broadening, whilst the Gaussian component was optimised, similarly to the work of Bagheri and Blaha.[59] VB lifetimes are expected to be quite long, compared to core hole lifetimes, therefore a small Lorentzian component is justified as lifetime and the Lorentzian component are inversely proportional.

In most cases in the current study, various degrees of Gaussian broadening have been sampled at intervals of 0.1 eV, and the uncertainty in the fitting method is estimated to be ca. ± 0.05 eV. In some cases, the resulting RSS data has been fitted with a polynomial, to achieve better resolution of the minimum RSS and corresponding Gaussian broadening to 0.01 eV. In these cases, the uncertainty in the fitting method is estimated to be ca. ± 0.005 eV.

2.2 Valence Electronic Structure of Coinage Metals (Group 11)

2.2.1 Intro: Historical Significance

Early comparative studies of experimental and simulated photoemission valence band spectra include the highly cited work of D. A. Shirley,[92] from which the Shirley background takes its name. The background, which Shirley assumes arises in the experimental spectra due to inelastic scattering of electrons, is modelled at a given energy $E_b(x)$ by the integrated area under the emission intensities between $E_b(x)$ and the lower binding energy at the limit of the region it is applied to. To compare with calculated spectra the modelled background is then subtracted from the experimental photoemission spectra, because simulated spectra from DOS calculations do not have any contributions from inelastically scattered electrons. Although Shirley did not make clear the physical meaning of this method for background subtraction,[93] good agreement has been found between experiment and theory using this method.[94]
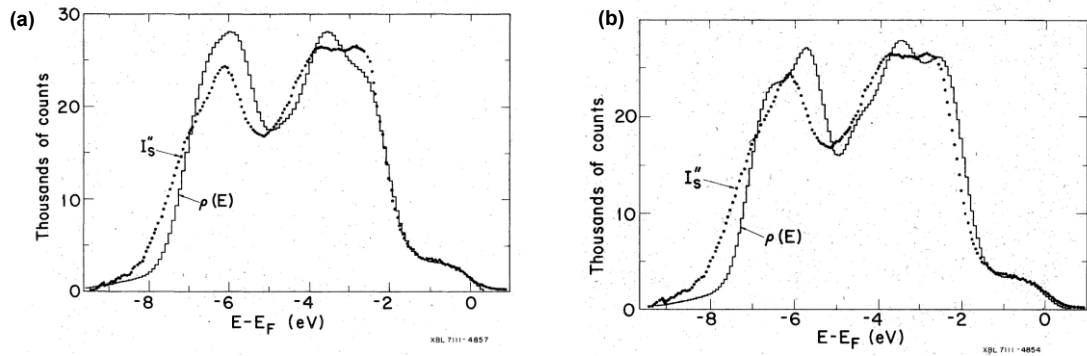
Figure 2.1. Comparative studies of the experimental valence band spectra of gold with contemporary theoretical spectra from an early work by Shirley.[92] The theoretical valence bands are based on RAPW calculations from the work of **(a)** Christensen and Seraphin,[95] and **(b)** Ramchandani.[96] The labels I_s'' and $\rho(E)$ indicate the experimental and theoretical curves, respectively.

Shirley applied his method to a single crystal sample of gold metal, which is then compared to a range of contemporary broadened theoretical density of state calculations by plotting them together. In doing so, Shirley also addresses the question "are XPS spectra sensitive enough to distinguish

critically among different theoretical band-structure calculations?" He concludes that relativistic band structure calculations are required to fit the spectrum and that contemporary relativistic augmented-plane-wave (RAPW) calculations give density of state results that follow the experimental curves closely after broadening, including calculations from Christensen and Seraphin (**Figure 2.1a**),[95] and Ramchandani (**Figure 2.1b**).[96] Also, Shirley acknowledges that the assumptions made in the inelastic background correction may not be entirely correct, but that the corrected spectrum would only be slightly affected and that the interpretations in his work would be the same.

2.2.2 Experimental Section

XPS Measurements on Coinage Metals (Group 11)

XPS was carried out using a Thermo Scientific K-alpha spectrometer equipped with a monochromated Al K-Alpha X-ray source (1486.6 eV) in constant analyser energy mode. Photoelectrons were collected at normal emission with a spot size of 400 μm. The measurements were carried out on Cu, Ag and Au standard samples that are housed on the standard sample strip within the analysis chamber, and consist of polycrystalline metallic foils. The metal surfaces were cleaned by Ar ion etching for 5 minutes, at a beam energy of 3000 eV. The conducting nature of the metallic samples means charge compensation was not necessary. A pass energy of 150 eV was used to record survey spectra and pass energies of 20 eV and 30 eV were used to record high resolution VB and core level spectra, respectively.

VB XPS spectra were processed as follows using CasaXPS:[97] A Shirley background was subtracted and spectra were aligned to 0 eV by fitting the Fermi edge with a complementary error function, which locates the point of intersection of straight lines fitted to the edge and the baseline. This method is known as linear extrapolation and is discussed in more detail in **Section 1.2.1.7**.

2.2.3 Computational Methodology

Calculations were performed using the Vienna *Ab initio* Simulation Package (VASP).[98] The convergence criterion for the k-point density and the plane wave cut-off energy parameters was that the total energy was converged to within 1 meV per atom. The resulting converged parameters are listed in **Table 2.1**.

Table 2.1. Converged plane wave cut-off energies and k-point densities for the selected materials (copper, silver, and gold metal).

Material	Plane Wave Cut-off Energy / eV	k-point density
Cu	450	9 x 9 x 9
Ag	400	9 x 9 x 9
Au	350	11 x 11 x 11

The PBEsol functional was implemented for geometry relaxation and electronic structure calculations. The electronic structure calculations were performed with increasing density to converge the appearance of the calculated density of states (DOS). As the simulated spectra in this work are compared graphically with experimental spectra it is important that the appearance of the DOS is converged. Therefore, a convergence criterion was introduced that after broadening the DOS by the nominal instrumental resolution of 0.4 eV, there were no significant changes in appearance on increasing the k-point density. Spin-orbit coupling (SOC) effects are expected to be significant in elements heavier than Sb,[99, 100] therefore SOC was included for Au after converging the k-point density. Full details showing the convergence testing are in **Appendix A**. For Cu and Ag, a k-point density of 12x12x12 was deemed sufficient. For Au, a k-point density of 14x14x14 was deemed sufficient, and was used for the subsequent calculation including SOC.

Photoionization Cross-section Correction Method

In this work, the values reported by Yeh and Lindau (YL),[84] and a second set of values modified from the original YL values, denoted modified YL (YL*), are investigated, as described in more detail in **Section 2.1.2**. The values used for the materials in this section are reported in **Table 2.2** below.

Table 2.2. Energy dependent photoionization cross-section values used in this work for Cu, Ag and Au. The top set are those reported by Yeh and Lindau (YL).[84] The bottom set (YL*) contain some values that have been modified, indicated by the shaded rows. The 'ratio' method used to modify these values is detailed in **Table A1**.

Cu		Ag		Au	
YL		**YL**		**YL**	
4s	2.70E-04	5s	2.90E-04	6s	2.90E-04
3p	5.50E-03	4p	4.50E-03	5p	3.67E-03
3d	1.20E-03	4d	2.10E-03	5d	2.60E-03
YL*		**YL***		**YL***	
4s	2.70E-04	5s	2.90E-04	6s	2.90E-04
4p	**1.33E-04**	**5p**	**1.86E-04**	**6p**	**1.34E-04**
3d	1.20E-03	4d	2.10E-03	5d	2.60E-03

2.2.4 Results

Geometric Structure

The selected Group 11 metals (Cu, Ag and Au) belong to the space group Fm-3m and have the cubic close-packed (CCP) structures (**Figure 2.2**). All structures were geometrically optimised using the PBEsol functional. After geometry optimisation, all compounds retained their cubic Fm-3m structure. The calculated lattice parameters are recorded and compared to reference experimental data in **Table 2.3**.[101-103]
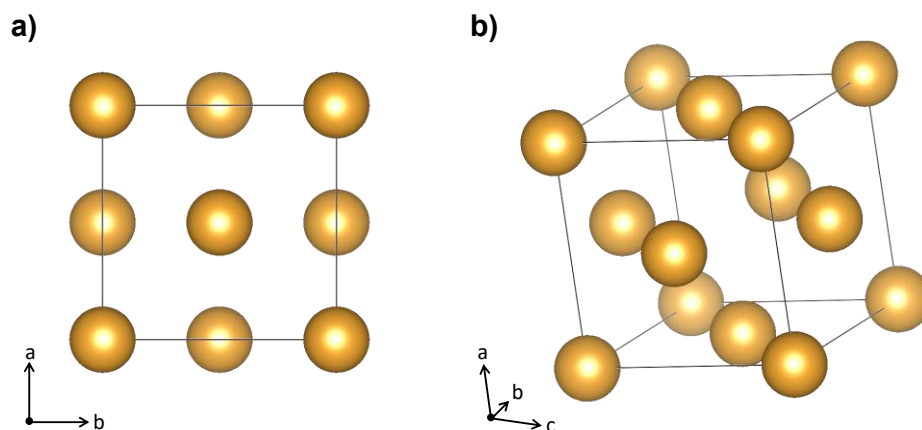
Figure 2.2a) The crystal structure of the selected Group 11 metals viewed along the [001] direction, **b)** a slightly rotated view, revealing the cubic close-packed (CCP) structure. The gold spheres represent Cu, Ag, or Au.

As the materials have the same crystal structure, the trend in the lattice parameter is due to the trend in the atomic size of the three elements. Cu is the lightest element and has the smallest atomic size and lattice parameter, as expected. However, Ag and Au have similar atomic sizes. This is due to the poor shielding of Au $4f$ electrons, which results in a greater effective nuclear charge, and thus a smaller atomic radius and lattice parameter a. The magnitude of the lattice parameter error, Δa, decreases with increasing atomic mass, according to the trend $\Delta a_{Cu} > \Delta a_{Ag} > \Delta a_{Au}$.

Table 2.3. Calculated and experimental lattice parameters for Cu, Ag, and Au, using GGA DFT (PBEsol). The lattice parameter errors (Δa) are given with respect to literature values[a].

	Cu	Ag	Au
Experiment	3.613 Å	4.086 Å	4.071 Å
PBEsol	3.569 Å	4.049 Å	4.082 Å
Δa PBEsol	-1.2 %	-0.9 %	0.3 %

[a] The experimental lattice parameters were sourced from ICSD references: Cu,[101] Ag,[102] and Au.[103]

33

Electronic Structure

Electronic structure calculations were performed for all optimised Group 11 structures (**Table 2.3**) using the PBEsol functional. In the case of Au, further calculations were also performed including SOC, due to its higher atomic mass. The resulting DOS are compared to the collected XPS data in **Figure 2.3**. An important processing step to arrive at these calculated DOS is to manually adjust the DOS above the Fermi level to zero to exclude the unoccupied states, which are not present in the XPS spectrum. This was done before spectral broadening was applied, to mimic the experimental edge. The appearance before this correction has been made can be seen in **Appendix A**. The spectral maxima have been normalised, and the experimental energy scale has been shifted to align with the theoretical DOS, which are broadened by the nominal instrumental resolution of 0.4 eV. This is a good match for the experimental VB width, except in the case of Au when no SOC effects are included (**Figure 2.3c**), where the calculated DOS is too narrow.

Note that at this stage no cross-section correction has been applied and no parameters have been optimised, which is discussed in the next section. However, it is already evident that the calculated gold VB requires relativistic SOC effects to be taken into account, to mimic the double lobed appearance of the experimental VB. This was similarly observed in the early work of Shirley, who concluded that relativistic calculations were required to compare to experimental valence bands.[92] The calculated VBs are mainly comprised of metallic *d* orbitals, which is consistent with other ab initio calculations on Cu,[104] Ag,[85] and Au,[92] and has been observed in experimental metallic valence bands since the early days of the XPS technique.[79] There is a small contribution from *p* and *s* orbitals, which peak in the middle and the high BE edge of the valence band, respectively.
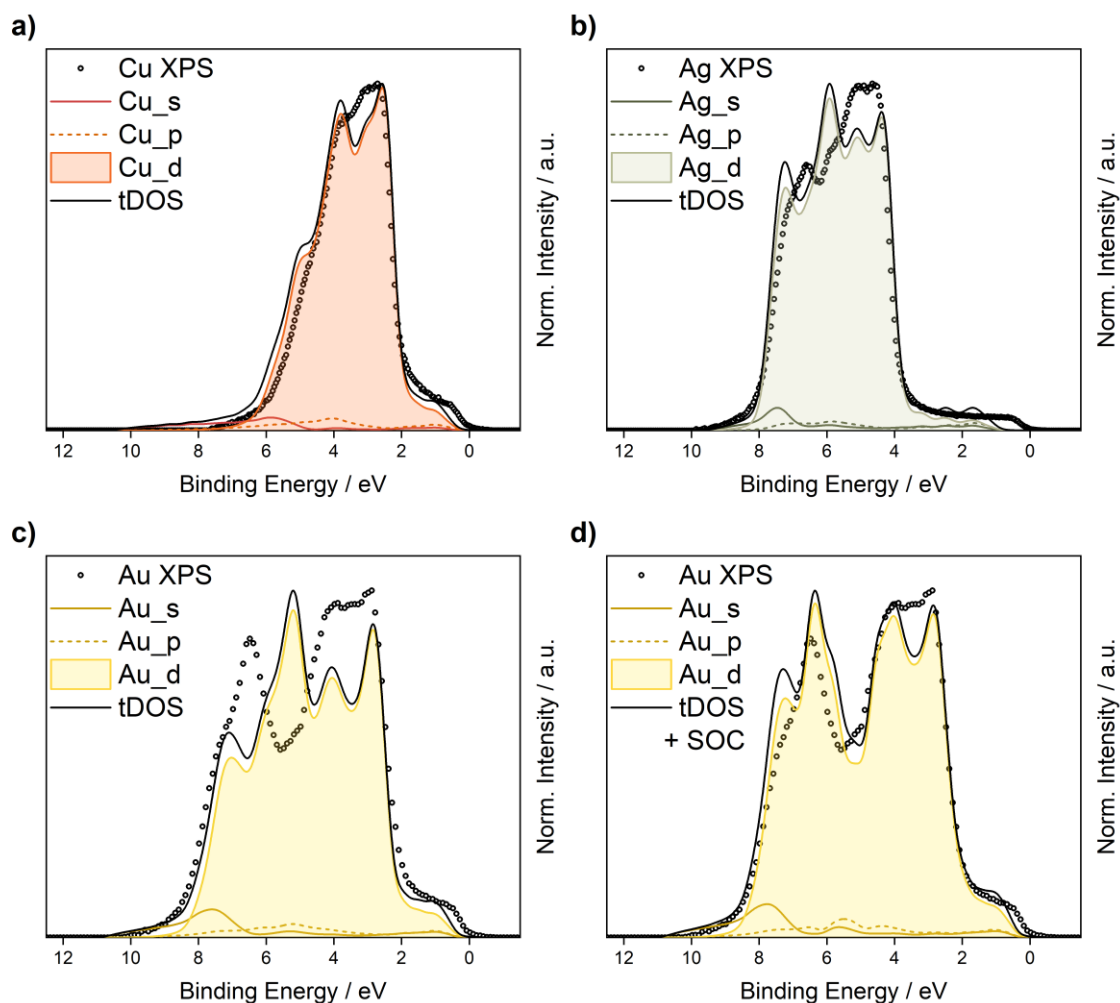
Figure 2.3. VB XPS spectra for the series of Group 11 metals **a)** Cu, **b)** Ag and **c-d)** Au, together with theoretical DOS, calculated using the DFT functional PBEsol. The spectral maxima have been normalised, and the experimental energy scale has been shifted to align with the theoretical DOS, which are broadened by the nominal instrumental resolution of 0.4 eV. In plots **a-c)** no SOC effects have been included, and in plot **d)** SOC effects have been included.

XPS/DFT VB Fitting

A least-squares refinement method was implemented as described in **Section 2.1.3** to evaluate the suitability of YL and YL* photoionization cross-section parameters, and to optimise the Gaussian component of applied spectral broadening. The resulting RSS curves, showing how the goodness of fit changes for different corrections, are shown in **Figure 2.4**. For all three metals, the modified YL* photoionization cross-sections produce the best fitting simulated spectra at almost all levels of broadening,

35

offering an improvement from both YL values and no cross-section correction at all (i.e. the plain DOS). For both Ag and Au, the plain DOS constitutes the worst fit, which is considerably improved by use of the YL values, and then slightly improved further using the YL* values. However, in the case of Cu, use of the YL values constitutes the worst fit, the plain DOS offers significant improvement over this and then finally the YL* values offer another significant improvement. The position of the minimum of each curve (i.e. the optimised spectral broadening) is not significantly affected by the cross-section correction method chosen, and is close to the nominal instrumental resolution of 0.4 eV in all cases. For the best fits with the YL* values, the optimised Gaussian components are 0.4 eV, 0.5 eV and 0.4 eV, for Cu, Ag and Au, respectively.
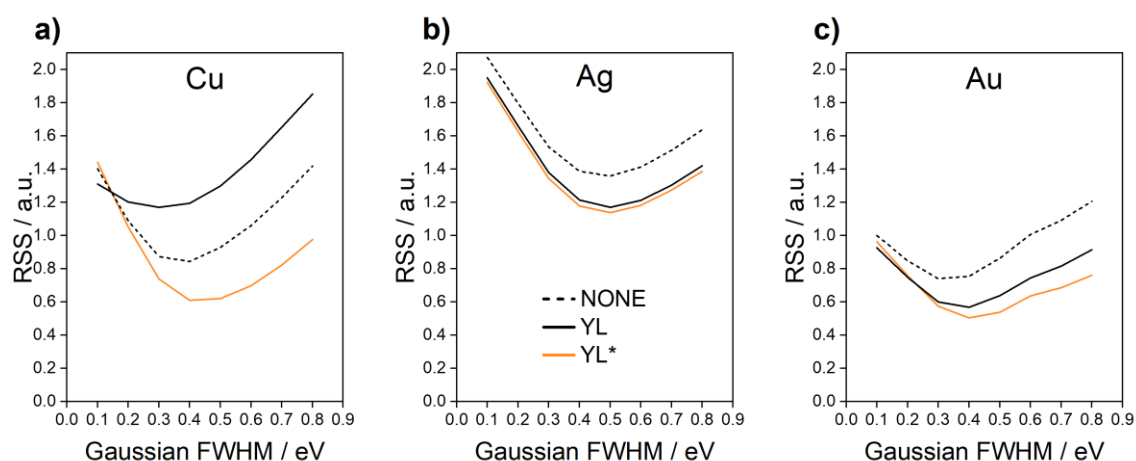

Figure 2.4. Optimisation of the Gaussian broadening applied to theoretical spectra in the Group 11 metallic series **a)** Cu **b)** Ag and **c)** Au. A fixed Lorentzian component of 0.1 eV was applied in each case. The RSS was calculated by fitting with VB XPS spectra simulated using PBEsol calculated DOS. The goodness of fit is compared when no correction is used (dashed black curve), to correction with YL cross-section values (solid black curve), and modified YL* values (solid orange curve).

The simulated spectra with optimised spectral broadening and energy scale alignment for each cross-section correction method are shown in **Figure 2.5**. The resulting simulated spectra offer a reasonable description of the experimental VB shapes, which all exhibit the signature Fermi edge of a conducting sample around 0 eV. The DOS gradually increases after the Fermi edge of the Cu VB for ~ 2.0 eV, after which it rises sharply to form a

spectral maximum. A secondary maximum occurs at ~ 4.0 eV, with a slight shoulder featured at ~ 5.0 eV that gradually tails off to complete the Cu *d* band at ~ 8.0 eV, in agreement with previous observations.[104] The general spectral shapes and relative energy positions of these key features are well represented, although the position of the shoulder at ~ 5.0 eV is slightly overestimated by all three simulated spectra. The intensity of the feature around the Fermi level and the distance to the spectral maximum are generally underrepresented by the theoretical spectra. There is also a slight discrepancy in the appearance of the DOS near the spectral maxima. Steiner et al. showed that surface states in the XPS VB of metallic Cu were responsible for a discrepancy to the bulk structure calculated spectrum in this region.[104]

The experimental Ag VB similarly exhibits a ledge feature below the Fermi level, that gradually increases slightly in intensity until a sharp increase at around ~ 4.0 eV. At higher BEs, there is another maximum close in proximity at ~ 5.0 eV with almost the same intensity, and a small shoulder around ~ 6.0 eV. This is followed by a more resolved peak feature around ~ 7.0 eV, after which the intensity decays to the background at ~ 9.0 eV. The simulated spectra for the silver metal have the poorest agreement with the experimental data, although the general features are still reproduced. Four distinct features can be identified, however, the relative intensity and position of the two higher BE features are slightly overestimated. Similarly to Cu, the BE difference between the Fermi edge and the spectral maximum is smaller in the calculated spectrum than in the XPS spectrum. The agreement is improved, particularly the appearance of the DOS near the Fermi edge, when the contributions from the *s* and *p* orbitals are reduced, i.e. by utilizing the YL* cross-section correction method over the YL values or the plain DOS. Panaccione et al. similarly found that increasing the ratio of the *d*:(*s*+*p*) orbital intensities in the DFT calculated DOS led to a better agreement with the XPS spectrum of Ag(111).[85]
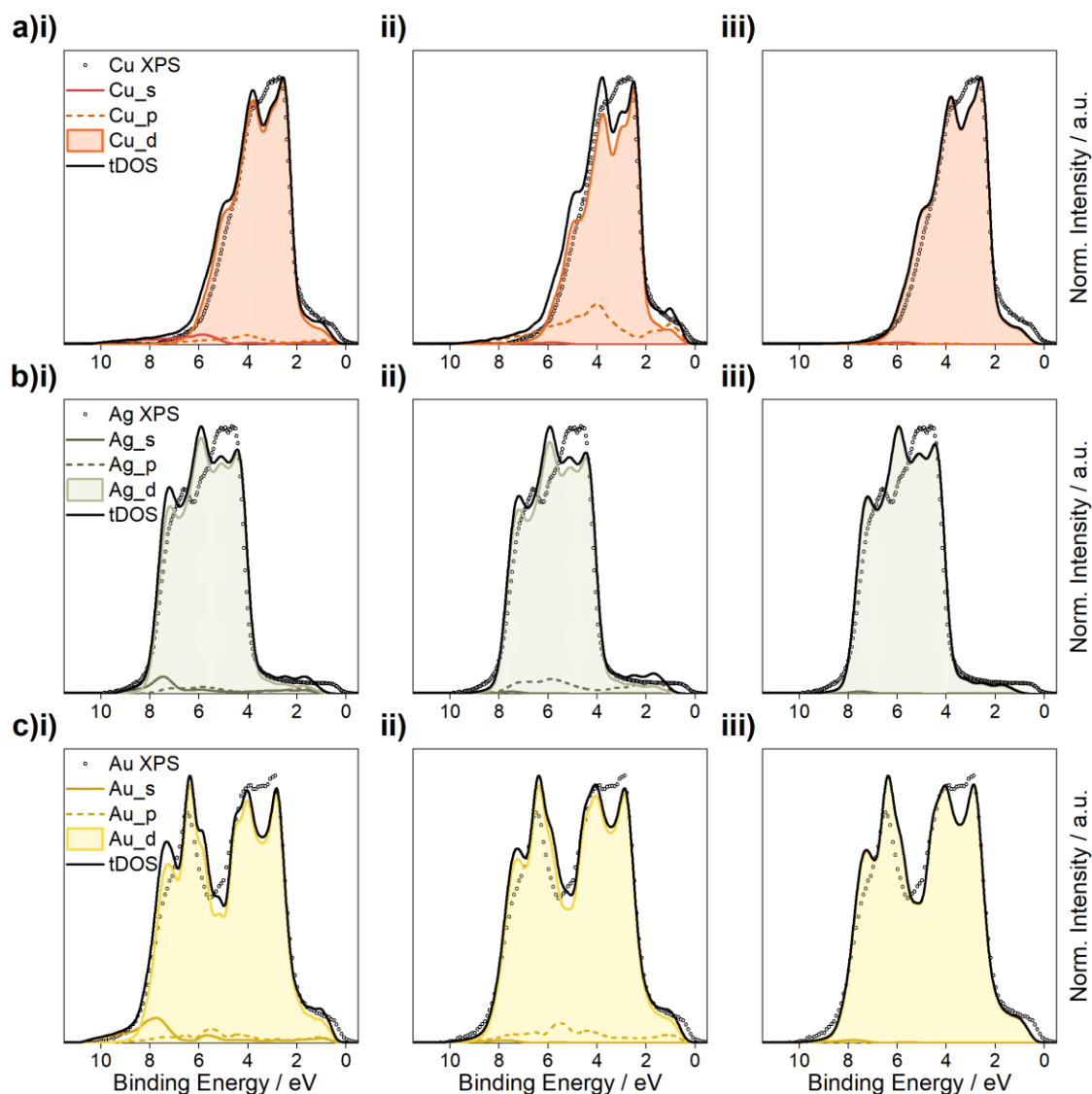
Figure 2.5. VB XPS spectra for the Group 11 metallic series **a)** Cu **b)** Ag and **c)** Au, fitted with PBEsol DFT simulated spectra. The pDOS have been broadened by Lorentzian and Gaussian functions to simulate lifetime and instrumental/vibrational broadening effects, respectively. A fixed Lorentzian component of 0.1 eV was applied in each case. The Gaussian component has been optimised and is discussed in the text, but is close to the nominal instrumental resolution of 0.4 eV in all cases. The array of spectra have been simulated using **i)** plain pDOS, **ii)** pDOS corrected with YL photoionization cross-section values, and **iii)** pDOS corrected with modified YL photoionization cross-section values (YL*).

Turning to the gold valence bands, the double lobed shape of the VB is reproduced well by all three approaches. As previously mentioned, and was also found in the early work of Shirley,[92] relativistic effects need to be incorporated to produce this characteristic shape. The first lobe begins at a BE ~ 2.0 eV higher than the Fermi edge, following a sharp increase in intensity to form the VB spectral maximum. A small shoulder feature

appears around ~ 4.0 eV, after which the intensity decays, before another sharp rise to the maximum of the higher BE lobe at ~ 6.5 eV. Another small shoulder appears at ~ 7.5 eV, after which the intensity decays to background level by around ~ 10.0 eV. Whilst all three approaches yield good representation of the key spectral features and relative energy positions, the relative intensity of the higher BE lobe is too high in the simulated spectra. This was also the case in Shirley's comparison with contemporary broadened band structure calculations.[92]

For the three metallic VBs there are some discrepancies in the fit around the Fermi edge and the inelastic tail. It is possible that higher levels of theory would better reproduce these regions. Kahla et al. found that using the GW+C approach, which includes lifetime effects, the inelastic tail in the VB spectrum of tungsten metal was much better reproduced than when using DFT. In addition, the appearance of the inelastic tail is affected by the method of background modelling and subtraction, which could affect the agreement. Another potential source of disagreement originates in the fundamental differences between the theoretical ground state and the XPS spectrum. XPS spectra are inherently affected by final state effects that will cause various deviations from the undisturbed ground state.[79] There are also potential shortcomings of DFT in the approximations of the exchange and correlation potentials, again pointing to the limitations of the current simulation methods. Furthermore, the simulated VBs are derived from bulk structure calculations, whilst XPS is a surface sensitive technique. Despite all these potential limitations, the DFT simulated VB spectra are still able to reproduce the experimental VB, and the fitting method allows evaluation of photoionization cross-section correction methods and spectral broadening optimisation.

2.3 Valence Electronic Structure of Cs_2TeX_6 series, X = Cl, Br, I

2.3.1 Review: Vacancy-ordered double perovskite semiconductors

Halide perovskite semiconductors have received a huge amount of interest among the sold-state chemistry and materials science communities due to their potential application in solar cell devices and encouraging reported efficiencies.[105-107] There are, however, several drawbacks when using this particular class of material, including ambient hydrolysis and phase transitions affecting long-term stability, and the presence of toxic lead compounds limiting widespread use.[108, 109]

To circumvent these issues, and to produce materials that exhibit analogous photovoltaic and optical performance, alternative structural and compositional derivatives of the archetypal ABX_3 perovskite family have been developed. Such variants include the double perovskite structure $(A_2B'B''X_6)$, which can exhibit rock-salt ordering of the B' and B" metal cations, thus offering a huge platform for substitution possibilities and potential application in photovoltaics.[110, 111]
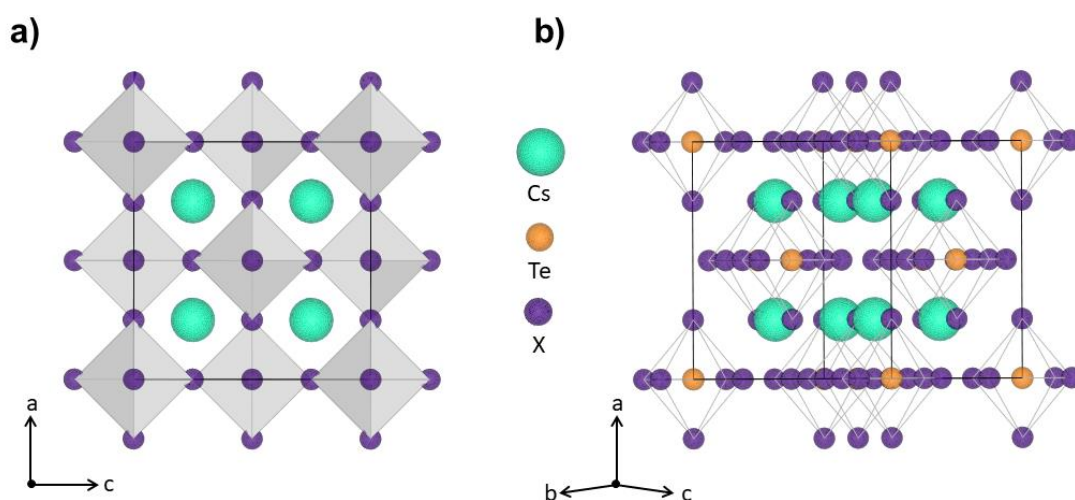

Figure 2.6a) The crystal structure of Cs_2TeX_6 compounds viewed along the [010] direction, **b)** a slightly rotated view, revealing the $[TeX_6]^{2-}$ octahedral units. The Cs, Te and X atoms are denoted by turquoise, orange, and purple spheres, respectively. The X site is filled by Cl, Br, or I atoms in the series investigated in this work.

An exciting structural variant can be formed by replacing one of the B cation sites with a vacancy, creating a material with the formula A_2BX_6, known as vacancy-ordered double perovskites (**Figure 2.6.**). A study by Lee et al. into Cs_2SnI_6 for application into next-generation solar cells demonstrated that caesium tin(IV) iodide can be used as a hole transporter in a solid-state dye-sensitised solar cell (DSSC),[112] and rekindled interest in the vacancy-ordered double perovskite family.[113]

The tellurium-based Cs_2TeX_6 (X = Cl, Br, I) system has been studied by Folgueras et al. as a route to explore the fundamental octahedral building block $[TeX_6]^{2-}$, and the effect of its isolation on the electronic and structural properties of these compounds.[114] The tuneable properties arising from substitution of the X site halide results in different potential applications, for example Cs_2TeCl_6 has been employed as a humidity sensor.[115]

In the present work, the valence electronic structure of the Cs_2TeX_6 (X = Cl, Br, I) series is studied experimentally with XPS and theoretically through DFT electronic structure calculations using the fitting method developed for the Group 11 metals (**Section 2.2.4**). For this group of materials, the approach is extended to include both PBEsol and hybrid HSE06 DFT calculations, together with additional corrections for van der Waals (vdW) forces and SOC effects.

2.3.2 Experimental Section

Preparation of Cs$_2$TeX$_6$ (X = Cl, Br, I) compounds

Analytical-grade reactants of Cs_2CO_3, TeO_2, HCl solution, HBr solution and HI solution were purchased from Sigma-Aldrich and used without further purification. The Cs_2TeX_6 (X = Cl, Br, I) compounds were synthesised via an adaptation of the method described by Lee et al.[112]

Cs$_2$TeI$_6$. In a beaker, 1.32 g TeO_2 was dissolved in excess HI solution and stirred to dissolve to produce a TeI_4 solution. Acetonitrile was added to help the TeO_2 dissolve. In a separate beaker, 2.70 g Cs_2CO_3 was added to excess

HI solution to produce a CsI solution. The addition was done slowly to account for the vigorous reaction producing CO_2 and heat. Once the solids were all dissolved, The CsI solution was added quickly to the TeI_4 solution, which resulted in a black precipitate that immediately crashed out of solution. The same procedure was used to prepare the X = Br analogue using HBr solution and forming an orange precipitate, and for the X = Cl analogue using HCl solution and forming a yellow precipitate. The resulting solids were filtered and washed with diethyl ether and dried at 60 °C.

XPS Characterisation of Cs₂TeX₆ (X = Cl, Br, I) compounds

XPS was carried out using a Thermo Scientific K-Alpha spectrometer equipped with a monochromated Al K-alpha x-ray source (1486.6 eV) in constant analyser energy mode. Photoelectrons were collected at normal emission with a spot size of 400 μm. Sample charging was prevented by use of a dual beam flood gun. A pass energy of 150 eV was used to record survey spectra and pass energies of 20 eV and 30 eV were used to record high resolution VB and core level spectra, respectively. Core and valence spectra were processed differently, using CasaXPS.[97] A Shirley background was used for all spectra.

Core level spectra were used to characterise the compounds and were thus charge corrected to gain more reliable binding energies (**Section 1.2.1.5**). Charge correction was performed by calibration with the adventitious carbon spectrum, based on the fitting method demonstrated by Biesinger et al. to give meaningful and satisfactory results in 95 % of 522 cases assessed.[30] The peak model (line shape Gaussian 70 % - Lorentzian 30 %) consists of a main peak assigned to alkyl type carbon (C-C, C-H). A second peak, constrained to have the same FWHM and a binding energy 1.5 eV higher than the main alkyl peak is added, which is ascribed to alcohol and/or ester functionality (C-OH, C-O-C). Additional components 2.8-3.0 eV and 3.8-4.3 eV higher than the main peak are added, again constrained to

the same FWHM, and ascribed to C=O and O-C=O functionality, respectively.

Experimental VB spectra were smoothed using a 5-point moving average filter, and the VBM was aligned to 0 eV by fitting the low binding energy edge with a complementary error function, which locates the point of intersection of straight lines fitted to the leading edge and the baseline. This method is known as linear extrapolation and is discussed in more detail in (**Section 1.2.1.7**).

2.3.3 Computational Methodology

Calculations were performed using the Vienna *Ab initio* Simulation Package (VASP).[98] The convergence criterion for the k-point density and the plane wave cut-off energy parameters was that the total energy was converged to within 1 meV per atom. The resulting converged parameters are listed in **Table 2.4**.

Table 2.4. Converged plane wave cut-off energies and k-point densities for the selected materials (Cs_2TeX_6, X = Cl, Br, I)

Material	Plane Wave Cut-off Energy / eV	k-point density
Cs_2TeCl_6	350	3 x 3 x 3
Cs_2TeBr_6	250	3 x 3 x 3
Cs_2TeI_6	200	4 x 4 x 4

Several functionals were used in this work: PBEsol and HSE06. For geometry relaxation both functionals were implemented, with and without the addition of Grimme's D3 dispersion correction.[58] Electronic structure calculations were performed using both functionals, with and without the inclusion of spin-orbit coupling. Spin-orbit coupling (SOC) effects are expected to be significant in elements heavier than Sb,[99, 100] therefore SOC was included for all compounds after converging the k-point density.

The electronic structure calculations were first performed without the inclusion of spin-orbit coupling for a series of k-point meshes with

increasing density to converge the appearance of the calculated density of states (DOS). As the simulated spectra in this work are compared graphically with experimental spectra it is important that the appearance of the DOS is converged. Therefore, a convergence criterion was introduced that after broadening the DOS by the instrumental resolution of 0.4 eV, there were no significant changes in appearance on increasing the k-point density. A second criterion for the electronic structure k-point density convergence is no significant change in the calculated band gap. Full details showing the convergence testing is in **Appendix A**. For all materials, a k-point density of 7x7x7 was deemed sufficient and was used subsequently when including spin-orbit coupling effects.

Photoionization Cross-section Correction Method

In this work, the values reported by Yeh and Lindau (YL),[84] and a second set of values modified from the original YL values, denoted modified YL (YL*), are investigated, as described in more detail in (**Section 2.1.2**) The values used for the materials in this section are reported in **Table 2.5** below.

Table 2.5. Energy dependent photoionization cross-section values used in this work for Cs, Te, Cl, Br and I. The top set are those reported by Yeh and Lindau (YL).[84] The bottom set (YL*) contain some values that have been modified, indicated by the shaded rows. The 'ratio' method used to modify these values is detailed in **Table A2**.

Cs		Te		Cl		Br		I	
YL		**YL**		**YL**		**YL**		**YL**	
5s	1.250E-03	**5s**	8.500E-04	**3s**	1.25E-03	**4s**	1.3E-03	**5s**	9.50E-04
5p	9.667E-04	**5p**	6.500E-04	**3p**	3.80E-04	**4p**	9.0E-04	**5p**	7.60E-04
4d	7.200E-03	**4d**	4.900E-03			**3d**	3.9E-03	**4d**	5.60E-03
YL*		**YL***		**YL***		**YL***		**YL***	
6s	1.098E-04	**6s**	6.741E-05	**4s**	8.24E-05	**5s**	9.62E-05	**6s**	7.534E-05
6p	4.685E-05	**5p**	6.500E-04	**3p**	3.80E-04	**4p**	9.00E-04	**5p**	7.60E-04
5d	5.758E-04	**5d**	3.915E-04			**4d**	2.50E-04	**5d**	4.376E-04

2.3.4 Results

XPS Characterisation

The survey and core level regions were recorded to characterise the samples obtained (**Figures 2.7, 2.8**). The survey spectra demonstrate that the expected elements are present in each case, with negligible contamination. Elemental quantification using the survey spectra are found in **Appendix A**. Elemental quantification by region was also performed using the high-resolution scans (**Figure 2.8**), showing the resulting compounds are close to the nominal composition (**Table 2.6**). Supporting characterisation by PXRD can be found in **Appendix A**.

Table 2.6. Elemental quantification by region from high resolution XPS spectra of the selected materials Cs_2TeX_6, X = Cl, Br, I.

Sample Identifier	Name	Raw Area	%At Conc	Ratio	Rounded Ratio
Cs_2TeCl_6	Cs 3d	572330	28.09	2.2	2
	Te 3d	203155	12.92	1.0	1
	Cl 2p	69144	58.98	4.6	5
Cs_2TeBr_6	Cs 3d	505609	31.49	2.6	3
	Te 3d	150493	12.14	1.0	1
	Br 3d	64278	56.37	4.6	5
Cs_2TeI_6	Cs 3d	261899	27.5	2.4	2
	Te 3d	84241	11.47	1.0	1
	I 3d	491712	61.03	5.3	5

The core level spectra have been charge corrected according to the procedure in (**Section 1.2.1.5**) using the AdC C 1s region (**Figure 2.7**). The Cs 3d signal (**Figure 2.8**) is composed of two different signals that are separated due to spin-orbit coupling: the lower binding energy peak arises from the Cs $3d_{5/2}$ peak and the higher binding energy peak from the Cs $3d_{3/2}$ state. The Cs $3d_{5/2}$ peak is around 724.4 eV for all three compounds synthesised, which is consistent with Cs(I) in related material Cs_2SnI_6.[116] The Te 3d signal is also split into a doublet consisting of Te $3d_{5/2}$ and Te $3d_{3/2}$ peaks. The Te $3d_{5/2}$ peak appears at 576.9 eV, 576.2 eV and 575.19 eV, for X=Cl, Br, and I, respectively. The binding energy of 576.9 eV is in perfect agreement with another compound containing $[TeCl_6]^{2-}$ octahedra in the literature,

$(NH_4)_2[TeCl6]$.[117] The trend in decreasing binding energy can be rationalised by the decreasing electronegativity of the X anion, following Cl>Br>I.

Turning to the binding energies of the halide X site anions, the Cl 2p signal is split into a doublet, with the $2p_{3/2}$ and $2p_{1/2}$ peaks overlapping. The Cl $2p_{3/2}$ signal is centred at 198.8 eV. The Br 3d signal is also split into an overlapping doublet, with the Br $3d_{5/2}$ peak centred at 68.9 eV. The narrow scan also captures the Cs 4d level, with the $4d_{5/2}$ peak centred at 75.6 eV. The I $3d_{5/2}$ peak appears around 619.1 eV, which is in close agreement of the recorded value of 619.0 eV in related material Cs_2SnI_6.[116] The I 3d scan also contains loss features.
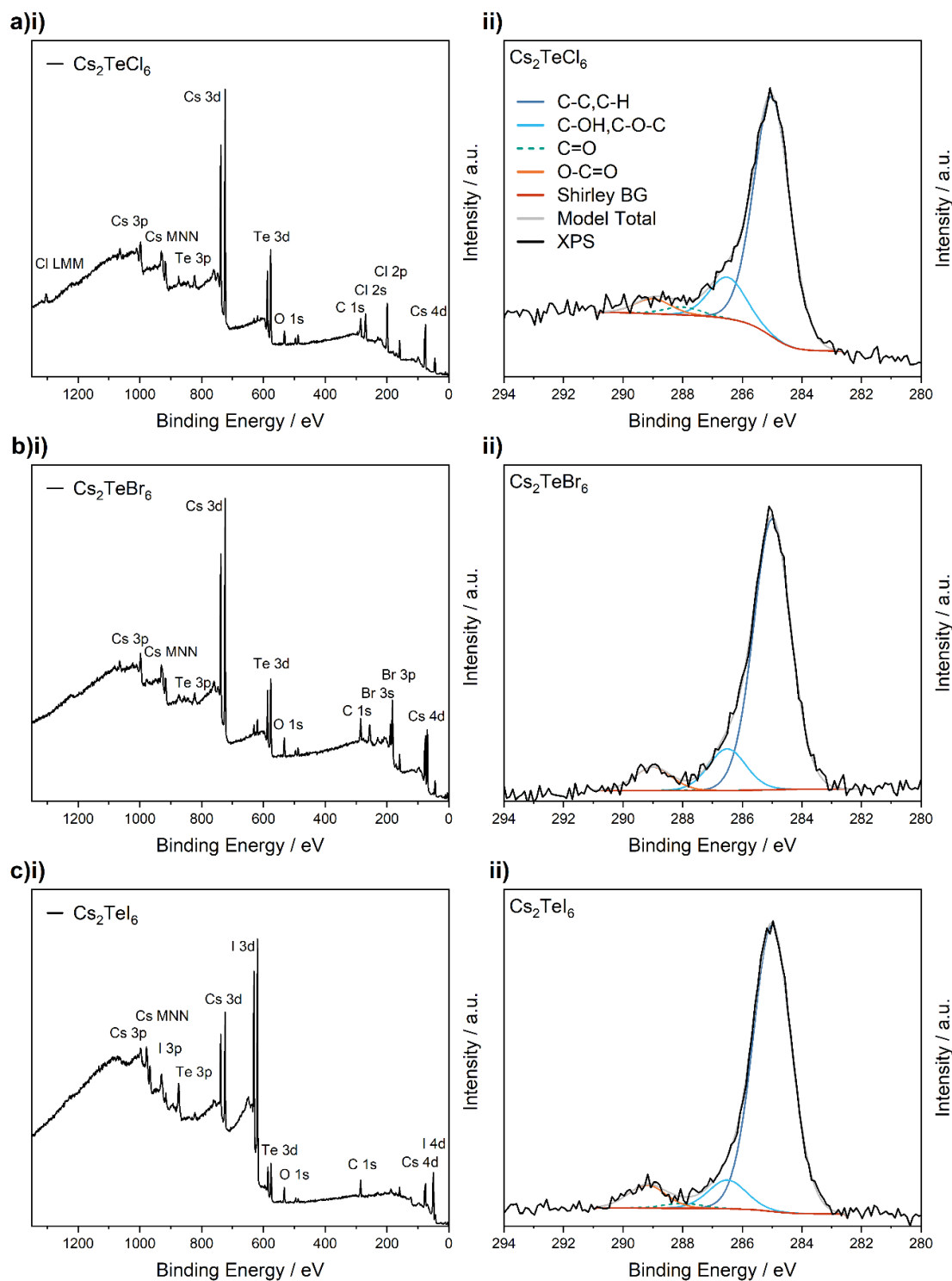
Figure 2.7. Selected XPS spectra for the series of Cs_2TeX_6 compounds **(a-c)** X = Cl, Br, I, showing **i)** survey spectra and **ii)** high resolution C 1s scans. The 'C-C, C-H' component in the peak model indicated in **(ii)** was calibrated to 285 eV and was used to charge correct all other narrow scans within the same compound.
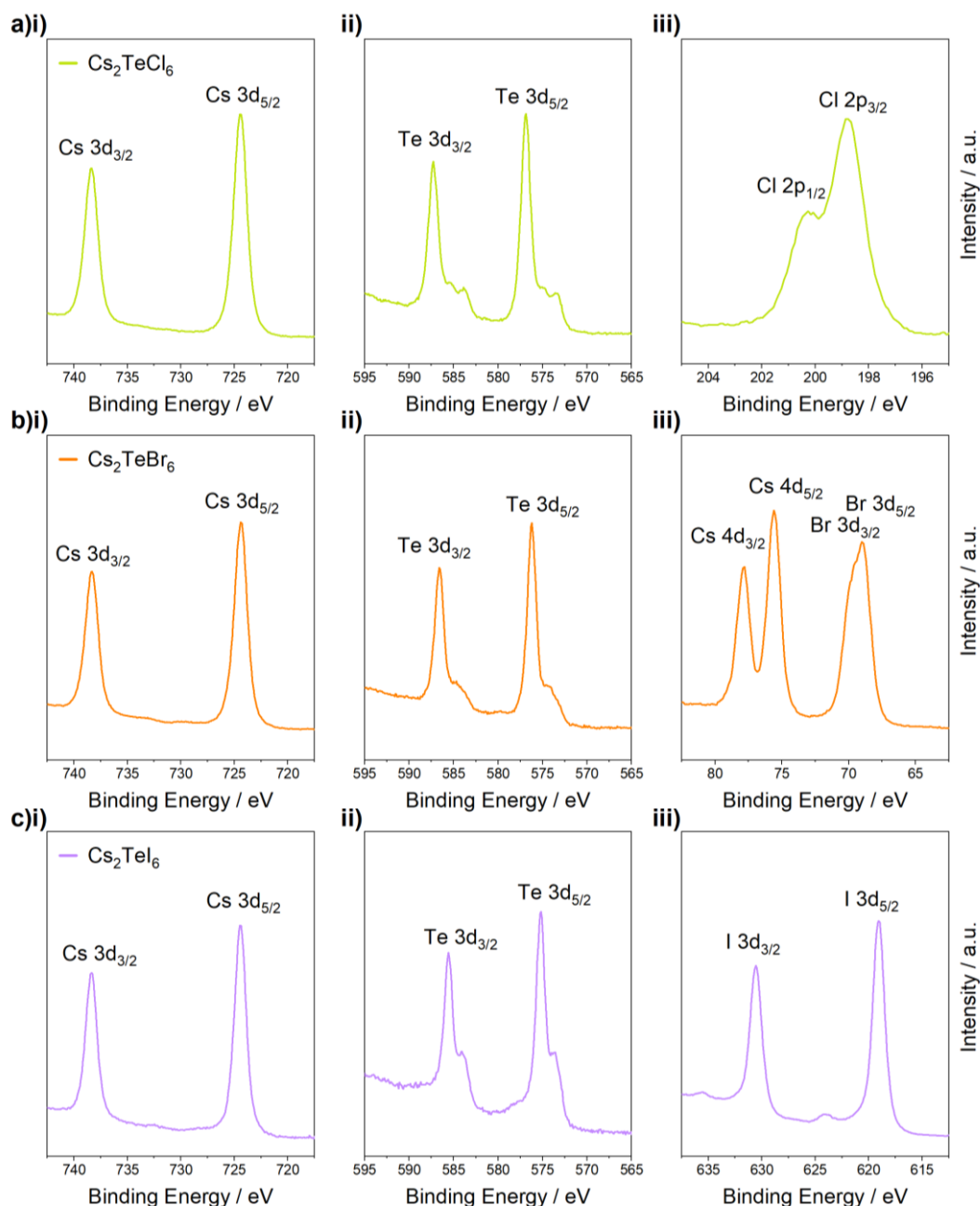
Figure 2.8. Core level XPS spectra for the series of Cs_2TeX_6 compounds **(a-c)** X = Cl, Br, I, showing high resolution scans for the regions: **i)** Cs 3d **ii)** Te 3d and **iii)** Cl 2p, Br 3d, I 3d.

Geometric Structure

The Cs_2TeX_6 (X = Cl, Br, I) family all crystalise in the space group Fm-3m, with the antifluorite structure K_2PtCl_6. The presence of the isolated $[TeX_6]^{2-}$ octahedra in the structure means there is potential for intermolecular interactions between them, such as van der Waals (vdW) forces. All structures were geometrically optimised using the PBEsol and HSE06 functionals, both with and without a correction to treat these vdW

interactions. After geometry optimisation, all compounds retained their cubic Fm-3m structure. The calculated a lattice parameters are recorded and compared to reference experimental data in **Table 2.7**. [118-120] All calculated and experimental data exhibit an increasing a parameter in the order X = Cl < Br < I, due to the increasing ionic radius of the X site anion.

Table 2.7. Calculated and experimental lattice parameters for Cs_2TeX_6 (X = Cl, Br, I) using GGA DFT (PBEsol) and hybrid DFT functionals (HSE06), both with and without correction for vdW interactions (Grimme's D3 correction). The lattice parameter errors (Δa) are given with respect to literature values[a].

	Cs_2TeCl_6	Cs_2TeBr_6	Cs_2TeI_6
Experiment	10.450 Å	10.918 Å	11.700 Å
PBEsol	10.434 Å	10.837 Å	11.584 Å
PBEsol + vdW	10.360 Å	10.780 Å	11.521 Å
HSE06	10.746 Å	11.141 Å	11.952 Å
HSE06 + vdW	10.597 Å	10.997 Å	11.817 Å
Δa PBEsol	-0.1 %	-0.7 %	-1.0 %
Δa PBEsol + vdW	-0.9 %	-1.3 %	-1.5 %
Δa HSE06	2.8 %	2.0 %	2.2 %
Δa HSE06 + vdW	1.4 %	0.7 %	1.0 %

[a] The experimental lattice parameters were sourced from ICSD references: Cs_2TeCl_6,[118] Cs_2TeBr_6,[119] and Cs_2TeI_6.[120]

Inclusion of the vdW correction results in lattice contraction independent of the DFT functional choice (0.6 % for PBEsol and 1.3 % for HSE06). The lowest mean absolute errors (MAEs) compared with experiment were 0.6 % and 1.0 % for PBEsol and HSE06 + vdW, respectively. The highest MAEs were 1.2 % and 2.3 % for PBEsol + vdW and HSE06, respectively. It has been demonstrated by Kavanagh et al. that vdW corrections lead to a contraction of calculated lattice constants when including dispersion corrections for related vacancy-ordered titanium halide perovskites (Cs_2TiX_6, X = Cl, Br, I), independent of the choice of DFT functional.[121] The work of Kavanagh et al. shows that the inclusion of dispersion forces when using hybrid DFT improves the agreement with experimental lattice parameters from ~3 % to < 1 %, which is comparable to the results

presented here. They also suggest that, given the uniform contraction across all functionals studied, the low MAEs for uncorrected PBEsol are likely to arise from a cancellation of errors.

Electronic Structure

Electronic structure calculations were performed for all optimised structures (**Table 2.7**), to investigate the influence of the functional choice (PBEsol or HSE06) and the effect of additional corrections (vdW and/or SOC). The array of calculated DOS resulting from these various levels of theory are compared to the experimental valence electronic structure in **Figure 2.9**. The collected XPS data is normalised to the intensity of the lowest level of theory for each functional (i.e. plain PBEsol/HSE06), and has been shifted along the binding energy axis to overlap with the calculated DOS, which by default have the VBM situated at 0 eV. Broadening the calculated DOS by the nominal instrumental resolution of 0.4 eV does not lead to a good reproduction of the spectral shape and is discussed later.

Key features in the experimental valence electronic structure for the Cs_2TeX_6 compounds (X = Cl, Br, I) are identified within the region 10 eV below the VBM and labelled **I-VI**. An increased binding energy indicates electronic states that are more tightly bound, thus denoting deeper valence levels. In Cs_2TeCl_6 and Cs_2TeBr_6, the upper valence band region (around $0 - 3$ eV) can be divided into two major features: a low intensity feature (**I**) near the VBM and a principal maximum (**II**) around 1.5 eV. There exists a small shoulder (**III**) to the high binding energy side of feature **II**, and a smaller feature (**IV**) around 4.5 eV. In the case of Cs_2TeI_6, feature **I** is much higher in intensity and overlaps more with feature **II**. Additionally, feature **III** is more pronounced for the iodide compound, and there appears some 'tail' like structure in feature **IV**. The Cs 5p semi-core level appears at higher BEs in all compounds and is split into a doublet, representing the Cs 5p 3/2 (**V**) and Cs 5p 1/2 (**VI**) states.
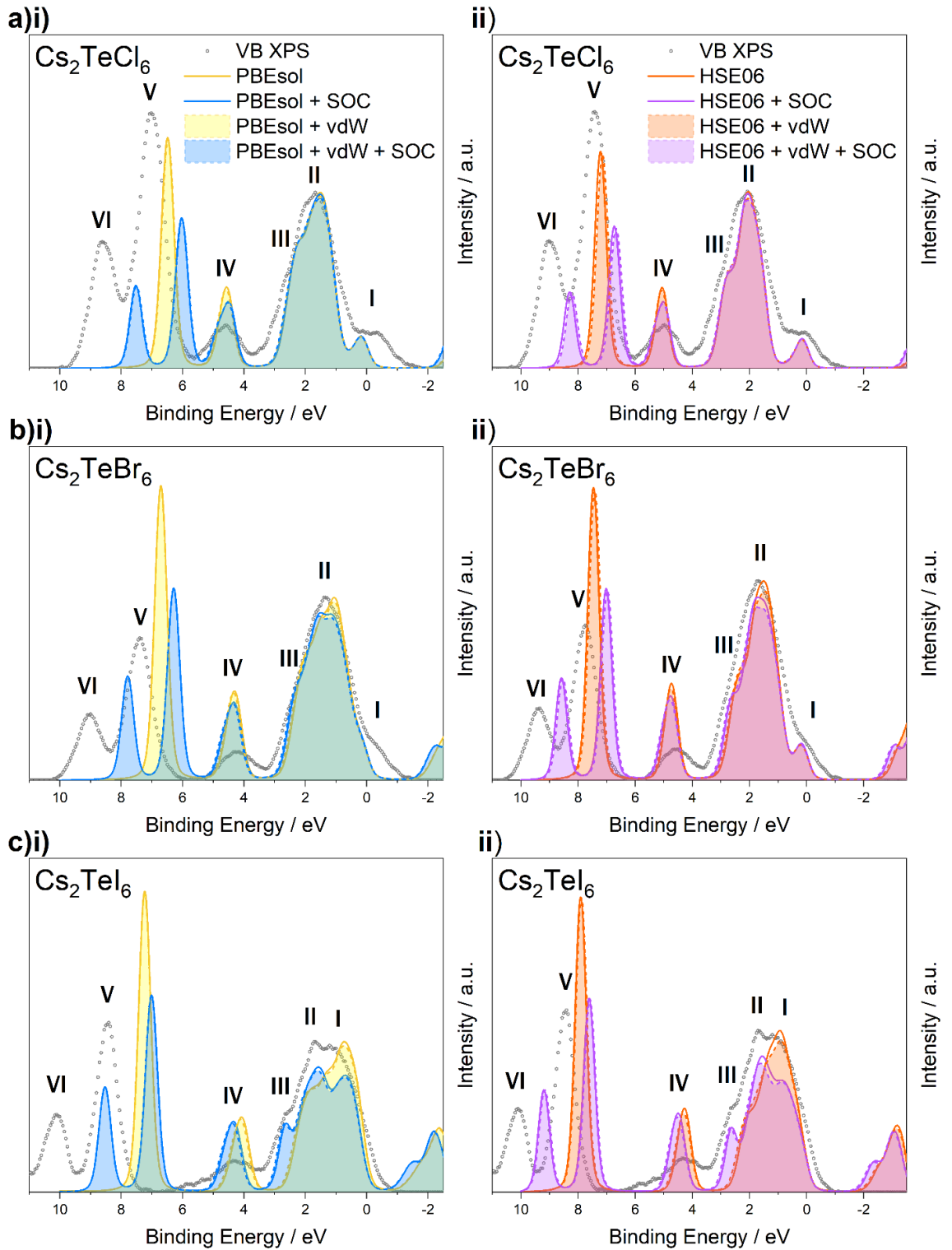
Figure 2.9. VB XPS spectra for the series of Cs$_2$TeX$_6$ compounds **(a-c)** X = Cl, Br, I, together with DFT calculated DOS using **i)** PBEsol and **ii)** HSE06 functionals and various corrections. The experimental VB is normalised to the VB spectral maximum of **i)** PBEsol and **ii)** HSE06 and shifted to align with the theoretical DOS, which are broadened by the nominal instrumental resolution of 0.4 eV. Features of interest in the experimental VB have been labelled **I-VI** and are discussed in the text.

For Cs_2TeCl_6, the appearance of features **I-III** are well predicted by both functionals, however, the hybrid theory gives much better agreement with the relative BE positions. The BE difference between feature **I** and **II** is underestimated by the PBEsol DOS. The inclusion of SOC and/or vdW effects has no observable impact on the appearance of features **I-III**. For the SOC effects, this can be rationalised by looking at the pDOS in **Figure 2.10**, and noting that these features are comprised mainly of Cl p orbitals, which are not expected to exhibit large relativistic effects. The inclusion of vdW effects led to slight changes in the lattice parameters (**Table 2.7**), which was more pronounced using the HSE06 functional. The resulting changes in geometric structure only impacts the appearance of the DOS very slightly, which is more significant in the case of HSE06, as expected, and becomes more noticeable going to higher BE features.

Feature **IV** of Cs_2TeCl_6 is similarly well represented by all methods independent of functional choice and additional corrections. There is a slight change in its shape and intensity on inclusion of SOC effects, as this feature contains contributions from heavy Te p orbitals (**Figure 2.10**). There is also some contribution from Cl p orbitals, indicating some degree of hybridization. Finally, SOC effects are required to reproduce the doublet appearance of the Cs $5p$ 3/2 (**V**) and Cs $5p$ 1/2 (**VI**) semi-core states, as expected. Although the theory is able to predict the appearance of the doublet, the BE positions are significantly underestimated by both PBEsol and HSE06 calculations.
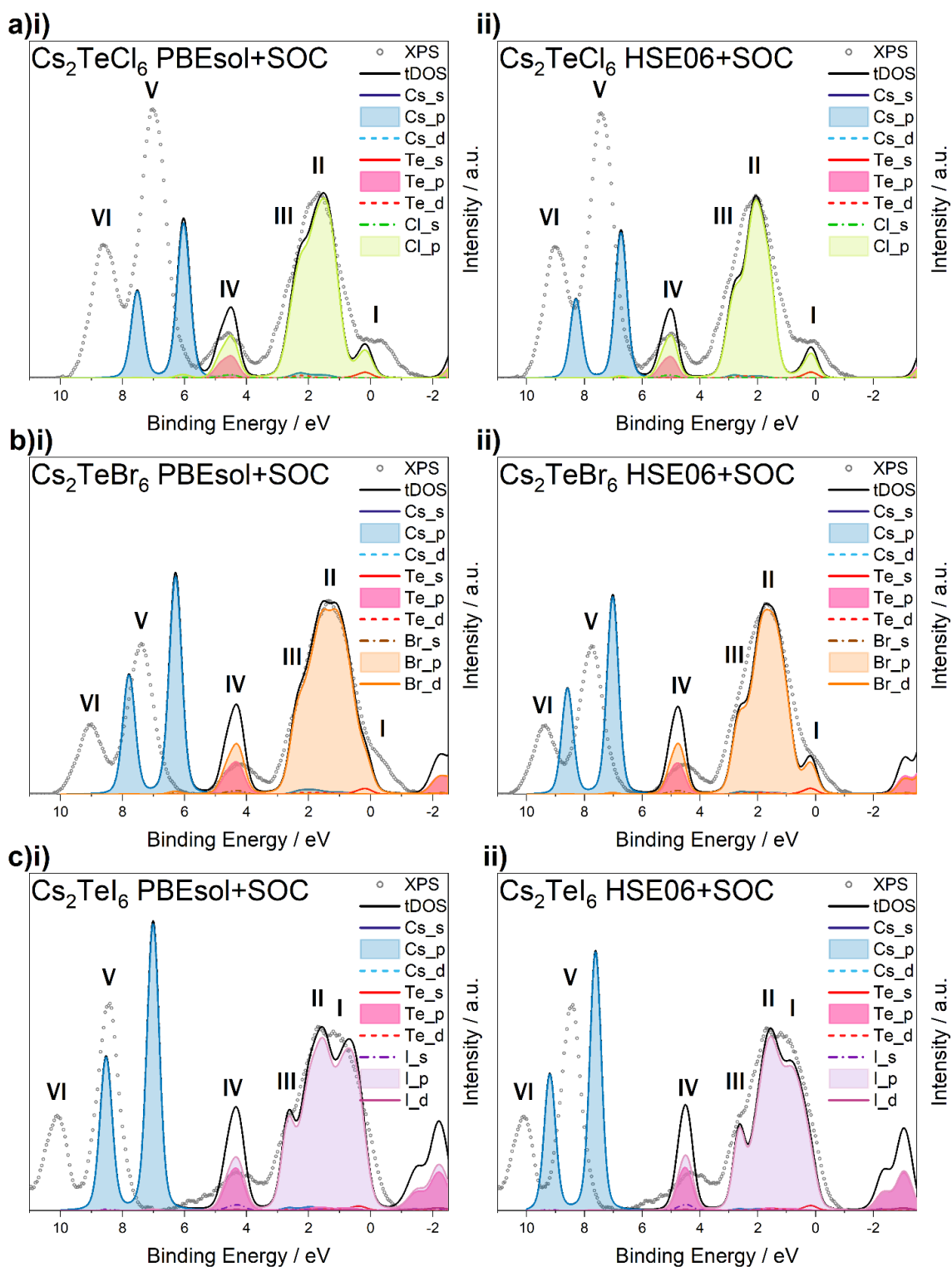
Figure 2.10. VB XPS spectra for the series of Cs_2TeX_6 compounds **(a-c)** X = Cl, Br, I, together with orbital projected DOS calculated using **i)** PBEsol+SOC and **ii)** HSE06+SOC. The experimental VB is normalised to the VB spectral maximum of **i)** PBEsol and **ii)** HSE06 and shifted to align with the theoretical DOS, which are broadened by the nominal instrumental resolution of 0.4 eV. Features of interest in the experimental VB have been labelled **I-VI** and are discussed in the text.

The observations made above can be generally extended to the Cs_2TeBr_6 valence electronic structure, with some slight differences. In the experimental spectrum of the X = Br analogue, feature **I** is closer in BE to the VB spectral maximum (**II**), which is mirrored in the calculated DOS. As seen above in Cs_2TeCl_6, the PBEsol similarly underestimates this BE difference in Cs_2TeBr_6, to the extent that feature **I** and **II** are barely distinguishable in the PBEsol DOS. The HSE06 DOS, however, reproduces both features well. The relative BE of feature **IV** is slightly overestimated in the Cs_2TeBr_6 calculations, and the Cs $5p$ semi-core doublet (**V-VI**) BEs are again severely underestimated.

Turning to the heavy X = I analogue, the incorporation of SOC effects can be seen to impact on all features **I-VI**. This is expected as materials containing iodine are known to display large relativistic renormalization.[99, 100] For either functional, features **I-III** are not reproduced without SOC effects, and the VB width is significantly narrower (**Figure 2.9**). Inspection of the pDOS reveals that these three features originate from the I p orbitals, as expected (**Figure 2.10**). The hybrid DOS gives a more accurate representation of the relative BEs of features **I-III** than the basic theory, which slightly overestimates the difference between **I** and **II**. The appearance of feature **IV**, which is comprised of Te p and I p orbitals, shifts to higher relative BE when including SOC effects, due to the widening of the VB region. As with the X = Cl, Br compounds, the semi-core doublet BE is underestimated relative to the VBM.

As discussed above, the Cs_2TeX_6 VB is mainly comprised of halide X p orbitals, and it can be seen from the pDOS in **Figure 2.10** that the CB is mainly comprised of Te p and X p states, which is consistent with other studies.[122, 123] It is also evident that the band gap decreases with the increasing halide anion size, and is smaller when calculated using PBEsol compared to HSE06. The calculated values for all levels of theory and the trends established are discussed in detail in the next section.

54

Band Gap

The pDOS in **Figure 2.10** clearly show that the size of the band gap (E_g) in the Cs_2TeX_6 compounds decreases with increasing halide X anion size. These findings agree with trends seen in the literature from both experimental and computational sources (**Table 2.8**), with the values obtained varying with the level of theory and corrections applied. Note that the values calculated in this work differ slightly from previous calculated values, particularly the PBEsol values which are slightly smaller in this work. This could be due to the convergence testing in the current study, which was performed based on the appearance of the valence DOS and not the magnitude of the band gap. Nonetheless, the trends in the values depending on the functional and corrections applied are still informative.

The following observations can be made for the series of Cs_2TeX_6, independent of the halide X anion. For PBEsol level of theory, the calculated E_g values in this and other work are smaller than reported experimental values. The tendency for PBEsol to underestimate E_g is widely reported in the literature.[124-127] The inclusion of vdW and/or SOC effects leads to a reduction in E_g with the largest reduction seen when including both corrections, leading to worse agreement with experimental values. The same trends are seen in the HSE06 calculations, however, as the calculated E_g values are overestimated when using this functional, the vdW and SOC corrections here lead to a closer agreement with experiment.

In previous literature reports, the use of hybrid theory has predicted slightly larger band gap values than experiment. Folgueras et al.[114] determine the optical absorption gap of Cs_2TeCl_6 to be 3.15 eV and calculate an indirect band gap of 3.4 eV using HSE06 + SOC. Similarly, they experimentally determine the optical bandgap of Cs_2TeBr_6 to be 2.68 eV and calculate an indirect band gap of 2.7 using HSE06 + SOC. Maughan et al.[123] utilised HSE06 + SOC to calculate an indirect band gap of 1.83 eV for Cs_2TeI_6 and an experimental optical gap of 1.59 eV. The optical gap was determined by

UV-visible diffuse reflectance data. This is in agreement with an experimental optical band gap of 1.52 eV reported by Peresh et al.[128] Cai et al.[122] reported a comparable HSE06 + SOC calculated indirect band gap of 1.98 eV and a larger value of 2.19 eV when using HSE06. They comment that an overestimate of 0.4 eV is acceptable when considering the mean absolute error of HSE calculated band gaps of 0.3eV.[129] It has been suggested by Maughan et al. that the disagreement between experimentally determined and calculated band gaps may arise from the fact that VASP does not account for absorption that arises due to configuration interactions with different excited states, thus obscuring the absorption edge.[123]

As seen in this work and the experimental and computational literature discussed above, the size of E_g depends on the X site halide, and decreases according to the series Cl > Br > I. This trend can be rationalised in terms of the valence electronic structure: the VBM is predominantly comprised of halide p orbitals, which have decreasing binding energies down the series, thus causing a reduction in the band gap. It has also been rationalised using an MO picture: with increasing halide anion size, the electronic structure transitions from more molecular-like in Cs_2TeCl_6 and Cs_2TeBr_6 to more dispersive in Cs_2TeI_6, due to the greater MO overlap between neighbouring $[TeX_6]^{2-}$ octahedra.[114]

Table 2.8. Experimental and calculated band gap values from the literature and the current work for the selected materials Cs_2TeX_6, X = Cl, Br, I.

Material	Calculated Level of Theory	Calculated E_g (This Work) / eV	Calculated E_g (Literature) / eV	Experiment E_g / eV
			Indirect	
Cs_2TeCl_6	PBEsol	2.61	2.55[115],2.76[130],3.07[131]	3.15[114]
	PBEsol + vdW	2.57		
	PBEsol + SOC	2.51	2.61[130]	
	PBEsol + vdW + SOC	2.47		
	HSE06	3.70		
	HSE06 + SOC	3.56	3.4[114]	
	HSE06 + vdW	3.63		
	HSE06 + vdW + SOC	3.50		
Cs_2TeBr_6	PBEsol	1.93	2.16[130]	2.20[128],2.68[114]
	PBEsol + vdW	1.90		
	PBEsol + SOC	1.85	2.04[130]	
	PBEsol + vdW + SOC	1.81		
	HSE06	2.92		
	HSE06 + SOC	2.82	2.7[114]	
	HSE06 + vdW	2.82		
	HSE06 + vdW + SOC	2.73		
Cs_2TeI_6	PBEsol	1.18	1.39[130]	1.59[123],1.52[128]
	PBEsol + vdW	1.14		
	PBEsol + SOC	0.96	1.16[130]	
	PBEsol + vdW + SOC	0.92		
	HSE06	2.21	2.19[122]	
	HSE06 + SOC	2.00	1.83[123],1.98[122]	
	HSE06 + vdW	2.10		
	HSE06 + vdW + SOC	1.91		

XPS/DFT VB Fitting

This section looks at the effect of cross-section correction and spectral broadening on the goodness of fit of DFT simulated VB spectra and XPS VB spectra, for the series of perovskite compounds Cs_2TeX_6, X = Cl, Br, I. The method of fitting the experimental and simulated spectra is the same as was described in **Section 2.2.4**, but this time the effect of either PBEsol and HSE06 DOS corrected with YL or YL* photoionization cross-sections is

57

investigated. The goodness of fit for the array of simulated spectra with respect to the applied spectral broadening is shown by the RSS curves in **Figure 2.11**. As can be seen from the minima of these curves, the optimised Gaussian component is much higher than the nominal instrumental resolution of 0.4 eV.
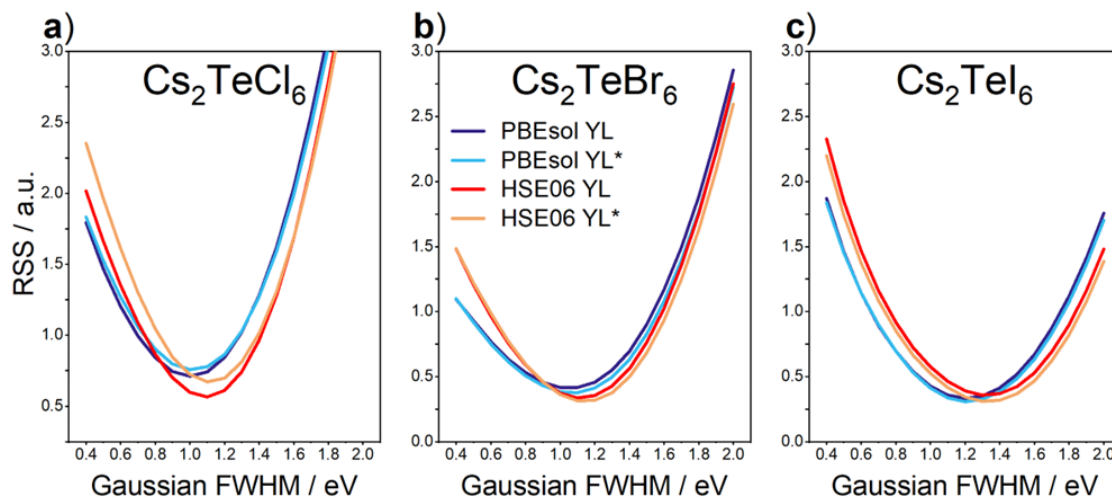

Figure 2.11. Optimisation of the Gaussian broadening applied to theoretical spectra in the Cs_2TeX_6 series **a)** X = Cl **b)** X = Br **c)** X = I. A fixed Lorentzian component of 0.1 eV was applied in each case. The RSS was calculated by fitting with VB XPS spectra for both PBEsol and HSE06 functionals, corrected by either YL or modified YL cross-sections (YL*), as indicated in **b)**.

The optimised spectral broadening lies between $1.0 - 1.3$ eV, depending on the material and simulation method. Changing the photoionization cross-section method (i.e. YL or YL* values) does not affect the optimised broadening in any case. The optimised Gaussian components for the PBEsol spectra were 1.0 eV, 1.1 eV and 1.2 eV for X = Cl, Br, and I, respectively. These values when using the HSE06 functional were 1.1 eV, 1.1 eV and 1.3 eV. The array of simulated spectra resulting from the different theory and photoionization cross-section methods are plotted for and HSE06 in **Figure 2.12**, showing the effects of using either the nominal instrumental resolution of 0.4 eV, or the optimised broadening values from **Figure 2.11**. Despite the reduced goodness of fit for the PBEsol spectra (**Appendix A**), this does not seem to have any significant impact on the broadening optimisation, indicating that the more basic theory may be adequate for investigating this parameter.
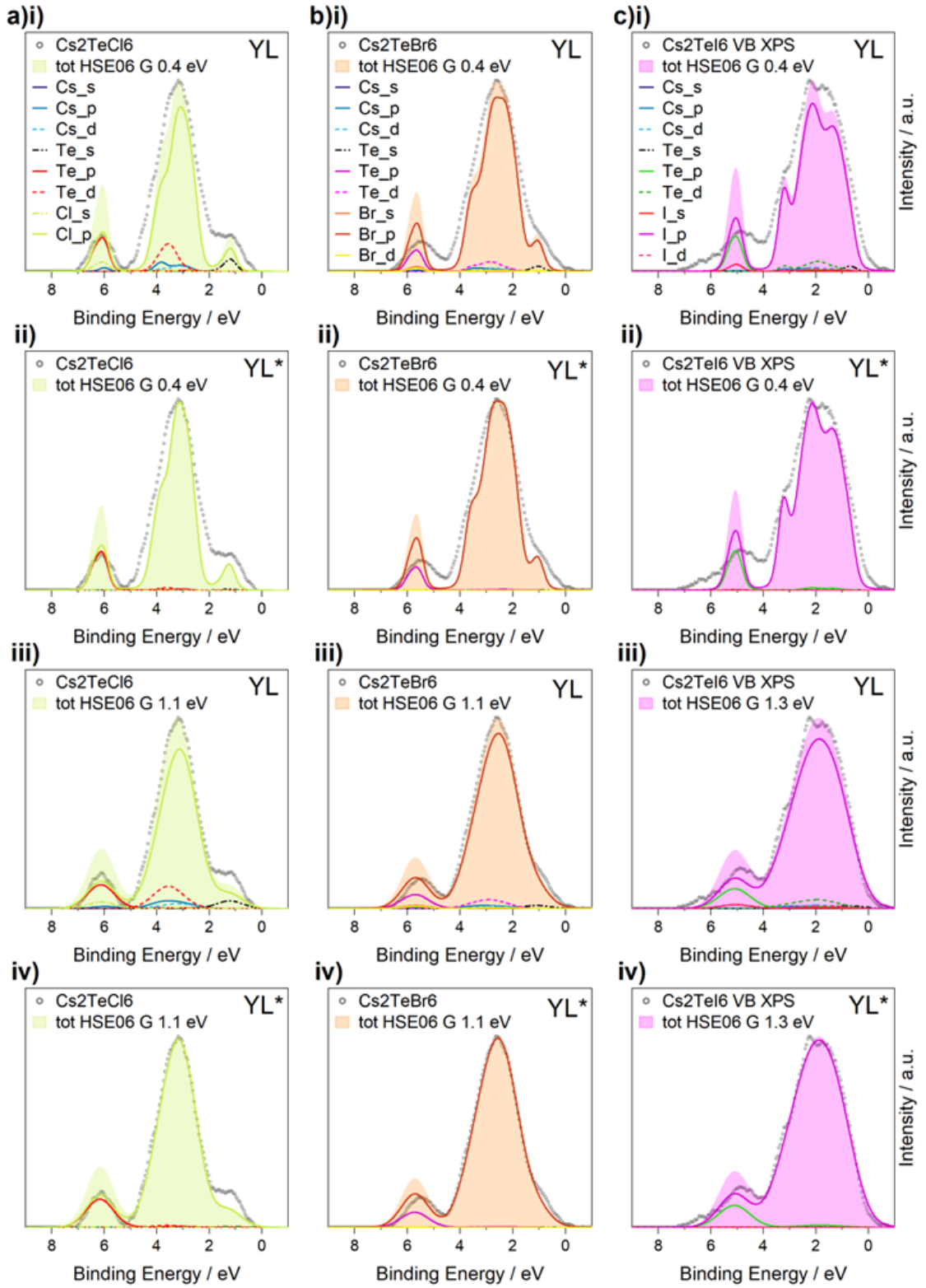
Figure 2.12. VB XPS spectra for the series of Cs_2TeX_6 compounds **(a-c)** X = Cl, Br, I, fitted with PBEsol DFT simulated spectra. The calculated DOS broadened by the nominal instrumental resolution of 0.4 eV and corrected by **i)** YL cross-sections, **ii)** modified YL cross-sections (YL*). The Gaussian component of the broadening optimised for **iii)** YL and **iv)** YL*

59

Clearly the increased spectral broadening produces a much better agreement between the experimental and theoretical spectra. Modifying the cross-section correction method from YL to YL* does not significantly alter the overall appearance of the simulated spectra, and results in similar RSS values. Areas of discrepancy include the VBM region of the Cs_2TeCl_6 spectra, which has a lower spectral intensity in the theoretical spectra. This is also seen to a much lesser degree in the case of the X = Br analogue. The spectral intensity of the secondary maximum feature is also not well reproduced for any of the compounds, which may arise from some error in the photoionization cross-section values, or the method of background modelling and subtraction. The increased broadening applied in the X = I analogue is expected to arise from the broader secondary maximum, which appears to be affected by some decay, judging from the spectral shape. This could well be the case, as Cs_2TeX_6 compounds are unstable under XPS analysis conditions.

Turning to the mechanisms of spectral broadening, the optimised Gaussian component is much larger for the Cs_2TeX_6 compounds than for the Group 11 metals, which was close to the instrumental resolution. This phenomenon may arise from the greater structural disorder found in the perovskite structure compared to the metallic samples. Liu et al. investigated how the disorder in different materials is related to peak broadening in XPS by DFT-based ab initio molecular dynamics (AIMD) calculations of core-level binding energies.[132] A pure metallic Pt system was shown to exhibit very little disorder broadening compared to substantial broadening exhibited in ionic systems. This behaviour is assigned to the homogenous nature of the structure and bonding in the Pt system. Disorder will also increase with thermal excitation and vibrational effects; thus the broadening optimisation could be used as tool to probe vibrational broadening in XPS. This topic will form the basis of the next chapter.

2.4 Part II Conclusions

In **Part II**, the use of DFT-simulated VB spectra has been evaluated for two different series of materials. Firstly, a metallic series is investigated consisting of three Group 11 coinage metals – Cu, Ag and Au. The second series involves three vacancy-ordered double perovskites with halide anions – Cs_2TeX_6 (X=Cl, Br, I). DFT-simulated spectra, using both PBEsol and HSE06 functionals, were fitted to experimental data using a least squares refinement method. Several parameters were optimised and evaluated in this way, including the spectral broadening and photoionization cross-section correction weightings. Additional theoretical corrections were also investigated in the Cs_2TeX_6 series, namely the inclusion of vdW and SOC effects.

The effect of using different cross-section values were mainly consistent across both series, with the modified YL* values providing the best agreement. In metals, the YL* values present the best for all materials. In Ag and Au, the plain DOS offer the worst fit, with YL values an improvement, whereas in Cu, the YL values offer the worst fit. In the halide perovskites, the YL and YL* values gave similar results, and were an improvement from using the plain DOS. The effect of SOC is essential to reproduce the splitting seen in experimental VB structure, which is most obvious when looking at the semi-core lines that appear as doublets in the halide perovskites, but also the VB structure of the X=I analogue, and the Au metal VB. The effect of intramolecular interactions between isolated octahedra were considered with the vacancy-ordered perovskite structure. The inclusion of vdW corrections significantly improves agreement with experimental lattice parameters and band gap for HSE06, which is further improved by SOC correction. However, it worsens the agreement with PBEsol calculations. The inclusion of the vdW effects do not significantly affect the appearance of the valence DOS and thus simulated XPS spectra.

In metals, the optimised Gaussian component of the spectral broadening is close to the nominal instrumental resolution of 0.4 eV. Optimised Gaussian

broadening is significantly larger for the halide perovskites than the instrumental resolution (~1.2 eV) and is material specific. Across the series of compounds studied, the optimised broadening is largely independent of the choice of cross-section correction (either YL or modified YL*), and the same trend is observed independent of the functional choice. This suggests that when determining the broadening optimisation, it may be adequate to use the cheaper functional, PBEsol. The larger broadening seen for the semi-conductors than the metals may be due to disorder broadening, as metals have highly ordered structures. As the optimised value varies with certain calculations such as the functional choice, then the optimised value does not necessarily signify an absolute measurement of additional broadening. However, it offers a probe to investigate differences in spectral broadening within a set of materials for a specific functional – which will be investigated in the next chapter.

Overall, across the materials studied, the DFT-simulated spectra largely reproduce the experimental data well when using the optimised spectral broadening and photoionization cross-section parameters. However, it is possible that higher levels of theory would produce even better agreement. In addition, the appearance of the inelastic tail is affected by the method of background modelling and subtraction, which could affect the agreement in this region. Another potential source of disagreement originates in the fundamental differences between the theoretical ground state and the XPS spectrum. XPS spectra are inherently affected by final state effects that will cause various deviations from the undisturbed ground state. There are also potential shortcomings of DFT in the approximations of the exchange and correlation potentials, again pointing to the limitations of the current simulation methods. Furthermore, the simulated VBs are derived from bulk structure calculations, whilst XPS is a surface sensitive technique. Despite all these potential limitations, the DFT simulated VB spectra are still able to reproduce the experimental VB, and the fitting method allows evaluation of photoionization cross-section correction methods and spectral broadening optimisation.

Part III – Vibrational Broadening in Photoemission Spectra

As seen in **Part II**, spectral broadening evidenced in VB XPS is material specific and can be probed by fitting theoretical and experimental spectra together. In **Part III**, the topic of spectral broadening is delved into more deeply, by investigating the effect of both charging and vibrational broadening contributions to core and VB line shapes as a function of temperature. This work comprises three case studies, encompassing a range of different materials: **i)** alkali halides, MX (M = Na, Cs; X = F, I), **ii)** bismuth oxy halides, BiOX (X = Cl, Br, I) and **iii)** a series of pure/niobium-doped strontium titanate single crystals, $SrTi_{(1-x)}Nb_xO_3$ (x = 0, 0.05, 0.5, 0.7). This chapter begins by reviewing some temperature dependent XPS investigations into vibrational broadening, followed by the three case studies and finally some comparisons of their behaviour and overall conclusions.

3.1 Review: Temperature Dependent Photoemission Studies

Varied temperature XPS allows the investigation of vibrational effects in materials by the broadening effect this has on the XPS line shape. Vibrational broadening in alkali halide ionic crystals has been studied using both experimental and theoretical methods. An XPS study on the temperature dependence of core level linewidth for the series of alkali halides KF, KCl and KI, found that the FWHM increased at high temperatures due to phonon broadening.[133] For the KF and KCl samples, the linewidth also increased at low temperatures, giving rise to a temperature dependence with a negative slope at low temperatures, and a positive slope at high temperatures. The authors attribute this behaviour to sample charging at low temperatures, which is more pronounced for the larger bandgap materials. The bandgaps for the series increase in the order KI < KCl < KF, along with the observed charging effects. This is in agreement with their previous work on the binding energies of alkali halides that they measure by XPS and compare to values calculated via a simple

point charge model.[134] For the sodium halides, a systematic disagreement was found between the measured and calculated energies, where the difference increases from about 0.9 eV for NaI to -4 eV for NaF. The origin is attributed to sample charging and relates directly to the magnitude of the respective bandgaps.

As mentioned at the end of **Part II**, the disorder in pure metals and ionic crystals and associated peak broadening in XPS has previously been investigated by DFT-based ab initio molecular dynamics (AIMD) calculations of core-level binding energies and disorder broadening.[132] Very little disorder broadening is seen for a pure metal Pt system in comparison to remarkable broadening seen for the ionic crystals KF and KI. This is rationalised by the homogeneous nature of the structure and bonding in a pure metal. The charge distribution and local screening in metals leads to nearly uniform core potentials, which damps the disorder of electrostatic potentials on the atomic sites. Their AIMD simulations of ionic crystals at a range of temperatures 300 – 600 K suggest that excess peak broadening in KF and KI arises from structural disorder from thermal movements. Significant broadening is seen on the elevation of temperature, which is consistent with the experimental results described previously for KF, KCl and KI,[133] and a similar study into NaCl thin films.[135] The AIMD simulations also predicted a larger disorder broadening of K^+ $2p$ in KF than KI, and a larger disorder broadening of cations than anions in the same material, which is consistent with the experimental observations.[133] A clear relationship was found between the FWHM and the square-root of the temperature ($\sqrt{T}$).

This relationship can be explained by phonon broadening, or Franck-Condon broadening, and can be modelled by:[75, 136]

$$\text{FWHM} = 2.35 \left(\hbar\omega E_R \coth \frac{\hbar\omega}{2k_BT} \right)^{1/2} \qquad \textbf{Eq.3.1}$$

where E_R is the nuclear relaxation energy and ω is the longitudinal optical phonon frequency. At high temperature $T > \hbar\omega/2k_B$, the FWHM approaches $2.35(2E_R k_B T)^{1/2}$, i.e. it is proportional to the square-root of the temperature ($\sqrt{T}$). In this model, broadening arises due to the changes of the equilibrium bond lengths in the final excited state from the initial ground state. This cause for broadening has also been studied by Nelin et al., who studied the vibrational broadening in the ionic crystal MgO.[75] They directly related the extent of vibrational broadening measured by XPS, to the change in bond lengths between the initial ground state and the core-hole ionised states from ab initio calculations.

Vibrational broadening in ionic crystals has also been investigated in terms of the magnitude of displacement of the ions. Messaoudi et al. calculated the temperature dependence of the vibrational amplitude of the ions in NaX alkali halides (X = F, Cl, Br, I) using GGA DFT.[137] The calculated mean-squared displacements increase for all species with increasing temperature, with the smallest difference in vibrational amplitudes observed for Na and F ions in NaF, reflecting the smallest mass mismatch of the series. In comparison, the Na ions in NaCl, NaBr and NaI show larger vibrational amplitudes than the X halide anions. The vibrational amplitudes decrease with increasing X anion mass, in the order NaCl > NaBr > NaI.

As previously discussed, metallic systems exhibit less broadening than the alkali halide ionic crystals due to the highly ordered structure. Alloys display more broadening which has been attributed to increased disorder in the system. Small Gaussian broadenings in the core-level XPS spectra of alloys have been observed for the Cu_xZn_{1-x} system,[138] the Cu_xPd_{1-x} system,[139] and the Ag_xPd_{1-x} system.[140] Metallic systems also exhibit temperature dependent broadening. A study on the vibrational broadening of core level photoemission from the surface of Na (110) metal found a strong temperature dependence of the Gaussian width of Na 2p core lines.[76] The temperature dependence was found to be enhanced for the surface signal

compared to the bulk and was attributed to phonon modes perpendicular to the surface.

Ionic liquids (ILs) have also been studied via temperature dependent XPS. The electronic and vibrational structure of ionic liquid (IL) [EMIm][Tf$_2$N] has been studied by Krischok et al.[141] The authors comment that the changing FWHM with temperature is not only influenced by vibrational effects, but that the temperature changes induce changes in viscosity and conductivity of the IL, which will also affect the FWHM. This is similar to the effects documented in the alkali halide literature, where there are two effects that broaden the FWHM: – charging effects in regions of poor conductivity and vibrational effects. They find the conductivity of the IL is reduced drastically at low temperatures and the XPS core levels broaden a lot and lose some peak structure, and there is evidence that the molecules are no longer randomly orientated. At elevated temperatures, the IL vaporises. Smith et al. make some similar observations when cooling down the IL [EMIm][EtSO$_4$] during *in situ* XPS measurements.[142] The shape of the C 1s spectrum becomes highly distorted and shifts to higher energy when the IL freezes, due to surface charging. However, on turning on charge compensation, the shape of the peak is restored.

3.2 Vibrational Case Study i) Alkali Halides

3.2.1 Intro: Structure of Alkali Halides

A series of alkali halide compounds MX (M = Na, Cs; X = F, I) were chosen to study using variable temperature XPS, in part due to the available literature on vibrational broadening (see **Section 3.1**) There have been several XPS studies that investigated the behaviour of the core level FWHM at different temperatures, but not that of the valence band spectra. The series of MX compounds studied was chosen to include both light and heavy metallic M cations and halide X anions, to investigate the effect of atomic weight on vibrational broadening in the valence band. Three of the alkali halides studied, NaF, NaI and CsF, crystalise in the NaCl structure, whilst CsI crystallises in the CsCl structure (**Figure 3.1**).
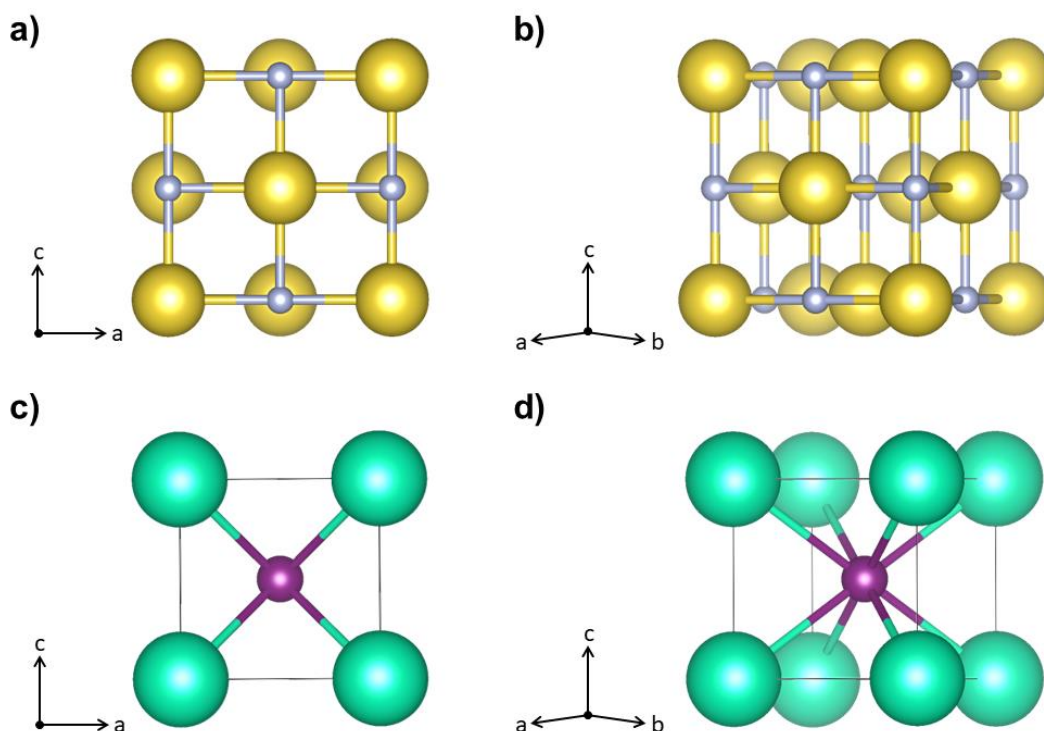
Figure 3.1 The crystal structure of the MX (M = Na, Cs; X = F, I) compounds. NaF, NaI and CsF all crystallise in the NaCl structure, shown **a)** along the [010] axis and **b)** slightly rotated to show the 6,6 coordination. CsI crystallises in the CsCl structure, shown **c)** along the [010] axis and **d)** slightly rotated to show the 8,8 coordination.

3.2.2 Experimental Section

Preparation of MX (M = Na, Cs; X = F, I) compounds

Analytical-grade samples of NaF, NaI, CsF and CsI powders were purchased from Sigma-Aldrich and used without further purification.

XPS Measurements on MX

XPS data was collected using a Kratos Axis SUPRA using monochromated Al K-Alpha X-ray source (1486.6 eV). Charge neutralization was achieved using an electron flood gun. Photoelectrons were collected at normal emission with a spot size of 400 μm. A pass energy of 150 eV was used to record survey spectra and pass energies of 20 eV and 30 eV were used to record high resolution VB and core level spectra, respectively. The sample stage was equipped with cryo/heat equipment, and measurements were taken at the following temperatures: -115 °C, -60 °C, 20 °C, 100 °C and 180°C.

XPS data were processed using CasaXPS.[97] A Shirley background subtracted. Experimental VB spectra were smoothed using a 5-point moving average filter, and the VBM was aligned to 0 eV by fitting the low binding energy edge with a complementary error function, which locates the point of intersection of straight lines fitted to the leading edge and the baseline. This method is known as linear extrapolation and is discussed in more detail in **Section 1.2.1.7**.

3.2.3 Computational Methodology

Calculations were performed using the Vienna *Ab initio* Simulation Package (VASP).[98] The convergence criterion for the k-point density and the plane wave cut-off energy parameters was that the total energy was converged to within 1 meV per atom. The resulting converged parameters are listed in **Table 3.1**.

Table 3.1. Converged plane wave cut-off energies and k-point densities for MX (M = Na, Cs; X = F, I) compounds.

Material	Plane Wave Cut-off Energy / eV	k-point density
NaF	500	4 x 4 x 4
NaI	250	5 x 5 x 5
CsF	500	3 x 3 x 3
CsI	300	5 x 5 x 5

Geometry relaxation and electronic structure calculations were performed using two functionals, PBEsol and HSE06, with and without the inclusion of spin-orbit coupling. Spin-orbit coupling (SOC) effects are expected to be significant in elements heavier than Sb,[99, 100] and was included after converging the k-point density.

The electronic structure calculations were first performed without the inclusion of spin-orbit coupling for a series of k-point meshes with increasing density to converge the appearance of the calculated density of states (DOS). As the simulated spectra in this work are compared graphically with experimental spectra it is important that the appearance of the DOS is converged. Therefore, a convergence criterion was introduced that after broadening the DOS by the instrumental resolution of 0.4 eV, there were no significant changes in appearance on increasing the k-point density. A second criterion for the electronic structure k-point density convergence is no significant change in the calculated band gap. Full details showing the convergence testing is in **Appendix B**. For all materials, a k-point density of 7x7x7 was deemed sufficient and was used subsequently if including spin-orbit coupling effects.

Photoionization Cross-section Correction Method

In this work, the values reported by Yeh and Lindau (YL),[84] and a second set of values modified from the original YL values, denoted modified YL (YL*), are investigated, as described in more detail in (**Section 2.1.2**). The values used for the materials in this section are reported in **Table 3.2** below.

Table 3.2. Energy dependent photoionization cross-section values used in this work for Na, Cs, F, and I. The top set are those reported by Yeh and Lindau (YL).[84] The bottom set (YL*) contain some values that have been modified, indicated by the shaded rows. The 'ratio' method used to modify these values is detailed in **Table B1**.

Na		Cs		F		I	
YL		**YL**		**YL**		**YL**	
3s	9.700E-05	5s	1.250E-03	2s	1.400E-03	5s	9.50E-04
2p	4.167E-04	5p	9.667E-04	2p	1.360E-04	5p	7.60E-04
		4d	7.200E-03			4d	5.60E-03
YL*		**YL***		**YL***		**YL***	
3s	9.700E-05	6s	1.098E-04	3s	4.683E-05	6s	7.534E-05
3p	2.049E-05	6p	4.685E-05	2p	1.360E-04	5p	7.60E-04
		5d	5.758E-04			5d	4.376E-04

3.2.4 Results

Geometric Structure

The alkali halides MX (M = Na, Cs; X = F, I) all crystalise in the Fm-3m space group, except for CsI, which crystallises in the Pm-3m space group. All structures were geometrically optimised using the PBEsol and HSE06 functionals. After geometry optimisation, all compounds retained their cubic structure. The calculated a lattice parameters are recorded and compared to reference experimental data in **Table 3.3**. Although the MAE for the HSE06 a parameters is lower (0.56 %) than for PBEsol (1.17 %), there is no clear trend in the errors across the series or functionals. The largest Δa values are

for PBEsol NaI (-2.24 %) and HSE06 CsI (1.80 %), and the smallest are for HSE06 NaF and NaI (0.01 and 0.0 %, respectively).

Table 3.3. Calculated and experimental lattice parameters for the MX (M = Na, Cs; X = F, I) compounds using GGA DFT (PBEsol) and hybrid DFT functionals (HSE06). The lattice parameter errors Δa are given with respect to literature values[a].

	NaF	NaI	CsF	CsI
Experiment	4.636 Å	6.479 Å	6.030 Å	4.550 Å
PBEsol	4.624 Å	6.334 Å	5.954 Å	4.509 Å
HSE06	4.637 Å	6.479 Å	6.056 Å	4.632 Å
Δa PBEsol	- 0.27 %	-2.24 %	-1.26 %	-0.90 %
Δa HSE06	0.01 %	0.00 %	0.43 %	1.80 %

[a] The experimental lattice parameters were sourced from ICSD references: NaF,[143] NaI,[144] CsF,[145] and CsI.[145]

Valence Electronic Structure

The experimental valence electronic structure for the MX (M = Na, Cs; X = F, I) compounds are compared to DOS calculated using PBEsol and HSE06 functionals, both with and without the inclusion of spin-orbit coupling (SOC) effects in **Figure 3.2**. The collected XPS data are normalised to the plain PBEsol or HSE06 DOS, and shifted along the BE axis to overlap with the calculated DOS, which at this stage have been broadened by the nominal instrumental resolution (0.4 eV) and have not been corrected with photoionization cross-sections. The appearance of the valence DOS is remarkably similar when comparing the two functionals. Inclusion of SOC effects has no effect on the NaF DOS, which is expected due to the light Na and F atoms. The NaI and CsI DOS are the most impacted due to the heavy I atoms, and the inclusion of SOC in these cases greatly improves the agreement with the experimental data. Although the CsF contains the heavy Cs atom, the SOC effects do not greatly affect the VB as this is mainly made up of F p orbitals, as shown in **Figure 3.3**.
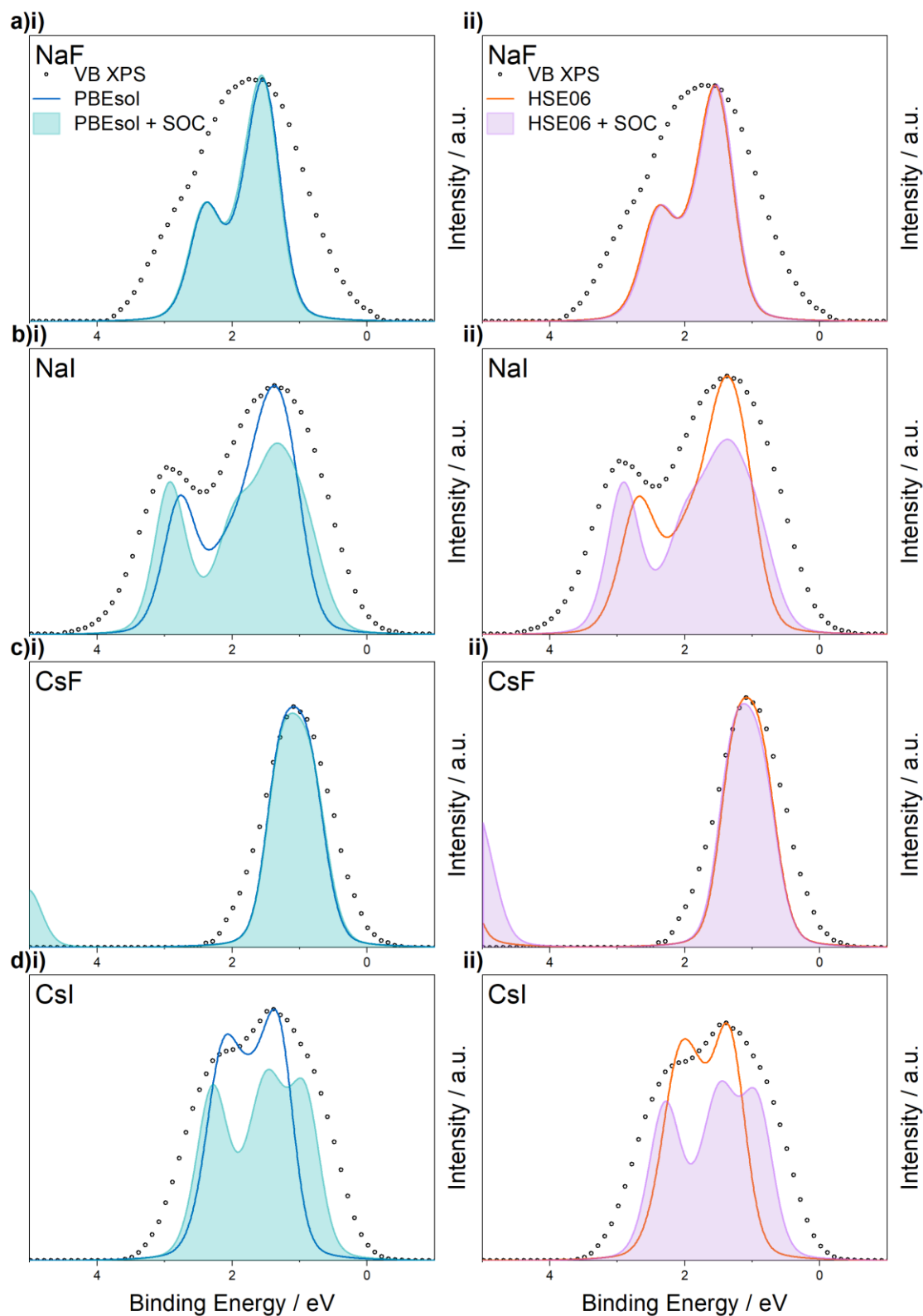
Figure 3.2. VB XPS spectra for the series of MX compounds **(a-c)** X = Cl, Br, I, together with DFT calculated DOS using **i)** PBEsol and **ii)** HSE06 functionals with and without including SOC effects. The experimental VB is normalised to the VB spectral maximum of plain **i)** PBEsol and **ii)** HSE06 and shifted to align with the theoretical DOS, which are broadened by the nominal instrumental resolution of 0.4 eV. The SOC DOS are also shifted slightly for comparison with the XPS VB.

To simulate the VB XPS spectra, the pDOS were corrected by modified YL*
photoionization cross-sections, which gives good agreement with the
experimental spectra. Cross-section correction does not significantly affect
the shape of the resulting simulated spectra (**Figure 3.3**). The simulated
VB is comprised mainly of halide p orbitals, which is consistent with
reported calculations.[146] As the VB for the hybrid and GGA calculations is
very similar, only the PBEsol spectra are displayed for clarity.
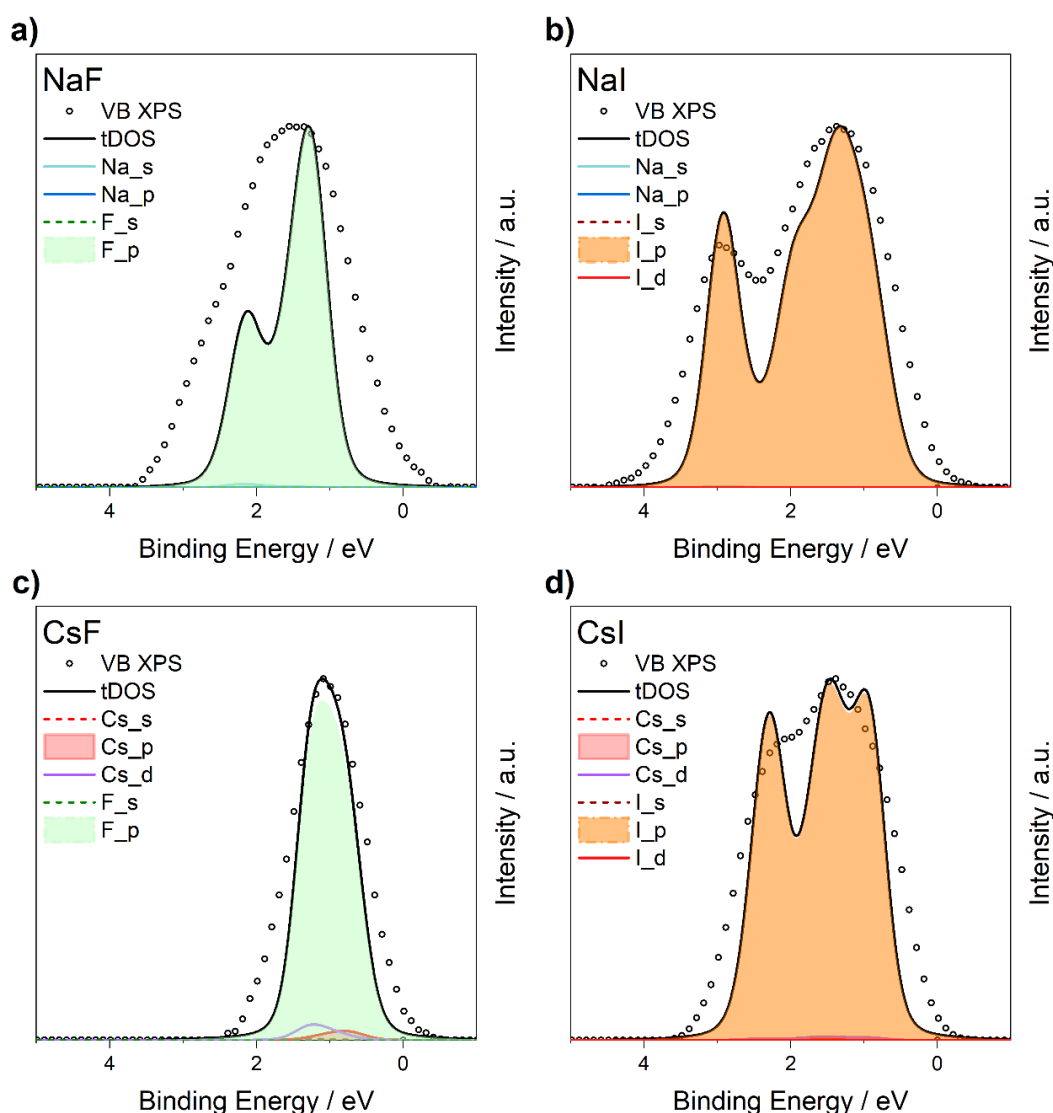
Figure 3.3. The RT VB XPS spectra for the series of alkali halide compounds **a)** NaF **b)** NaI
c) CsF **d)** CsI, fitted with DFT simulated spectra. The DFT simulated spectra were derived
from pDOS calculated with PBEsol + SOC theory, corrected by modified YL* cross-sections
and broadened by Gaussian and Lorentzian functions to simulate instrumental and lifetime
broadening, respectively. A nominal instrumental resolution of 0.4 eV has been applied.

The main difference between the hybrid and GGA electronic structure lies in the magnitude of the bandgap. This is clear from **Figure B2** and the values reported in **Table 3.4**. The tendency for PBEsol to underestimate E_g is widely reported in the literature.[124-127] Here, the HSE06 calculations also underestimate the bandgap, although the values are closer to experiment. The inclusion of SOC effects serves to narrow the gap for the compounds containing heavy atoms: NaI, CsF and CsI.

Table 3.4. Experimental and calculated band gap values from the literature and the current work for the series of MX compounds (M = Na, Cs; X = F, I). The cationic and anion radii from literature sources are also listed.

Material	Cationic radii / Å.[147]	Anionic radii / Å.[147]	Experimental Bandgap / eV.[148]	DFT calculated (PBE) bandgap.[146] / eV	Calculated bandgap – Current work / eV			
					PBEsol	PBEsol + SOC	HSE06	HSE06 + SOC
NaF	1.02	1.33	11.5	6.16	6.20	6.17	8.47	8.44
NaI	1.02	2.20	5.9	3.55	3.68	3.34	4.66	4.31
CsF	1.67	1.33	9.8	5.29	5.77	5.71	7.56	7.50
CsI	1.67	2.20	6.1	3.75	3.91	3.57	4.85	4.51

Despite the fact that the calculated bandgaps are smaller than the experimental, they still follow the correct trend for both functionals with or without the inclusion of SOC effects: NaF > CsF > CsI > NaI. This has previously been observed by Gopikrishnan et al., who studied the alkali halides using the PBE functional.[146] They also show that the valence states are mainly comprised of halide p orbitals, whilst the conduction band originates from the alkali cation. They show that for a fixed cation, the halide valence electrons become less stabilised following the order F > Cl > Br > I. The larger, more diffuse Br⁻ and I⁻ ions allow charge transfer to the

alkali ion, which allows for a degree of covalency and thus a narrowing of the band gap.

Valence Band XPS / DFT Fitting

Valence band spectra were recorded at a range of 5 different temperatures: -115 °C, -60 °C, 20 °C, 100 °C and 180°C. These are shown in **Figure 3.4**, normalised and calibrated to 0 eV after Shirley background subtraction. Using the method described previously (**Section 2.2.4**) the VB XPS spectra in **Figure 3.4** were fitted with the PBEsol simulated spectra plotted in **Figure 3.3**, with varying degrees of Gaussian broadening applied (0.5 – 2.0 eV) and a fixed Lorentzian broadening of 0.1 eV. The RSS for the resulting spectra are plotted in **Figure 3.5**. The minimum of the curve is taken to be the optimum Gaussian broadening. The spectra with the optimised broadening values are plotted in **Figure 3.6**.
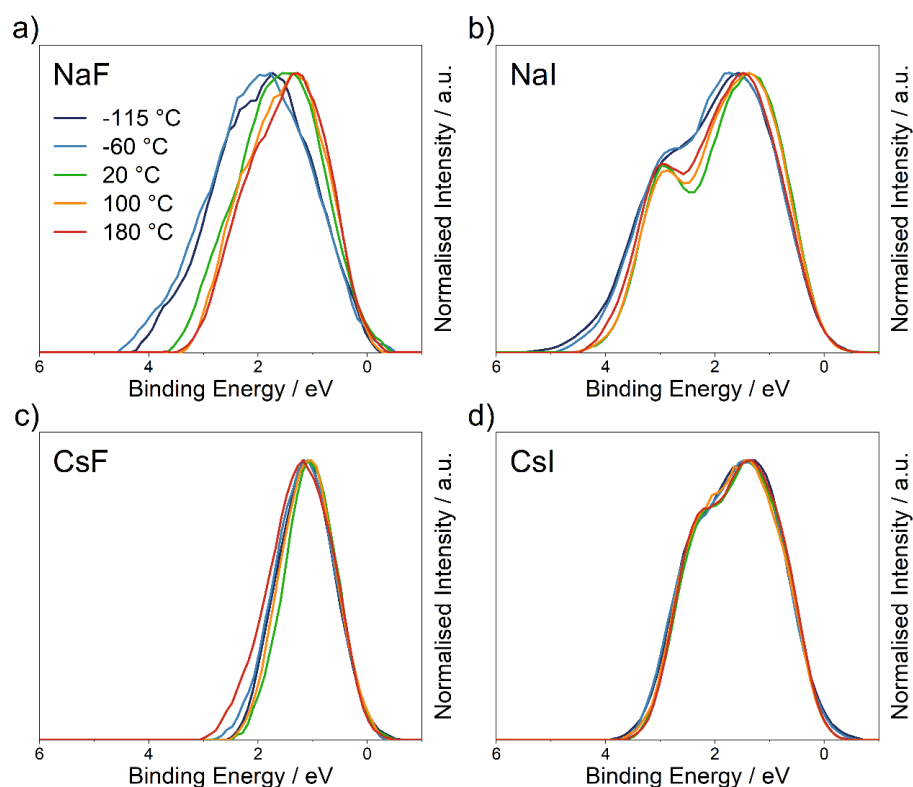
Figure 3.4. The temperature dependent VB XPS spectra for the series of alkali halide compounds **a)** NaF **b)** NaI **c)** CsF **d)** CsI. The data have been smoothed with a MA filter (width 5) followed by Shirley background subtraction, and calibration of the VBM to 0 eV.
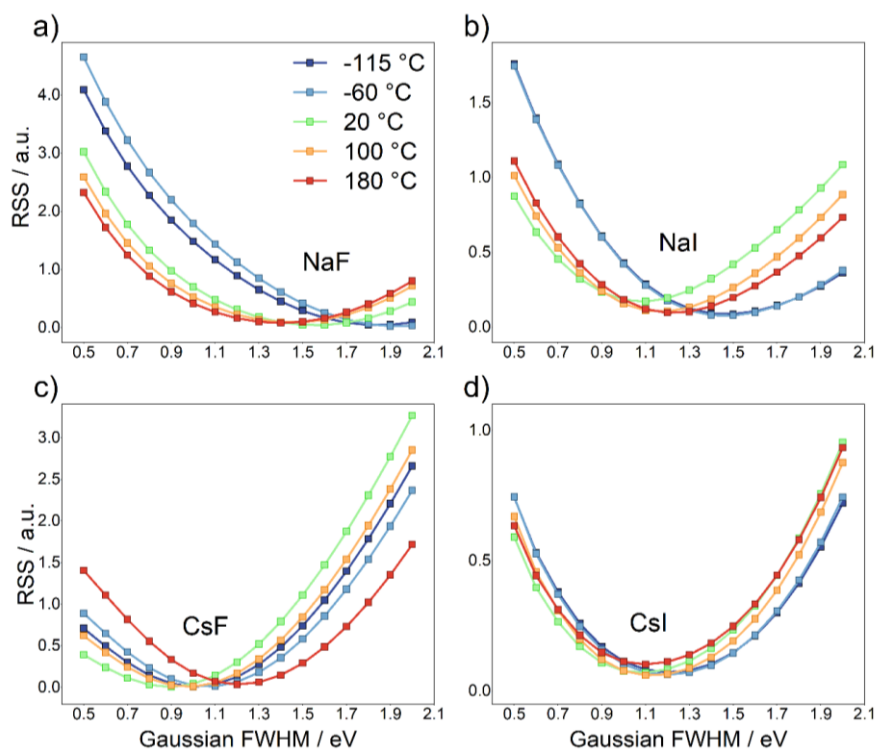
Figure 3.5. Optimisation of the Gaussian broadening applied to theoretical spectra in the alkali halide series **a)** NaF **b)** NaI **c)** CsF **d)** CsI. A fixed Lorentzian component of 0.1 eV was applied in each case. The RSS was calculated by fitting with VB XPS spectra at the range of temperatures indicated in **a)**. The temperature dependent optimised broadening is taken as the minimum of each curve.

As can be seen from the fitted simulated spectra, the optimised spectral broadening produces excellent fitting spectra. The resolution of the higher BE shoulder in the NaI and CsI spectra is slightly reduced, however, the main spectral shape is still retained on the application of higher levels of Gaussian broadening. The positions of the minima of the RSS curves in **Figure 3.5** show that the temperature dependence of the broadening is material specific. In all cases, the optimised Gaussian component is much larger than the instrumental resolution. In this case, the temperature dependence arises from multiple origins, and is discussed in detail along with core-level broadening in the next section.
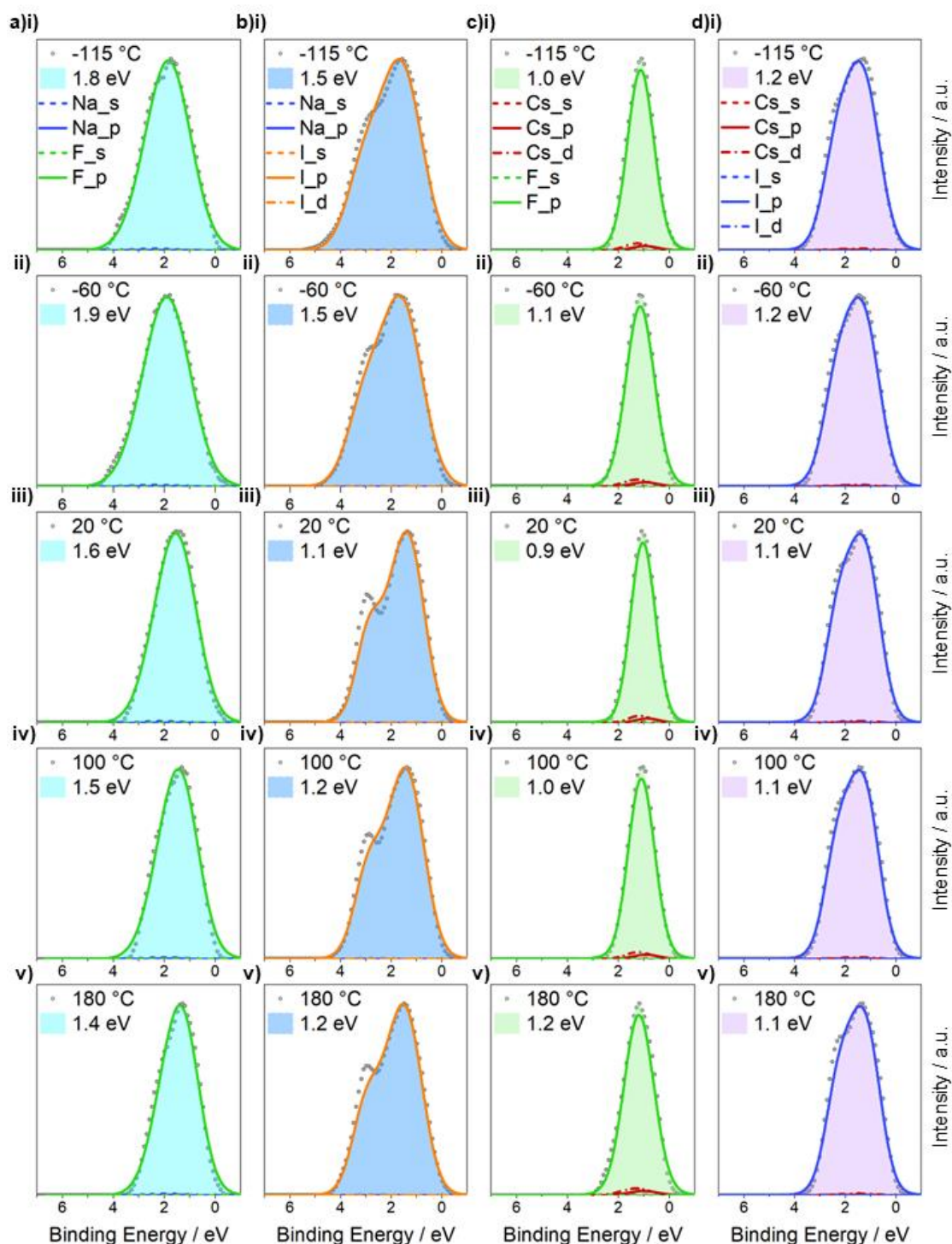
Figure 3.6. The temperature dependent VB XPS spectra for the series of alkali halide compounds **a)** NaF **b)** NaI **c)** CsF **d)** CsI, fitted with DFT simulated spectra. The experimental data were recorded at temperatures of **i)** -115 °C, **ii)** -60 °C, **iii)** 20 °C, **iv)** 100 °C and **v)** 180 °C. The Gaussian component of the broadening applied to produce the simulated spectra was optimised in each case and is indicated in each figure.

Core Level & Valence Band Broadening

Temperature dependent broadening in the core levels was also investigated by measuring the FWHM for the alkali cation and halide anion species. The resulting widths are plotted and compared to the optimised Gaussian broadening in the valence band in **Figure 3.7**. The trend in FWHM vs temperature is similar for the same compound across the anion and cation, and has general correlation with the VB trend. The compound that seems to be the least affected by the change in temperature is CsI, the heaviest compound studied. As the temperature dependent vibrational amplitude in alkali halides has been shown to decrease with atomic mass,[137] the heavy nature of the CsI could account for the subtle trend observed. CsI structure is different from the others (bcc rather than fcc). In addition to the effect of disorder and vibrational effects broadening the XPS line shape, the presence of surface charging has also been shown to play a role.[133, 141] The effects of surface charging have been linked to the size of the band gap in alkali halides for a common cation.[133, 134] CsI has the second smallest band gap (**Table 3.4**), only slightly smaller than the smallest NaI, which may also contribute to a lack of charging induced broadening.

In contrast to CsI, the lightest compound, NaF, exhibits the most broadening in the series. At any given temperature, the VB is much broader than the ground state DOS than for the other compounds. This is also true for the halide anion (**Figure 3.7a**), if comparing NaF and CsF, the FWHM of the F 1s spectra is always larger for NaF. Similarly, if looking at the alkali cation FWHM (**Figure 3.7b**), the Na 1s spectra is always broader for NaF than for NaI, except for at the highest temperature. NaF has the largest band gap (**Table 3.4**), and so may be expected to exhibit the most charging effects. The broadening effects exhibited by NaF within the temperature range studied are likely a combination of both vibrational and charging effects. Citrin et al. observed charging effects in KF up to ~450 K.[133] As the general trend with increasing temperature is a decrease in spectral broadening, it is likely that the charging effects are dominating.
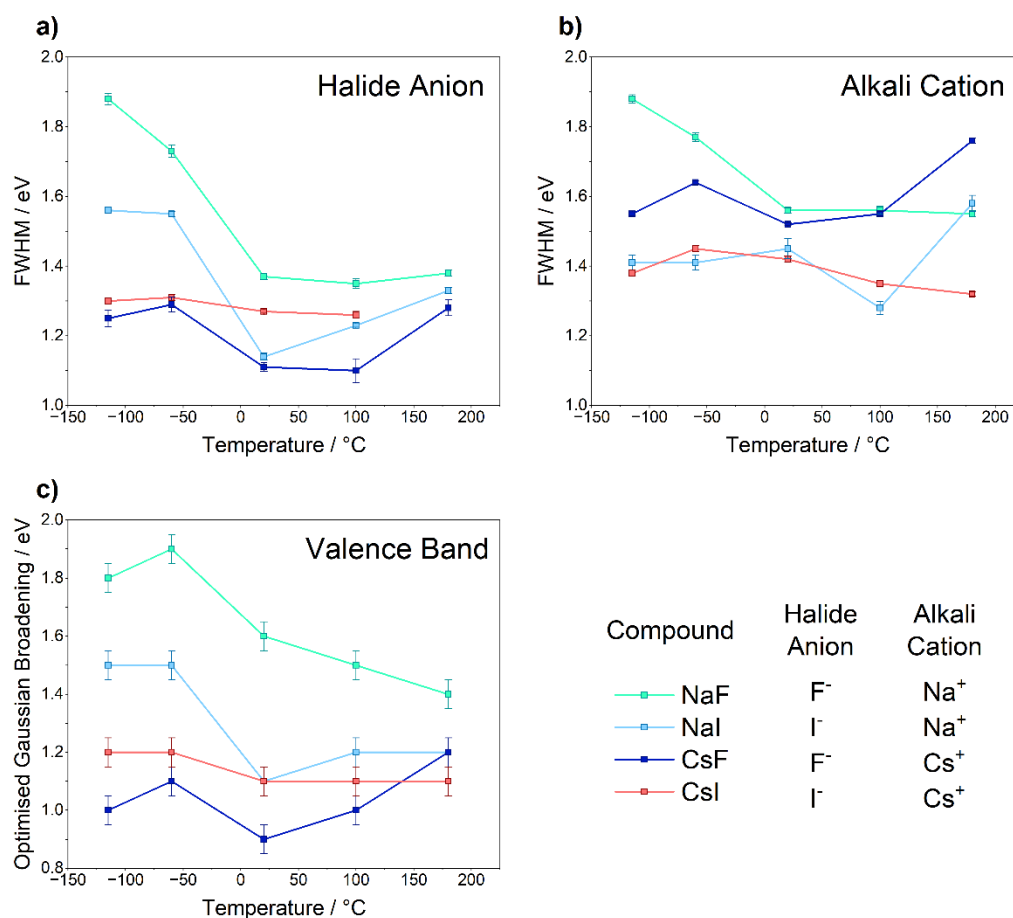
Figure 3.7. The variation with temperature of the **a)** halide anion FWHM **b)** the alkali cation FWHM and **c)** the optimised Gaussian broadening determined from the XPS/DFT VB fitting results, for the alkali halide compounds MX (M = Na, Cs; X = F, I). The error bars in **a,b)** correspond to errors in the fitted FWHM peak parameter estimated by Monte Carlo simulations using CasaXPS (**Table B2**). The error bars in **c)** correspond to the estimated uncertainty in the fitting method.

Spectral broadening optimisation of the VB (**Figure 3.7c**) facilitates comparison between more materials, not just those with a common anion or cation. For the isostructural compounds, NaF, NaI and CsF, the trends in the temperature dependent VB broadening can be rationalised in terms of an interplay between the effects of both vibrational broadening and charging effects.

3.3 Vibrational Case Study ii) Bismuth Oxyhalides

3.3.1 Intro: Bismuth Oxyhalides – Structure and Applications
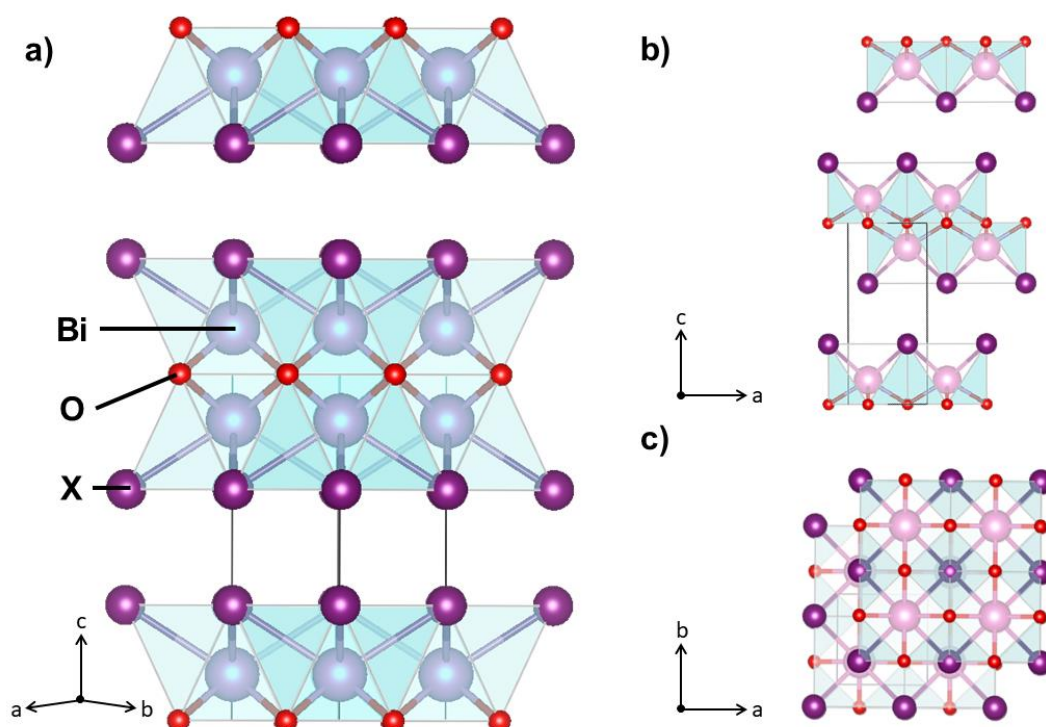
Figure 3.8 a) The crystal structure of BiOX (X = Cl, Br, I) compounds contains layers of [X-Bi-O-Bi-X] slabs, **b)** as viewed along the [010] direction, and **c)** the [001] direction. The Bi, O and X atoms are denoted by pink, red, and purple spheres, respectively, and are labelled in part **a)**. The X site is filled by Cl, Br, or I atoms in the series investigated in this work. The unit cell outlined in black represents the unit cell used in the calculations.

This second case study into vibrational broadening investigates a series of bismuth oxyhalides BiOX (X = Cl, Br, I); a class of V-VI-VII ternary semiconductor material that crystalise in a tetragonal matlockite structure. The structure consists of fluorite-like [Bi_2O_2] layers in a double halide [X_n]$^-$ sandwich, forming [X-Bi-O-Bi-X] slabs held together by van der Waals (vdW) forces (**Figure 3.8**). It is suggested that an internal static electric field is present along the c axis, between the [Bi_2O_2] and double [X_n]$^-$ slab, which assists efficient separation of photogenerated electron-hole pairs.[149-151] Their excellent photocatalytic activity has led to numerous studies into their structure and applications as photocatalysts.[149-153] Li et al. review the numerous experimental methods developed to synthesise bismuth oxyhalides, and their application as photocatalysts for degradation of organic pollutants in wastewater:[154]

80

3.3.2 Experimental Section

Preparation of BiOX (X = Cl, Br, I) compounds

Analytical-grade reactants of $Bi(NO_3)_3 \cdot 5H_2O$, KCl solution, KBr solution and KI solution were purchased from Sigma-Aldrich and used without further purification. The BiOX (X = Cl, Br, I) compounds were synthesised via an adaptation of the mechanical grinding method described by Long et al.[155]

BiOCl. A mixture of $Bi(NO_3)_3 \cdot 5H_2O$ (1 mmol) and KCl (1 mmol) were added to an agate mortar and ground for 5 min. The resulting white mash was collected and washed with water and absolute ethanol several times by centrifugation to remove the water-soluble by products and then dried at 60 ºC. A similar process was adopted for the BiOBr and BiOI. PXRD characterisation of the resulting BiOX powders can be found in **Appendix B**, confirming the structure of the products.

XPS Measurements on BiOX

XPS data was collected using a Kratos Axis SUPRA using monochromated Al K-Alpha X-ray source (1486.6 eV). Charge neutralization was achieved using an electron flood gun. Photoelectrons were collected at normal emission with a spot size of 400 µm. A pass energy of 150 eV was used to record survey spectra and pass energies of 20 eV and 30 eV were used to record high resolution VB and core level spectra, respectively. The sample stage was equipped with cryo/heat equipment, and measurements were taken at the following temperatures: -115 °C, -60 °C, 20 °C, 100 °C and 180°C.

XPS data were processed using CasaXPS.[97] A Shirley background subtracted. Experimental VB spectra were smoothed using a 5-point moving average filter, and the VBM was aligned to 0 eV by fitting the low binding energy edge with a complementary error function, which locates the point of intersection of straight lines fitted to the leading edge and the baseline. This

method is known as linear extrapolation and is discussed in more detail in **Section 1.2.1.7**.

3.3.3 Computational Methodology

Calculations were performed using the Vienna *Ab initio* Simulation Package (VASP).[98] The convergence criterion for the k-point density and the plane wave cut-off energy parameters was that the total energy was converged to within 1 meV per atom. The resulting converged parameters are listed in **Table 3.5**.

Table 3.5. Converged plane wave cut-off energies and k-point densities for the selected materials (BiOX, X = Cl, Br, I)

Material	Plane Wave Cut-off Energy / eV	k-point density
BiOCl	500	4 x 4 x 2
BiOBr	500	5 x 5 x 2
BiOI	500	6 x 6 x 3

Several functionals were used in this work: PBEsol and HSE06. For geometry relaxation both functionals were implemented, with and without the addition of Grimme's D3 dispersion correction.[58] Electronic structure calculations were performed using both functionals, with and without the inclusion of spin-orbit coupling. Spin-orbit coupling (SOC) effects are expected to be significant in elements heavier than Sb,[99, 100] therefore SOC was included for all compounds after converging the k-point density.

The electronic structure calculations were first performed without the inclusion of spin-orbit coupling for a series of k-point meshes with increasing density to converge the appearance of the calculated density of states (DOS). As the simulated spectra in this work are compared graphically with experimental spectra it is important that the appearance of the DOS is converged. Therefore, a convergence criterion was introduced that after broadening the DOS by the instrumental resolution of 0.4 eV, there were no significant changes in appearance on increasing the k-point density. A second criterion for the electronic structure k-point density

convergence is no significant change in the calculated band gap. Full details showing the convergence testing is in **Appendix B**. For all materials, a k-point density of 7x7x4 was deemed sufficient for PBEsol, and a k-point density of 6x6x3 was deemed sufficient for HSE06, which were used subsequently when including spin-orbit coupling effects.

Photoionization Cross-section Correction Method

In this work, the values reported by Yeh and Lindau (YL),[84] and a second set of values modified from the original YL values, denoted modified YL (YL*), are investigated, as described in more detail in **Section 2.1.2**. The values used for the materials in this section are reported in **Table 3.6** below.

Table 3.6. Energy dependent photoionization cross-section values used in this work for Bi, O, Cl, Br, and I. The top set are those reported by Yeh and Lindau (YL).[84] The bottom set (YL*) contain some values that have been modified, indicated by the shaded rows. The 'ratio' method used to modify these values is detailed in **Table B2**.

Bi		O		Cl		Br		I	
YL		**YL**		**YL**		**YL**		**YL**	
6s	6.50E-04	**2s**	9.50E-04	**3s**	1.25E-03	**4s**	1.3E-03	**5s**	9.50E-04
6p	4.67E-04	**2p**	6.00E-05	**3p**	3.80E-04	**4p**	9.0E-04	**5p**	7.60E-04
5d	4.30E-03					**3d**	3.9E-03	**4d**	5.60E-03
YL*		**YL***		**YL***		**YL***		**YL***	
6s	6.50E-04	**3s**	3.18E-05	**4s**	8.24E-05	**5s**	9.62E-05	**6s**	7.534E-05
6p	4.67E-04	**2p**	6.00E-05	**3p**	3.80E-04	**4p**	9.00E-04	**5p**	7.60E-04
6d	3.47E-04					**4d**	2.50E-04	**5d**	4.376E-04

3.3.4 Results

Geometric Structure

The BiOX (X = Cl, Br, I) family all crystalise in a tetragonal matlockite structure, which consists of layers of [X-Bi-O-Bi-X] slabs, held together by van der Waals (vdW) forces. All structures were geometrically optimised using the PBEsol and HSE06 functionals, both with and without a correction to treat these vdW interactions. After geometry optimisation, all compounds retained their tetragonal matlockite structure. The calculated a and c lattice parameters are recorded and compared to reference experimental data in **Table 3.7**. All calculated and experimental data exhibit increasing a and c parameters in the order X = Cl < Br < I, due to the increasing ionic radius of the X site anion.

Table 3.7. Calculated and experimental lattice parameters for BiOX (X = Cl, Br, I) using GGA DFT (PBEsol) and hybrid DFT functionals (HSE06), both with and without correction for vdW interactions (Grimme's D3 correction). The lattice parameter errors Δx (x=a, c) are given with respect to literature values[a].

	BiOCl		BiOBr		BiOI	
	a	*c*	*a*	*c*	*a*	*c*
Experiment	3.886 Å	7.349 Å	3.923 Å	8.105 Å	3.995 Å	9.152 Å
PBEsol	3.879 Å	7.343 Å	3.909 Å	8.187 Å	3.978 Å	9.240 Å
PBEsol + vdW	3.869 Å	7.223 Å	3.904 Å	7.940 Å	3.976 Å	8.890 Å
HSE06	3.874 Å	7.764 Å	3.911 Å	8.780 Å	3.986 Å	9.747 Å
HSE06 + vdW	3.856 Å	7.386	3.898 Å	8.099 Å	3.980 Å	9.062 Å
Δx PBEsol	-0.17 %	-0.08 %	-0.36 %	1.01 %	-0.43 %	0.97 %
Δx PBEsol + vdW	-0.42 %	-1.71 %	-0.49 %	-2.04 %	-0.48 %	-2.86 %
Δx HSE06	-0.30 %	5.65 %	-0.31 %	8.33 %	-0.23 %	6.51 %
Δx HSE06 + vdW	-0.76 %	0.50 %	-0.64 %	-0.08 %	-0.38 %	-0.98 %

[a] The experimental lattice parameters were sourced from ICSD references: BiOCl,[156] BiOBr,[157] and BiOI.[158]

Without the inclusion of vdW forces, the PBEsol calculated a and c parameters are in good agreement with the experimental values, with MAEs of 0.32 % and 0.69 %, respectively. However, introducing vdW correction imparts larger Δx values in all cases, that increase with

increasing halide anion size, and are the largest in the c direction. The c direction is most impacted by the vdW corrections because this is the direction the layers are stacked in, and the MAE here increases to 2.20 %. The good agreement of the uncorrected PBEsol values probably arises from a cancellation of errors.[121] In the case of the HSE06 parameters, the vdW corrections brings the values closer to the experimental values. The MAE in the c direction is reduced from a significant 6.83 % to 0.52 %. The inclusion of the dispersion forces is thus necessary for obtaining an accurate geometry when using the HSE06 functional, which has also been documented by previous computational work into the BiOX family.[149, 159]

Valence Electronic Structure

The experimental valence electronic structure for the BiOX (X = Cl, Br, I) family are compared to an array of calculated DOS resulting from various levels of theory in **Figure 3.9**. The electronic structure calculations were performed on all optimised geometries (**Table 3.7**), to investigate the effect of the DFT functional (PBEsol or HSE06) and any additional corrections (vdW and/or SOC). Note that additional HSE06 + vdW + SOC calculations were not included in the interest of computational expense. The experimental data are normalised to the intensity of the plain PBEsol/HSE06 DOS, and are shifted along the binding energy axis to maximise overlap. At this stage, the DOS have been broadened by the nominal instrumental resolution of 0.4 eV, and no cross-section corrections have been applied.
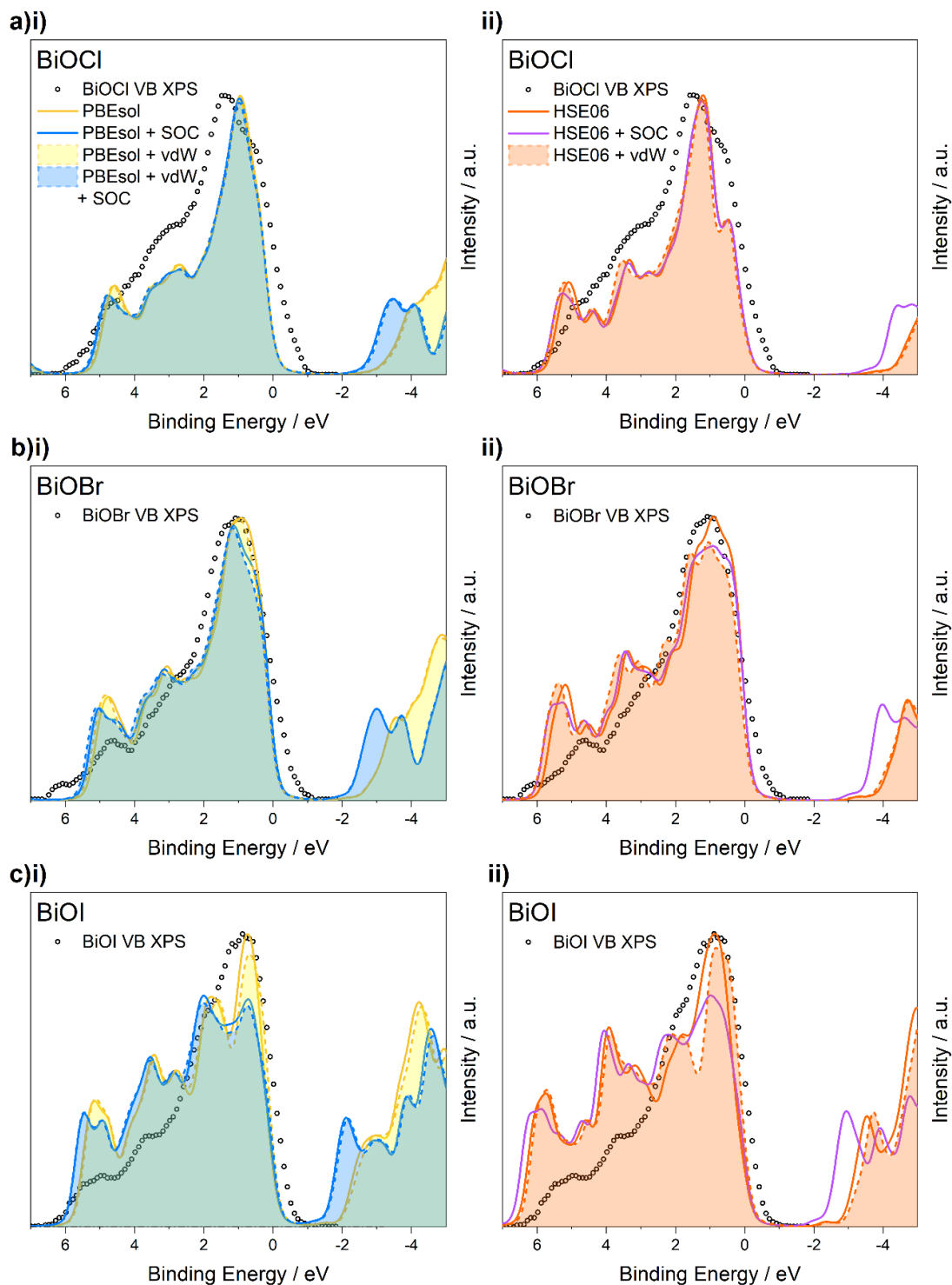
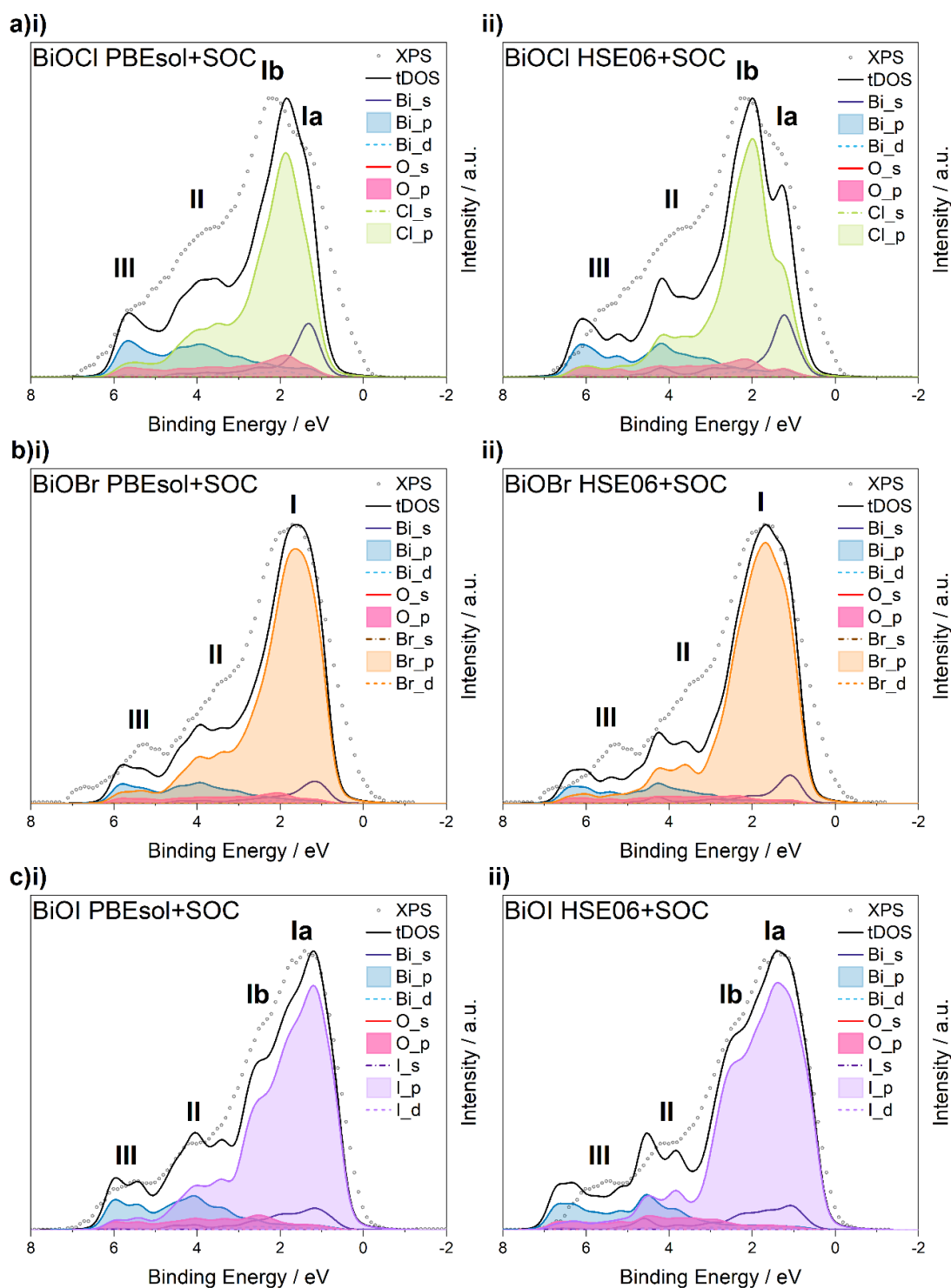**Figure 3.9**. VB XPS spectra for the series of BiOX compounds **(a-c)** X = Cl, Br, I, together with DFT calculated DOS using **i)** PBEsol and **ii)** HSE06 functionals and various corrections. The experimental VB is normalised to the VB spectral maximum of **i)** PBEsol and **ii)** HSE06 and shifted to align with the theoretical DOS, which are broadened by the nominal instrumental resolution of 0.4 eV.

The width of the calculated DOS increases BiOCl > BiOBr > BiOI, and the hybrid calculations (HSE06) generate a broader DOS than the GGA (PBEsol) functional for all materials. The impact of including vdW forces results in a smaller calculated c lattice parameter (**Table 3.7**) which results in a small broadening of the calculated DOS. This effect is more exaggerated when using HSE06 than PBEsol, as the change in lattice parameter is larger. However, there is no substantial change to the general appearance of the valence DOS when using the structure relaxed with vdW forces included. The inclusion of SOC effects has a varied degree of impact depending on the halide substituent, although it serves to broaden the calculated DOS in each case. The biggest change in appearance when including SOC is for BiOI, which is expected due to the heavy iodine atom.

The orbital projected DOS (pDOS) without cross-section correction are in Appendix B. The general appearance of the hybrid and GGA pDOS are in agreement – the VBM states are primarily composed of halide p orbitals and O $2p$ orbitals, and the CBM is primarily composed of Bi $6p$ states, which is consistent with other DFT calculations.[149, 159, 160] The relative position of the CBM is also affected by the inclusion of the SOC effects, moving closer to the VBM in all cases and decreasing the size of the calculated band gap, E_g. The PBEsol E_g is smaller than the HSE06 E_g which is consistently reported throughout literature.[124-127] The magnitude of E_g decreases in the order BiOCl > BiOBr > BiOI, which is consistent with the experimental trend.[152, 154] Ganose et al. explain the decreasing band gap down the series as arising from both relativistic and orbital effects, as the inclusion of SOC effects alone is not enough to explain the trend.[149] They show that the ionization potential (IP) of the BiOX gets smaller on descending the group, as expected due to the relative energy levels of the halide p orbitals. Thus the large halide orbital contribution at the VBM plays a major role in the observed trend in E_g.

Figure 3.10. VB XPS spectra for the series of BiOX compounds **(a-c)** X = Cl, Br, I, together with simulated spectra calculated using **i)** PBEsol+SOC and **ii)** HSE06+SOC. The original pDOS were corrected with modified YL* cross-sections, as described in the text. The experimental VB is normalised to the VB spectral maximum of **i)** PBEsol and **ii)** HSE06 and shifted to align with the theoretical spectra, which are broadened by the nominal instrumental resolution of 0.4 eV. The labels **I-III** indicate features of interest and are discussed in the text.

After correction with modified YL* photoionization cross-sections, the features and spectral shape of the simulated spectra are in much better agreement with the experimental data (**Figure 3.10**). Although the pDOS at the VBM has a large contribution from O $2p$ orbitals, the contribution to the XPS spectra is relatively small, due to the larger photoionization cross-section of the halide orbitals, combined with the large halide p pDOS. The XPS VB is thus dominated by photoemission from the halide p orbitals. Features of interest in the XPS VB have been labelled **I-III** for the purpose of discussion. Feature **I** constitutes the principal maximum in each spectrum, which peaks following a sharp increase in intensity after the VBM. This feature has been divided into two components, **Ia** and **Ib**, due to a small shoulder in the BiOCl and BiOI spectra, in the rising and falling edge of the maximum, respectively. Feature **II** arises at mid BE with lower intensity, and finally feature **II** appears at the high BE end of the VB, with the lowest spectral intensity.

All features **I-III** are well predicted by both PBEsol and HSE06 simulated spectra. The position of **Ia** and **Ib** are better predicted by the hybrid theory, especially BiOCl, but they are in reasonable agreement with the GGA spectra. However, the BEs for features **II** and **III** are much better matched in the GGA theory, whereas the hybrid calculations tends to place these two features at slightly higher BE than the XPS data. Due to better agreement of the GGA features, the PBEsol spectra were utilised going forward for broadening optimisation, although it is expected that the results would be similar for either functional (as was found for Cs_2TeX_6 series in chapter A). The GGA level of theory also offers advantages in future work such as lower computational expense.

Valence Band XPS / DFT Fitting

Valence band spectra were recorded at a range of 5 different temperatures: -115 °C, -60 °C, 20 °C, 100 °C and 180°C. The experimental data were smoothed once using a moving average (MA) filter (width 5), the VBM was

calibrated to 0 eV followed by Shirley background subtraction. The collected XPS data were fitted with a series of theoretical spectra, which were broadened by Gaussian functions of varying FWHM, ranging from $0.5 - 2.0$ eV, following the method previously described (**Section 2.2.4**). The PBEsol simulated spectra (**Figure 3.10**) were chosen to fit the experimental VB, although the results are expected to be similar using HSE06, as previously discussed.
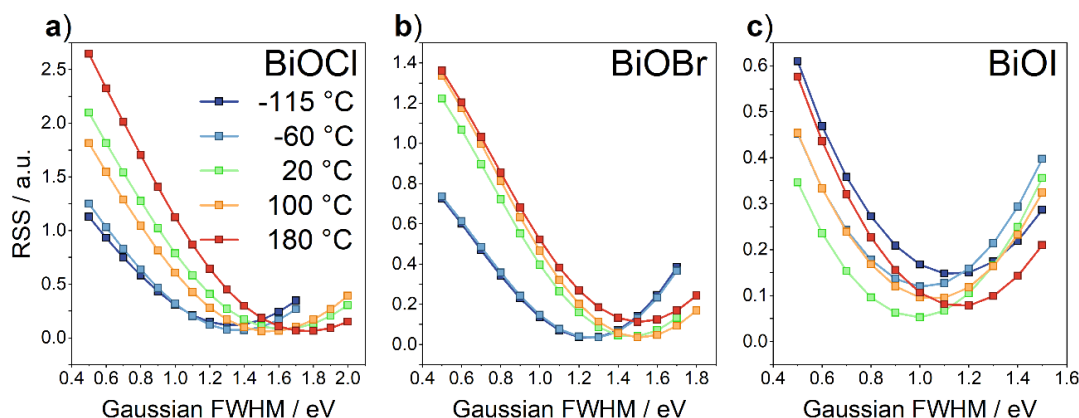
Figure 3.11. Optimisation of the Gaussian broadening applied to theoretical spectra in the BiOX series **a)** X = Cl **b)** X = Br **c)** X = I. A fixed Lorentzian component of 0.1 eV was applied in each case. The RSS was calculated by fitting with VB XPS spectra at the range of temperatures indicated in **a)**. The temperature dependent optimised broadening is taken as the minimum of each curve.

The goodness of fit across the range of simulated spectra is indicated by the RSS in **Figure 3.11** for **a)** BiOCl **b)** BiOBr and **c)** BiOI. When the applied broadening is close to the instrumental resolution ~0.5 eV, the RSS is highest for the range of values trialled. As the FWHM is increased the RSS decreases until it reaches a minimum and then increases again at larger values. The minimum of each curve was taken to be the optimum broadening at that temperature. The optimised simulated spectra are shown in **Figure 3.12**, and show good agreement with the experimental VB. The trends observed across the temperature range and the series of halide X anions is compared to the trends observed in the Bi and halide core-levels in the next section.
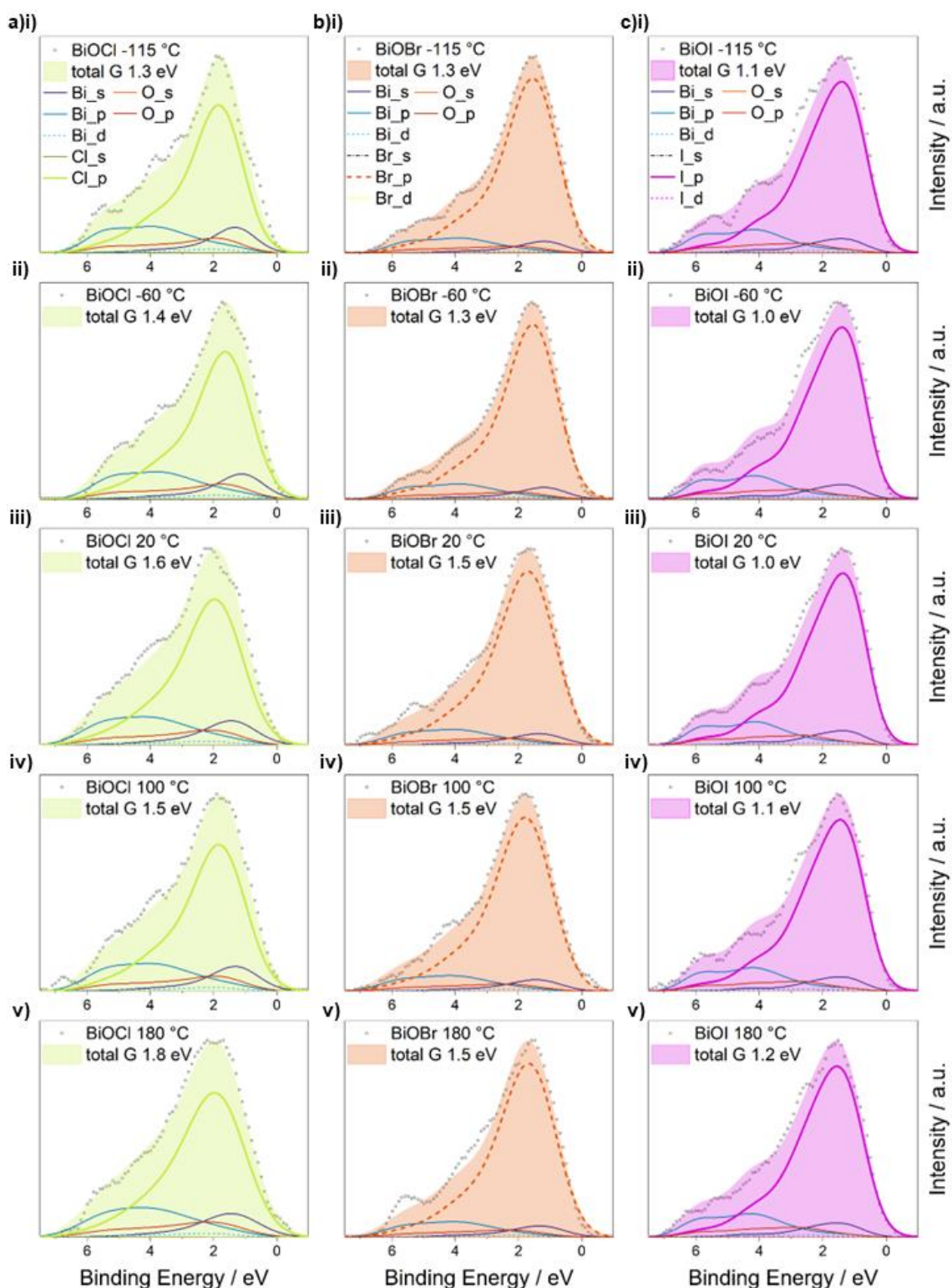
Figure 3.12. The temperature dependent VB XPS spectra for the series of BiOX compounds **a)** X = Cl **b)** X = Br **c)** X = I, fitted with DFT simulated spectra. The experimental data were recorded at temperatures of **i)** -115 °C, **ii)** -60 °C, **iii)** 20 °C, **iv)** 100 °C and **v)** 180 °C. The Gaussian component of the broadening applied to produce the simulated spectra was optimised in each case and is indicated in each figure.

Core Level & Valence Band Broadening

Vibrational broadening in the core levels was investigated by measuring the FWHM at the same temperatures as the VB and are plotted in **Figure 3.13**. There is a general trend of increasing FWHM for both the **a)** Bi 4f FWHM and the **c)** halide FWHM, which is in agreement with the trend seen in **d)** the VB spectral broadening. There appears to be an outlier in the BiOBr trend, at 100 °C, where both core level spectra have a higher FWHM than expected, although this is not mirrored in the VB broadening. The measured BE with no charge correction is shown for **b)** Bi 4f 7/2 BE, which seems to have no strong correlation with temperature nor able to identify any BE shift related charging effects.
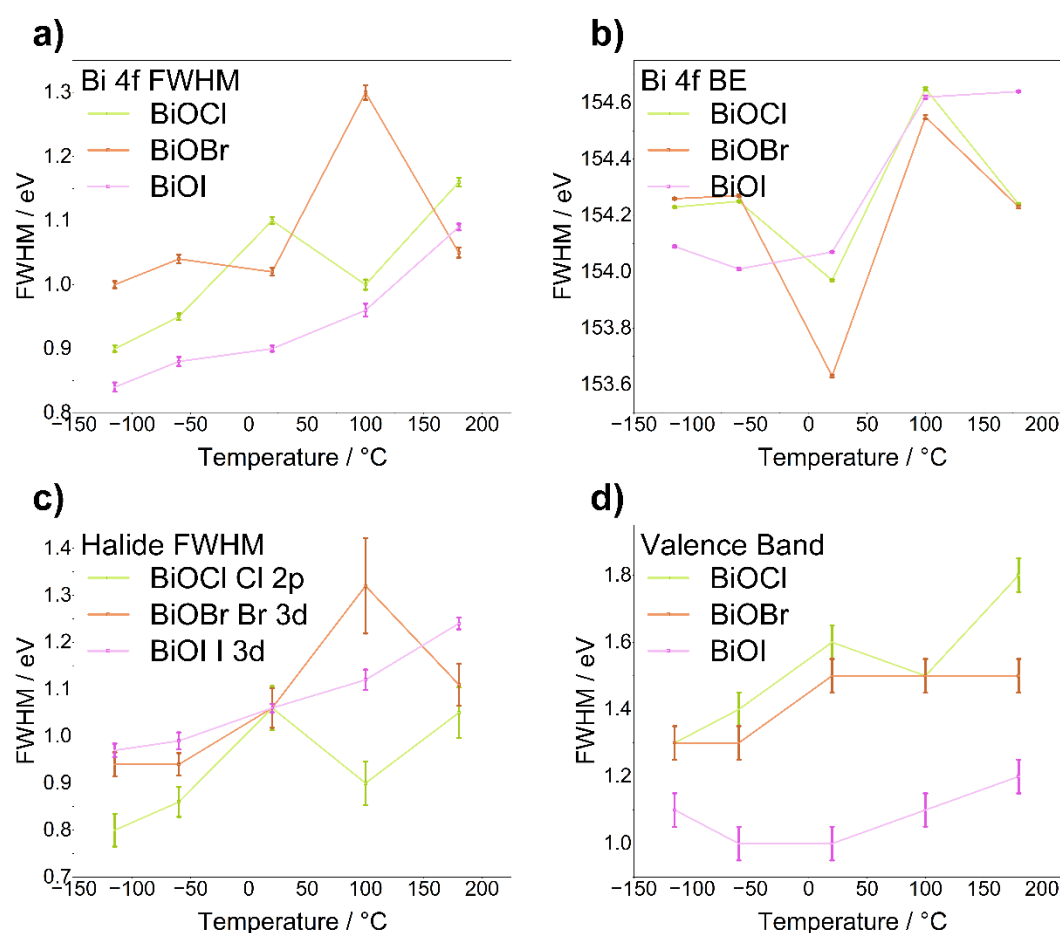
Figure 3.13. The variation with temperature of the **a)** Bi 4f FWHM **b)** the Bi 4f 7/2 uncorrected binding energy **c)** the Cl 2p, Br 3d and I 3d FWHM and **d)** the optimised Gaussian broadening determined from the XPS/DFT VB fitting results, for the BiOX (X = Cl, Br, I) series. The error bars in **a,b,c)** correspond to errors in the fitted FWHM peak parameter estimated by Monte Carlo simulations using CasaXPS (**Table B4**). The error bars in **d)** correspond to the estimated uncertainty in the fitting method.

For the valence band, at any given temperature, the optimised broadening increases for the series BiOI ≤ BiOBr ≤ BiOCl, in line with the decreasing mass of the halide X anion. This is consistent with increased vibrations in lighter atoms compared to heavier atoms. The effect of increasing temperature also had the biggest impact on the material with the lightest halide substituent. The optimised Gaussian FWHM increased by 0.5 eV from 1.3 eV to 1.8 eV over the full temperature range for BiOCl, whereas this was reduced in the BiOBr to an overall 0.2 eV increase.

There is little evidence for charging at low temperatures, except for a small increase in broadening in the BiOI VB, that is not mirrored in the core level behaviour. Going back to the RSS plots (**Figure 3.11**), it can be seen that the data point for BiOI at -115 °C has the highest RSS. The RSS could possibly be used as some kind of error bar for the fitting, indicating that this optimised broadening is not as good as the others. A high RSS could indicate sample charging, as the spectral shape deviates more from normal.

3.4 Vibrational Case Study iii) Nb-doped Strontium Titanate Single Crystals

3.4.1 Intro: Crystal Structure of STO

In this third case study into vibrational broadening, a series of pure/niobium-doped strontium titanate (STO) single crystals, $SrTi_{(1-x)}Nb_xO_3$ (x = 0, 0.05, 0.5, 0.7) were studied. STO belongs to the perovskite family ABO_3 (**Figure 3.14**), and exhibits suitable layer mismatch for many overlayer oxides, making it a popular choice for many functional heterostructures.[161-163] STO has been studied extensively as a model transition-metal oxide system, but also has numerous potential applications in new technologies due to its tuneable optical, electronic and transport properties. Doping is a simple and effective method to modify the properties, and the Nb doping in this study increases the carrier concentration and thus conductivity of STO.[163] Vacuum annealing also increases the conductivity of pure STO.[161, 162] In this case study, the variable temperature measurements performed on STO samples with different Nb doping levels are thus expected to exhibit a range of conductivities and temperature-dependent behaviour.
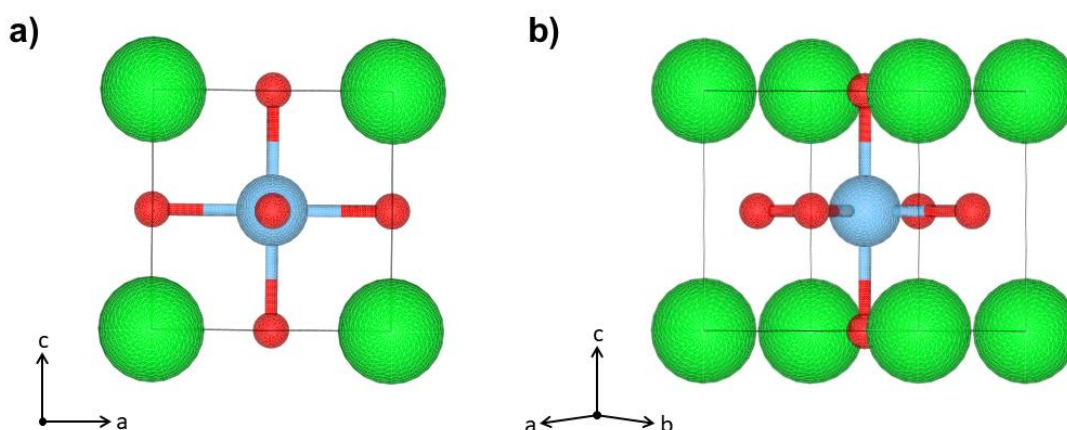
Figure 3.14 a) The crystal structure of $SrTiO_3$ (STO) viewed along the [010] direction and **b)** a slightly rotated view, revealing the TiO_6 octahedra. The Sr, Ti and O atoms are represented by the green, blue, and red spheres, respectively.

3.4.2 Experimental Section

Preparation of Nb-STO compounds

A pure strontium titanate (STO) single crystal (100) substrate and three Nb-doped STO (Nb-STO) single crystal substrates of various doping concentration (0.05, 0.5 and 0.7 wt %) were purchased from MSE Supplies. The single crystals were all single side polished (SSP) and 5x5x0.5 mm size. Before XPS measurements, the crystals were washed with acetone followed by IPA.

XPS Measurements on Nb-STO

Kratos XPS data was collected using a Kratos Axis SUPRA using monochromated Al K-Alpha X-ray source (1486.6 eV). Charge neutralization was achieved using an electron flood gun. Photoelectrons were collected at normal emission with a spot size of 400 µm. A pass energy of 150 eV was used to record survey spectra and pass energies of 20 eV and 30 eV were used to record high resolution VB and core level spectra, respectively. The sample stage was equipped with heat equipment, and measurements were taken at the following temperatures: 20 °C, 40 °C, 80 °C, 120 °C, 180 °C, 240 °C, 300 °C, 400 °C, 500 °C, 600 °C and 700 °C.

Thermo XPS was carried out using a Thermo Scientific K-alpha spectrometer equipped with a monochromated Al K-Alpha X-ray source (1486.6 eV) in constant analyser energy mode. Sample charging was prevented by use of a dual beam flood gun. Photoelectrons were collected at normal emission with a spot size of 400 µm. A pass energy of 150 eV was used to record survey spectra and pass energies of 20 eV and 30 eV were used to record high resolution VB and core level spectra, respectively. Measurements were taken at RT with varying FG currents: 0 µA, 50 µA, 75 µA and 100 µA. A new spot on each sample was analysed each time.

XPS data were processed using CasaXPS.[97] The inelastic background was modelled and subtracted using a Shirley background function. Experimental

VB spectra were smoothed using a 5-point moving average filter, and the VBM was aligned to 0 eV by fitting the low binding energy edge with a complementary error function, which locates the point of intersection of straight lines fitted to the leading edge and the baseline. This method is known as linear extrapolation and is discussed in more detail in **Section 1.2.1.7**.

3.4.3 Computational Methodology

Calculations were performed using the Vienna *Ab initio* Simulation Package (VASP).[98] The convergence criterion for the k-point density and the plane wave cut-off energy parameters was that the total energy was converged to within 1 meV per atom. The resulting converged parameters are listed in **Table 3.8**.

Table 3.8. Converged plane wave cut-off energies and k-point densities for $SrTiO_3$

Material	Plane Wave Cut-off Energy / eV	k-point density
$SrTiO_3$	500	5x5x5

The PBEsol functional was implemented for geometry relaxation and electronic structure calculations. The electronic structure calculations were performed with increasing density to converge the appearance of the calculated density of states (DOS). As the simulated spectra in this work are compared graphically with experimental spectra it is important that the appearance of the DOS is converged. Therefore, a convergence criterion was introduced that after broadening the DOS by the instrumental resolution of 0.4 eV, there were no significant changes in appearance on increasing the k-point density. Spin-orbit coupling (SOC) effects are expected to be significant in elements heavier than Sb,[99, 100] therefore SOC was not included. Full details showing the convergence testing are in in **Appendix B**. A k-point density of 11x11x11 was deemed sufficient.

Photoionization Cross-section Correction Method

In this work, the values reported by Yeh and Lindau (YL),[84] and a second set of values modified from the original YL values, denoted modified YL (YL*), are investigated, as described in more detail in **Section 2.2.4**. The values used for the materials in this section are reported in **Table 3.9** below.

Table 3.9. Energy dependent photoionization cross-section values used in this work for Sr, Ti, and O. The top set are those reported by Yeh and Lindau (YL).[84] The bottom set (YL*) contain some values that have been modified, indicated by the shaded rows. The 'ratio' method used to modify these values is detailed in **Table B3**.

Sr		Ti		O	
YL		**YL**		**YL**	
5s	1.500E-04	**4s**	2.500E-04	**2s**	9.50E-04
4p	1.667E-03	**3p**	1.833E-03	**2p**	6.00E-05
3d	6.900E-03	**3d**	8.500E-05		
YL*		**YL***		**YL***	
5s	1.500E-04	**4s**	2.500E-04	**3s**	3.18E-05
5p	9.63E-05	**4p**	1.23E-04	**2p**	6.00E-05
4d	3.90E-04	**3d**	8.500E-05		

3.4.4 Results

Geometric Structure

$SrTiO_3$ crystalises in cubic Pm-3m symmetry. After geometry optimisation, the structure retained its cubic structure. The calculated a lattice parameter is recorded and compared to reference experimental data in **Table 3.10**, showing good agreement.

Table 3.10. Calculated and experimental lattice parameters for $SrTiO_3$ using GGA DFT (PBEsol). The lattice parameter errors Δa is given with respect to literature values.[164]

	SrTiO₃ *a* lattice parameter
Experiment	3.907 Å
PBEsol	3.895 Å
Δ*x* PBEsol	-0.31 %

Valence Electronic Structure

The collected VB XPS at RT for the series of pure/niobium-doped strontium titanate single crystals, $SrTi_{(1-x)}Nb_xO_3$ (x = 0, 0.05, 0.08, 0.5) (**Appendix B**) show that the small amount of Nb doping does not make any significant changes to the appearance of the XPS VB, therefore it was considered sufficient to use the calculated valence DOS for pure STO to fit all samples. This vastly saves on computational expense, since the incorporation of minor doping levels will greatly complicate the simulation process. The STO VB XPS is shown with the calculated DOS in **Figure 3.15**, together with the DOS corrected with YL and YL* cross-sections. The corresponding RSS for the fit of the plain DOS, the YL corrected DOS and the YL* corrected DOS is 1.01, 2.79 and 0.79, respectively. This shows that the YL* simulated spectrum is the best fit with the experimental data. However, the fit still has some disagreement. To improve this, the weightings of the different orbital components were further modified, by comparing the RSS for a range of Gaussian broadenings and optimising the weightings (**Appendix B**). The resulting simulated spectrum with the optimised weightings and Gaussian broadening of 1.0 eV is shown in **Figure 3.15d**. Notably, the contribution from Ti *p* orbitals is increased, and is necessary to reproduce the spectral shape of the higher BE lobe. These optimised weightings were used when fitting the simulated spectrum for all STO and Nb-STO samples herein.
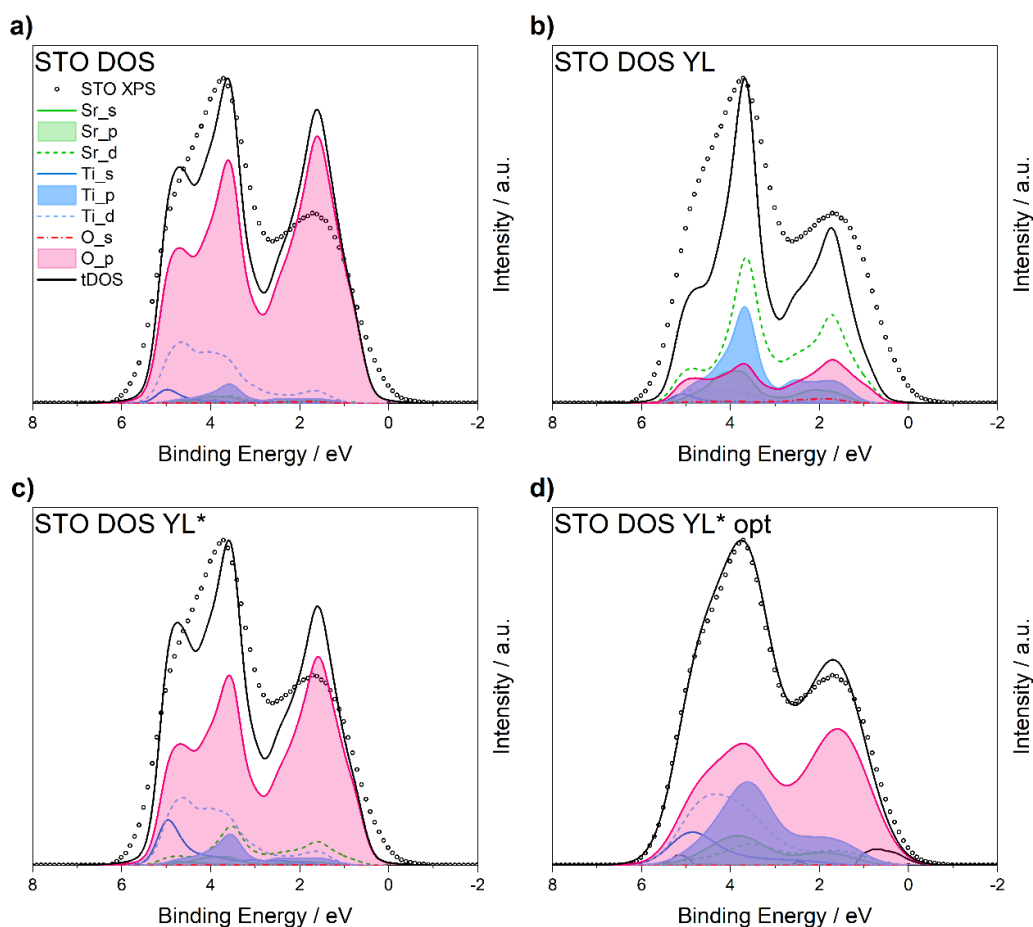
Figure 3.15. VB XPS pure STO single crystal at RT, fitted with **a)** the PBEsol calculated DOS, **b)** the PBEsol calculated DOS corrected with YL cross-sections, **c)** the PBEsol calculated DOS corrected with modified YL* cross-sections and **d)** the PBEsol calculated DOS broadened by a Gaussian of width 1.0 eV and modified YL* cross-sections with optimised weightings.

Valence Band XPS / DFT Fitting

The collected XPS data were fitted with a series of theoretical spectra, which were broadened by Gaussian functions of varying FWHM, ranging from 0.5 – 2.0 eV, following the method previously described (**Section 2.2.4**). The temperature dependent RSS curves showing the goodness of fit for various Gaussian broadening parameters are plotted in **Figure 3.16**. To gain higher resolution of the optimised FWHM, polynomials (order 2) were fitted to the calculated RSS values. The minimum of each curve is taken to be the optimised parameters at each temperature. The minimum RSS values are

99

similar across the series, indicating the good fits for all doping levels and temperatures. Examples of the optimised simulated spectra, fitted to the experimental VB are plotted in **Figure 3.17** for a range of selected temperatures. As the appearance of the VB was similar for all samples, independent of the doping level (**Appendix B**), only the STO VB are shown for clarity. The optimised Gaussian component increases with increasing temperature due to the increased vibrational broadening and does not have any strong dependence on the level of Nb doping. However, the undoped STO sample has the narrowest VB at the lowest temperature levels. The trend in the VB broadening is discussed in more detail alongside the trends seen in the core-levels, in the following section.
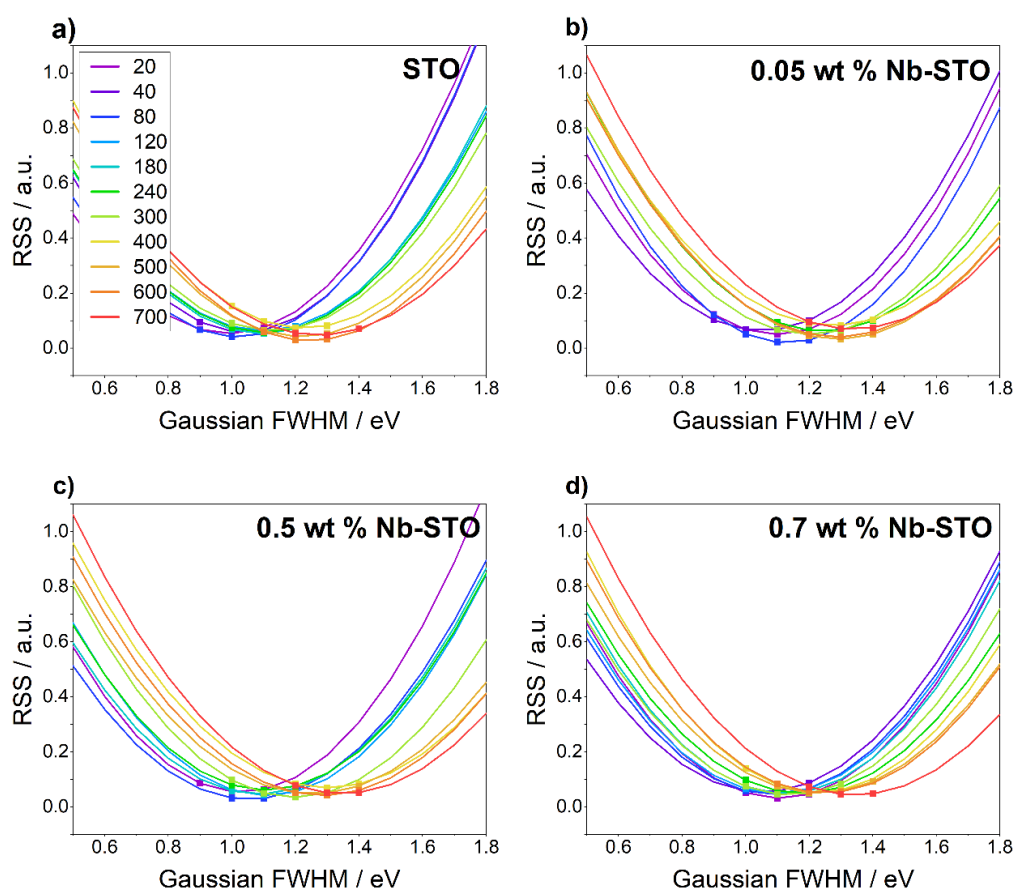
Figure 3.16. Optimisation of the Gaussian broadening applied to theoretical spectra for the series of pure/niobium-doped strontium titanate single crystals, $SrTi_{(1-x)}Nb_xO_3$; $x =$ **a)** 0, **b)** 0.05, **c)** 0.5 and **d)** 0.7). A fixed Lorentzian component of 0.1 eV was applied in each case. The RSS was calculated by fitting with VB XPS spectra at the range of temperatures indicated in **a)**. The temperature dependent optimised broadening is taken as the minimum of each curve.
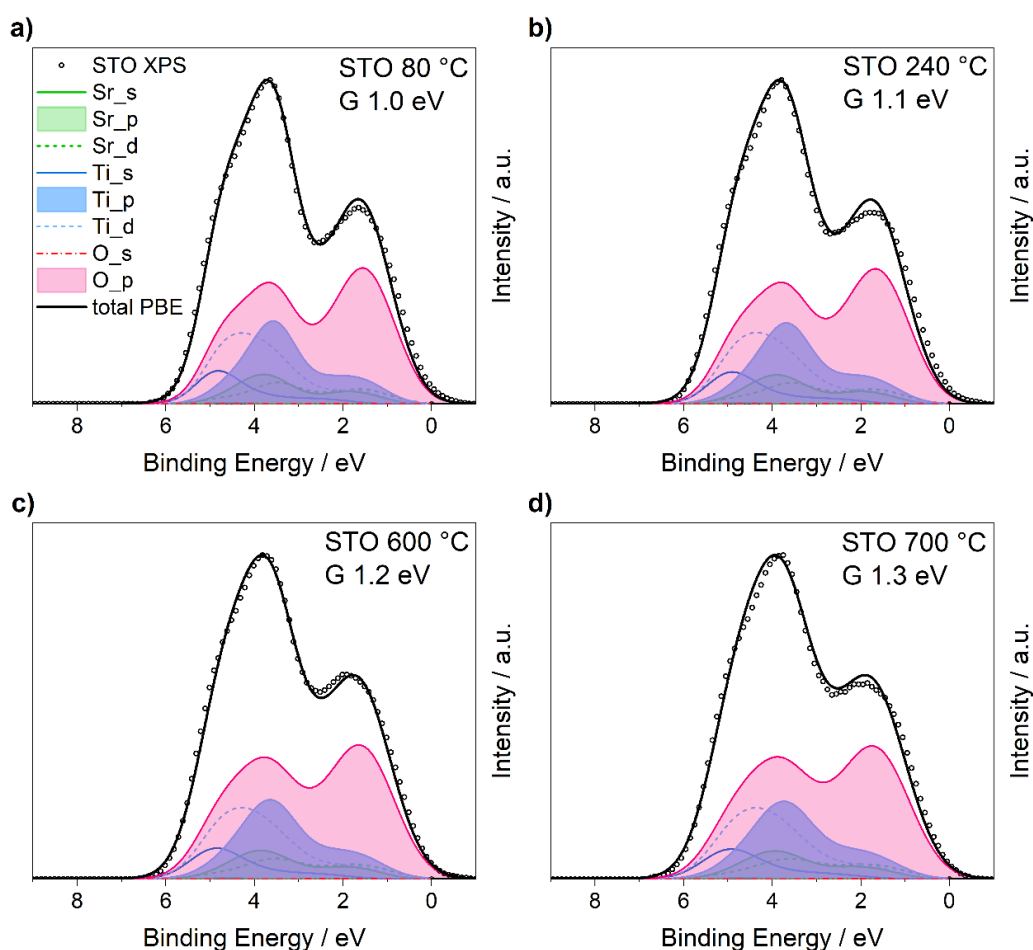
Figure 3.17. DFT simulated VB spectra fitted to XPS VB spectra for STO single crystal, recorded at **a)** 80 ºC, **b)** 240 ºC, **c)** 600 ºC and **d)** 700 ºC. The spectra were simulated using PBEsol pDOS, corrected with optimised YL* photoionization cross-sections, and broadened with Gaussian and Lorentzian functions to simulate the XPS line shape. A fixed Lorentzian broadening of 0.1 eV has been applied in each case to simulate lifetime broadening. The Gaussian component has been optimised in each case. The optimised Gaussian FWHM values for the selected temperatures are: **a)** 1.0 eV, **b)** 1.1 eV, **c)** 1.2 eV and **d)** 1.3 eV, showing an increase with the increasing temperature.

Core Level & Valence Band Broadening

In addition to the VB investigations, vibrational broadening and charging effects in the core levels were investigated by measuring the variation in FWHM and the measured BE. First, the temperature dependence and doping level effects on the core-level BEs is discussed. The measured BEs and charge corrected values are plotted in **Figure 3.18**, where the charge calibration was achieved using the AdC present at all temperatures from RT to 700 °C. Note that any spectra that displayed signs of differential

101

charging, in the form of distorted line shapes, are not included in the plots. The first thing to note is that both the temperature and the Nb doping level have an effect on the measured BEs of the core-level spectra. The effect of the doping level is most obvious when looking at the uncorrected BEs measured at temperatures below ~400 °C, where there is a difference of ~ 5 eV between pure STO and the 0.7 wt % Nb doped sample. This difference can be attributed to charging effects in the pure STO crystal, because after charge correction, the BE difference is reduced to ~ 0.2 eV. For the sample with the smallest amount of Nb doping (0.05 wt % Nb), these charging effects are also present at lower temperatures, but are absent in the highest doping level (0.7 wt % Nb). This illustrates that the higher Nb doping level results in an increase in conductivity, in agreement with Zhang et al., who showed that carrier concentration is correlated with doping concentration in Nb-doped STO.[163]

As the temperature is increased, the measured BEs show interesting trends, both in the uncorrected and charge corrected values. Looking at the uncorrected values, above ~ 400 °C, the difference between values recorded on difference samples decreases, and continues to decrease as temperatures rise. Similar effects of charging being mitigated at higher temperatures have been reported by previous researchers.[161, 162] Lim et al. studied the effect of annealing $SrTiO_3$ in UHV and under oxygen environments from 200 – 600 °C by *in-situ* AP-XPS.[161] They observe slightly higher BEs for core levels measured at 200 °C, which is explained by the insulating characteristics of STO, and they do not see any charging effects above 300 °C due to the increased conductivity. Gonzalez et al. studied the reduction of (100) STO via *in situ* XPS using synchrotron radiation and heating up to 830 °C.[162] All spectra recorded without thermal treatment are shifted to higher BEs by ~18.4 eV, due to the insulating nature of STO. This shift disappears at 300 °C when the sample becomes conducting. Notably, the sample with the lowest Nb-doping level begins to become conducting at a lower temperature than the pure crystal.

102
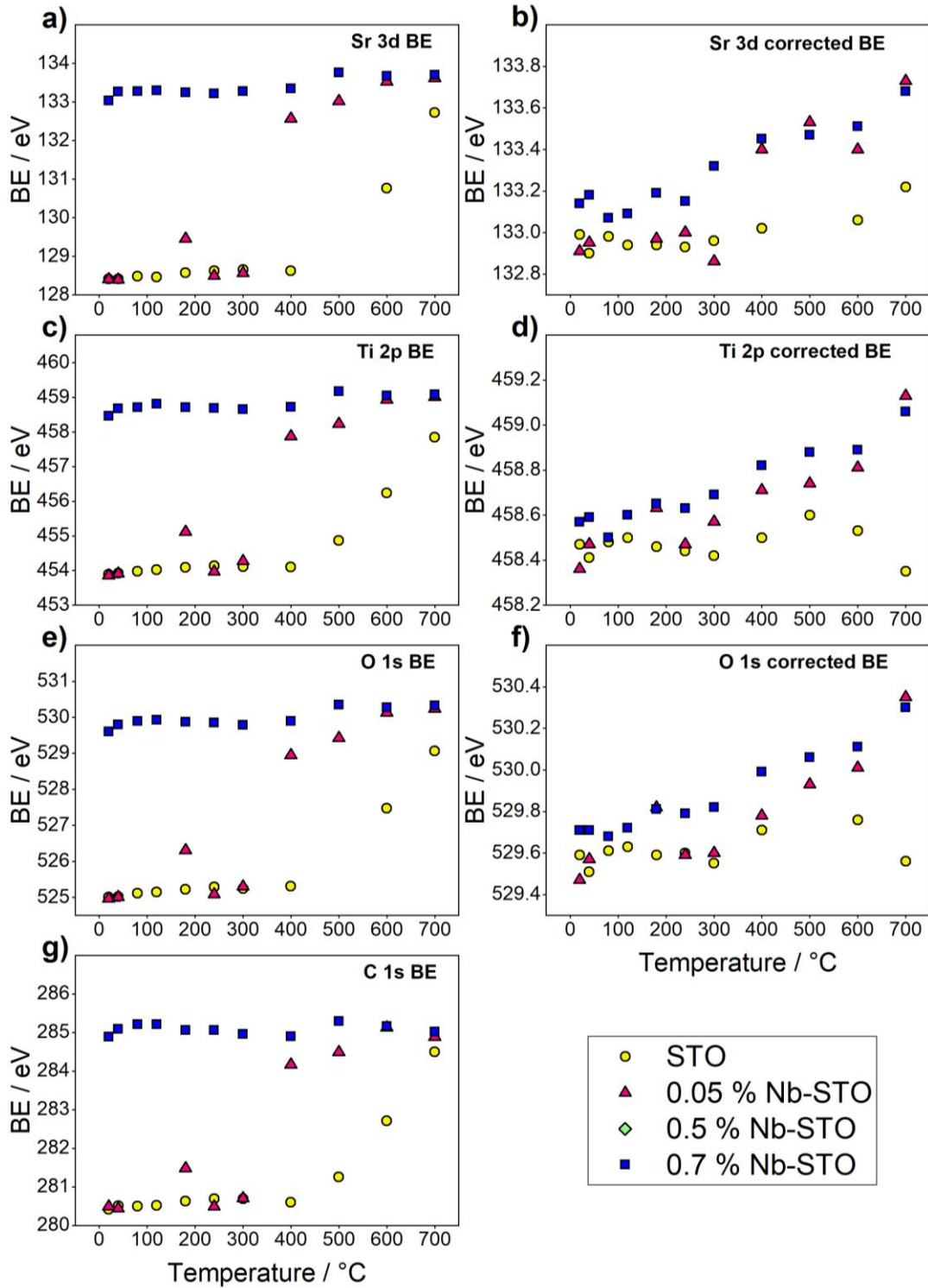
Figure 3.18. The variation of the BE and FWHM with temperature of the core levels **a-b)** Sr 3*d* **c-d)** Ti 2*p* **e-f)** O 1*s* and **g)** C 1*s*, measured by region for the series of pure/niobium-doped strontium titanate single crystals, $SrTi_{(1-x)}Nb_xO_3$ ($x = 0, 0.05, 0.7$). The corrected BEs are given with respect to the AdC BEs shown in **g)**. The estimated errors in the BEs are too small to be seen on the current scale (**Tables B7-B10**).

Turning to the trends in the charge corrected values, the charge correction method with AdC is expected to be reliable. Although great care should be taken when calibrating BEs to AdC,[25] Lim et al. found that calibration to AdC C 1s and Au foil attached to their STO sample gave consistent results between the temperature range of when the STO became conducting and when the AdC was fully desorbed from the surface.[161] In the current study there is a good signal to noise ratio for AdC at all temperatures, although the spectral intensity at 700 °C is greatly reduced and charge correction here may be less reliable than at lower temperatures. Above 300 °C, the charge corrected BEs shift to higher values with increasing temperature. As discussed by Astley et al. temperature-induced changes in BE need to be analysed closely as they can have multiple and different origins.[165]

The temperature induced changes are illustrated in **Figure 3.19** by the changes in the core-level spectra for the case of 0.7 wt % Nb-STO. The changes are similar for the other three samples and are plotted in **Appendix B**. All regions show broader FWHM at higher temperatures, due to increasing vibrational broadening. There are also different changes observed depending on the element region. The C 1s region shows the decreasing carbon contamination with increasing temperature, and also the shift of the Sr 3p ½ level, which shifts to higher BE with increasing temperature. The O 1s spectra also shows loss of contaminant species, from the decreasing spectral intensity at higher BEs, which corresponds to adsorbed -OH groups and water.[166] The loss of carbon and water contamination from the surface of STO is expected at around 600 °C,[162] which is mainly observed here except a small amount of carbon remains at the highest temperature of 700 °C.
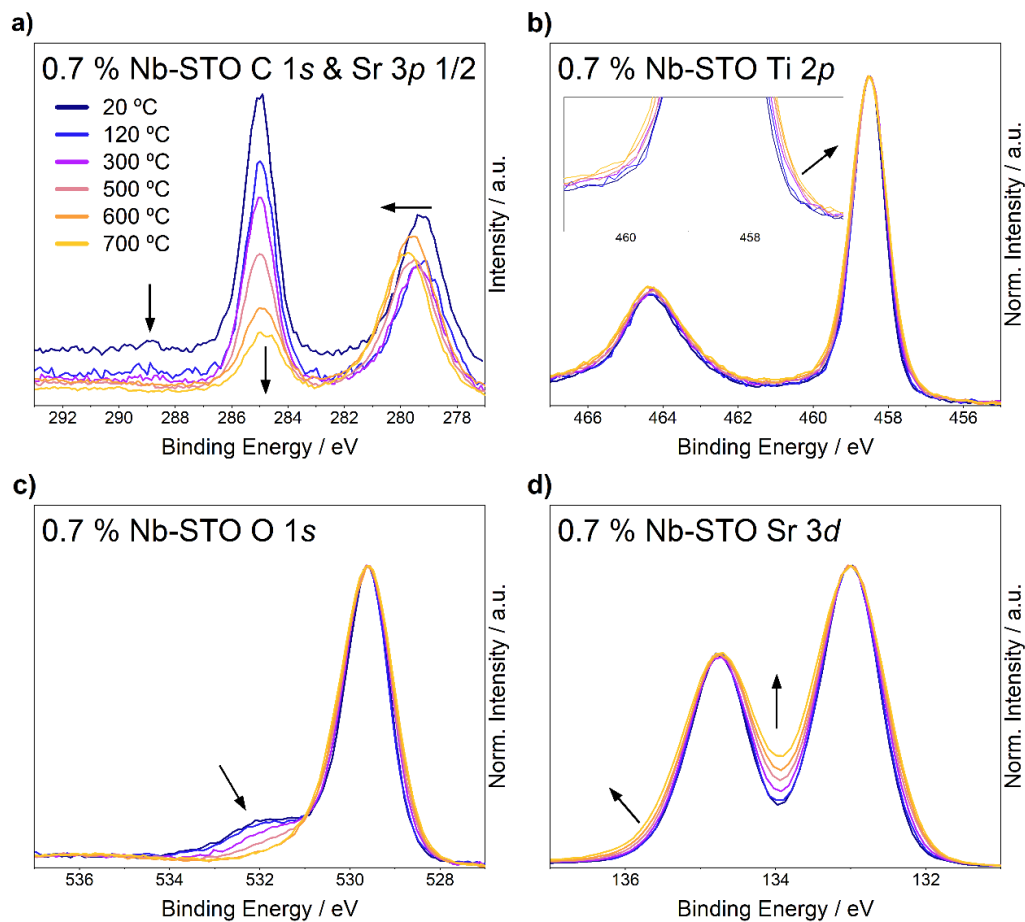
Figure 3.19. The variation with temperature of the core levels of the 0.7 wt % Nb-STO sample: **a)** C 1*s* showing both the C 1*s* and Sr 3*p* ½ peaks, **b)** the Ti 2*p* peak, **c)** the O 1*s* peak and **d)** the Sr 3*d* peak. The arrows indicate some directions in spectral intensity changes with increasing temperature and are discussed in the main text. All spectra have been normalised and overlayed at the BE for charge corrected undoped STO at RT for clarity, except for the C 1*s* region, which is not normalised to show the decreasing carbon contamination with the increasing temperature. A selected range of temperatures are shown for clarity.

Moving to the Sr 3*d* spectra, there is a clear asymmetry observed at all temperatures, with increased spectral intensity at higher BE. This higher BE component has been observed in several other studies on STO surfaces. In the *in-situ* AP-XPS study by Lim et al. into the effect of annealing SrTiO$_3$ in UHV and under oxygen environments they observe a small amount of SrO surface oxide evident in the Sr 3d spectra.[161] This is shown to be at the surface by a higher concentration occurring at a probing depth of 1.5 nm than at 3.3 nm. Under UHV, the amount of SrO present at 3.3 nm probing depth is estimated at about 5 % at RT, which then increases as annealing temperature increases, making the biggest increase between 500 and 600

ºC. At low temperature, it is suggested to originate from dissociated O_2 molecules on the surface that are bound to Sr. Therefore, under the O_2 conditions, the proportion of SrO is much higher at 200 ºC than in the UHV conditions. At higher temperatures, the amount of SrO grows in UHV conditions to a similar concentration seen in the O_2 environment but is formed as a result of the formation of O vacancies and surface reconstruction.
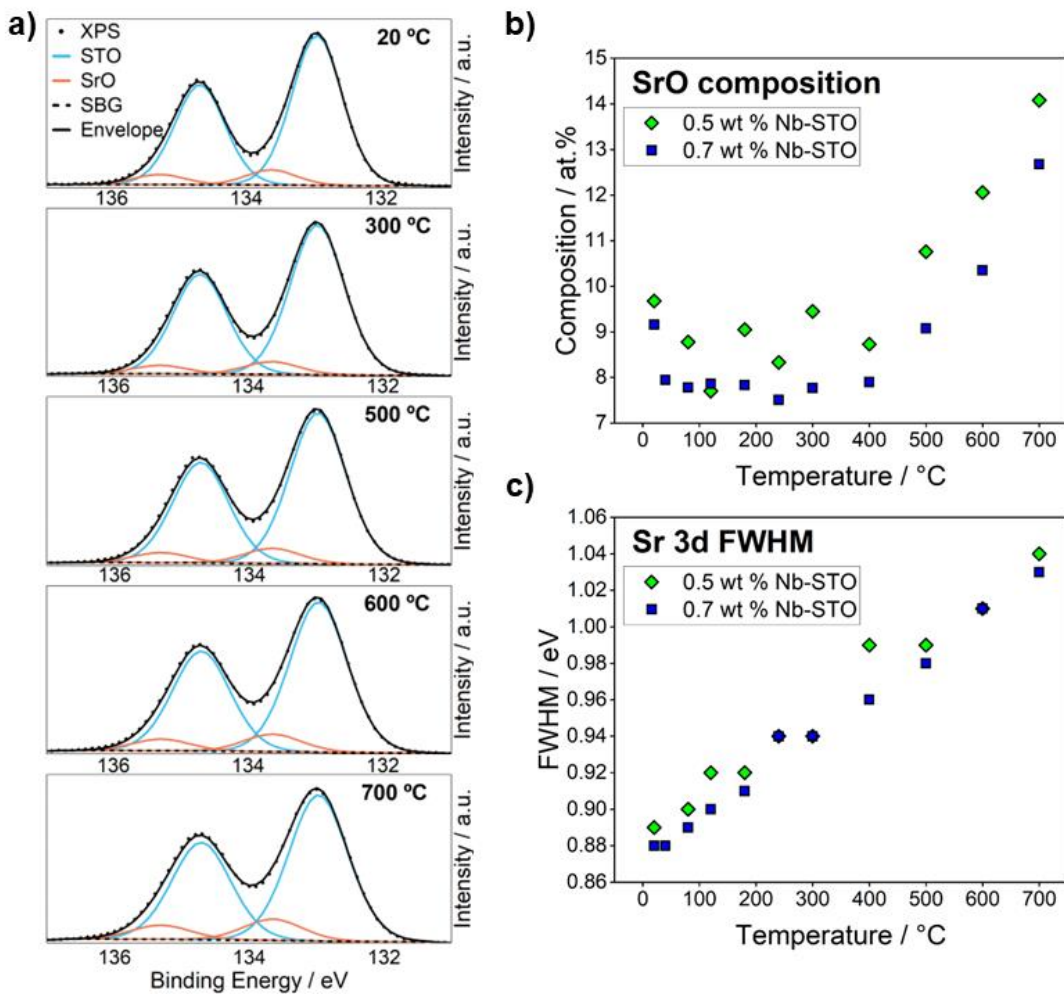
Figure 3.20. The variation with temperature of **a)** the Sr $3d$ core levels of the 0.7 wt % Nb-STO sample, fitted with two doublets to indicate STO and surface SrO components, **b)** the composition of SrO present for the 0.5 and 0.7 wt % Nb-STO samples, and **c)** the Sr $3d$ components FWHM for the 0.5 and 0.7 wt % Nb-STO samples. SBG indicates Shirley background.

Andra et al. studied Nb-doped STO by *in-situ* AP-XPS, where the sample was grown by pulsed laser deposition onto a single crystal STO surface.[167] The Sr $3d$ spectra are fit with two doublets, one for the bulk STO and one for surface SrO phase at higher BE. The concentration of the SrO phase

increases with decreasing probing depth and is around ~ 30 % at 1.2 nm probing depth. It is possible at low temperatures that the high BE doublet also contains some contribution from surface species; Chambers et al. have previously assigned the higher BE component in the Sr 3d spectrum to surface bound $Sr(OH)_x$ by angle resolved XPS measurements of an STO surface.[168]

The Sr 3d spectra for the 0.7 wt % Nb-STO in this work are fit with two doublets in **Figure 3.20a**. The peak model was initially constructed for the RT sample, with GL(30) peaks and a Shirley background. Since the spectra become broader at higher temperature, the FWHM of STO and SrO species were constrained to be equal so any broadening was not erroneously fitted by either doublet. The STO Sr 3d 5/2 peak appears at around 133.0 eV, around 0.70 eV lower than the SrO Sr 3d 5/2 peak. The doublet splitting was 1.74 eV and 1.65 eV for the STO and SrO components, respectively. The relative positions of the four components were constrained to these values when fitting the model to spectra recorded at higher temperatures.

As it can be seen in **Figure 3.20a** the peak model fits well for the displayed temperatures and was also the case at all temperatures for the highest doping level (0.7 wt % Nb-STO), and at all temperatures except 40 °C in the case of the 0.5 wt % sample, where some distortion and charging effects are evident. There is also charging effects observed for the lowest doping concentration (0.05 wt % sample) in several Sr 3d spectra up to 300 °C, and in multiple cases for the pure STO crystal that persist up to 400 °C. Some examples of charging seen in the Sr 3d spectra are plotted in **Figure 3.21**, showing the variation in severity of the effects. Although the extent of distortion does not correlate with the doping concentration, the number of affected spectra and the maximum temperature at which it is observed both increasing with the doping concentration.
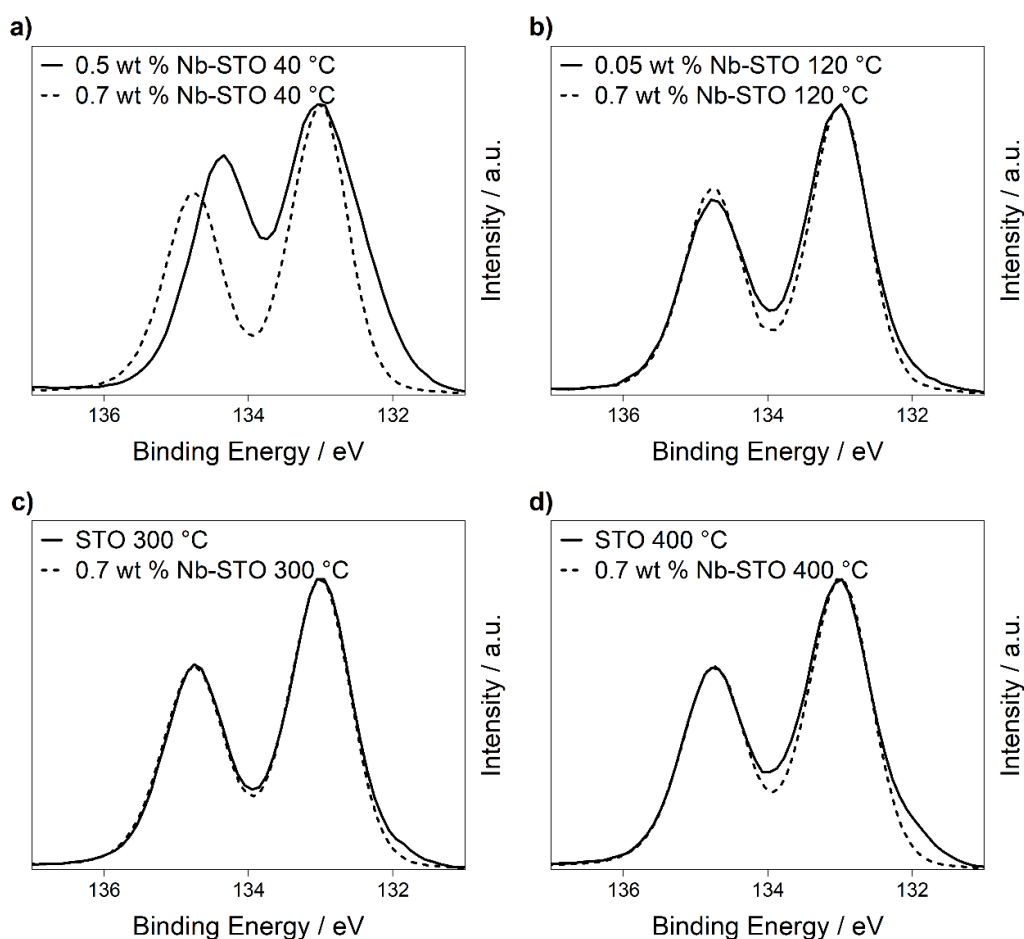
Figure 3.21. Some examples of charging in the Sr $3d$ core levels for **a)** of the 0.5 wt % Nb-STO sample, **b)** of the 0.05 wt % Nb-STO sample and **c-d)** the pure STO crystal. In each case the 0.7 wt % Nb-STO spectra recorded at the same temperature are displayed for reference, which showed no obvious charging effects at any temperature. As can be seen, the extent of distortion ranges from mild to more severe and can make component fitting unreliable.

The composition of the higher BE doublet, attributed to SrO, and the corresponding FWHM at varying temperature is displayed for the two highest doping concentrations in **Figure 3.20b,c** The concentration of SrO increases with increasing temperature, above temperatures ~400 °C, which is similar to the observations of Lim et al.[161] The composition of surface oxide observed in this work may be less than the values reported at synchroton sources because the probing depth is slightly larger in the lab based XPS, meaning the measurements are not as surface sensitive. The FWHM of the two Sr $3d$ doublets similarly increase with increasing temperature **Figure 3.20c)**, indicative of the increasing vibrational broadening.

Relationship with √T

As mentioned in the introduction to this chapter, a clear relationship has previously been found between the measured FWHM in core-level XPS and the square-root of the temperature ($\sqrt{T}$) for temperature dependent XPS studies on alkali halides.[132] This has been explained in terms of phonon broadening (**Eq. 3.1**). This relationship has been investigated for the core-level temperature dependent data recorded for the Nb-STO samples in **Figure 3.22**.
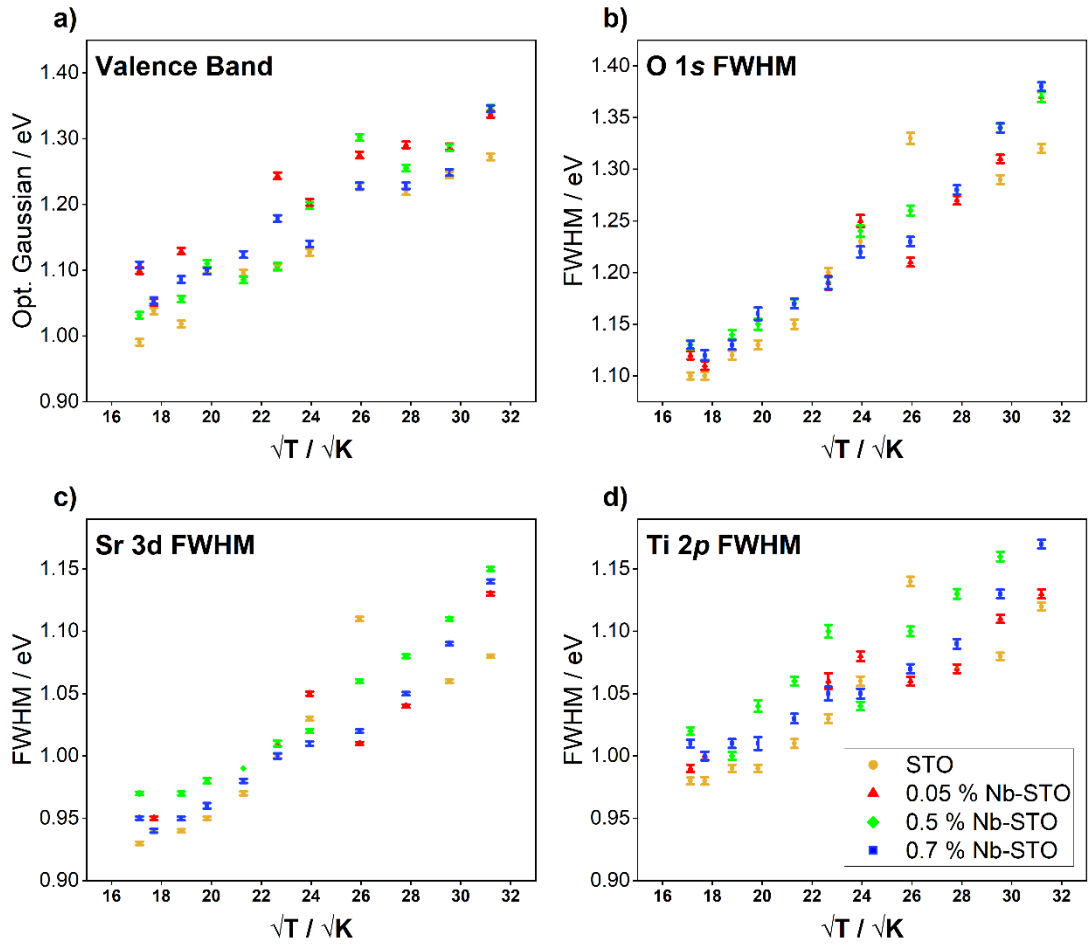
Figure 3.22. The variation with √T of **a)** the optimised Gaussian broadening in the VB fitting, compared to the measured FWHM **b)** O 1*s*, **c)** Sr 3*d*, and **b)** Ti 2*p* for the series of pure/niobium-doped strontium titanate single crystals, $SrTi_{(1-x)}Nb_xO_3$ (x = 0, 0.05, 0.5, 0.7). The error bars in **a)** correspond to the estimated uncertainty in the fitting method. The error bars in **b-d)** correspond to errors in the fitted FWHM peak parameter estimated by Monte Carlo simulations using CasaXPS (**Tables B8-B10**).

For all species, the FWHM increases with increasing temperature, and displays an approximately linear trend with $\sqrt{T}$. The oxygen sites exhibit increased vibrational broadening than the heavier Ti and Sr atoms, which is expected due to the lower atomic mass. An interesting observation is that the optimised Gaussian broadening in the VB, determined using the XPS/DFT VB fitting method is similar to the broadening exhibited in the O $1s$ spectra. As the valence DOS is mainly located on the O site, this could explain the similar temperature-dependent broadening behaviour. It is therefore possible that broadening the O pDOS more than the Sr and Ti pDOS could be justified in an alternative broadening optimisation method and would be an interesting avenue for future research.

FG Current Effects on Charging

Further experiments were done using the Thermo Scientific K-alpha, which uses a different method of charge compensation to the previous experiments. This is a dual beam source that uses a combination of low energy electrons and argon. In these experiments the FG current was varied to see the effect on the FWHM and BE of the core levels (**Figure 3.24**). The undoped STO crystal core levels Sr 3d and Ti 2p shows a positive BE shift with no charge compensation due to charging, and then takes a big negative shift when charge compensation is turned on. This ends up around 2 eV lower than the doped samples, probably due to overcompensation by the filament. The FWHM of the Sr 3d is much higher with no charge compensation and is obviously charging from the distorted peak shape, however this is not mirrored in the Ti 2p or the VB spectra. The doped samples have a constant BE regardless of the charge compensation, which shows that the doping is increasing the conductivity of the samples, as previously observed. The larger FWHM for the higher doped sample is probably caused by disorder broadening.
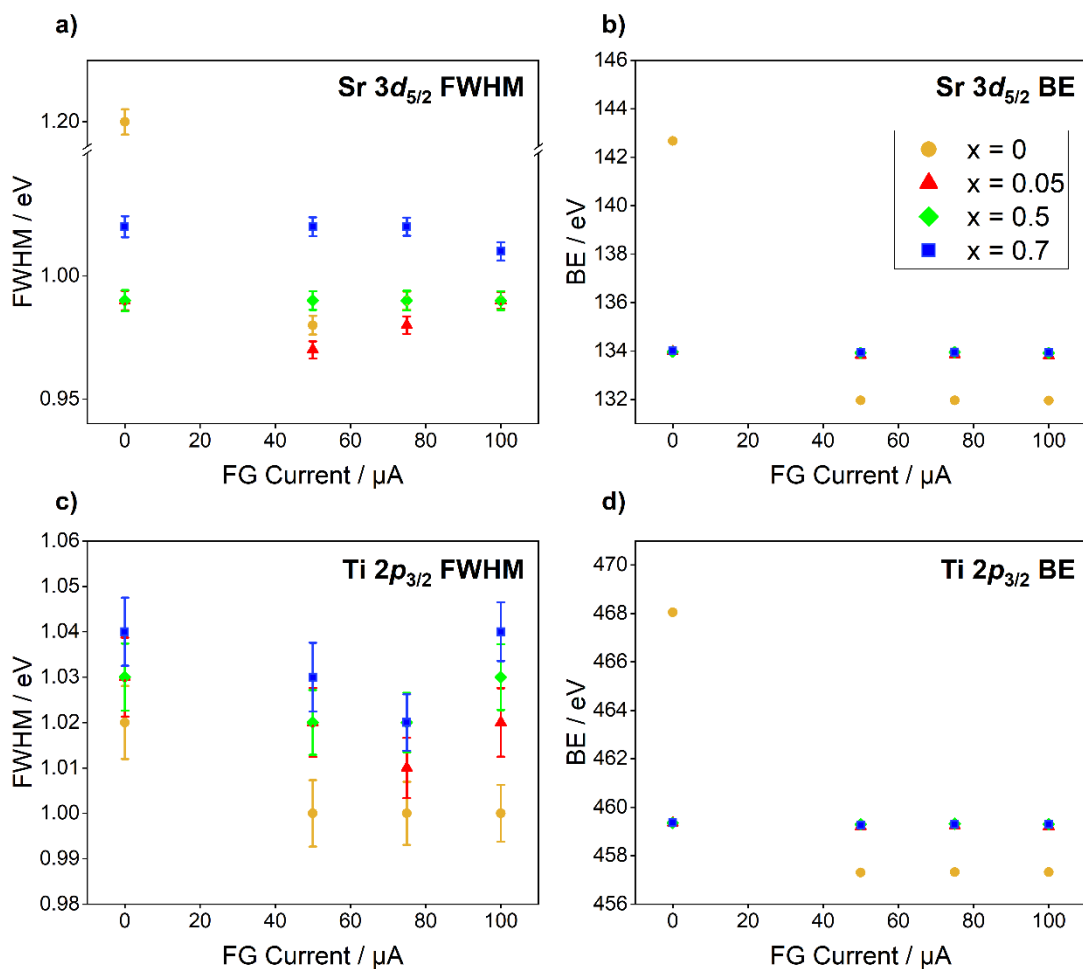
Figure 3.24. The variation with FG current of the **a)** Sr 3d FWHM, **b)** the Sr 3d 5/2 uncorrected binding energy, **c)** the Ti 3p FWHM and **b)** the Ti 3p 3/2 uncorrected binding energy for the series of pure/niobium-doped strontium titanate single crystals, $SrTi_{(1-x)}Nb_xO_3$ (x = 0, 0.05, 0.5, 0.7). The doping concentrations are indicated in the key. The error bars in **a,c)** correspond to errors in the fitted FWHM peak parameter estimated by Monte Carlo simulations using CasaXPS, and the estimated errors in the BE peak parameter are too small to be seen on the current scale (**Table B11**).

3.5 Part III Conclusions

In **Part III**, the topic of spectral broadening is investigated by the effect of both charging and vibrational broadening contributions to core and VB line shapes as a function of temperature. This work comprises three case studies, encompassing a range of different materials: **i)** alkali halides, MX (M = Na, Cs; X = F, I), **ii)** bismuth oxy halides, BiOX (X = Cl, Br, I) and **iii)** a series of pure/niobium-doped strontium titanate single crystals, $SrTi_{(1-x)}Nb_xO_3$ (x = 0, 0.05, 0.5, 0.7). For all three case studies, the PBEsol simulated spectra gave good fits to the experimental data. This requires optimised spectral broadening involving a Gaussian component much larger than the instrumental resolution. These additional sources of broadening can be linked to disorder and vibrational broadening in the compounds.

In addition, HSE06 spectra were also simulated for the MX and BiOX materials, which also well matched the experimental VB spectra. In the case of MX, the HSE06 theoretical VB were remarkably similar to the PBEsol spectra. The HSE06 BiOX spectra were slightly wider than the PBEsol spectra, but the main spectral features were predicted by both functionals. The PBEsol spectra were chosen to fit to the temperature dependent XPS data, due to the excellent fits and low computational expense, but comparable results are expected using the HSE06 spectra as was seen previously in **Part II**. The use of YL* photoionization cross-sections gave good agreement with the XPS spectra for the MX and BiOX compounds (similarly to the compounds studied in **Part II**). However, this was not the case for STO. The cross-section weightings were thus optimised to give better fitting spectra, simulated using PBEsol. Notably, a larger contribution from Ti p orbitals was required to reproduce the experimental VB shape.

Turning to the temperature dependent behaviour of the different classes of materials, insulators and semi-conductors were found to behave very differently. In MX, for the isostructural compounds, NaF, NaI and CsF, the trends in the temperature dependent VB broadening can be rationalised in

112

terms of an interplay between the effects of both vibrational broadening (influenced by the size of the ions) and charging effects (influenced by the band gap). At low temperatures charging effects dominate due to the decreased conductivity. The largest charging contributions to spectral broadening were seen for the insulating MX compounds. Furthermore, the largest charging effects were seen for the widest bandgap material NaF, which also experienced the largest vibrational broadening of the group due to the lightest atoms. The broadening in NaF was therefore the highest at every temperature recorded. The CsI sample behaved differently to the other MX compounds and did not exhibit much temperature dependent behaviour. As the heaviest compound, the ions are expected to exhibit least vibrational amplitude. The structure is also different from the other crystals (bcc rather than fcc.) At the highest recorded temperature, when the charging effects should be at the minimum, the degree of Gaussian broadening increases with decreasing atomic mass CsI < CsF ~ NaI < NaF.

In BiOX, the smaller bandgap and increased conductivity means negligible charging effects were seen. The spectral broadening is thus dominated by vibrational effects. At higher temperatures, an increased Gaussian component is required to fit VB spectra, which is increased further for the lighter halide substituents due to the increased vibrational amplitude of lighter atoms. The magnitude of vibrational broadening decreases with increasing atomic weight of the halide anion substituent Cl > Br > I. Small variations in the lattice parameter only caused minor changes in the width of the calculated DOS. When including vdW forces, the larger the change in the c lattice parameter, the larger the widening of the calculated VB DOS, therefore the starting structure and inclusion of these forces could impact the absolute value of the Gaussian broadening optimisation. The choice of functional also impacts the width of the calculated DOS and thus the width of the simulated spectra. In all cases studied, the hybrid functional produces a slightly wider VB than the GGA functional. Although the absolute value of the optimised Gaussian broadening may change slightly depending on the

level of theory used, the overall trend for a group of materials is expected to be similar, as was observed for the Cs_2TeX_6 series in **Part II**.

In Nb-STO, an increase in vibrational broadening is seen across both core and valence spectra with increasing temperature. The measured FWHM of the core-lines and the optimised Gaussian component of the VB spectral broadening exhibit a roughly linear relationship with $\sqrt{T}$, in agreement with theoretical phonon broadening. At temperatures below 400 °C, charging effects are observed in the uncorrected BEs relating to the conductivity of the samples. The charging effects are greatest for pure STO, and reduce on increasing the Nb doping level, consistent with increased conductivity. Changes in charge corrected BEs at increasing temperatures coincide with several effects: thermal expansion as evidenced by broader FWHM, the desorption of surface species as evidenced by the reduction of C and O contaminant peaks, the mitigation of charging effects observed in the uncorrected BEs, and surface reconstruction to form an SrO surface layer as evidenced by the growth of an SrO component in the Sr $3d$ spectra.
An interesting observation is that the optimised Gaussian broadening in the VB, determined using the XPS/DFT VB fitting method, is similar to the broadening exhibited in the O $1s$ spectra. As the valence DOS is mainly located on the O site, this could explain the similar temperature-dependent broadening behaviour. It is therefore possible that broadening the O pDOS more than the Sr and Ti pDOS could be justified in an alternative broadening optimisation method and would be an interesting avenue for future research.

Part IV – Mapping Heterogeneous Photocatalytic Surfaces

In **Part IV**, the methodology of refining DFT-simulated spectra for the analysis of VB XPS spectra is extended to the modelling of mixed phase systems. This is applied to the quantitative mapping of mixed phase TiO_2 surfaces. A brief overview of traditional phase quantification methods is given first, followed by an introduction of mixed phase TiO_2 systems and the methodology used in this chapter, which includes additional experimental techniques. A more detailed introduction to these techniques is given in the **Section 1.2**. Finally, the results are presented before some overall conclusions. Note that some of the mixed phase TiO_2 results have been published elsewhere in a different format.[1] Additional results and details appear in this chapter.

4.1 Review: Phase Quantification

Quantifying the concentrations of crystalline phases present in a sample has been a vital tool in chemistry, physics, geology, materials science, and related disciplines for over 80 years.[169] The practice of quantitative phase determination is largely, but not exclusively, carried out using diffraction methods: most commonly X-ray,[170] neutron,[171] or electron diffraction.[172] In the well-known Rietveld method, an atomistic structural model for each phase is used to calculate angular-dependent diffraction intensities, which are compared with experiment, and the model, including parameters representing phase fraction, is then iteratively refined against the data.[173] The high penetrating power of x-rays and neutron beams make these diffraction techniques typically able to probe many micrometres or further into a sample, making the phase fractions obtained from refinement representative of the bulk material. However, for functional materials with applications dominated by surface processes (as is the case in heterogenous catalysis), a major challenge lies in the quantification of crystalline phases at the surface. With this view, the surface sensitivity of XPS (**Section**

1.2.1.3) is advantageous in the characterisation of the surface structure, which is of vital importance in understanding reaction mechanisms and chemical processes in fields such as interfaces, nanotechnology, and heterogeneous catalysis.

Recently, it has been shown that structural information can be extracted from the XPS VB spectrum of mixed phase samples, such as identification of crystalline phase,[174] and quantification of phase fractions.[175-177] Breeson et al. reported a method of phase quantification for anatase-rutile mixtures of TiO_2.[175] By fitting the spectral shapes of VB XPS measured on pure anatase and rutile powders to VB spectra measured on mixed phase powders, the surface phase fraction was determined by the ratio of the pure phase components. Krishna et al. utilised a similar method for mixed polymorphs of iron oxide nanopowder (α- Fe_2O_3 and γ-Fe_2O_3).[177] The phase fraction was found to have a linear relationship with the ratio of the pure phase spectral shapes, fitted to the mixed phase data, and agreed well with the phase fraction determined by XRD. In the current work, this concept is extended to investigate the use of simulated spectra for the pure phase components in place of experimental spectra.

4.2 Mixed Phase TiO_2

4.2.1 Intro: TiO_2 Structure & Properties

Polymorphs of TiO_2

Titanium dioxide (TiO_2) exists in several different polymorphs, including anatase and rutile (**Figure 4.1**). The anatase polymorph displays photocatalytic properties whilst rutile is inactive, however, the mixed phase system been studied extensively due the enhanced activity of anatase-rutile mixtures.[178-182] Determining the surface phase fraction is therefore important in understanding the activity of such systems.
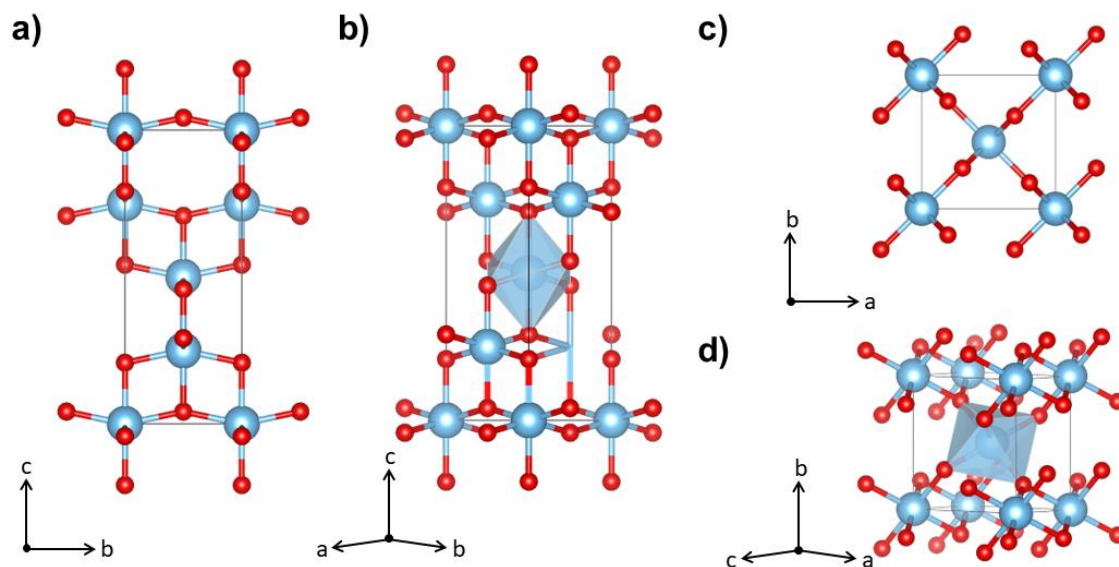
Figure 4.1a) The crystal structure of anatase TiO_2 viewed along the [100] direction, **b)** a slightly rotated view revealing the central TiO_6 octahedra, compared to **c)** the crystal structure of rutile TiO_2 viewed along the [001] direction, and **d)** a slightly rotated view revealing the central TiO_6 octahedra. The titanium and oxygen atoms a represented by the blue and red spheres, respectively.

Classic MO Theory and the Valence Electronic Structure of TiO₂

The valence electronic structure of both anatase and rutile polymorphs can be interpreted in terms of the molecular orbital (MO) bonding scheme for a first row transition metal in an octahedral field.[89, 183, 184] Asahi et al. calculated densities of states and charge densities for anatase and interpret their features in terms of an MO picture.[183] Woicik et al. compared the experimental partial densities of states from site-specific XPS spectra of rutile to theoretical partial densities of states, and interpret the spectral features in terms of a classical MO bonding framework.[89] Sorantin et al. calculated electron densities of rutile and also interpreted charge density contour plots in terms of an MO scheme.[184]

Despite the different distortions of the two polymorphs from perfect octahedral geometry, a classical MO scheme offers an instructive interpretation for both the theoretical and experimental valence electronic structure. The anatase TiO_6 octahedral MO bonding scheme as described by Asahi et al.[183] is summarised schematically in **Figure 4.2**. In this scheme, the most stable σ bonding interactions arise from hybridization of the O p_σ

and Ti e_g orbitals. At a higher energy, there are π bonds between O p_π and Ti t_{2g} states. The highest occupied molecular orbital (HOMO) is mainly non-bonding O p_π in character, and the lowest unoccupied molecular orbital (LUMO) is predominantly formed from Ti d_{xy} orbitals.
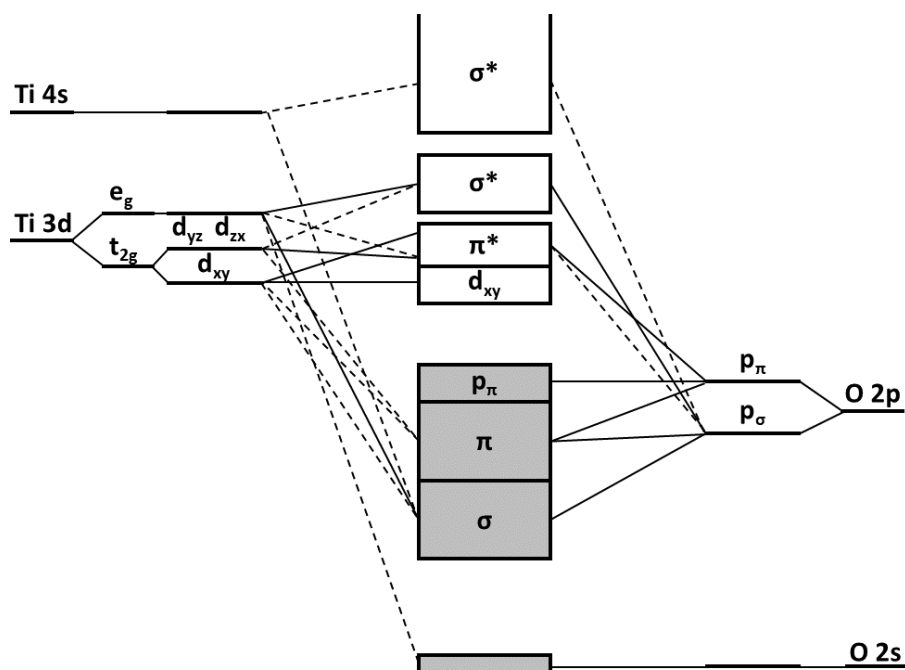
Figure 4.2. Molecular orbital bonding model for anatase TiO$_2$, depicting the atomic levels, crystal-field split levels and final interactions, adapted from the work of Asahi et al.[183] The dashed and solid lines represent weak and strong interactions respectively.

4.2.2 Experimental Section

Preparation of TiO$_2$ Thin Films

All chemicals were purchased from *Sigma-Aldrich.* Four anatase TiO$_2$ thin films were deposited on quartz substrates (25×25 mm^2) using atmospheric-pressure chemical vapour deposition (APCVD). The synthesis was carried out using titanium isopropoxide as a single source precursor. The precursor was initially contained in a stainless-steel bubbler at 150 ºC and subsequently carried (precursor gas flow, 1.5 L min^{-1}) under pre-heated nitrogen carrier gas through a mixing chamber heated to 200 ºC into a cold-wall reactor. The CVD reactor consisted of a quartz tube with a 320 mm-long graphite block with three inserted *Whatman* heaters. The total gas flow

118

in the system was 10 L min^{-1}. All components of the CVD apparatus were kept at 150 ºC and temperature control of the individual components was monitored using Pt-Rh thermocouples.

Initial deposition of anatase TiO_2 coatings was carried out at a substrate temperature of 500 °C for 2 min. This procedure resulted in formation of an anatase TiO_2 film, with no rutile phase detected by thin film XRD or Raman spectroscopy (**Appendix C**). One of these films was retained with no further treatment as a pristine anatase reference. Two of the films were subsequently treated under oxy-propane flame annealing localised at the corner and centre regions of the films in order to induce local formation of rutile though thermally induced phase transformation.[178] These samples are herein referred to as *r-corner* and *r-centre* samples, respectively. The temperature in the flame annealed area was estimated using a Mikron 9104 IR-camera, ranging between T= 1000-1200 °C. A fourth sample was annealed in furnace at 1000 °C for 5 h to allow for a complete transformation into pure rutile phase. Both pristine anatase and the rutile films produced by furnace annealing were used as reference samples.

XPS Measurements on TiO_2 Thin Films

XPS was carried out using a Thermo Scientific K-alpha spectrometer equipped with a monochromated Al K-Alpha X-ray source (1486.6 eV) in constant analyser energy mode. Photoelectrons were collected at normal emission with a spot size of 400 μm. No special steps were taken to clean the samples prior to measurement, and no etching was carried out on the samples as this is known to cause reduction of TiO_2. Sample charging was prevented by use of a dual beam flood gun. A pass energy of 50 eV was used to record high resolution valence band spectra for the TiO_2 thin films samples detailed above. For the anatase and rutile samples, VB spectra were recorded at four points and averaged to produce representative VB spectra for each polymorph. For the mixed phase samples, spectra were

recorded for a square grid of 12 x 12 points, which were spaced 2.1 mm apart.

The spectra were processed as follows using CasaXPS:[97] experimental VB spectra were smoothed using a 3-point moving average filter, a Shirley background was subtracted and the VBM was aligned to 0 eV by fitting the low binding energy edge with a complementary error function, which locates the point of intersection of straight lines fitted to the leading edge and the baseline. This method is known as linear extrapolation and is discussed in more detail in **Section 1.2.1.7**.

Raman Spectroscopy

Raman spectra were acquired using a *Renishaw* micro-Raman spectrometer with a sensitive CCD detector coupled to a microscope for point-by-point analyses. Spectra were measured using an incident wavelength of 514 nm with an exposure time of 3 x 60 s. The spectra for horizontal linear cross-sections of all samples were recorded for a set of 12 analysis points spaced 2.1 mm along a diagonal of the substrate, to include the rutile-rich corner region with analysis points. Phase quantification via Raman spectroscopy was achieved using a methodology for determining the concentration of anatase or rutile in mixed-phase TiO_2 systems.[185] The analysis region was confined to 310–750 cm^{-1}, with five individual phonon modes, 3 anatase and 2 rutile, fitted with Lorentzian functions using the OriginLab platform.[186]

Photoactivity Mapping

Local photocatalytic activities were assessed using a standard test following the photoreduction of a resazurin-based (*smart*) ink.[187, 188] The ink was prepared from a 1.5 % hydroxyethyl cellulose (HEC) solution that was cooled to 2 °C overnight prior to further use. The rest of components in the ink (given per 10 g of HEC) were subsequently added under strong stirring conditions, in order: 1 g glycerol (30 min stirring time), 10 mg of resazurin dye (2 h stirring time) and 20 mg polysorbate (30 min stirring time). The

stock dye mixture was then stored at 2 °C and again stirred for 30 min prior to each use. The ink was coated onto the thin film samples by spin coating. The samples were irradiated under blacklight-bulb (BLB) UVA lamp (Vilber-Lourmat, 2×8 W, λ= 365 nm). The irradiance of the lamps at sample-point was measured using a UVX radiometer (*UVP*) as I= 2 mW cm^{-2}. Colour mapping was traced using RGB analysis (12x12 pixel grid) in MATLAB software.

4.2.3 Computational Methodology

Calculations were performed using the Vienna *Ab initio* Simulation Package (VASP).[98] The convergence criterion for the ***k***-point density and the plane wave cut-off energy parameters was that the total energy was converged to within 1 meV per atom. The resulting converged parameters are listed in **Table 4.1**.

Table 4.1. Converged plane wave cut-off energies and k-point densities for the anatase and rutile polymorphs of TiO_2.

Material	Plane Wave Cut-off Energy / eV	*k*-point density
Anatase	600	6 x 6 x 3
Rutile	600	5 x 5 x 8

The PBEsol functional was implemented for geometry relaxation and electronic structure calculations. For the electronic structure calculations, ***k***-point densities of 8x8x3 and 5x5x8 were used for anatase and rutile, respectively.

Additional calculations were carried out on different slab models for the anatase structure, to simulate the electronic structure of three low index surfaces: (001), (010) and (101). The 'slab' contains a few layers of crystal structure, bordered at either side by a vacuum. The periodic boundary conditions of the VASP calculation still apply, thus the size of the vacuum is converged to ensure that slabs in neighbouring cells do not interact. The

generation of the slab models and the convergence of the slab and vacuum thickness was performed using the surfaxe code written by Brlec et al.[189]

Photoionization Cross-section Correction Method

In this work, the values reported by Yeh and Lindau (YL),[84] and a second set of values modified from the original YL values, denoted modified YL (YL*), are investigated, as described in more detail in **Section 2.2.4**. The values used for the Ti and O in this section were previously reported for STO in **Table 3.9**.

4.2.4 Results

Valence Electronic Structure

The calculated DOS of the anatase and rutile polymorphs are plotted in **Figure 4.3a,b**. The VB DOS is dominated by the O p states for both polymorphs, consistent with other reported calculations.[190, 191] There are also non-zero overlap integrals between Ti d and O p states, indicating a degree of covalency between metal and oxygen states.[183, 192] The data collected from 4 points across the anatase and rutile thin films was collated to produce an average spectral shape for each polymorph, and is plotted in **Figure 4.3c,d** with the fitted DFT-derived spectra.

The DFT fitting method for the pure phases is the same as was previously descried (**Section 2.2.4**). Similar to the case of STO (**Section 3.4.4**), the plain DOS, YL and YL* modifications do not reproduce the spectral shape well and the YL* values were further optimised to give a better fit. As was the case for the STO, a significant contribution from the Ti p orbital is required to reproduce the experimental spectral shape. Details of the optimised parameters are in **Appendix C**. An optimised Gaussian broadening of 1.3 eV has been applied, along with a fixed Lorentzian contribution of 0.1 eV.
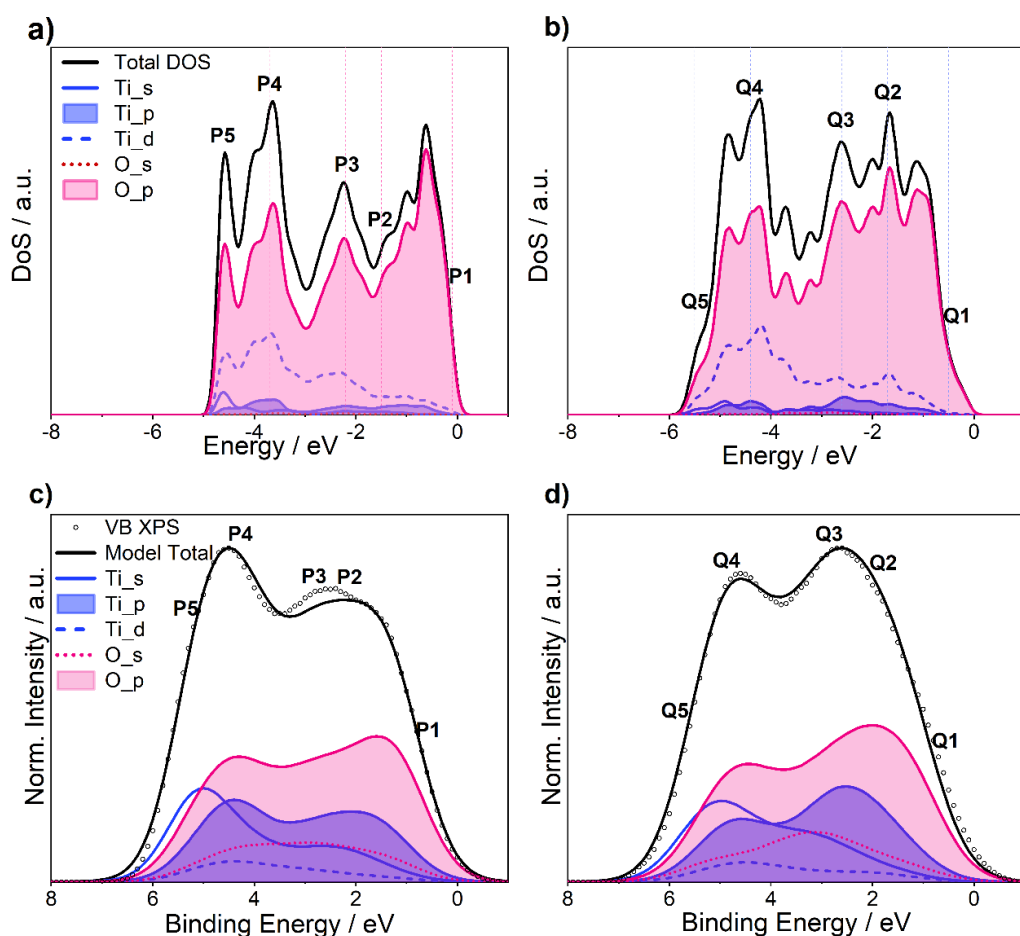
Figure 4.3. The calculated DOS for **a)** anatase and **b)** rutile. The average experimental spectra for **c)** anatase and **d)** rutile thin films, fitted with DFT-simulated spectra, derived from the DOS in **a)** and **b)**, respectively. The labels **P1-P5** and **Q1-Q5** refer to features of interest and are discussed in the next section.

The simulated spectra (**Figure 4.3**) well represent the characteristic shapes of the two polymorphs: both spectra have similar spectral widths and two distinct local maxima. In the case of rutile, the lower BE peak has the highest intensity, whereas in anatase, the higher BE peak has the highest intensity. The labels **P1-P5** and **Q1-Q5** refer to features of interest and are discussed in the next section.

Classical MO Bonding Scheme Vs. Partial Charge Density

To investigate the origins of the characteristic spectral features of the anatase and rutile polymorphs, partial charge densities were calculated and

visualised as contour maps for slice planes bisecting the central TiO_6 octahedra (**Figure 4.4**). The partial charge densities were calculated for small energy intervals in the valence band region, which were selected to correspond to characteristic features in the experimental spectra. These regions are labelled **P1-P5** and **Q1-Q5 (Figure 4.3)** for anatase and rutile, respectively, and correspond to the following energy intervals relative to the DFT energy scale: **P1** -0.1 eV; **P2** -1.5 eV; P3 -2.2 eV; **P4** -3.7 eV and **Q1** -0.5 eV; **Q2** -1.7 eV; Q3 -2.6 eV; **Q4** -4.4 eV; **Q5** -5.5 eV. Note that these positions in the simulated spectra are approximate due to the broadening of the pDOS.

In agreement with the MO bonding scheme described in (**Figure 4.2**), states sampled close to the VBM (**P1** and **Q1**) are predominantly non-bonding O p in character for both polymorphs. This is evidenced by no electron density on the Ti sites within the range of isosurface values (0.05 ~ 0.10 $e/Å^3$). The VBM can thus be described by the HOMO in the MO model. At intermediate energies there are π bonding characteristics displayed in anatase and rutile by regions **P3** and **Q2**, respectively. Towards the higher BE (lower energy) edge, regions **P4, P5** and **Q4, Q5** display σ bonding characteristics, which is the most stable form of interaction in the MO scheme.

The states sampled near the characteristic spectral maxima reveal differences between the anatase and rutile partial charge densities. The regions labelled **Q2** and **Q3** show bonding interactions and high electron densities, which correspond to the high intensity of the principal maximum in the rutile XPS spectrum. In contrast, regions sampled at similar energies in anatase, **P2** and **P3**, show lower electron density and much weaker bonding interactions, with **P2** being essentially O p in character. Turning to the location of the characteristic principal maximum in the anatase XPS spectrum, regions sampled towards the higher BE edge, **P5** and **Q5**, exhibit higher partial charge densities and stronger bonding interactions in anatase. These charge density contour maps can help identify bonding

interactions that contribute to the characteristic high BE maximum in anatase and the shallower high BE tail in rutile.
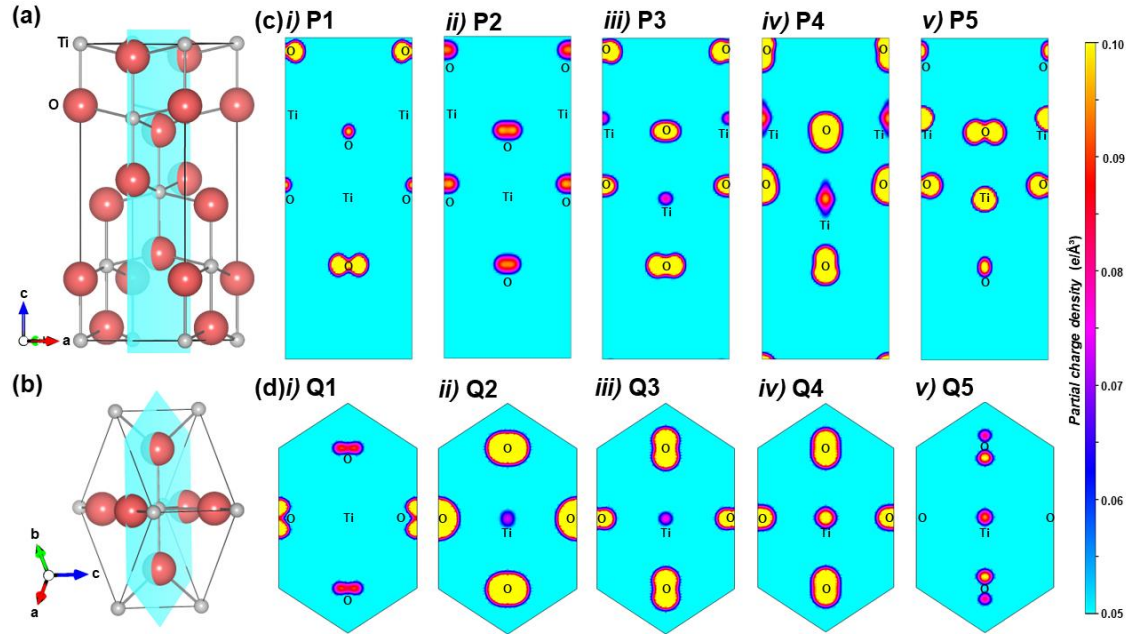
Figure 4.4. Lattice planes bisecting the central Ti atom (grey spheres), both axial and two equatorial oxygen atoms (red spheres) of the central TiO_6 octahedra in the unit cell are shown for **a)** anatase and **b)** rutile. Contour plots of the partial charge density across these planes can be used to visualise electronic contributions to the characteristic VB spectra. The partial charge densities were calculated for states between selected small energy intervals in **c)** anatase **i)** P1 **ii)** P2 **iii**) P3 **iv)** P4 **v)** P5 and in **d)** rutile **i)** Q1 **ii)** Q2 **iii)** Q3 **iv)** Q4 **v)** Q5. The range of isosurface values in each plot is set to 0.05 ~ 0.10 e/Å³.

Surface Electronic Structure

Additional electronic structure calculations were carried out on slab models, for different low index surfaces of anatase, (001), (010), and (101) (**Figure 4.5**). The motivation here is the surface sensitive nature of the XPS data, whereas the conventional DFT calculations are performed for bulk structures. However, calculating the density of states for the three low index surfaces in did not make any significant differences to the DFT-simulated spectra, after the application of photoionization cross-sections and spectral broadening (**Appendix C**).
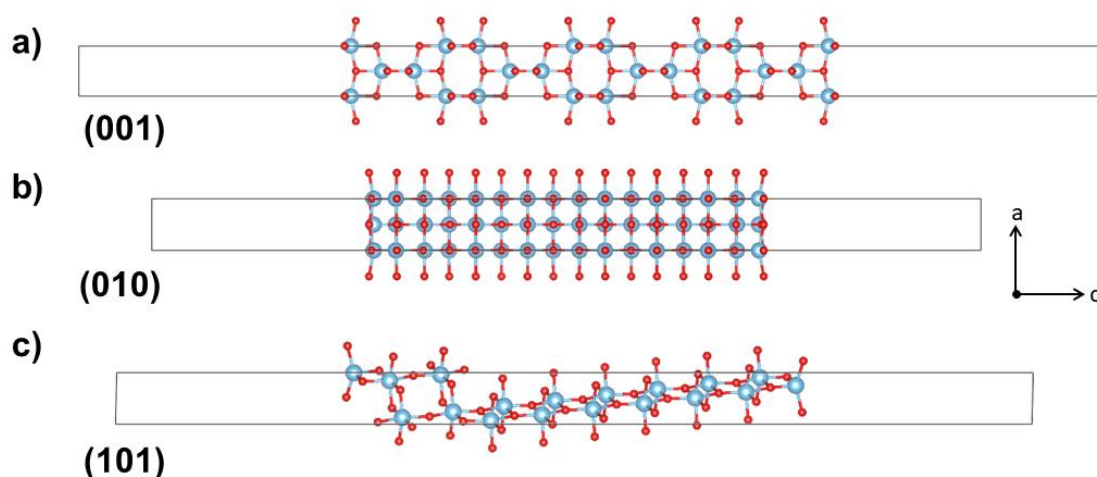
Figure 4.5. Slab models used to calculate the electronic structure of different low index surfaces of anatase, **a)** (001), **b)** (010), and **c)** (101).

Mixed Phase Valence Band XPS / DFT Fitting

A quantitative mixed phase fitting model was developed using simulated VB spectra, based on previously reported methods that use experimental VB XPS spectra to determine the phase fraction of mixed phase systems.[175, 177] This is applied to mapping the composition of anatase and rutile phases across the surface of 25 x 25 mm² mixed phase thin films. Two different mixed phase samples were analysed in this way: one with a higher concentration of rutile in the corner (denoted *r-corner*) and one with a higher concentration of rutile in the centre (denoted *r-centre*).

In the fitting model, the anatase and rutile simulated spectra behave as components, where a linear sum of the two phases is fit in a least squares sense (see **Section 2.1.3**) to experimental spectra recorded on a grid of 12 x 12 points across the samples. During fitting, the two components were enabled to shift along the BE axis and vary from 0 – 100 % of the model total. The ratio of each phase was taken as the phase fraction, assuming equal relative sensitivity factors of anatase and rutile. In addition to the simulated mixed phase model, an empirical mixed phase model was applied in the same way, using experimental VB spectra recorded on anatase and rutile reference samples. Examples of both simulated and empirical mixed

126

phase models are given in **Figure 4.6**, fitted to VB XPS recorded on **5** different points across the *r-centre* thin film.
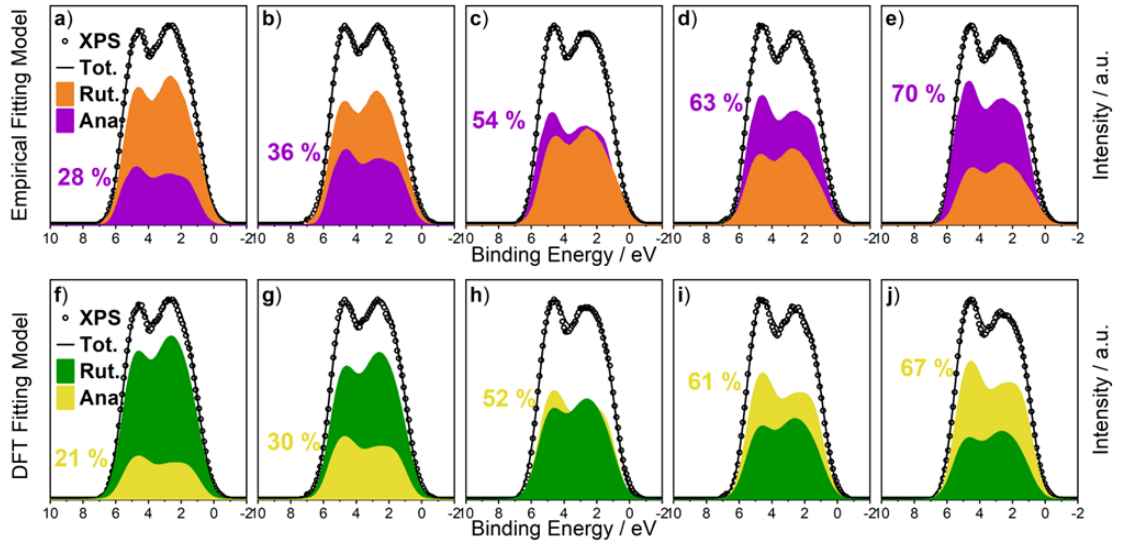
Figure 4.6. Mixed phase fitting models applied to VB XPS spectra recorded across the surface of a mixed phase anatase-rutile thin film (the *r-centre* sample), using **a)** simulated and **b)** empirical spectra for the anatase and rutile components.

The validity of the DFT-simulated model is supported by the close agreement with the compositions determined by the empirical fitting model. A correlation of all fitting results is given in **Appendix C**. To map the composition of anatase and rutile phases across the surface of the mixed phase thin film samples, the fitting models were applied to each point across the surface of the *r-centre* and *r-corner* thin films. This method allowed clear identification of the rutile-rich regions in each case (**Figure 4.7**). Although both methods offer similar composition mapping results, the theoretical model offers unique advantages in elucidating the origins of spectral features. The mixed phase fitting models determine the composition to reach ~ 80 % rutile in the centre of the *r-centre* sample, and 100 % rutile in the corner of the *r-corner* sample. The XPS/DFT determined phase fractions are compared to the results of a quantitative Raman spectroscopy fitting method in the next section.
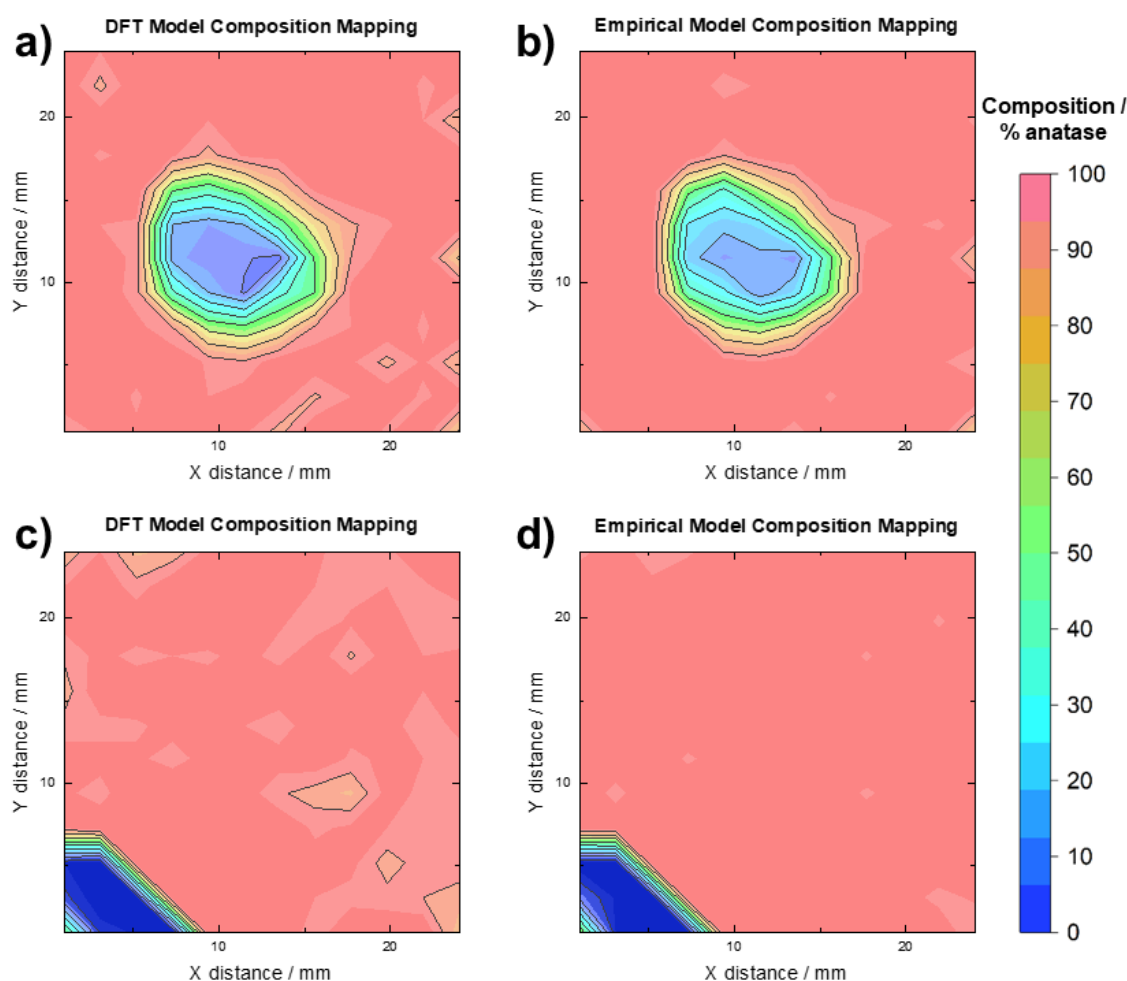
Figure 4.7. Mixed phase fitting models applied to VB XPS spectra recorded on a grid of 12 x 12 points across the surface of two mixed phase anatase-rutile thin films using **a,c)** DFT-simulated spectra and **b,d)** experimental spectra. The rutile-rich regions in **a,b)** the *r-centre* sample and **c,d)** the *r-corner* sample are clearly identified by both theoretical and empirical fitting models.

Mixed Phase Raman Spectroscopy Mapping

To compare with the XPS/DFT determined anatase-rutile phase fractions, Raman spectra were recorded across linear regions in all four TiO_2 thin films, and phase quantification was achieved based on the method reported by Zanatta et al.[185] The linear regions examined bisect the films horizontally, except in the case of the *r-corner* film, where a diagonal region was sampled to include the rutile-rich corner region. The Raman spectra recorded on the pristine anatase and rutile films confirm the crystalline identify of the reference samples (**Appendix C**). The analysis region is confined to 310–750 cm^{-1}, which contains anatase modes at:[193] 395 cm^{-1}

(B_{1g}), 515 cm^{-1} ($A_{1g}+B_{1g}$) and 637 cm^{-1} (E_g) and rutile modes at:[194] 438 cm^{-1} (E_g) and 605 cm^{-1} (A_{1g}). The mixed phase Raman spectra were normalised and fitted with linear background functions before fitting with Lorentzian peaks, to simulate the 3 anatase and 2 rutile modes detailed above. The modes were allowed to vary ± 5 cm^{-1} in frequency and constrained to the average FWHM found in the pristine samples. The relative intensity of the anatase: rutile modes was used to determine the phase fraction, which is shown in **Figure 4.8** applied to the Raman spectra recorded at 3 points on the *r-centre* film.
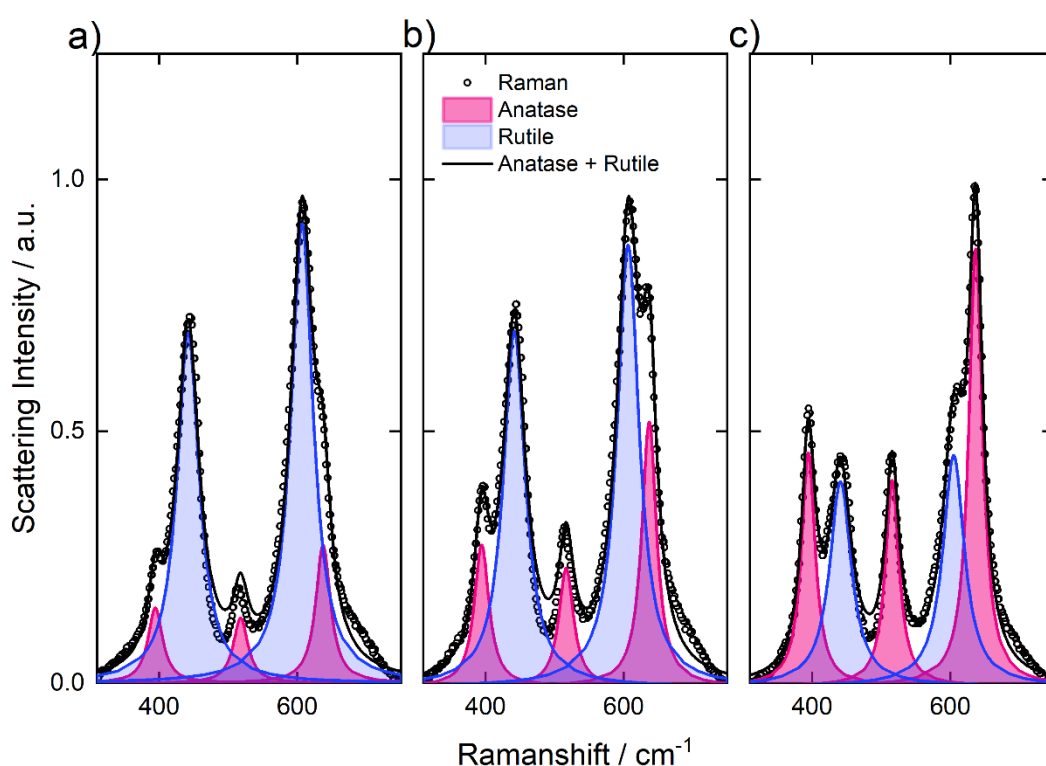
Figure 4.8. Mixed phase Raman fitting models applied to spectra recorded at 3 points across the surface of the *r-centre* sample. The phase fraction of anatase determined by the Raman quantification method at these 3 points is **a)** 26 %, **b) 40** %, and **c) 60** %.

Applying the Raman quantification method to the anatase and rutile pristine films determined the composition to be 100 % anatase and 100 % rutile, respectively. A comparison of the compositions determined by the XPS/DFT mixed phase fitting model and the Raman quantification method is shown in **Figure 4.9**. Both methods identify the rutile-rich regions in the

mixed phase samples, however, Raman spectroscopy determines a wider rutile-rich centre in the *r-centre* samples. This discrepancy is attributed to the different sampling depth of the two techniques; Raman spectroscopy is expected to penetrate a deeper area than XPS, which is accentuated by the transparent nature of the films in the current study. The compositions determined by the outermost spectra in some cases disagree, possibly owing to the reduced film quality at the edge of the samples. In the next section, the anatase phase composition across TiO_2 samples is correlated with the photocatalytic activities, mapped across the surfaces.
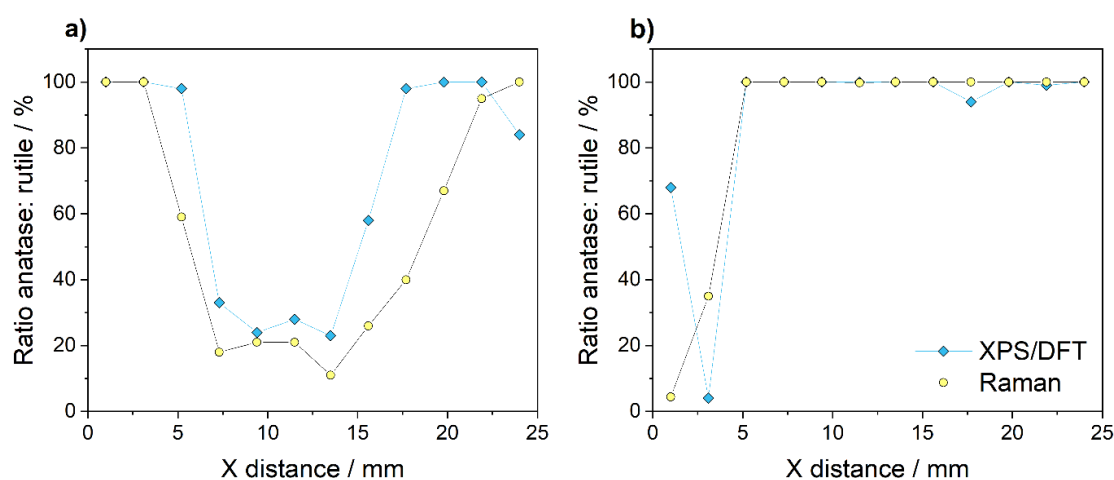
Figure 4.9 A comparison of the compositions determined via the missed phase XPS/DFT and Raman fitting methods for **a)** the *r-centre* and **b)** the *r-corner* samples.

Photocatalytic Activity Mapping

To map the functional properties across the surface of the thin films, the photocatalytic activity was measured using a standard test, based on the reduction of resazurin dye (a smart ink).[188] The underlying mechanism of the process (**Figure 4.10a**) relies on the photo-oxidation of a sacrificial electron donor (SED) driven by positive holes (h^+) trapped at the surface upon excitation by UV light. The SED in this work was glycerol, which acts as a hole scavenger to produce an electron rich surface. In turn, the electron rich surface irreversibly reduces the resazurin molecule (R_z) to resofurin (R_f). This process is evidenced by a colour change from blue to pink, and

thus can be monitored by photographic analysis of the reaction. Selected photographs taken during the reaction, at different exposure times to UV light are shown in **Figure 4.10b**. The transformation from R_z (blue) R_f (pink) was observed within the first five minutes of exposure, except for the pure rutile film, which remains inactive. For the three active films, complete degradation of the ink was evidenced by the disappearance of the pink colour (bleaching) at prolonged irradiation times (t = 100 min).
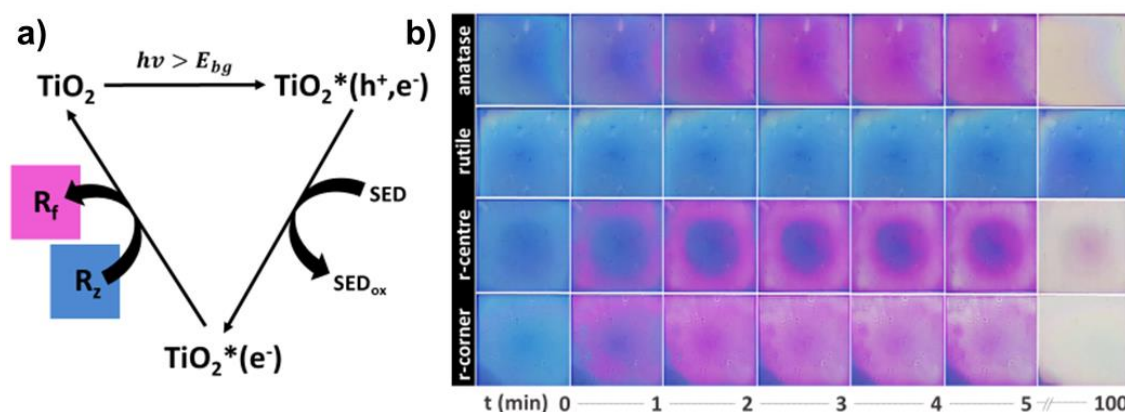
Figure 4.10a) Reaction scheme proposed for the transformation of the resazurin-based ink upon irradiation.[187] **b)** Photographic monitoring of the reaction at selected time intervals during UV exposure (λ= 365 nm, I= 2 mW cm^{-2}).

To investigate these transformations quantitatively, colour mapping of the photographs was carried out, using the red, green, and blue components (RGB values) over a 12 x 12 grid to compare with the XPS analysis. Following the procedure described in the ISO test,[188] RGB values were transformed into normalised RGB(red) values, R_t, at irradiation time t, according to:

$$R_t = \frac{RGB(R)_t}{RGB(R)_t + RGB(G)_t + RGB(B)_t} \qquad \textbf{Eq.4.1}$$

where $RGB(R)_t$, $RGB(G)_t$, and $RGB(B)_t$ correspond to red, green, and blue components at time t, respectively. The rate of change of R_t with radiation time thus gives an indication of the photocatalytic activity of the surface. This parameter can be extracted easily from R_t curves (**Figure 4.11a**) by

the time taken for to reach 90 % of the maximum R_t value. This parameter is known as the time-to-bleach, or ttb(90) value.

Figure 4.11a shows the R_t curves for 5 points on a linear cross-section of the r-centre film, labelled A-E. The anatase composition decreases from A: 100 % > B: 93 % > C: 27 % > D: 22 % > E: 21 %, which was determined by the XPS/DFT refinement method. It can be seen that as the rate of change of R_t decreases, the ttb(90) value increases, corresponding to deceasing anatase content. It is widely known that the anatase and rutile polymorphs of TiO_2 exhibit different photocatalytic behaviours – anatase is a more efficient photocatalyst.[195, 196] The decrease in photocatalytic activity therefore correlates well with the phase quantification determined from the VB XPS/DFT refinement method. This is further demonstrated by mapping of the ttb(90) values across the surface of the mixed-phase samples (**Figure 4.12**), where the same rutile-rich regions are highlighted as were previously using the XPS/DFT mapping method (**Figure 4.7**).
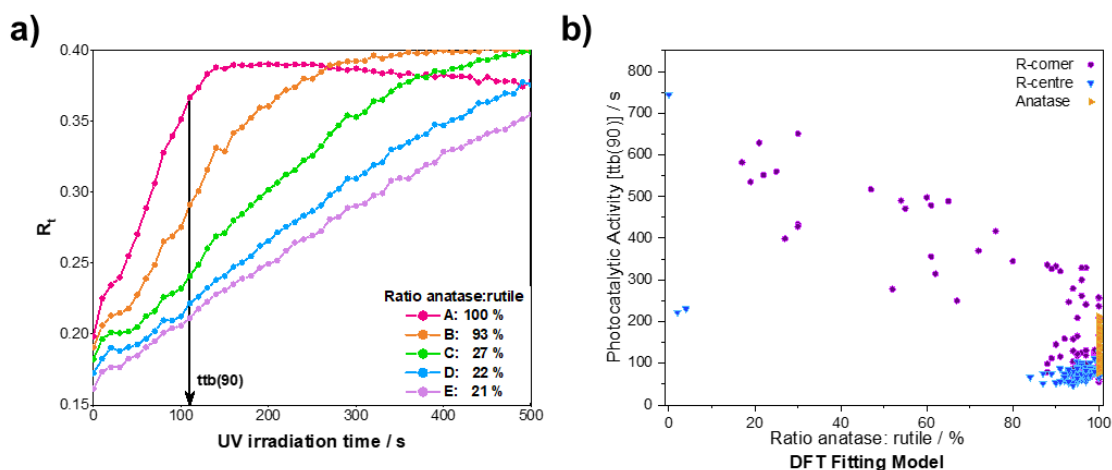
Figure 4.11. (a) Normalised red components (R_t) of resazurin dye upon increasing irradiation time over the r-centre sample. **(b)** The corresponding percentages of surface anatase as determined by the DFT fitting model are indicated and refer to the points labelled **A-E**. **(b)** The compositions estimated by the DFT fitting model and by Raman analysis for a linear cross-section of the r-centre film.

Finally, turning to the comparison of the ttb(90) values obtained for the three active films in **Figure 4.11b**, the r-centre film shows an almost linear correlation between the activity and the composition. This would indicate

non-interacting particles, as no enhancement in activity is seen for any compositions, that would suggest synergistic effects.[175] The ttb(90) values for the r-corner sample show some of the highest activities across the active samples, for the regions with high anatase compositions. Regarding the inactive regions (i.e. 0 % anatase), the ttb(90) values are much larger, with the largest value arising from the corner most analysis point. The smaller two ttb(90) values arise from '0 %' anatase points with neighbouring active anatase regions.
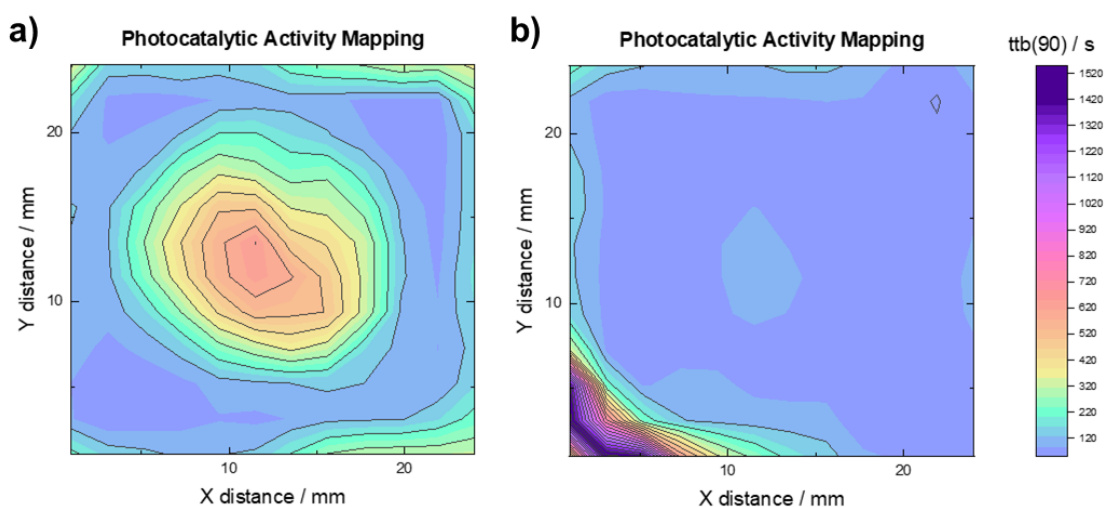
Figure 4.12. The photocatalytic activity was mapped across the surface of the mixed-phase films for **(a)** the r-centre sample, and **(b)** the r-corner sample

It is possible that a higher resolution of the photoactivity, i.e. pixel by pixel analysis, or smaller x-ray spot size in XPS analysis, would benefit further analysis in these cases. There is also a spread of activities calculated for the pure anatase sample, with overall lower activities compared to the active areas in the r-corner sample. The photocatalytic activity therefore also arises from more factors than just the composition alone. These factors could include the film thickness and morphology, and ink thickness, and could form the basis of future investigations.

4.3 Part IV Conclusions

In **Part IV**, the methodology of refining DFT-simulated spectra for the analysis of VB XPS spectra used in **Parts II-III** is extended to the modelling of mixed phase systems. This is applied to the quantitative mapping of mixed phase TiO_2 surfaces. The DFT-simulated spectra were derived from PBEsol calculated DOS. Similarly to the case of STO in **Part III**, the YL and YL* photoionization cross-section values were not found to well reproduce the experimental VB structure, and were thus optimised further. A large contribution from the Ti p component was found necessary to reproduce the XPS VB, which was also the case for STO. As was found for all other non-metallic materials studied in **Parts II-III**, the optimised Gaussian broadening was much larger than the nominal experimental resolution and was ~ 1.3 eV for both anatase and rutile phases. Spectra simulated for low index surfaces of anatase using a slab/vacuum model did not show significant differences to the bulk structure calculations after application of optimised broadening and cross-section parameters.

The mixed-phase XPS/DFT fitting model was applied to mapping the surface phase fraction on the mixed-phase films, with clear identification of the rutile-rich regions. Use of an empirical method, where experimental VB were used as the reference spectra, resulted in close agreement to the compositions predicted by the DFT model. Spatially resolved photocatalytic activity was measured using photocatalytic reduction of a resazurin-based *smart ink*, which highlighted the same rutile-rich areas as evidenced by XPS and DFT analysis. Therefore, a clear connection was established between the XPS/DFT determined phase fraction and the experimentally determined photocatalytic activity, and allows large scale mapping using the two complementary techniques. The activity was also suspected to arise from additional factors other than the composition alone, such as film thickness and morphology, and ink thickness, which could form the basis of future investigations.

Part V – Ionic Liquids and Electrochemical XPS

5.1 Review: Ionic Liquids and XPS in Electrochemistry

Electrochemistry is a broad field of study and research encompasses both fundamental studies and more applied topics, including double layer formation, adsorption/desorption phenomena, electrocatalysis, electrode studies, and energy storage and conversion. An electrochemical cell typically consists of two or three electrodes, contacted by an electrolyte that enables charge transfer and the generation of electricity in an external circuit. The range of electrolytes, electrode materials, and the electrochemical reactions that occur between them is also vastly varied. For example, an electrolyte may be aqueous, solid, or ionic liquid in nature and there is a plethora of various electrode materials in use. It is widely acknowledged that it is crucial to have a better understanding of the underlying processes at the electrode/electrolyte interface and that any restructuring of the electrode during charge transfer is extremely important.[197]

The complexity of applying XPS to electrochemistry lies in the UHV conditions of the analysis chamber. Although this means that conventional liquid electrolytes cannot be introduced, this can be overcome by using an ionic liquid (IL) electrolyte. ILs are composed solely of ions and exhibit several desirable properties including high electrical conductivity (up to 100 mS cm^{-1}), a wide electrochemical window (up to 5.8 V), and extended liquid-state temperature range (ca. 173-523 K).[198] In addition, their negligible vapour pressure means that they can be introduced into the XPS analysis chamber. Lovelock et al. reviewed the application of XPS to IL-based interfaces, demonstrating the vast and unique information that the technique can provide.[199] Much research has been conducted into the IL-vacuum interface and the solid-IL interface, and this is expected to be a continuingly growing field.

When combining electrochemical research with the XPS technique, three distinct experimental procedures can be distinguished with respect to the transfer of material into the spectrometer's analyser chamber: *ex-situ*, quasi *in-situ* and *in-situ*.[200] The term *ex-situ* refers to the situation where electrochemical reactions occur outside of the analysis chamber, prior to the transfer of samples through air, where subsequent 'post-mortem' XPS analysis is then carried out. Despite the obvious risk of contamination and oxidation in air, there have been numerous *ex-situ* electrochemical XPS studies showing that this approach can provide important information.[200, 201]

The value of *ex-situ* electrochemical XPS has been demonstrated by Andreu et al. by their research into the modification of the positive electrode material in lithium ion batteries.[201] One way to improve the performance of the positive electrode is to use mixed transition metal oxides $LiNi_xMn_xCo_{1-2x}O_2$ where ($0.33 \leq x \leq 0.5$).[202-206] The electrochemical performance at high voltages can be improved further by coating the electrode with a metal oxide coating, for example ZrO_2 or Al_2O_3.[207-209] Andreu et al. investigated the surface reactivity of pristine and coated electrodes via chemisorption of gas-phase probes.[201] For the case of SO_2 chemisorption, they recorded XPS S 2p core level spectra for both $LiCoO_2$ and $LiNi_{1/3}Mn_{1/3}Co_{1/3}O_2$ (NMC) electrode surfaces with and without Al_2O_3 coatings. Only one absorption mode due to sulphate species was detected in the $LiCoO_2$ spectra, whereas both sulphite and sulphate species could be detected on the NMC material. After surface modification, the reactivity of both electrode materials decreased, and furthermore, a modification in the surface reactivity was seen for the $LiCoO_2$ electrode, evidenced by the appearance of both sulphite and sulphate species in the XPS spectra. The authors attribute this to the substitution of Co by Al changing the absorption mode.

Turning to quasi *in-situ* methods, this term refers to situations where there is a controlled method of transfer from the original experimental set-up to the analysis chamber, i.e. not directly through air. Inert transfer methods thus intend to cause as little disturbance or contamination to the original

136

system as possible, and have been developed since the 1970's.[210-212] Such methods range from transfer from a glove box via a vacuum suitcase, to complex and sophisticated systems that are directly attached to the XPS system. An early example of the latter is the electrochemical preparation chamber reported by Neff et al., which consisted of an electrochemical chamber attached to the load lock of the Kratos Es-300 Electron Spectrometer.[213] The chamber is filled with argon during electrochemical processes, which is then pumped down afterwards before transfer to the XPS system, allowing the electric double layer (EDL) to be studied.

The EDL is of vital importance in electrochemical processes and is formed in the spatial region where the electrode and electrolyte are in contact. Adsorbed on the electrode surface is layer of ions, which in turn attracts a second, more diffuse layer, together forming a complex double layered structure (the EDL). Early XPS studies into the nature of the EDL include the pioneering works of Hansen and Kolb into the so-called electrode emersion technique.[214-217] This involved removing an electrode under potential control and investigating any remaining species in the XPS analysis chamber. Using this technique, Kolb et al. studied gold electrodes emersed from 0.01 M caesium halide solutions.[217] Not only did they prove that the EDL could be retained in the vacuum, from the presence of both cations and anions in the XPS spectra, but that the spectra could be correlated with the applied emersion potential. Further electrode emersion studies include the that of Kotz et al., who emersed a gold electrode from H_2SO_4 and $HClO_4$ at different potentials.[218] They observed that Cl $2p$ and O $1s$ core-levels shifted -1 eV/V to lower BEs with increasing positive emersion potentials.

Finally, the term *in-situ* electrochemical XPS refers to investigations performed directly in the XPS analysis chamber. The UHV conditions inside the chamber require vacuum compatible materials, and *in-situ* XPS methods have been utilised to study solid-state electrolytes,[219, 220] and IL electrolytes,[221-223] to investigate a variety of electrochemical phenomena.

Several researchers have used a 2-electrode set-up to monitor electrochemical processes via *in-situ* XPS methods. This involves the use of a working electrode (WE) and a counter electrode (CE) in contact with an electrolyte. Due to the symmetric nature of the cell, an equal and opposite current must flow at the CE when a potential is applied to the WE, and vice versa. Benayad et al. utilised a 2-electrode cell to perform operando XPS measurements on Li ion batteries using an IL electrolyte.[224] They utilised a planar cell with two Li foils, focussed on the Li/IL interface, and observed a roughly 1 eV/V shift in the measured BEs of their IL species. They describe the interface as a dynamic, evolving analysis point. Additionally, charge neutralization was found to disturb the electrochemical processes within the cell through impedance measurements, and so was not used.

Turning to the use of 3-electrode cells, this set-up involves the use of an additional electrode, the reference electrode (RE). The potential is measured between the WE and the RE, whilst the current flows between the WE and the CE. This set-up is more stable than the 2-electrode configuration because the potential at the reference electrode is more stable during measurement. Wibowo et al. observed the electrodeposition of Rb metal at a nickel mesh WE from the IL *N*-butyl-*N*-methylpyrrolidinium *bis*(trifluoromethylsylfonyl)imide ([C$_4$mpyrr][NTf$_2$]) containing Rb[NTf$_2$] salt, via *in-situ* electrochemical XPS measurements.[221] At high current, they observed the relative compositions of the IL to change, where the C signal increased and the F signal decreased, consistent with the breakdown of the IL. The deposition of the Rb metal and the breakdown of the IL were shown to be in competition, with low currents favouring the deposition process.

Liu et al. monitored the formation of anionic gold species from corrosion of a Au electrode in the IL 1-butyl-1-methylpyrrolidinium *bis*(trifluoromethylsylfonyl)amide ([Py$_{1,4}$]TFSI) by *in-situ* electrochemical XPS.[222] Their 3-electrode cell consisted of Pt CE and Pt quasi RE, along with a grounded gold sputtered Cu mesh WE. On applying a negative bias to the WE, the BEs of all core levels of the IL shift to higher BEs and experience a

138

~-0.9 eV/V shift. At -3.0 V, additional peaks appear in the Au 4*f* spectra, and are attributed to the formation of Au⁻ species. Weingarth et al. also utilised a 3-electrode cell to perform *in-situ* electrochemical XPS measurements, on the IL 1-ethyl-3-methylimidazolium tetrafluoroborate ([EMIm][BF$_4$]]) with a Pt WE.[223] They observed a -1.0 eV/V shift of all measured BEs for the IL species, and the appearance of a new peak in the N 1*s* spectra at a potential of -1.9 eV and below, which is attributed to decomposition of the IL. The position of the new peak shifts with the applied potential, indicating that the new species is dissolved in the electrolyte and not formed at the Pt surface. Species that are in the bulk electrolyte are expected to experience the full potential drop, and thus a precise -1.0 eV/V shift, whereas any deviation from this can be expected from species in direct contact with the electrode or within the EDL, where the potential is different.[222, 223, 225]

Velasco-Velez et al. compared different types of in-situ cells.[225] For a grounded WE, the measured BE$_{app}$ can be related to the applied potential, dU, the charge on an electron q$_e$ and the 'real' BE$_{real}$ by the following equation:

$$BE_{app} = BE_{real} + q_e dU \qquad \textbf{Eq.5.1}$$

They also observe broadening of FWHM with increasing potential v RHE, but peak shape changes only marginally. They observe -0.9 eV/V shifts, which they attribute to a modest contribution from the EDL, where the potential deviates from the bulk value.

Finally, some groups have performed similar *in-situ* electrochemical XPS studies, but at the liquid/electrode interface, using AP-XPS. Shalom et al. investigated the liquid/solid interface by using a graphene window.[226] They ground the CE and apply a bias to the WE. The C 1*s* spectrum of the graphene WE shifts to higher BEs on application of positive bias, but does not return on reverse of the polarity which they attribute to irreversible functionalization of the graphene surface. Favaro et al. probe the EDL by spectral broadening of pyrazine (neutral spectator molecule) and water

(electrolyte) core levels by AP-XPS.[227] XPS spectra were recorded *in-situ* at a gold WE, using the dip-and-pull method. BE shifts are measured as a broadening of the XPS peak, where the peak can be separated into many components that depend on their position within the EDL and the bulk electrolyte. Molecules close to the electrode experience a smaller BE shift than the molecules in the bulk electrolyte. The FWHM represents the direct link between the spectroscopy and the electrochemistry, with the double-layer capacitance directly linked to a pure spectroscopic feature. Note that the concept of an EDL is quite different when using aqueous solutions compared to ILs, because the diffuse layer consists of small molecules in solution. In an IL, the arrangement of species close to the electrode surface consists of much larger, bulky ions.

To summarise, there is a wealth of information that can be accessed using electrochemical XPS methods, where *ex-situ,* quasi *in-situ* or *in-situ* techniques offer unique insights. In this chapter, the first half focusses on the XPS of imidazolium-based ionic liquids – their characterisation, charging properties under XPS measurement conditions and experimental/theoretical valence electronic structure. The second half involves *in-situ* electrochemical XPS – the design and fabrication of an *in-situ* XPS cell, and its application to investigate Na ion behaviour in an IL electrolyte, in the interest of Na-ion battery research.

5.2 XPS of Ionic Liquids

5.2.1 Review: XPS of Imidazolium-based Ionic Liquids

Structure and Applications of Imidazolium-based Ionic Liquids

Imidazolium-based ILs are ILs that contain the cationic imidazolium moiety, which typically exist as a 1,3-dialkylimidazolium cation associated with a relatively weakly coordinated anion like hexafluorophosphate or tetrafluoroborate (**Figure 5.1**).[228] In the mid-1990s there were the first reports of the synthesis of imidazolium ILs and their applications in

organometallic catalysis.[229-231] Chauvin et al. utilised 1-*n*-butyl-3-methylimidazolium salts [BMIm]+ in the Rh-catalysed hydrogenation of unsaturated substrates, and achieved hydrogenation rates five times higher than the comparable reaction in acetone.[229] Suarez et al. showed that [BMIm]+ salts also catalyse the hydrogenation of cyclohexene, and highlighted the ease of separation of the product from the reaction mixture as a major advantage of this method.[230] Bonhôte et al. reported the synthesis of a range of imidazolium ILs with various alkyl substituents and investigated the resulting influence on various properties, such as density, melting point, viscosity, conductivity, electrochemical window and thermal stability.[231] This highlighted the potential to fine-tune the properties of these remarkable materials to a host of potential applications.

R = Alkyl group X = BF_4, PF_6, NTf_2
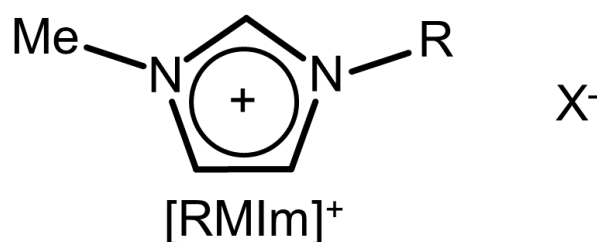
Figure 5.1. The general structure of 1,3-dialkylimidazolium ionic liquids.

This rekindled interest in ILs has led to a plethora of research activity into their diverse properties and their widespread applications, such as catalysis, fuel and solar cells, lubricants, and separation technologies. They also offer potential as corrosion inhibitors in industrial applications, such as acid descaling, acid pickling and petrochemical processes and have been shown to increase inhibition efficiency for corrosion resistance of mild steel in

hydrochloric acid solution.[232] Finally, they have been investigated for use in electrochemistry research (**Section 5.1**).

XPS insights into Imidazolium-based Ionic Liquids

There has been an array of different XPS studies into imidazolium ILs demonstrating the varied analytical powers of the XPS technique. Lockett et al. studied the surfaces of three imidazolium ILs with alkyl substituents of increasing chain length (RMIm) by angle-resolved XPS.[233] Comparison of high-resolution C 1*s* spectra at normal emission (0º) to spectra at take-off angles between 60 - 84° revealed a higher amount of carbon at the higher take-off angles. For increasing chain length of the RMIm cation, the larger the proportion of aliphatic carbon detected, indicating that the ILs were orientated with the alkyl chains pointing away from the IL surface. Caporali et al. combined XPS with low energy ion scattering (LEIS) studies to show that the -CF_3 group in 1-butyl-3-methylimidazolium bis(trifluoromethane)sulfonimide (BMIm.Tf_2N) is also orientated away from the IL surface.[234]

Smith et al. studied the commercially available 1-ethyl-3-methylimidazolium ethylsulfate (ECOENG™ 212) by XPS and demonstrated the sensitivity of the technique by monitoring the *in-situ* reduction of a Pd catalyst by the IL.[235] Two IL droplets containing the Pd catalyst Pd(OAc)$_2$(PPh$_3$)$_2$ were prepared simultaneously, however, only one aliquot was introduced into the analysis chamber and x-ray exposure. After 6 h, the appearance of both samples changed significantly, changing from a transparent straw colour to much darker and more opaque. This was accompanied by decay in the Pd^{2+} photoemission peak and a corresponding increase from Pd^0, signifying the instability of the catalyst in the IL. These studies show some of the different information that XPS can acquire, in addition to standard elemental identification and quantification for which it is well known.

Curve Fitting Procedure

All the studies described above included peak modelling of the high-resolution C $1s$ region of imidazolium ILs.[233-235] The works are largely in agreement with the curve fitting procedure, with some minor differences in the model constraints. The main principle of the model is to fit the broad C $1s$ envelope that appears around ~285 eV with four different peaks, to represent carbon in the four environments present in the imidazolium cation. In the case of C being present in the anion species, for example a -CF_3 moiety, this will appear as an additional separate peak at higher binding energies ~292.6 eV.[234] Going from lower to higher BE: the lowest BE peak can be attributed to aliphatic carbon in the alkyl chain substituent (C_{alkyl}), and the next peak can be assigned to the two carbons in the aliphatic chains that are directly bonded to the N atoms of the imidazolium ring. Peaks 3 and 4 can then be attributed to carbons within the ring, C-C*-N and N-C-N, with the latter having the highest BE due to being directly attached to 2 nitrogen atoms within the imidazolic ring.

Turning to the specifics of the peak models imposed, typically a GL(30) peak shape – a symmetrical Gaussian-Lorentzian (70 %-30 %) – was used,[233, 235] or GL(25).[234] Locket et al. restricted the FWHM of the 4 components to 1.1 eV, and found a that the area ratio gave values close to the nominal stoichiometry when allowing the BEs and the areas to vary.[233] Caporali et al. similarly fix the FWHM of all components, but this time to a wider 1.6 eV based on their -CF_3 component at higher BE, and derive compositions close to nominal stoichiometry when allowing the area and BE to vary freely.[234] Smith et al. take a slightly different approach, by fixing the ratio of the peaks to the sample stoichiometry, and allowing the FWHM to vary (from 1.2 – 1.7 eV) they also achieve a good fit to their experimental data.[235]

Although the models described above generate good fits to the experimental data, there are other aspects that can be added that have seen good results in other cases, namely the shake-up effect of the aromatic ring and the

increased vibrational structure in the case of longer aliphatic chains.[142, 236] The shake-up effect refers to a process seen in aromatic species, whereby shortly following the photoemission process, the photoelectron interacts with a valence π electron and excites it to a vacant π* orbital. The interaction causes the photoelectron to lose energy, which thus appears as a satellite at a higher BE than the main peak, and normally constitutes ~10 % of the original intensity. At the same time as the shake-up, valence electrons are ejected into the continuum in a process called shake-off. The shake-off process does not produce a defined signal (due to the disperse nature of this transition) but can be assumed to be of equal intensity as the shake-up feature, meaning a total intensity loss of ~20 % will be observed for the main peak.[199] This means that the aromatic C components in the C $1s$ model described previously for the imidazolium cation should in fact appear at intensities ~20 % less than the stoichiometric values of the IL.

The inclusion of the shake-up and shake-off effects into the curve-fitting procedure requires fixing the ratio of the N-C-N: C-C*-N: C_{alkyl} components to 0.8: 1.6: 2.0, which has been implemented with great success by Smith et al. and Garcia et al.[142, 236] These works also separately constrain the FWHM of the C_{alkyl} component, which is broader than that of the other components, typically by around 0.2 eV. This is attributed to increased vibrational structure in long carbon chains. [237, 238]

Charging and Conductivity of Ionic Liquids in XPS Measurements

The complexity of XPS studies regarding the conductivity of IL samples, the use of charge compensation and problems in the measurement of absolute BEs has been explored by an in-depth and systematic study by Smith et al.[142] They observed a change in conductivity of $EMIm.EtSO_4$ upon change of state to a solid, which was monitored by *in-situ* cooling. No changes were observed in the C $1s$ peak shape until the IL drop showed signs of freezing, which was then accompanied by distortion of the peak shape and large BE shifts. However, when charge neutralisation was introduced, the peak shape

144

was restored and the BE was close to its original position. The slightly lower BE shift when using the charge compensation is attributed to a slight overcompensation by the filament. They note that even though ILs are conducting, small variations in efficiency of grounding the sample can lead to deviations from absolute BEs and turn to internal referencing for BE calibration.

Villar-Garcia et al. demonstrated that ILs become electrically charged during XPS measurements, by recording the BE shifts of a series of ILs under x-ray radiation and charge neutralisation exposure for extended periods.[236] The surfaces of the ILs become increasingly positively charged with increasing x-ray exposure, because of the photoemission process, thus causing shifts to higher BEs. Upon switching on charge neutralisation, the BEs suddenly shift towards lower values, which continue to decrease upon further exposure. These observations point towards limited conductivity in ILs, where they are tending towards an equilibrium surface charge by a sluggish conduction mechanism. The authors thus point towards the need for an internal BE referencing system and compare the use of the alkyl carbon chain and the imidazolium nitrogen. Both referencing systems are evaluated to work well, with the condition that the alkyl carbon chain has more than 8 carbons if choosing the C_{alkyl} method.

Foelske-Schmitz et al. have published several works into the charging of ILs and BE referencing in XPS, and suggest that the origins of charging effects are more likely related to the electronic properties of the IL/substrate interface.[239, 240] They investigated the charging of the IL [EMIm][TFSI] on a range of different metallic and semiconductor substrates under both x-ray and flood gun exposure.[239] Compared to when measured on an annealed glassy carbon (GC) substrate, the IL samples mounted on other substrates had positive relative BE shifts when measured without charge compensation, and negative relative BE shifts when measured with charge compensation. The magnitude of these BE shifts were intermediate and comparable for metallic Au and Ag, and most exaggerated for n-type Si. The

subject of the substrate was investigated further by measuring the BEs of IL drops supported by a series of pure and doped germanium and silica substrates with and without exposure to charge compensation.[240] Measurements using the flood gun caused the BEs to shift to lower values, and the magnitude of this shift was found to be proportional to the electron beam intensity and related to the nominal resistivity of the surfaces.
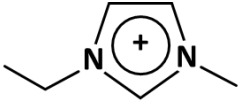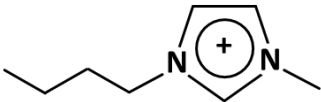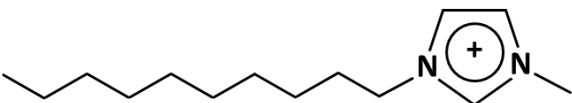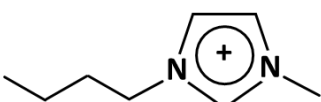
To explain these observations, the authors propose that the IL/substrate interface is behaving as a heterojunction, in which the accumulation of charge causes band bending and thus a BE shift. The magnitude and direction of this shift depends on the nature of the interface and the accumulation of charge induced x-ray of electron beam exposure. They also describe the formation of an electric double layer (EDL) at the interface, which could be modelled as a parallel plate capacitor, with properties that depend on the capacitance of both the IL and substrate, and various physical properties of the IL itself. The charging of ILs under both x-ray and flood gun exposure is obviously non-trivial and there are many phenomena that are not well understood.

Current Study

To further investigate several themes of interest found in the literature on XPS of imidazolium ILs that are discussed above, namely x-ray and flood-gun induced charging effects and the use of different C 1s curve-fitting procedures. Four different ILs were studied: three with a common BF_4 anion and an imidazolium cation with varying alkyl chain length, and a fourth with a different PF_6 anion but identical cation to one of the others. Thus, it was intended to study both the effect of changing the alkyl substituent chain length, and effect of switching the anion. The IUPAC names, abbreviated names and skeletal structures of the IL series are given in **Table 5.1**.

146

Table 5.1. IUPAC names, abbreviated names, and skeletal structures of the IL series in this study.

Skeletal Formula	IUPAC nomenclature	Abbreviated name
	1-ethyl-3-methylimidazolium tetrafluoroborate	$C_2H_5MIm.BF_4$
	1-butyl-3-methylimidazolium tetrafluoroborate	$C_4H_9MIm.BF_4$
	1-decyl-3-methylimidazolium tetrafluoroborate	$C_{10}H_{21}MIm.BF_4$
	1-butyl-3-methylimidazolium hexafluorophosphate	$C_4H_9MIm.PF_6$

5.2.2 Experimental Section

XPS Measurements on Imidazolium Ionic Liquids

The ILs in this work were synthesised by Yutong Shen. Four different ILs were synthesised, $[C_2H_5MIm][BF_4]$, $[C_4H_9MIm][BF_4]$, $[C_{10}H_{21}MIm][BF_4]$, and $[C_4H_9MIm][PF_6]$. XPS was carried out using a Thermo Scientific K-alpha spectrometer equipped with a monochromated Al K-Alpha X-ray source (1486.6 eV) in constant analyser energy mode. Photoelectrons were collected at normal emission with a spot size of 400 µm. A pass energy of 150 eV was used to record survey spectra and pass energies of 20 eV and 30 eV were used to record high resolution VB and core level spectra, respectively. Core and valence spectra were processed using CasaXPS.[97] A Shirley background was used for all spectra.

Sample charging was investigated by varying the environment of droplets of ILs. The IL droplets were measured on top of both glass substrates (isolated from the spectrometer ground) and metallic copper sheets (connected to the spectrometer ground). Data was collected for each environment both with and without the use of the FG.

5.2.3 Results

Structure of IL Ion Pairs
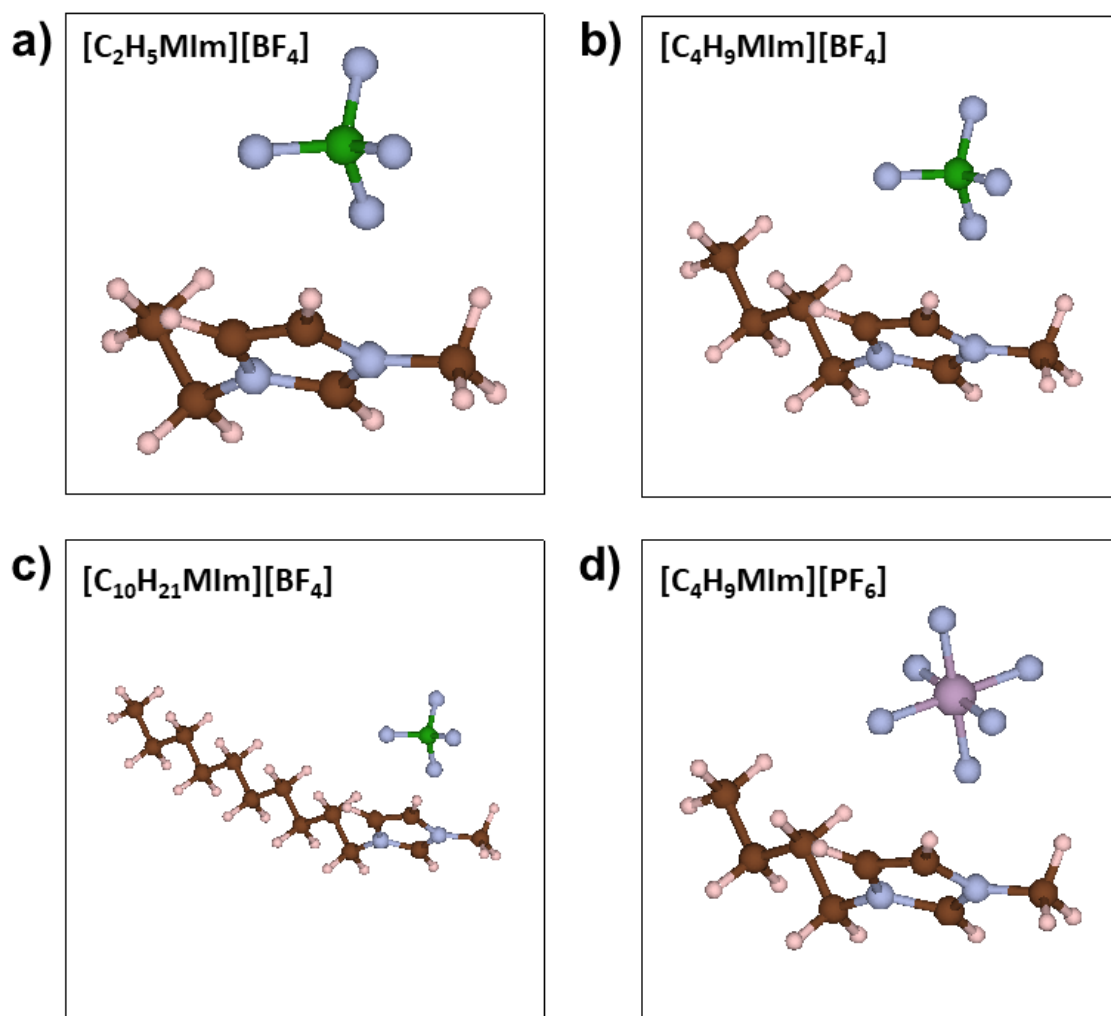
Figure 5.2. The structures of the IL ion pairs used in this study as relaxed using the Avogadro platform:[241] **a)** [C₂H₅MIm][BF₄] **b)** [C₄H₉MIm][BF₄] **c)** [C₁₀H₂₁MIm][BF₄] **d)** [C₄H₉MIm][PF₆].

To generate structures of the IL pairs, the single ions were first relaxed using the Avogadro platform.[241] The relaxed ions were then placed in pair configurations, based on those reported by Zhao et al.[242] The ion pairs were then relaxed again using the Avogadro platform, with the resulting structures shown in **Figure 5.2**.

XPS Analysis: Curve Fitting Procedure

For the initial stage of analysis, the use of two curve fitting procedures was evaluated, for the XPS measurements made on the grounded Cu substrate with no charge compensation were studied. The C $1s$ region was fitted with two different component models based on two different approaches found in the literature (see intro section of this sub-chapter) to compare the two methods. The major difference in between the two approaches trialled here is that one model incorporates shake-up/shake-off effects, and one does not, referred to herein as 'simple' and 'shake-up' models, respectively. In both cases, the C $1s$ envelope is fitted with four components, to account for the four different carbon environments found in the imidazolium cation. In the 'simple' model, the component peak areas are restrained to the stoichiometric ratios of the cation carbons, whereas in the 'shake-up' model, the ratios are modified to account for shake-up and shake-off effects in the aromatic carbons.

The results of fitting the C $1s$ data with the 'simple' model are shown in **Figure 5.3**. In this model, the FWHM were constrained to be equal, and the areas of the component peaks were initially constrained to be equal to the stoichiometric ratios found in the cations with alkyl substituents C_nH_{2n+1} , i.e. C^1: C^2: C^3: $C^4 = 1$: 2: 2: (n-1). This was found to give very good agreement with the experimental data in the cases of **c)** $[C_{10}H_{21}MIm][BF_4]$ and **d)** $[C_4H_9MIm][PF_6]$. The relative BEs of the components also appear in the expected order, i.e. the highest BE is found for C^1 and the second highest BE for C^2, which are directly attached to 2 and 1 imidazolic nitrogen atom(s)

within the ring, respectively. Carbons C^3 and C^4 belong to the alkyl substituents, and appear at lower BEs, with C^3 carbons being slightly higher due to the direct bond to nitrogen.
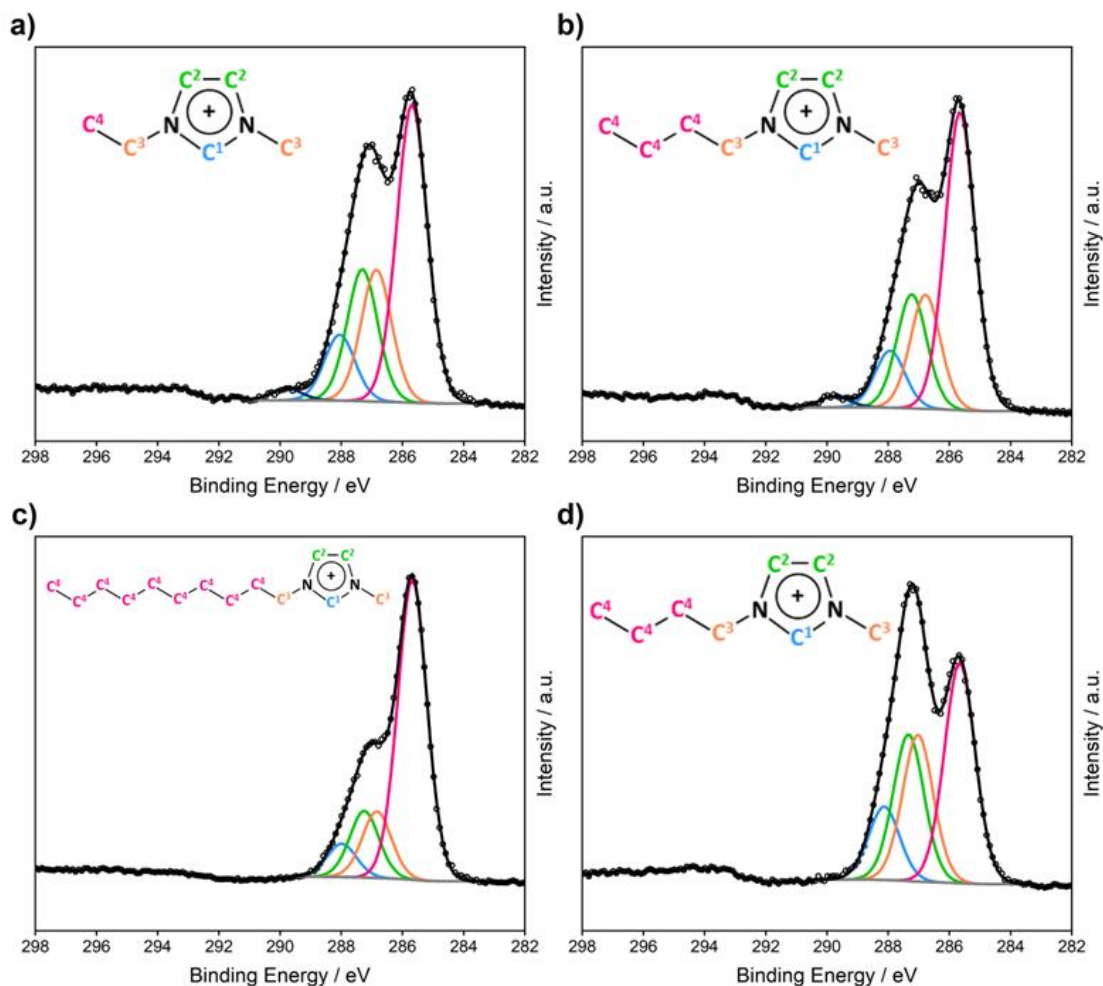
Figure 5.3. The XPS C 1*s* region of the imidazolium ILs **a)** [C$_2$H$_5$MIm][BF$_4$] **b)** [C$_4$H$_9$MIm][BF$_4$] **c)** [C$_{10}$H$_{21}$MIm][BF$_4$] and **d)** [C$_4$H$_9$MIm][PF$_6$]. The different components correspond to the different carbon environments seen in the cation, which are colour coded in the skeletal diagrams for each IL. The curve fitting procedure is detailed in the main text. A Shirley background was used in each case. Raw XPS data and the model total are represented by the open circles solid black curve, respectively. There is evidence of some contamination in ILs **a)** [C$_2$H$_5$MIm][BF$_4$] and **b)** [C$_4$H$_9$MIm][BF$_4$], which is evidenced by the larger than nominal area of the C^4 peak, and includes a contribution from adventitious carbon in these cases. In addition, O-C=O contamination has been modelled by a fifth component in dark blue. There is also a shake-up feature visible around 293.0 eV, which is not accounted for in the component model in this case.

There is evidence of some contamination in ILs **a)** [C$_2$H$_5$MIm][BF$_4$] and **b)** [C$_4$H$_9$MIm][BF$_4$], which has been modelled by a fifth component in dark blue, and constrained to be 4.1 eV above the C^1 component. This BE is

150

characteristic of O-C=O moieties.[30] The stoichiometric constraint of the C^4 component was also removed as this gave a very poor fit to the data. With the area allowed to vary, a good fit is achieved with a ratio much larger than the nominal, which suggests that there is a large amount of C_{alkyl} contamination, either dissolved as impurities within the IL or as AdC. The C_4 component and the AdC are thus modelled by the same component, as AdC appears at the same position as alkyl carbons with chain length $n>8$.[236]
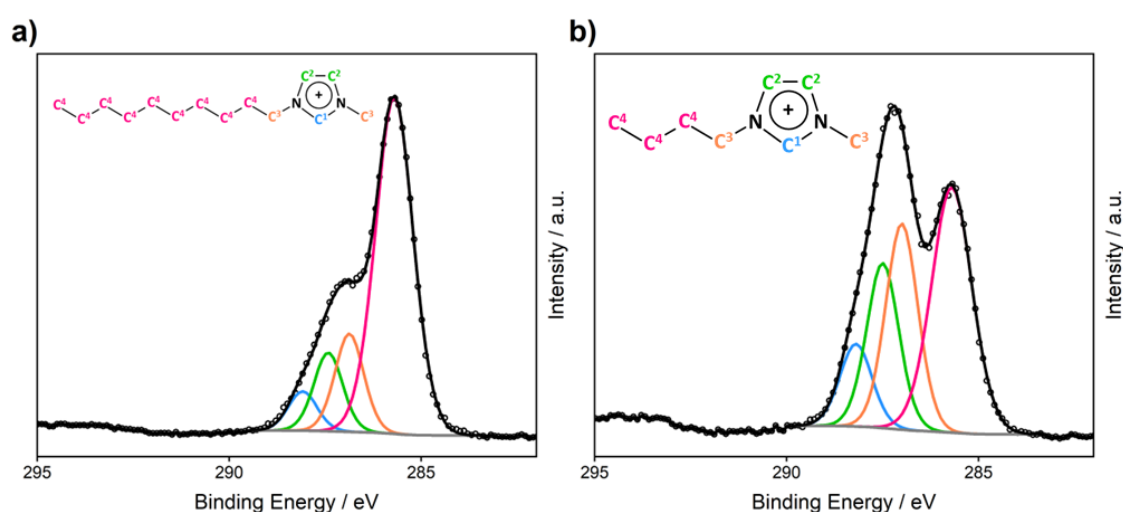
Figure 5.4. The XPS C 1s region of the imidazolium ILs **a)** [$C_{10}H_{21}MIm$][BF_4] and **b)** [C_4H_9MIm][PF_6]. The different components correspond to the different carbon environments seen in the cation, which are colour coded in the skeletal diagrams for each IL. The curve fitting procedure is detailed in the main text. A Shirley background was used in each case. Raw XPS data and the model total are represented by the open circles solid black curve, respectively. There is a shake-up feature visible around 293.0 eV, which is has been accounted for in the component model in this case.

It is also possible that there are other carbon impurities present, i.e. C-O, C-OH and C=O species, however, modelling of these components would be complex due to the overlap with the C^2 and C^3 components. The existence of impurities in ILs **a)** [C_2H_5MIm][BF_4] and **b)** [C_4H_9MIm][BF_4] is further supported by a strong O 1s signal for these ILs, which is absent in the **c)** [$C_{10}H_{21}MIm$][BF_4] and **d)** [C_4H_9MIm][PF_6] spectra (**Appendix D**). Impurity species are also evident for the same ILs measured on the glass substrates, which are separate aliquots from the same sample.

The two ILs that showed particularly good fits using the 'simple' model were also fitted using the 'shake-up' model (**Figure 5.4**). When using the shake-up corrected ratio, the C_{alkyl} FWHM must be constrained separately to obtain the good fit shown in the figure. Separately constraining the C_{alkyl} component leads to a FWHM ~0.2 eV larger than the other components, which have FWHM values ~0.9 eV. These values are in close agreement to a study that also adopted this procedure, and has been justified by the alkyl chain carbons having a vibrationally broadened peak structure.[236] To summarise, both 'simple' and 'shake-up' models provide reasonable fits to the IL C 1*s* region, however, the 'shake-up' model is more accurate and provides additional information on the different carbon environments.

XPS Analysis: Substrate Conductivity and Charging

In this section, the effect of x-ray and flood gun induced charging effects in XPS measurements is investigated for the series of ILs (see the intro section of this sub-chapter). The study aims to investigate how the nature of the XPS measurement (i.e. the charging environment) effects the measured BEs and peak shapes of core and valence spectra in ILs. The ILs were measured on two different substrates: the first being a grounded Cu foil and the second being a 'floating' glass substrate. XPS measurements were made both with and without use of charge compensation from a low energy electron beam flood gun (FG) to create four different electric field environments: 1) grounded (Cu) FG off, 2) grounded (Cu) FG on, 3) floating (glass) FG off and 4) floating (glass) FG on.
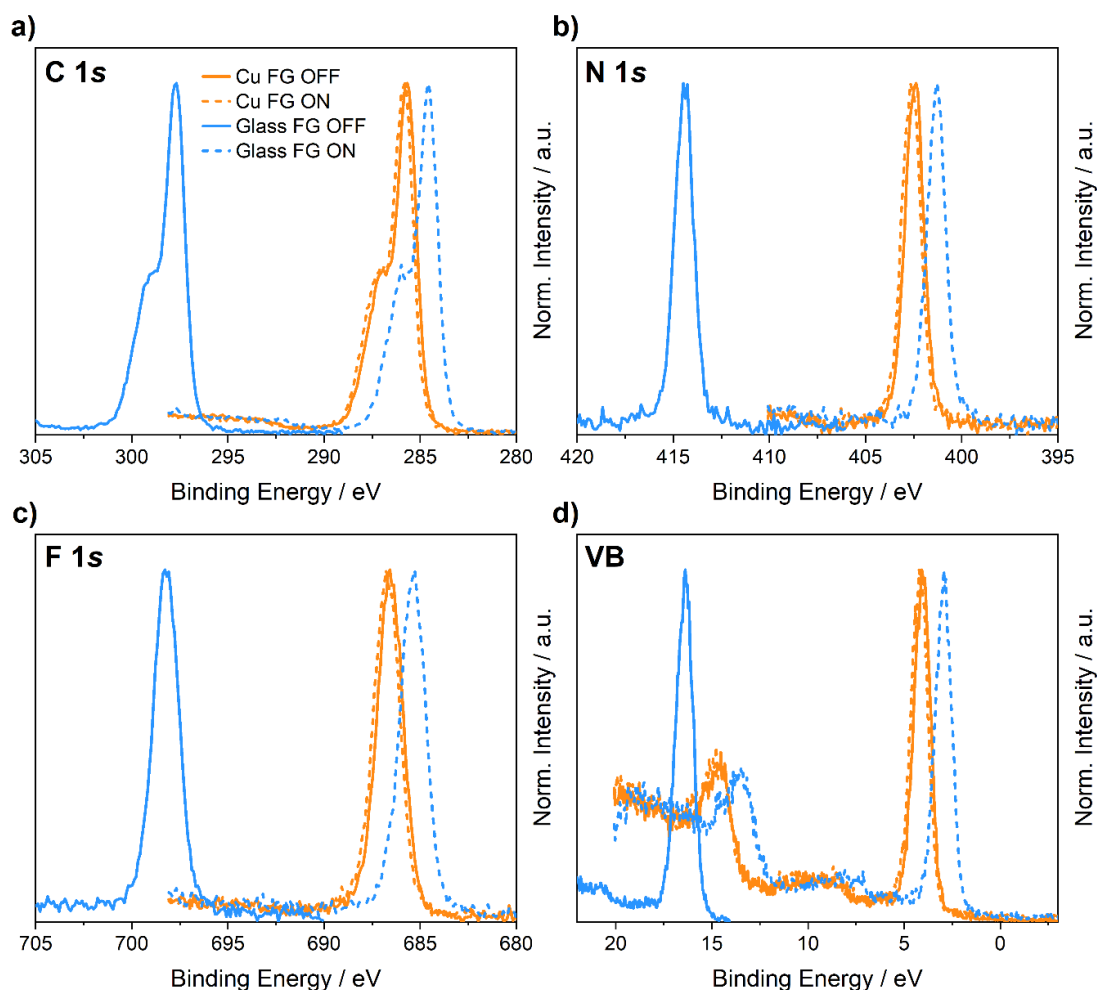
Figure 5.5. The XPS narrow scans [$C_{10}H_{21}MIm$][BF_4] **a)** C 1s, **b)** N 1s, **c)** F 1s, and **d)** valence band. The scans were recorded in four diverse ways indicated in the key: 1) grounded (Cu) FG off, 2) grounded (Cu) FG on, 3) floating (glass) FG off and 4) floating (glass) FG on. All spectra have been normalised for clarity.

The effect of these different environments on the C 1s, N 1s and F 1s core level and valence band spectra for [$C_{10}H_{21}MIm$][BF_4] are shown in **Figure 5.5**. The core level BE values for the IL drop measured on Cu without charge compensation are in close agreement with BEs determined by Villar-Garcia et al. via an internal calibration method with the imidazolium nitrogen:[236] C 1s ~285.0 eV, N 1s ~ 402.0 eV and F 1s ~686.0 eV. This confirms the conducting nature of the IL. When the charge neutralisation is switched on, the BE of all species increased slightly by a constant value ~0.17 eV. When measured on the glass substrate, the BE is around 12.5 eV higher than the IL/grounded Cu sample. Again, the shift is roughly constant for all species. Similar shifts were reported for all four ILs (**Table D1**). It is

153

interesting that the peak shape has not changed compared to the grounded sample, as specimens isolated from the spectrometer ground (floating) are expected to exhibit surface and near surface charge build-up.[29] Often, significant charge build up leads to the distortion of peak shape, decreased signal to noise ratio as well as BE shifts. In the case of the floating IL drop, positive charge induced by x-ray exposure does not cause any peak distortion, nor any significant change in the signal to noise ratio. In switching on the charge compensation, the BE takes a big negative step, closer to the values measured on the grounded Cu substrates, but around - 1.1 eV lower. The relative negative BE shift could be due to overcompensation by the FG leading to a build-up of negative charge at the surface of the IL, as suggested by Villar-Garcia et al.[236] These observations can be understood in terms of the charge on the IL drop as arising from different rates of electron removal and replenishment, where the rate of removal is controlled by the x-ray photoemission process, and the rate of replenishment is controlled by the conductivity of the sample. On the grounded copper substrate, the conductivity is immensely greater than the floating insulating substrate, resulting in a much smaller build-up of charge.

The observations made above for the peak shape of ILs measured on glass substrates were also made for all other ILs in the series studied. To investigate the peak shape further, the FWHM were measured and compared, along with the variation in BE in **Figure 5.6**. The FWHM of the N 1s and F 1s core-level spectra remain quite constant and do not vary more than +/- 0.04 eV from the first measurement on grounded Cu. This is also the case for C 1s if data points of the two ILs that showed impurities are ignored (see earlier discussion). The presence of contaminant peaks within the C 1s envelope introduces a larger uncertainty in the measured FWHM and BE values. Even considering this, there appears to be no strong trends in the measured FWHM for any species. There is therefore no differential charging effects, even when measured on a floating insulator with no charge compensation.

154
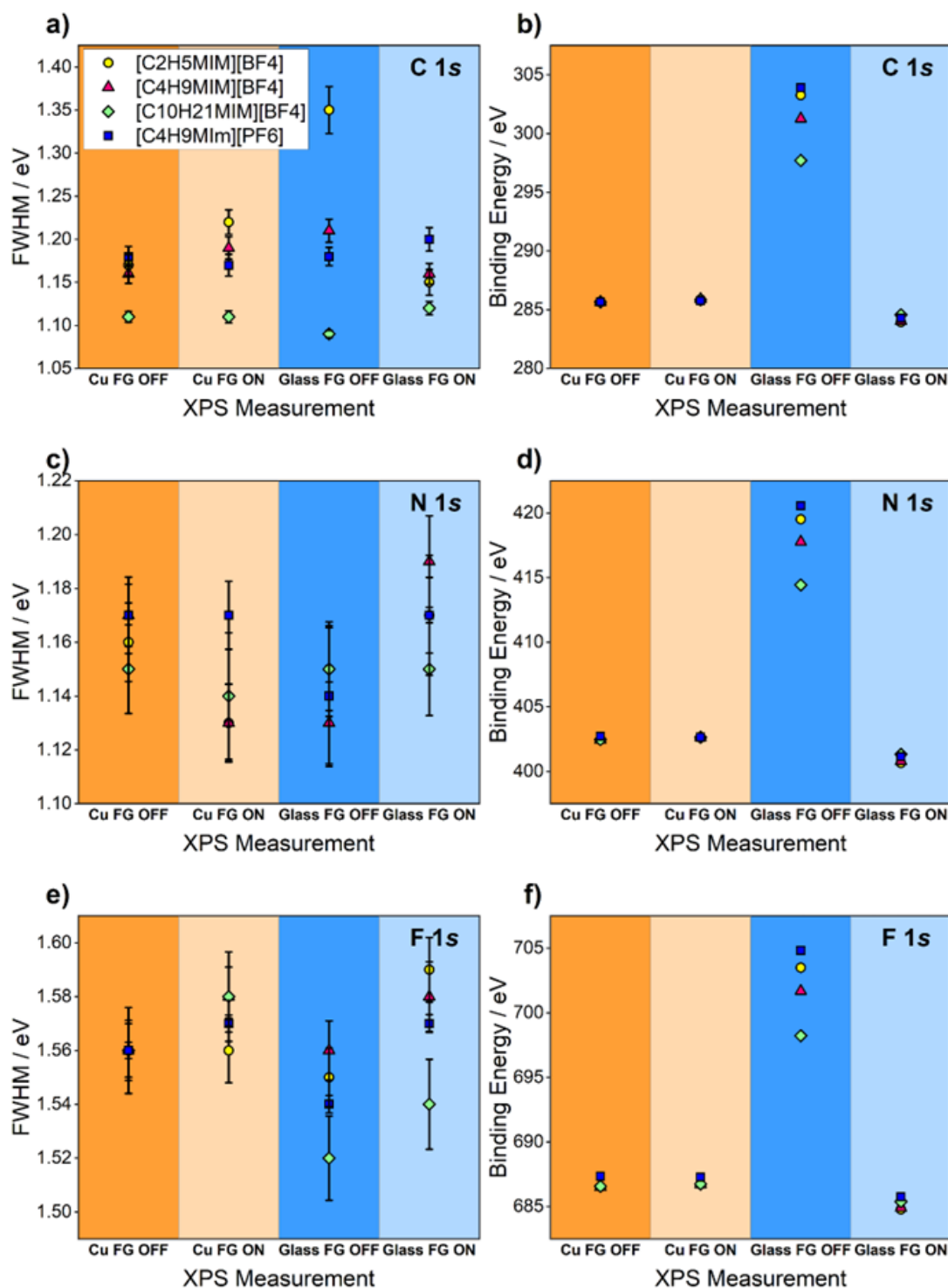
Figure 5.6. The measured BE values and FWHM for all ILs studied for the following high-resolution scans: **a-b)** C 1*s*, **c-d)** N 1*s*, **e-f)** F 1*s*. The scans were recorded in four diverse ways indicated on the XPS Measurement axis: 1) grounded (Cu) FG off, 2) grounded (Cu) FG on, 3) floating (glass) FG off and 4) floating (glass) FG on. The C 1*s* plots refer to the C^4 component in the 'simple' curve fitting model described in the main text. The error bars in **a,c,e)** correspond to errors in the fitted FWHM peak parameter estimated by Monte Carlo simulations using CasaXPS, and the estimated BE errors are too small to be seen on the current scale (**Table D2**).

Valence Electronic Structure

The VB spectra for the four ILs as recorded on the grounded Cu substrate with no charge compensation are shown in **Figure 5.7**. There is almost no change in the appearance of the ILs with the same anion: **a)** [C$_2$H$_5$MIm][BF$_4$] **b)** [C$_4$H$_9$MIm][BF$_4$] and **c)** [C$_{10}$H$_{21}$MIm][BF$_4$]. This shows that the increasing chain length has little effect on the appearance of the VB. This is in agreement with a study by Ikari et al. where little difference was seen between VB spectra for a series of imidazolium cations with increasing chain length and a common Tf$_2$N anion.[243] The VB XPS spectra for **d)** [C$_4$H$_9$MIm][PF$_6$] has a different appearance due to the different anion, and the VBM is higher than in the [BF$_4$]$^-$ anion species.
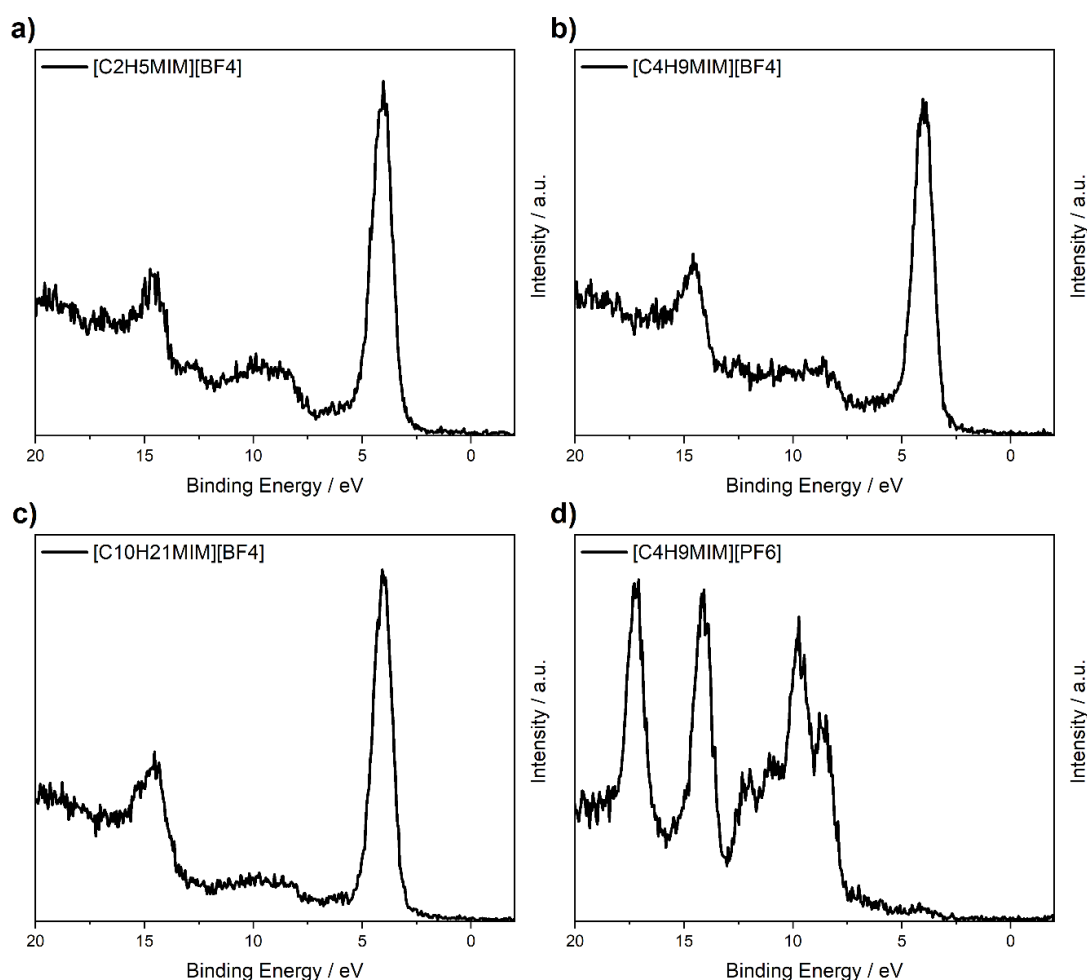
Figure 5.7. The XPS VB spectra of the imidazolium ILs **a)** [C$_2$H$_5$MIm][BF$_4$] **b)** [C$_4$H$_9$MIm][BF$_4$] **c)** [C$_{10}$H$_{21}$MIm][BF$_4$] and **d)** [C$_4$H$_9$MIm][PF$_6$]. The measurements were made on grounded Cu substrates with no charge compensation and no charge correction applied.

156

There has been a mixture of success when using single ion pairs to simulate XPS VB spectra with DFT. Ikari et al. studied surface electronic structure of imidazolium based ILs with XPS and DFT, for a common Tf_2N anion, and a series of cations with varying alkyl chain lengths.[243] They used relaxed single ions, then created a guess for the ion pair, which was then relaxed again before electronic structure calculations. They find the XPS and DFT simulated VB spectra are in good agreement of the general spectral features, even without cross-section correction. Kuusik et al. also found good agreement between XPS and DFT simulated VB spectra for a single ion pair of [EMIm][BF_4].[244] They observe a broadening of features in the liquid phase spectra compared to the gas phase. The same authors later report that the single ion-pair picture is not enough to describe the electronic structure of [EMIm][$B(CN)_4$], but that bulk structure gives a better representation.[245] Rangan et al. studied a series of three cyano-ionic liquids based on the imidazolium cation, by simulated UPS and XPS spectra using a single ion pair and also increasing numbers of ion pairs up to five pairs.[246] They conclude that the increased size of the ion pair significantly improves the agreement with the experimental spectra. However, by shifting the DOS of the anion and cation for the single ion pair, they are able to reach a good agreement with the experimental spectra. They do this for two photoemission energies, He II and Al Kα radiation, and find good agreement when weighting the DOS with the appropriate photoemission cross-sections. Future work could thus include simulation of IL VB spectra, to compare with the experimental data.

5.3 Operando Electrochemical XPS

In this work, an *operando* XPS cell was designed and fabricated for electrochemical XPS measurements in the Thermo Scientific Nexsa G2 spectrometer. This cell was used to investigate the behaviour of IL electrolytes and Na ion electrochemistry in the interest of Na ion battery research. Na ion batteries have received much attention as an alternative to Li ion batteries due to their lower cost and sustainability.[247-249] Although

much progress has been made, there is still a long way to go regarding the development of Na ion batteries for grid-scale applications.[250] A thorough understanding of the fundamental processes occurring in the battery components is thus a major contender in furthering research, in which surfaces and interfaces play a critical role.

During the initial charge and discharge processes in a battery (termed the first cycle), decomposition of the electrolyte at the electrodes results in the formation of a layer known as the solid electrolyte interphase (SEI). The SEI is a passivating layer that ultimately contributes to the stability and lifetime of the system; thus an improved understanding of the formation and evolution of this phase is crucial to obtain higher performance. Although *ex-situ* characterisation of cycled materials can provide valuable information, *in-situ* techniques can facilitate a much deeper understanding of real-time processes (see **Section 5.1**).

In this work XPS is performed in tandem with two different electrochemical measurement techniques: chronoamperometry (CA) and cyclic voltammetry (CV). In CA, a direct current (DC) voltage step is applied to the system, whilst the current is measured over time. In CV, the voltage at the working electrode is cycled, whilst the current is measured over time. By optimising the speed of data acquisition in both XPS and CV measurements, techniques are developed to obtain *operando* measurements, where the XPS spectra collected reflect the real-time processes occurring in the electrochemical system.

The electrochemical system studied in this chapter consists of a Na ion salt (NaTFSI), dissolved in the IL [BMIM][TFSI] in a 3-electrode set-up. The electrode materials used are Al for the working electrode (WE), and Pt for the counter electrode (CE) and reference electrode (RE). Two separate studies are detailed herein: the first investigates the behaviour of the IL electrolyte without the Na salt, and the second study investigates the system with the addition of 0.5 M NaTFSI. The first study is referred to as

the [BMIM][TFSI] system, and the second study is referred to as the [BMIM][TFSI]/NaTFSI system. When studying the [BMIM][TFSI] system, a simple cell was used whereby the 3-electrodes were connected via a small amount (~ 4 µL) of IL on top of a glass slide. In the [BMIM][TFSI]/NaTFSI investigation, a more advanced cell was developed for use in the Thermo Fisher Nexsa G2 spectrometer. The experimental section will cover the two cell designs used in this work, and the methods used to optimise data to perform *operando* measurements. Then the results from the [BMIM][TFSI] system followed by the [BMIM][TFSI] system will be presented and finally some conclusions regarding the work from this chapter.

5.3.1 Experimental Section

Electrode and Electrolyte Materials

Pt wire (0.5 mm diameter, 99.99 % purity) and Al foil (0.2 mm thickness) were purchased from Goodfellow UK. NaTFSI salt was purchased from SOLVIONIC, France. The IL [BMIM][TFSI] was synthesised by Avishek Dey (all precursors from Sigma Aldrich). The [BMIM][TFSI]/NaTFSI system was prepared by dissolving 0.5 M NaTFSI in [BMIM][TFSI]. All IL systems were dried in a vacuum oven at 75 °C for 48 hours prior to XPS measurements.

Cell Design & Assembly

Two different *operando* XPS cells were utilised in this work. In both set-ups, measurements were performed using an Al WE and Pt wire for both the RE and CE. The first design is a quite simple cell, which consists of three electrodes contacted by an IL electrolyte on top of a glass slide. This design is adapted from one reported by Gokturk and Suzer, who investigate the behaviour of an IL drop connected by two Pt wires on a glass slide.[251] The cell in this design is modified to include a 3 -electrode system, as previously described. This cell will be denoted the 'glass' cell herein and was used to investigate the [BMIM][TFSI] system.

The second *operando* XPS cell was designed and 3D-printed using AutoCAD 3D software.[252] A 3D schematic of the cell is detailed in **Figure 5.8** with key features labelled **1**-**7**. The 3D printed cell (**1**) is designed to fit the stage (**2**) for the Thermo Scientific Nexsa G2 spectrometer and can be easily fastened using the standard stage clips (**3**). The basin is filled with the [BMIM][TFSI]/NaTFSI system (**4**) in contact with the Pt RE (**5**), which is fastened in place by a screw (**6**) connected to the bias contacts within the spectrometer (not shown for clarity). The Pt CE has an identical set-up to the RE, whilst the Al WE (**7**) is optimally positioned for electrochemical XPS measurements.
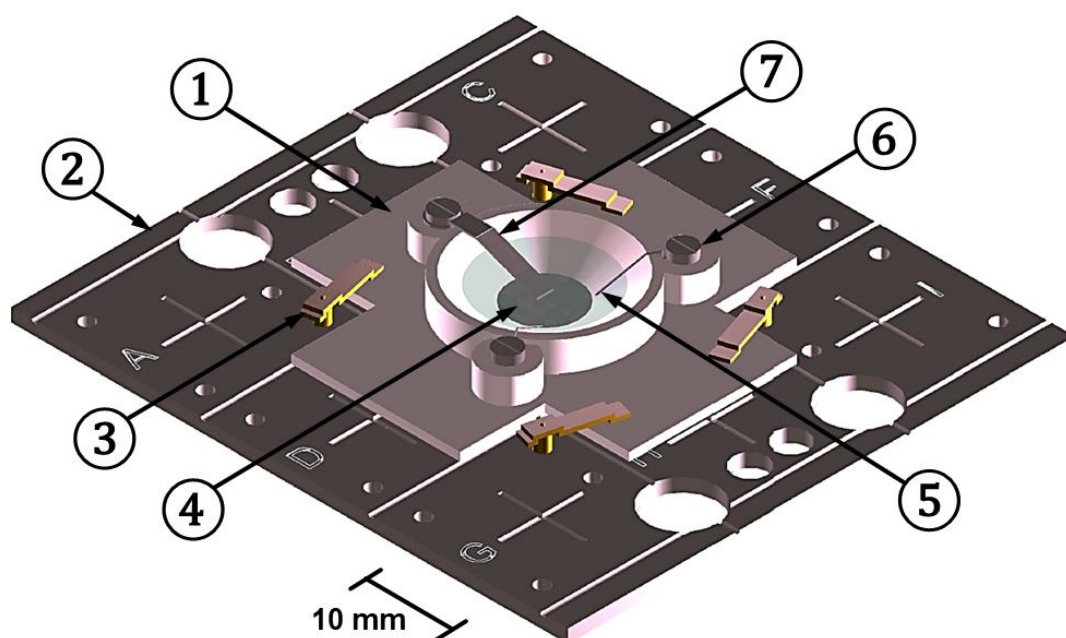
Figure 5.8. A 3D schematic of the *operando* XPS cell design, features **1**-**7** are detailed in the text.

The electrode/electrolyte interface at the WE is of significant interest and therefore the design exhibits several features to enable and enhance signal from this key region. As the position of the detector in the spectrometer and the angle of incident X-rays are fixed, the WE is positioned to maximise the number of ejected photoelectrons reaching the detector. The shallow angle of the basin ensures that incoming X-rays may be focussed on the interface

and the WE is submerged in the IL electrolyte at a shallow angle (< 45°) to allow ejected photoelectrons to escape the cell and reach the detector. The angle of incoming X-rays focussed on the boundary and ejected photoelectrons that will reach the detector is shown schematically in **Figure 5.9**, corresponding to normal emission geometry. The procedure to focus the X-ray beam at the interface involves collecting XPS survey spectra for a line scan that spans the boundary between the WE and the IL. The interface may then be identified by the position at which strong signals can be seen from both the electrode and the electrolyte.
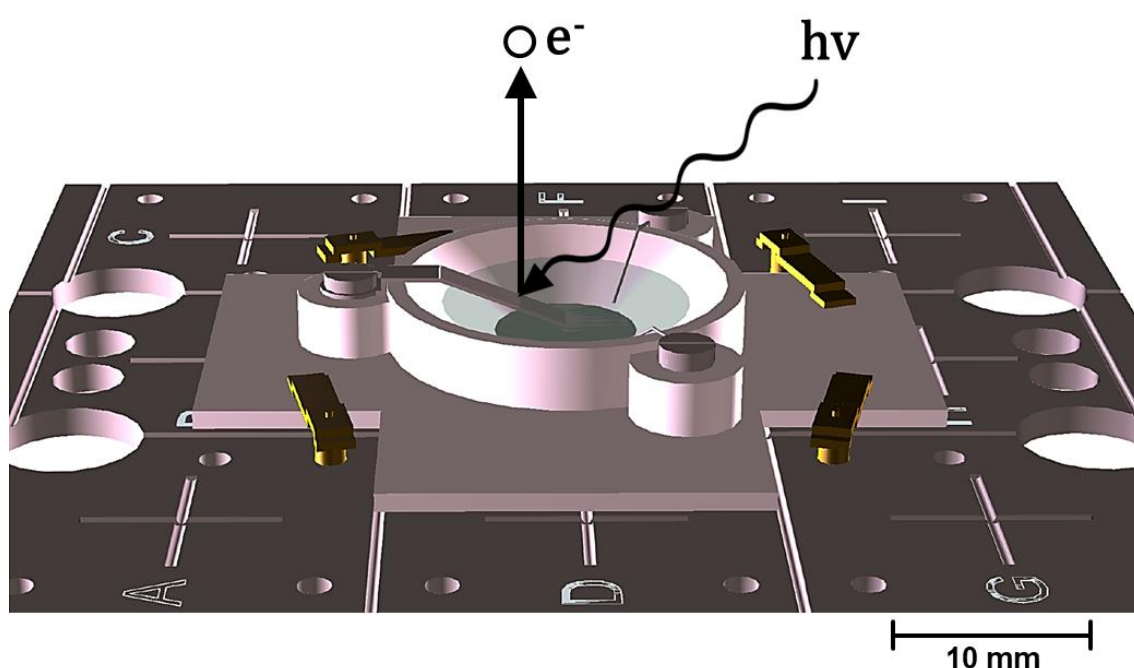
Figure 5.9a) The cell is designed to enhance signal from the electrode/electrolyte boundary. The angle of incoming x-rays and the direction of emitted photoelectrons that will be captured by the detector are indicated.

Data Acquisition Methods – Combining XPS & CV Measurements

Performing both XPS measurements and electrochemistry in tandem requires some attention to the speed at which both datasets are acquired. In conventional XPS measurements, a longer scan time is often preferred as it begets higher resolution data. For example, a typical core level scan could take ca. 1 – 2 minutes, but may be extended to > 10 minutes in some cases.

Conventional scanned mode also requires 'over-scanning' when using multi-detector XPS spectrometer, as both the energy range of the spectrum and the energy range of the detector (which scans from low to high BE) contribute to the scanning time. However, to capture any chemical changes during the running of CV measurements, faster data acquisition is required. This can be achieved by using snapshot mode.[253] In snapshot mode, the energy range of the spectrum and the energy range of the detector are set to be equal, and electrons from the whole energy range are collected simultaneously, thus massively reducing the acquisition time. For example, snapshot data may be acquired in ca. 5 – 10 s. The penalties of snapshot mode are a loss in resolution of the spectrum, so testing must be made beforehand to evaluate the dwell time and number of frames required to collect snapshot data with sufficient resolution.

For the [BMIM][TSFI] system in the glass cell, each XPS spectrum was acquired in 7.5 s per core-level (15 frames for a dwell time of 0.5 s each). This is slightly faster than the measurements acquired for the [BMIM][TSFI]/NaTFSI system, which were collected in 10 s per core-level (10 frames for a dwell time of 1 s each). However, by utilizing a CV scan rate of 2 m Vs^{-1}, this results in a voltage change of 0.02 V and 0.015 V per core-level for the systems with and without Na ions, respectively. This is not expected to cause any broadening due to the potential variation during XPS data collection or significant differences between the snapshot acquisition times.

5.3.2 Results i) [BMIM][TFSI] System

Electrochemical Measurements - [BMIM][TFSI] system

The first study was conducted to investigate the behaviour of the IL electrolyte [BMIM][TFSI] without any salt, and to optimise the XPS and CV acquisition methods to perform operando investigations inside the 3-electrode XPS cell. A simple cell design was used, using a small volume of the IL (~ 4μL) contacted with an Al WE, Pt CE, and Pt RE on a glass slide.

Two types of electrochemical measurements were performed, chronoamperometry (CA) and cyclic voltammetry (CV). During CA measurements, a constant direct current (DC) voltage was applied at a series of potential steps, and XPS measurements were taken at each voltage. The XPS measurements were taken ~ 120 s after the voltage was applied to allow the ions time to respond, and the measurements were taken in two analysis locations: one point in the centre of the IL electrolyte, away from any of the electrodes, and another point focussed on the WE/IL interface. The potential was increased in steps of 0.2 V from -1.0 to 1.0 V, to investigate the response to both negative and positive applied potentials. After the measurement at 1.0 V, the voltage was then switched back to 0.0 V to investigate the effect of changing the potential to 0.0 V from the positive direction.
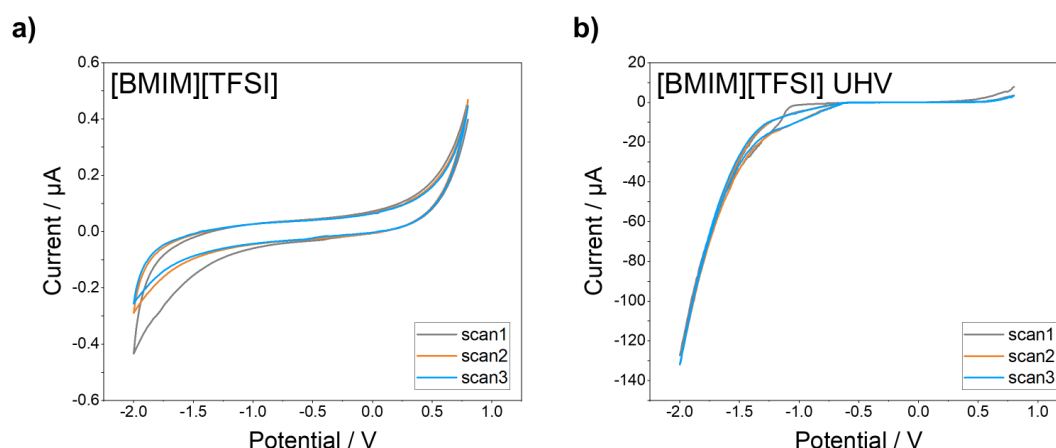
Figure 5.10. CV measurements performed just before **a)** and just after **b)** transferring the system to the UHV, from 0.8 to -2.0 V at a scan speed of 0.2 Vs^{-1}.

After CA measurements, CV measurements were performed at a scan rate of 2 mVs^{-1}, starting at 0.8 V and sweeping to -1.0 V and back, again performing the XPS measurements at the same two analysis locations as before. The CV settings were chosen to be the same as CV measurements performed just before and just after transferring the system to the UHV, from 0.8 to -2.0 V at a scan speed of 0.2 Vs^{-1} (**Figure 5.10**). A much higher current was observed in the UHV environment, which could be due to the decrease in air and water molecules, both in an above the IL.

Before any CA measurements were taken, preliminary XPS data was recorded at the centre of the IL electrolyte, and for a set of points making a line scan across the boundary between the WE and the IL. The measurements taken at the IL centre were obtained using conventional scans, whereas the line scan data was obtained using fast snapshot spectra. For these measurements, the FG was turned on as the three electrodes are isolated from the spectrometer ground - the WE is only grounded through the potentiostat when it is in operation. The raw spectra are plotted in **Figure 5.11** for the IL centre scans, and for two positions on the line scan: position 0 – towards the IL centre, and position 21 – close to the WE. The C $1s$ region has been fitted using the shake-up curve fitting procedure used earlier (**Figure 5.4**) with the addition of a component for the CF_3 environment in the TFSI anion. The C $1s$ region for position 21 also shows an additional peak for adventitious carbon (AdC), which is present on the surface of the WE. Although the spectra at the IL centre have a higher resolution than the data collected using the snapshot spectra, the required chemical information is still attainable from the snapshot spectra.

To locate the interface between the WE and the IL, the relative At % of F $1s$ and Al $2p$ species were compared for all the points recorded on the line scan spanning the boundary (**Figure 5.12a**). The increase in Al $2p$ and the corresponding decrease in F $1s$ species occurs between the positions 21 and 22, and a point between these two locations was selected for further data collection and denoted the WE/IL interface. The ratio of the IL species to the anion N species were compared for the spectra displayed in **Figure 5.11** for three different analysis locations (the IL centre, position 0 and position 21 across the WE/IL boundary) are summarised in **Figure 5.12b**.
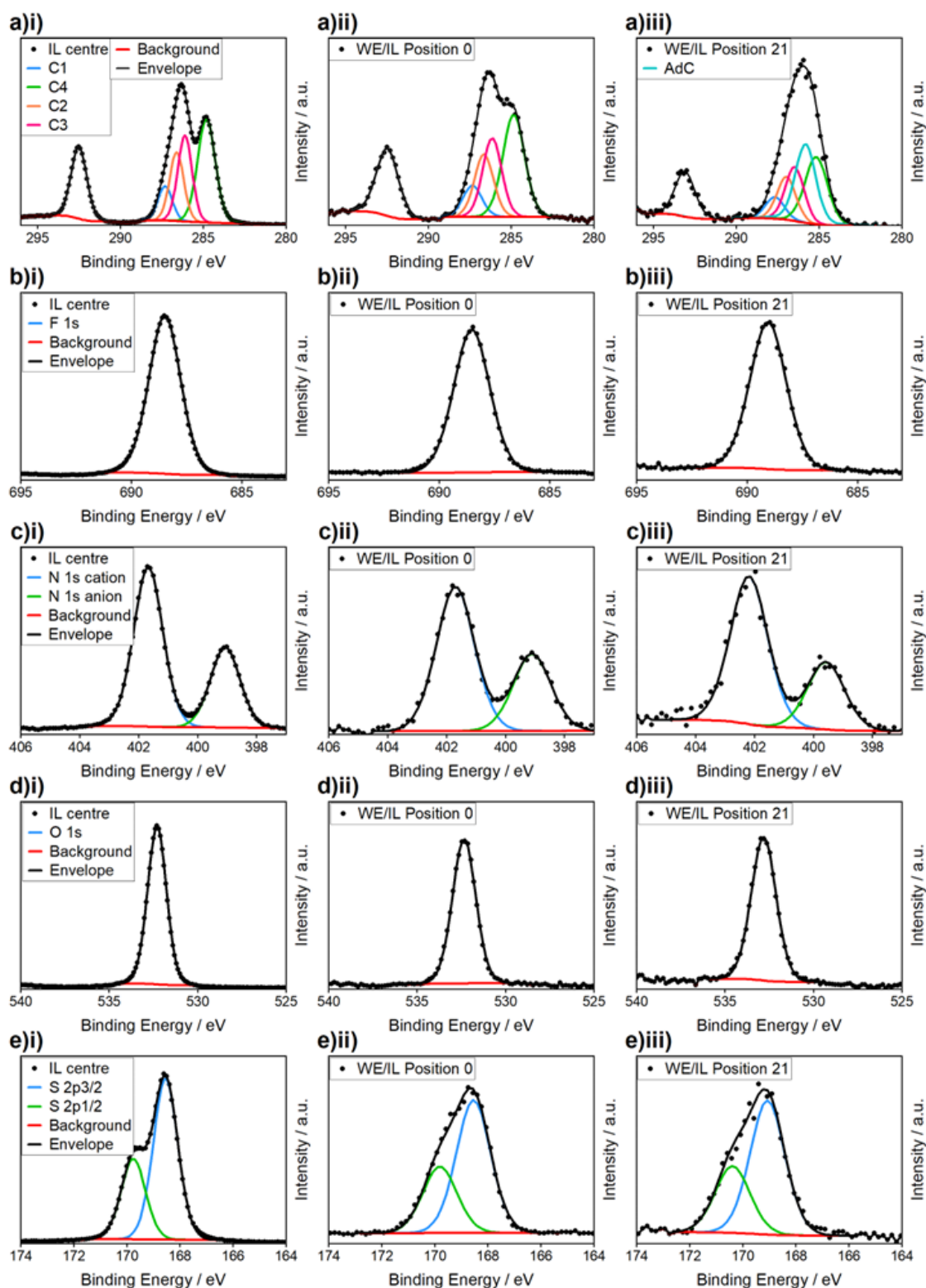
Figure 5.11. Preliminary XPS spectra recorded for core-levels **a)** C 1*s*, **b)** F 1*s*, **c)** N 1*s*, **d)** O 1*s*, and **a)** S 2*p*. Spectra were recorded at **i)** the centre of the IL using conventional scanned mode, and along a line scan spanning the WE/IL boundary using snapshot mode. Plotted here are snapshot spectra from two positions: **ii)** position 0 – towards the IL centre and **iii)** position 21 – close to the WE.

There is an increased concentration of S and F species compared to nominal values for all three locations, although this is highest for the position 21, which is closest to the electrode. Due to the system already being cycled before these data were collected (**Figure 5.10**), this may be attributed to breakdown of the IL. These decomposition species are present throughout the bulk IL at this stage but have higher concentration at the electrode. It is evident that surface species are being detected at position 21 due to the AdC and Al 2*p* signals. There is also an increase in the oxygen composition, which is attributed to decomposition products or native Al oxide, Al₂O₃.
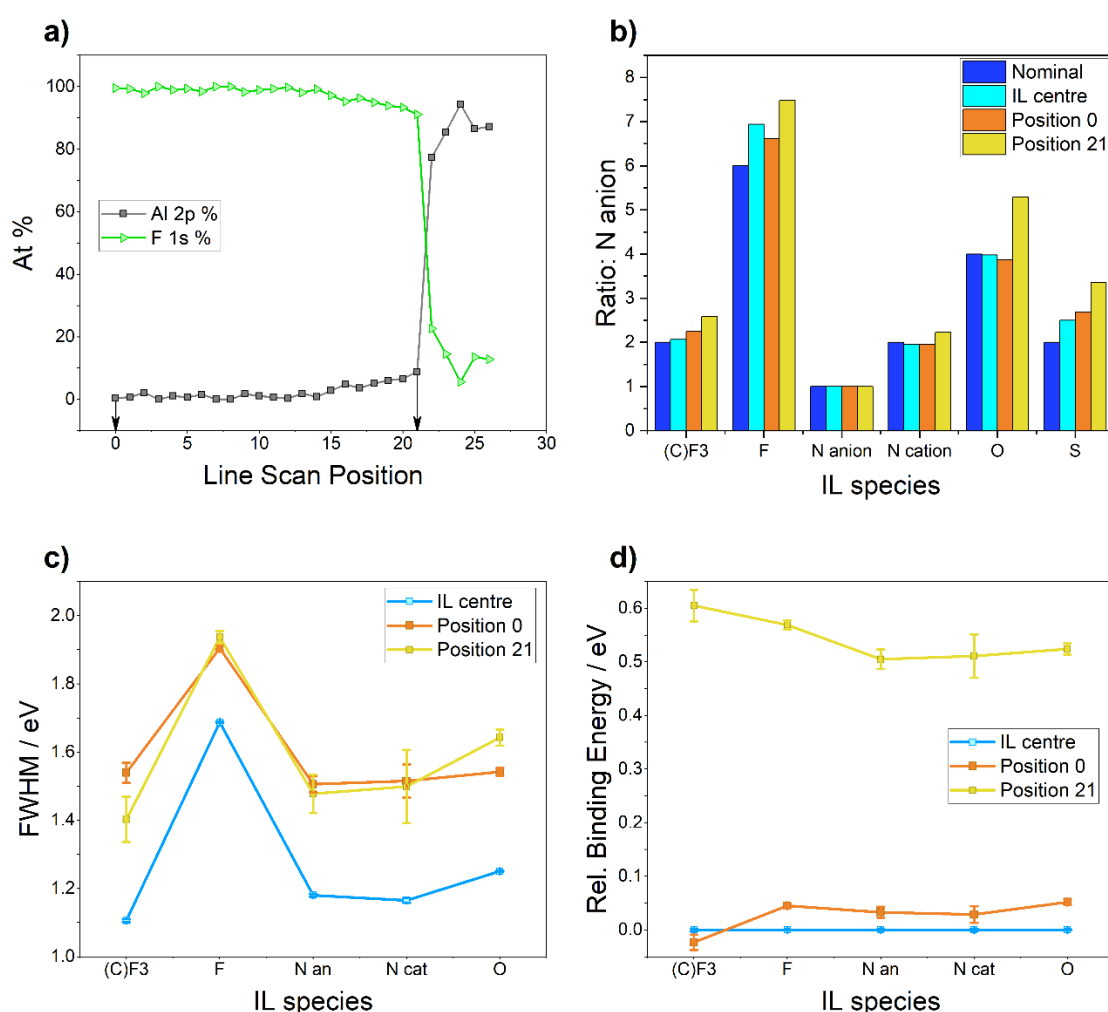
Figure 5.12a) The relative At % of F 1*s* and Al 2*p* at different positions collected on a line scan spanning the WE/IL boundary. The interface is located between positions 21 and 22. Positions 0 and 21 are studied in more detail and are indicated by the arrows. **b)** The ratio of different IL species to the N in the TFSI anion, for positions 0 and 21 near the WE/IL boundary, and a position in the centre of the IL. **c)** The FWHM of different IL species and **d)** the BEs of different IL species relative to the BE measured at the centre of the IL. The error bars in **c,d)** correspond to errors in the fitted FWHM and BE peak parameters estimated by Monte Carlo simulations using CasaXPS (**Table D3**).

A comparison of the FWHM of the scanned and snapshot spectra (**Figure 5.12c**) evidences the change in resolution of the two data types. There is no change in FWHM between the two different line scan positions, however, there is a change in the measured BE of all IL species (**Figure 5.12d**). The spectra recorded close to the WE are roughly ~ 0.6 eV higher in BE than those recorded ~ 1000 µm closer to the IL centre, where the BEs are roughly the same as those recorded at the centre. This is probably due to the conducting nature of the metallic electrode. In the study earlier in this chapter on the measured BEs of ILs recorded on metallic and insulating materials with and without the use of charge compensation (**Figure 5.5**), a higher BE was measured for the IL in contact with the metallic surface, than on a glass substrate, when the FG was turned on. This is suggested to arise from overcompensation from the FG resulting in a build-up of negative charge when the IL is not in contact with a conducting substrate.

Chronoamperometry Measurements – [BMIM][TFSI] System

The raw spectra for all core-levels recorded during CA measurements are plotted in **Figure 5.13**. The spectral maximum of each region follows the same trend for the XPS data collected at the IL centre and at the WE/IL interface, however, there are some major differences in the spectral features depending on the analysis location. The overall behaviour of all core-level spectra at both analysis positions is to shift in a negative direction on the application of a positive potential, and vice versa. This is expected for a system with a grounded electrode (see **Section 5.1**). However, the gradient of these shifts is far from the expected values of ~-1.0 eV/V, indicating that some non-Faradaic processes are occurring in the cell. This is most likely due to a capacitive current resulting from a large build-up of charge at the electrode surfaces, due to the large WE surface area (SA) in this case. The trend in the BEs with the applied potential will be discussed in more detail later, together with the BE trends observed during operando CV measurements.
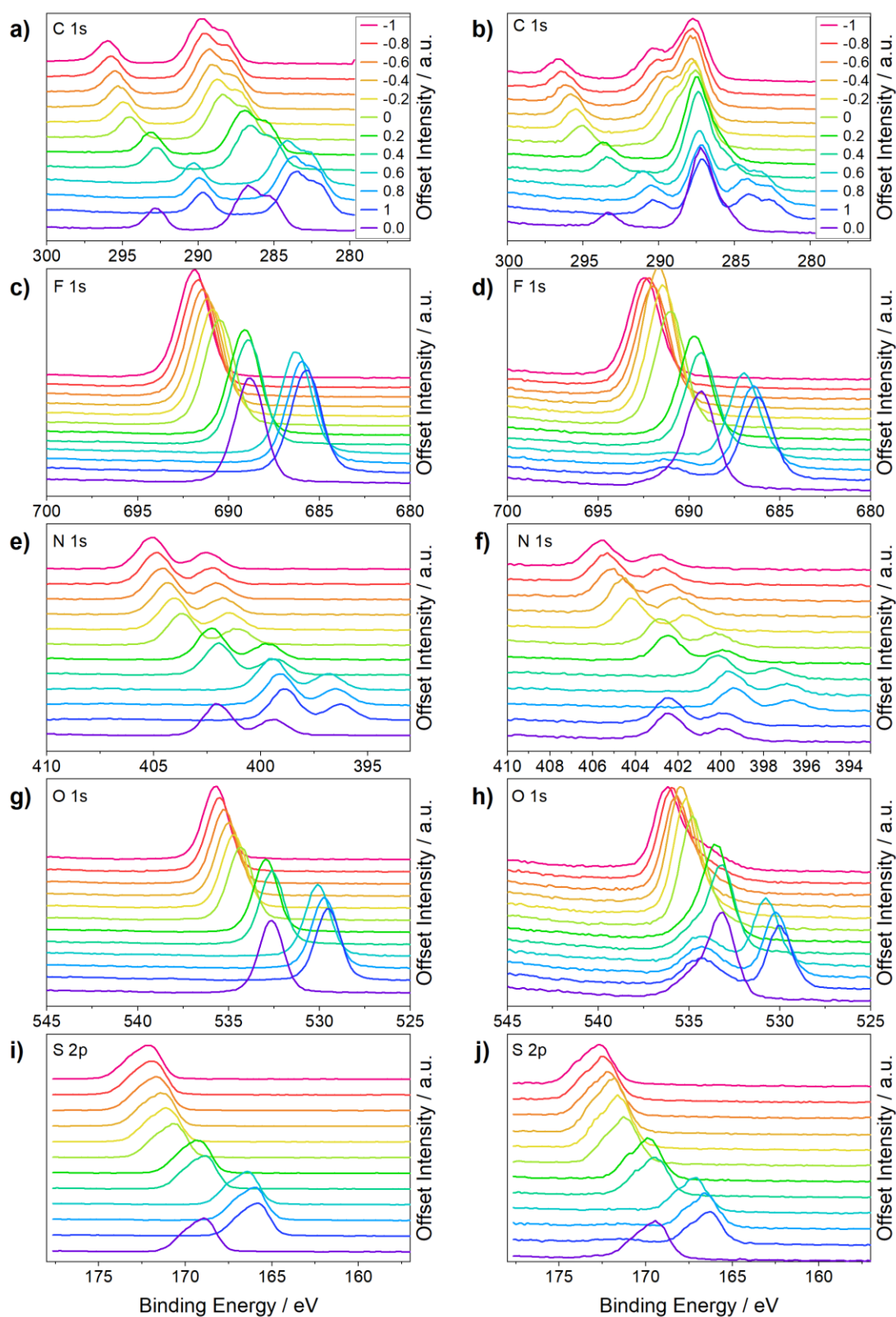
Figure 5.13. Raw spectra collected during CA measurements recorded from -1.0 to 1.0 V in steps of 0.1 V. After scanning at 1.0 V, the spectra were measured at 0.0 V again. XPS snapshot spectra were collected at 7.5 s per core-level (15 frames for a dwell time of 0.5 s each), for the regions **a,b)** C 1s, **c,d)** F 1s, **e,f)** N 1s, **g,h)** O 1s, and **i,j)** S 2p. The left column **(a,c,e,g,i)** and the right column **(b,d,f,h,j)** were collected at the centre of the IL basin and the interface of the WE/IL, respectively.

168

Firstly, the appearance of additional peaks in the F 1s spectra during the CA measurements will be examined in more detail. Selected F 1s spectra in **Figure 5.14** are plotted for a series of potentials, from CA measurement at 0.0 V, on increasing the potential in the positive direction to 1.0 V, and then finally returning the potential to 0.0 V. At both analysis locations, the final measurement at 0.0 V does not see the F 1s peak return to the position measured at 0.0 V before CA at positive potentials. Again, this indicates non-Faradaic current flowing, which could be due to charge build up by the asymmetric WE/IL SAs. When a positive potential is applied, there is breakdown of the electrolyte, as evidenced by a new peak in the F 1s spectra. This is also visible in the S 2p spectra in **Figure 5.13**. These peaks grow upon further positive potentials, but do not shift in binding energy due to the grounding of the WE, indicating that they are formed at the electrode surface and can be attributed to the formation and evolution of the SEI layer.

Cyclic Voltammetry Measurements – [BMIM][TFSI] System

During CV measurements, the potential at the WE was cycled from 0.8 V to -1.0 V, resulting in the *operando* CV in **Figure 5.16a**. The shape of the CV has changed significantly since the preliminary CVs recorded (**Figure 5.10**), and further confirms non-Faradaic behaviour at the electrode surface. Measurements taken just before and just after CV (**Figure 5.16b**) with no applied potential also reveal different compositions. Inspection of the changes in composition during CV cycling (**Figure 5.16c**) reveal that the electrolyte undergoes further decomposition during the CV measurements, and that the biggest changes occur at the electrode surface, as expected. These observations show how dynamic the system is, continually evolving over time and with the applied potential. The FWHM (**Figure 5.16d**) of the F 1s components showed no variation due to measurement type or applied potential, indicating that no differential charging is occurring during the measurements.
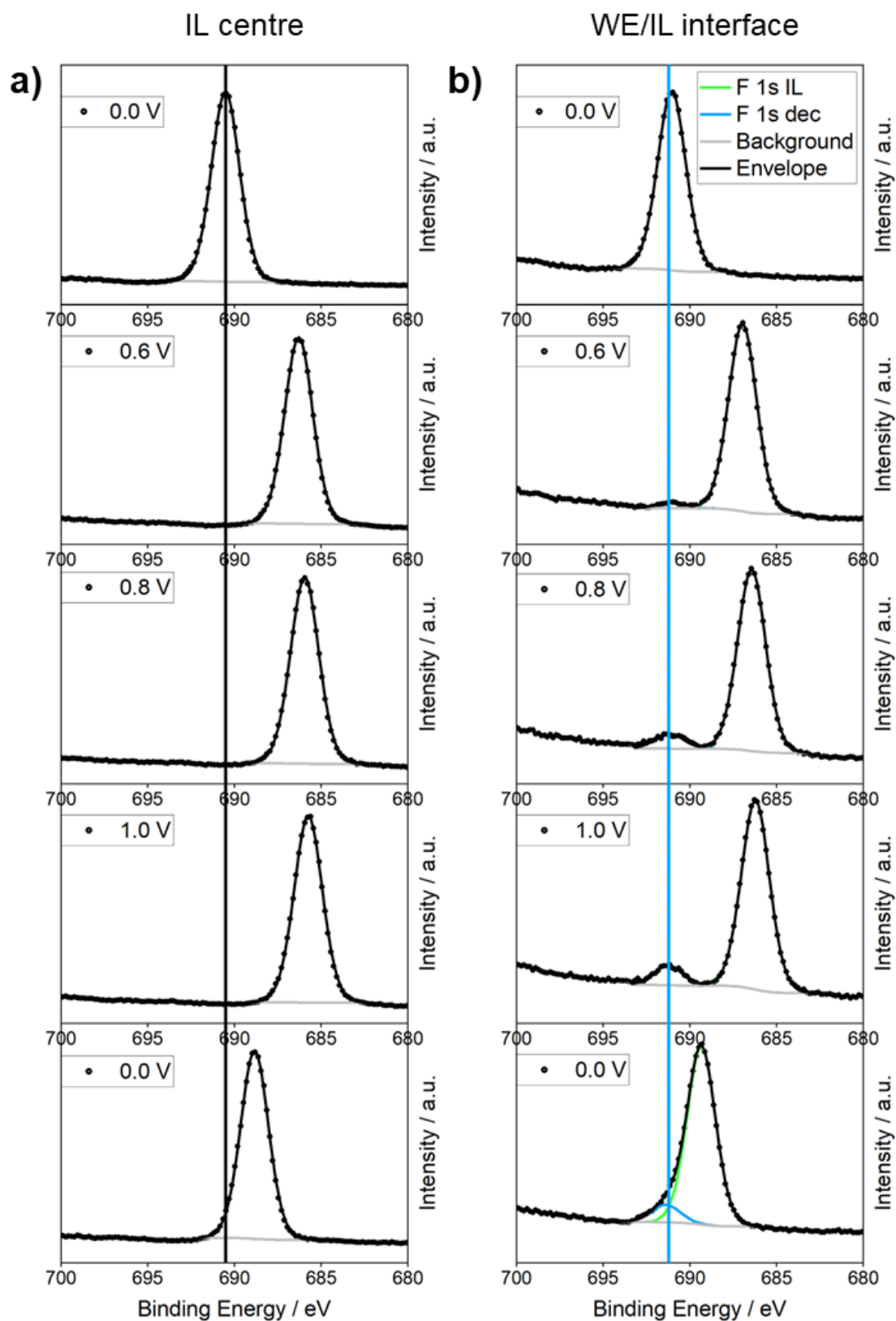
Figure 5.14. F 1s spectra recorded at selected potentials during CA measurements, focussing on **a)** the IL centre and **b)** the WE/IL interface. The lines are included as a guide to the eye. The scanning direction is from the top to the bottom of the figure.
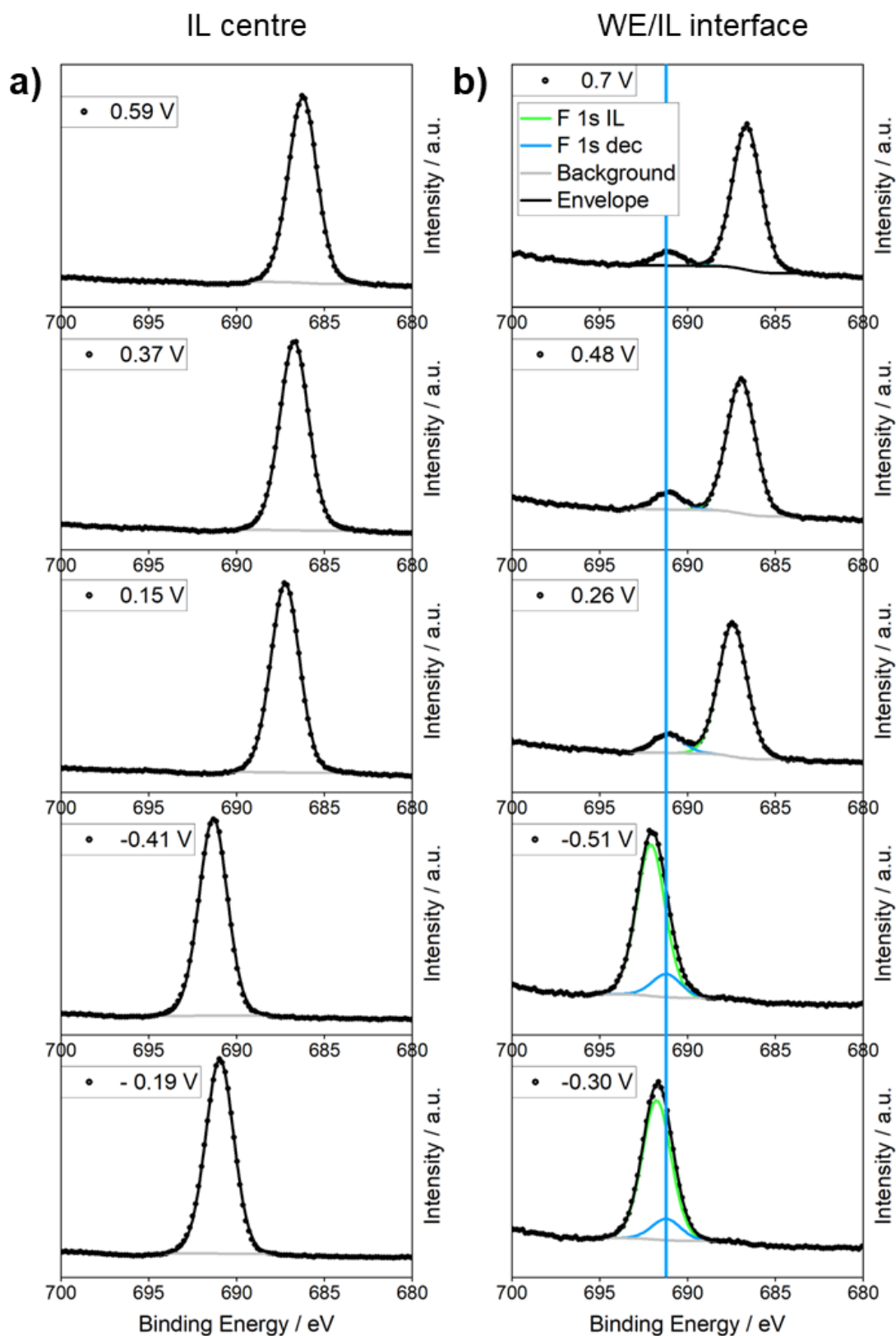
Figure 5.15. F 1*s* spectra recorded at selected potentials during CV measurements from 0.8 to -1.0 V, focussing on **a)** the IL centre and **b)** the WE/IL interface. The lines are included as a guide to the eye. The scanning direction is from the top to the bottom of the figure.

The SEI peaks in the F 1*s* spectra during CV continue to grow at positive potentials (**Figure 5.15**), whilst there are no changes to the shape of the F 1*s* spectra recorded at the centre of the IL. In the spectra recorded at -0.51 V and -0.30 V, the peak due to the decomposition of the IL and formation of SEI overlaps with the main F 1*s* peak from the IL. The area and position of the peak have been constrained to values +/- 0.1 eV of the positions measured at positive potentials, to illustrate the convolution of these signals. Without prior knowledge of the two environments, it would be difficult to identify the overlapping species. In this way, the shift of the spectra with applied potential can be used as an advantage if the WE is grounded, to identify species found at the electrode surface.
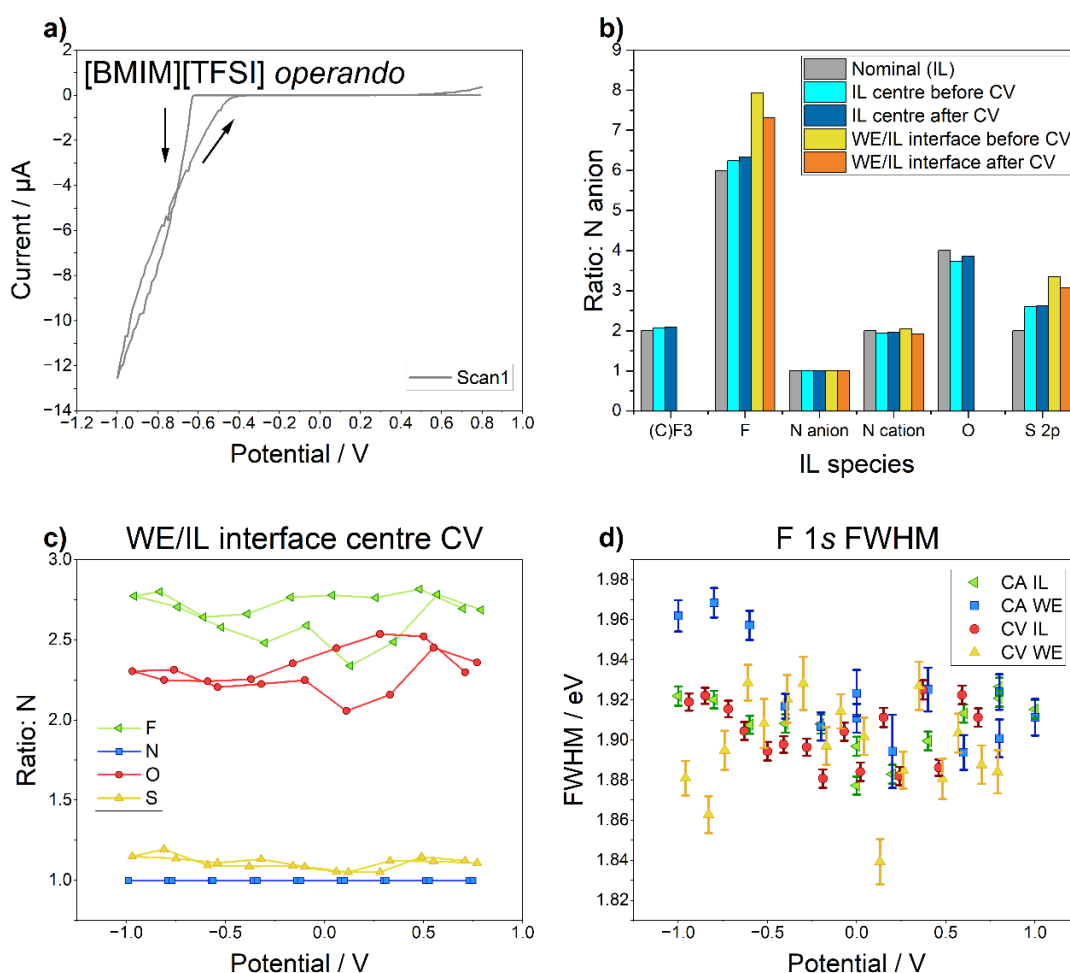
Figure 5.16. a) The *operando* CV recorded from 0.8 to -1.0 V at a scan rate of 2 mVs^{-1}. **b)** The change in composition before and after the CV scan at the IL and at the WE/IL interface. **c)** The change in composition of the IL species during the CV measurement, showing how dynamic the analysis region is. **d)** The FWHM of the F 1*s* components for all CA and CV measurements, showing little variation across measurement type and applied potential. The error bars in **d)** correspond to errors in the fitted FWHM peak parameter estimated by Monte Carlo simulations using CasaXPS (**Table D4**).

Finally, a comparison of the BE shifts with the applied potential at both analysis locations (the IL centre and the WE/IL interface) using both CA and CV techniques is shown in **Figure 5.17**. The shifts have been calculated relative to the spectra measured at 0.8 eV in the CA measurements, to facilitate easier comparison to the CV measurements, which were started at 0.8 V. The species at the IL centre and at the WE/IL interface behave almost uniformly, indicating that the IL species probed at the interface are behaving as bulk electrolyte. The C $1s$ spectral maximum at the interface arises from AdC on the surface of the electrode, and thus does not exhibit large potential-induced shift. This is also observed in the metallic and Al_2O_3 $2p$ signals due to the grounding of the WE. The C $1s$ spectral maximum shifts slightly more than the Al species as this region also contains overlapping peaks from the [BMIM] cation.

An interesting feature in both CA and CV measurements is the non-Faradaic behaviour of the IL at positive potentials, as previously mentioned, and the BE shifts during CV mimic the shape of a hysteresis loop. An important observation is that the BE shifts do not significantly change between the two measurement types, which is most noticeable for the negative to positive scanning direction from -1.0 to 0.0 V, which follows the expected gradient of -1.0 eV/V. This means that the slow CV scan rate of 2 mVs^{-1} is sufficient to allow the ions to respond to the applied potential, and that the XPS spectra and CV acquisition speeds are well aligned to perform *operando* measurements.
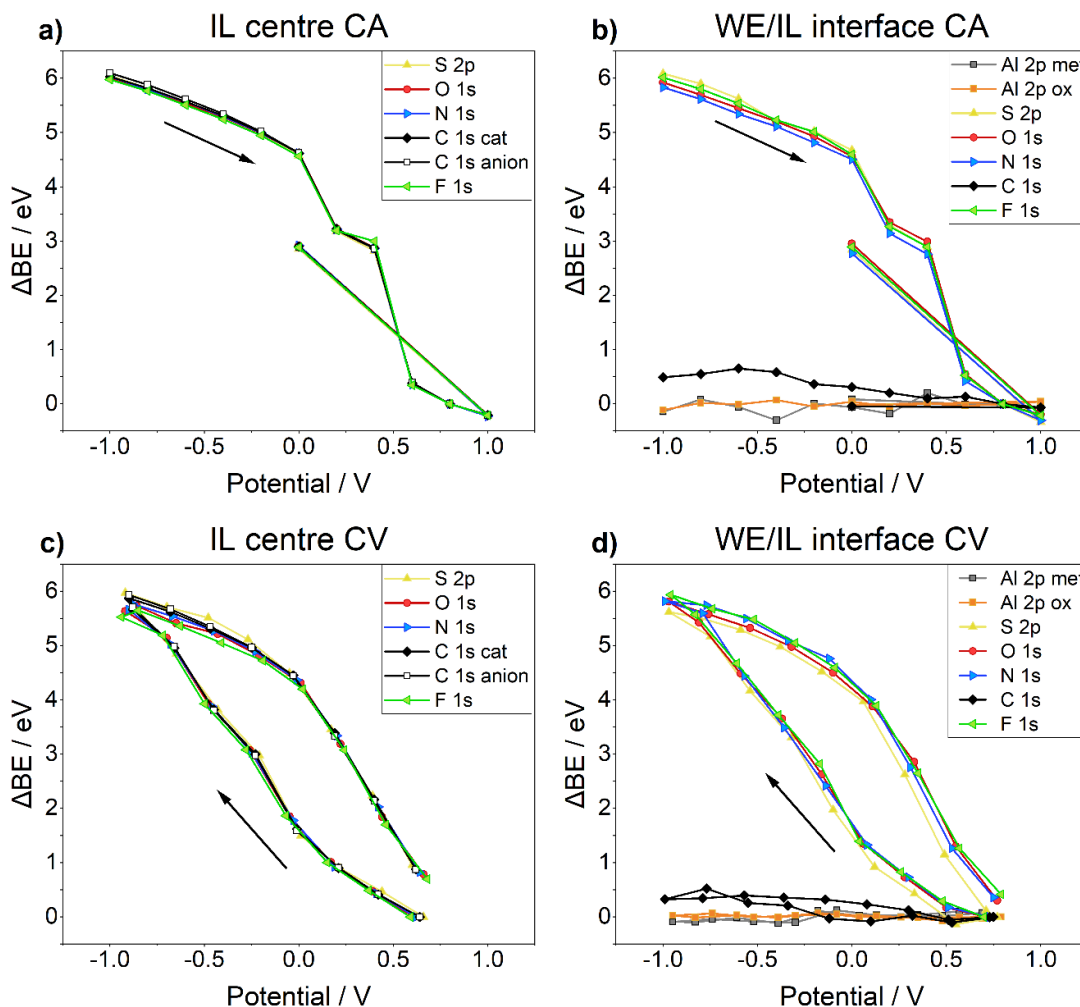
Figure 5.17. The binding energy shifts due to the applied potential at **a,c)** the IL centre and **b,d)** the WE/IL interface. The shifts in the CA measurements **(a,b)** are calculated relative to the spectra recorded at 0.8 V, in order to compare with the shifts observed in the CV measurements **(c,d)**. The direction of the forward scan is indicated by the black arrow in each plot.

5.3.3 Results ii) [BMIM][TFSI]/NaTFSI System

Preliminary XPS Measurements – [BMIM][TFSI]/NaTFSI System

The initial stage of the *operando* experiments involves the transfer of the experimental set-up to the UHV analysis chamber, via the low-pressure load lock (**Figure 5.18a**). As this cell has a larger volume of IL (~ 30 μL), particular care was taken during the experimental set-up. Although the ILs were dried in a vacuum oven overnight, tiny amounts of gas were still dissolved in the IL, which are removed at around ~ 10^{-2} mbar. As the turbo pump attached to the load lock reduces the pressure quickly, the first stage

of the pumping process was performed manually, by opening/closing the backing line to reduce the pressure slowly. This allows the dissolved gas molecules to surface in a controlled manner, minimising disturbance to the experimental set-up. After the pressure had dropped below 10^{-2} mbar, the turbo pump was switched on and the cell was left pumping in the load lock overnight, resulting in a load lock pressure of 4×10^{-7} mbar.
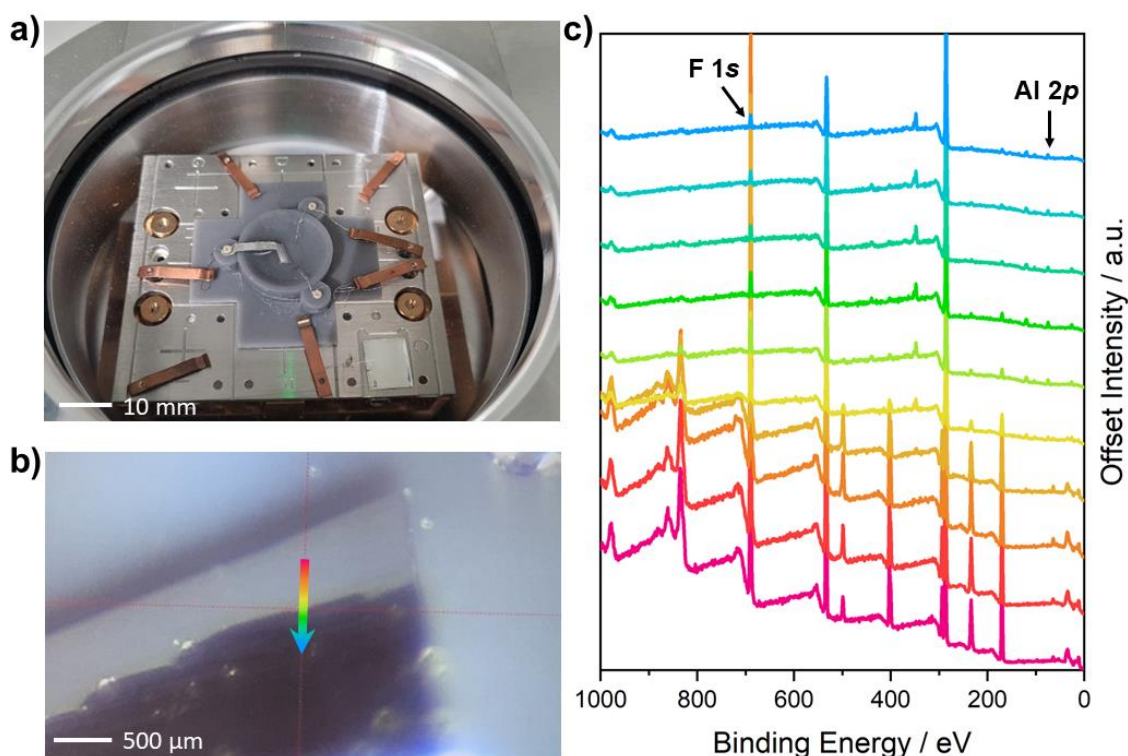
Figure 5.18a) The *operando* XPS cell attached to the Thermo Scientific Nexsa G2 stage, pumping down in the load lock. **b)** The camera view in the Thermo Avantage software, showing the scanning position from a camera inside the analysis chamber, indicated by the centre of the red cross hairs. The view shows the Al WE submerged in the IL electrolyte. **c)** A series of survey spectra, recorded along a line scan across the IL/WE interface, indicated by the arrow in **(b)**.

The cell was then transferred to the analysis chamber, where preliminary measurements were then performed to optimise the measurement location (**Figure 5.18b,c**). Whilst the design allows the x-rays to reach the WE/IL boundary, the precise scanning location can be optimised by balancing the signals from the WE and the IL, in this case the F 1s signal from the IL electrolyte [BMIm][TFSI] and the Al 2p signal from the Al WE. Once the optimum position for scanning the WE/IL interface was located high

resolution narrow scans were recorded (**Figure D2**), showing clear signals from all species.

Cyclic Voltammetry Measurements – [BMIM][TFSI] / NaTFSI System

During CV measurements, the potential at the WE was cycled from 0.0 to -2.5 V. This results in the BE shifts displayed in **Figure 5.19**. Like the previous study on the [BMIM][TFSI] system, different components in the spectra respond differently to the applied potential, depending on whether they are in contact with the electrode surface or not. This can be seen clearly in the Al 2*p* and C 1s spectra. The strong signals for the metallic Al and native oxide do not move with the applied potential, because the WE is grounded. The Al 2*p* curve fitted with metallic and oxide components is shown in **Figure D3**, with metallic line shapes taken from a previously reported model.[254]
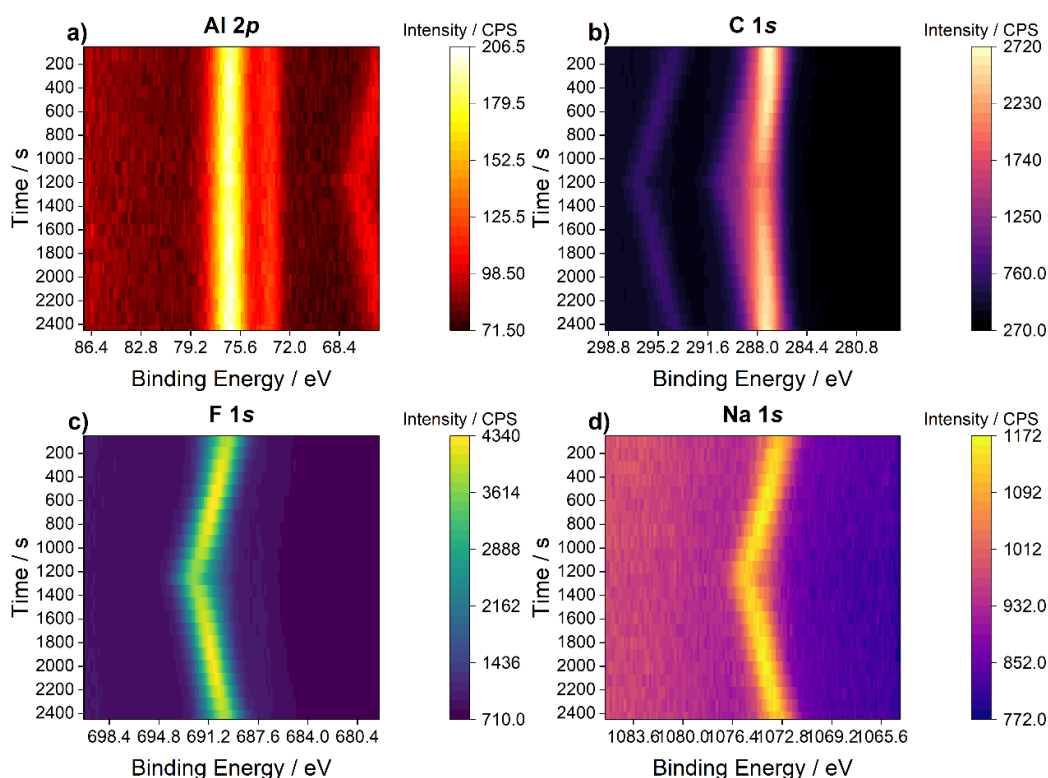
Figure 5.19. *Operando* electrochemical XPS measurements, showing how the BEs shift during CV scans from 0 to -2.5 V, for the core-levels: **a)** Al 2*p*, **b)** C 1s, **c)** F 1s and **c)** Na 1s. The spectra were recorded at the interface between the WE and IL.

The Na 2*s* core-level is just visible at the low BE limit, and moves towards higher BEs on the application of negative potential, as expected. Similarly, in the C 1*s* spectra, the spectral maximum, which arises from AdC on the surface of the electrode, does not move significantly during cycling, whereas the low BE components from the [BMIM] cation and the high BE components from the [TFSI] anion, (i.e. the electrolyte species) shift in unison with the applied potential. This is also observed in the F 1*s* and Na 1*s* spectra: the position of the spectral maximum illustrates the behaviour of the bulk IL species, however, a lower intensity feature can be seen at a constant BE, and thus can be attributed to species formed at the surface of the electrode.
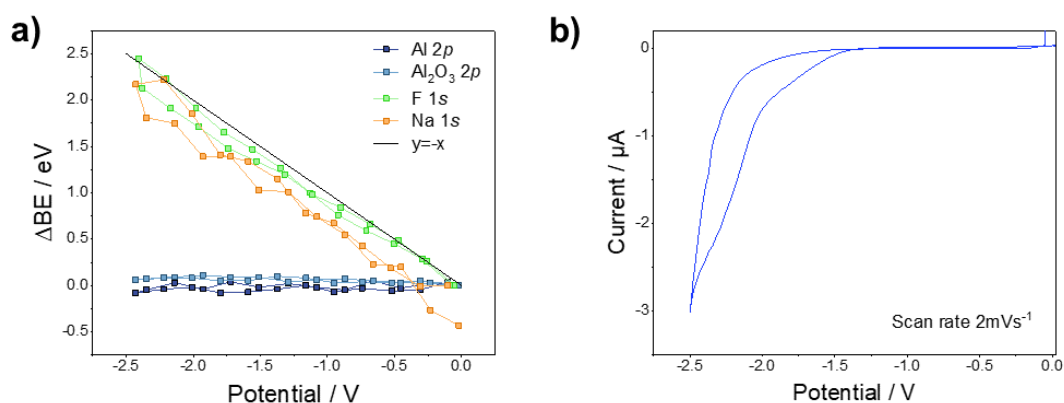
Figure 5.20. **a)** The changes in BE of the core level spectra during **b)** the operando CV measurement from 0 to -2.5 V.

The gradient of the BE shifts with the applied potential are easily visualised in **Figure 5.20a**, with close agreement to a shift of -1.0 eV/V. This is in agreement with the previous study on the [BMIM][TFSI] system and also with literature reports (see **Section 5.1**) and indicates bulk-like behaviour for the majority of IL species probed at the interface. The corresponding *operando* CV is plotted in **Figure 5.20b**, showing characteristic reduction currents. Again, there are some spectral changes during cycling because the XPS is also probing species formed at the electrode surface.
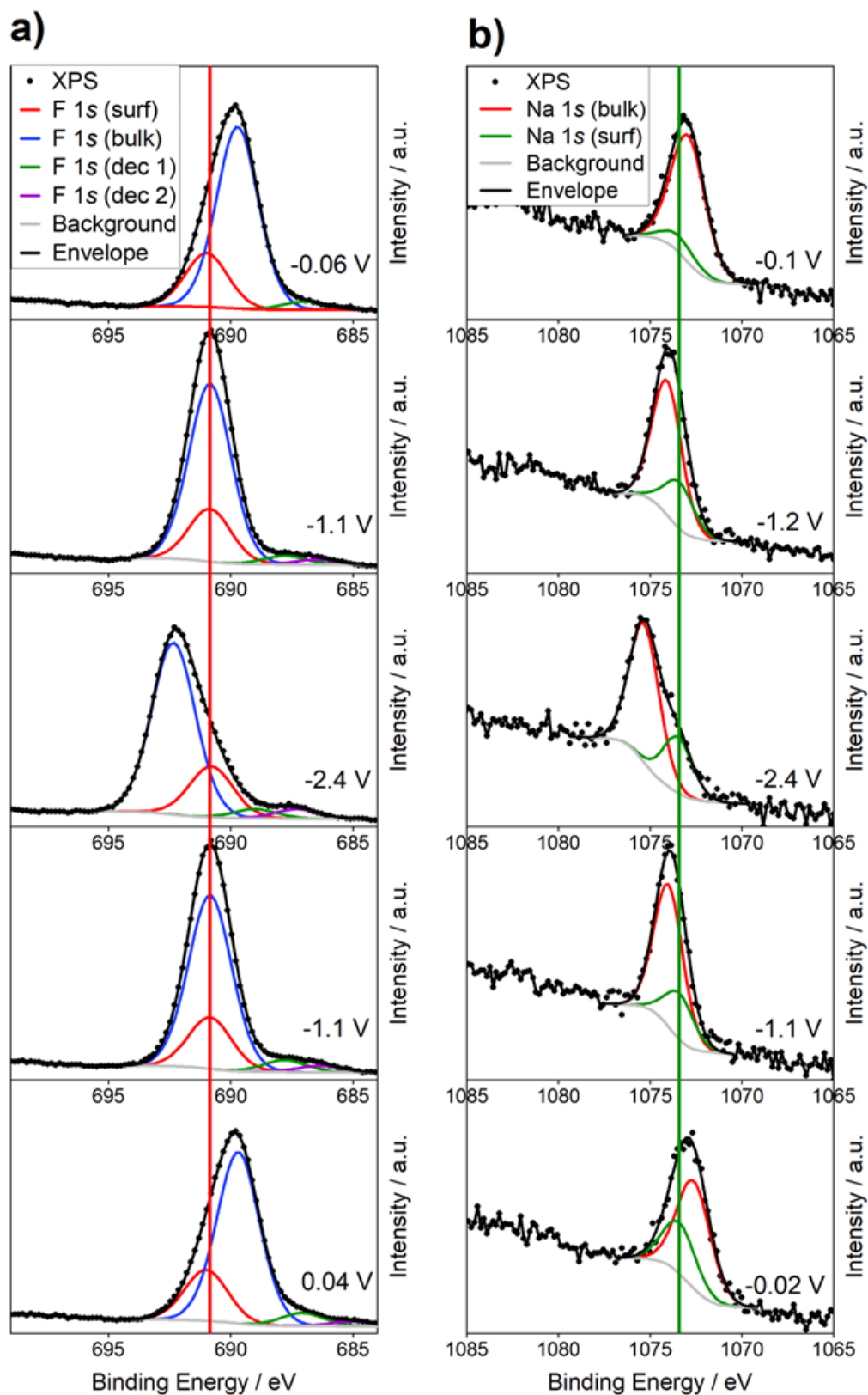
Figure 5.21. Operando XPS spectra recorded during CV measurements from 0 to -2.5 V, showing the **a)** F 1*s* and **b)** Na 1*s* spectra at different potentials. The vertical lines are added as a guide to eye, highlighting species that do not shift due to the applied potential, which are located at the electrode surface.

To investigate these changes in more detail, F $1s$ and Na $1s$ spectra collected at selected potentials are plotted in **Figure 5.21**. The F $1s$ curves have been deconvoluted to model species at the electrode surface (labelled surf) and species in the IL (labelled bulk). The surface species is likely inorganic, formed from decomposition of the IL and formation of the SEI. During cycling, the lower intensity region of the spectra may be fit with two components (denoted dec 1 and dec 2). These are likely to be additional decomposition products and are probably dissolved in the IL as they shift with the applied potential. Turning to the Na $1s$ spectra, a similar component model may be used to distinguish Na species dissolved in the IL (labelled bulk) and deposited at the surface of the electrode (labelled surf). As the cycling progresses, the proportion of the surface Na species increases, indicating growth of the SEI layer. These changes in the Na $1s$ and F $1s$ spectra correspond to irreversible electrochemical changes observed in the CV measurements.

5.4 Part V Conclusions

In **Part V**, XPS and electrochemistry techniques were performed in tandem, to obtain *operando* electrochemical XPS data. The [BMIM][TFSI] system was studied using a simple 3-electrode cell via *operando* electrochemical XPS. An Al WE, Pt CE, and Pt WE were connected via ~ 4 µL [BMIM][TFSI] on a glass slide. For this system, a CV scan rate of 2 mV s^{-1} was coupled with XPS snapshot acquisition time of ~ 7.5 s per core-level, allowing true *operando* measurements to be obtained. As expected, the potential variation of ~ 0.015 V during collection of each core-level did not result in any broadening of the spectra. This was evidenced by the FWHM of the spectra, which was the same in CA measurements, where a constant potential was applied, and the CV measurements. The FWHM was also the same for species measured at the IL centre, and at the WE/IL interface.

Decomposition of the [BMIM][TFSI] IL electrolyte was observed via the changing composition after CA measurements, and before and after CV measurements. New peaks appeared in F 1s and S 2p spectra, which can be attributed to this decomposition and formation of SEI species. This was observed at positive applied potentials. It is evident these species are formed at the grounded electrode because they do not experience any binding energy shift with the applied potential. For the [BMIM][TFSI] system, the binding energy shifts followed similar trends with the applied potential, whether measured using CA or CV techniques, illustrating that the slow CV scan rate of 2 mVs^{-1} is sufficient to allow the ions to respond. The main peaks in the IL centre and at the WE/IL interface follow the same trend, which indicates that the major IL species probed by XPS at the interface are behaving as bulk electrolyte.

The BE shifts in the [BMIM][TFSI] system exhibit non-Faradaic behaviour, particularly at application of positive potentials, or scanning in the positive to negative direction. This behaviour is also confirmed by the shape of the CV recorded under *operando* conditions. This is attributed to the asymmetric nature of the WE and CE, where the WE has a much larger SA,

180

which results in charge build up at the electrode. This can lead to a large capacitive current to flow and is likely the cause of this behaviour. The application of positive potential may be driving this build-up of charge, as the large [TFSI] anions are attracted to the WE and decompose, as evidenced by the additional peaks in the F 1s and S 2p spectra.

The [BMIM][TFSI]/NaTFSI system was studied using a second, more developed cell, in which a larger volume of IL was used (~ 30 µL) in a 3D printed basin, using the same electrode materials detailed above. The increased depth and volume of the IL meant that a much larger SA of the CE was in contact with the electrolyte, and a smaller relative SA of the WE. The BE shifts of the IL and Na species measured at the WE/IL interface in the [BMIM][TFSI]/NaTFSI system exhibited a ~ -1.0 eV/V shift, and the shape of the *operando* CV displays expected reduction characteristics on cycling from 0.0 to -2.5 V. During cycling, the appearance of new spectral features in the F 1s and Na 1s spectra is attributed to the formation of SEI species at the surface of the electrode. Although the peaks do not separate, due to the expected -1.0 eV/V shift, the fitted components for species at the electrode do not move with the applied potential, as was observed for the [BMIM][TFSI] system.

To summarise, an *operando* electrochemical XPS cell was designed and developed for the Thermo Fisher Nexsa G2 spectrometer. The system was used to study the behaviour of Na ions at the WE/IL interface under *operando* conditions, for the [BMIM][TFSI]/NaTFSI system. Optimised data acquisition methods were utilised for CV and XPS techniques, where a CV scan rate of 2 mVs^{-1} and fast snapshot XPS spectra collected at 10 s per core-level were able to monitor real-time electrochemical changes at the WE/IL interface.

Part VI – Summary & Outlook

In **Part II**, the use of DFT-simulated VB spectra has been evaluated for two different series of materials. Firstly, a metallic series is investigated consisting of three Group 11 coinage metals – Cu, Ag and Au. The second series involves three vacancy-ordered double perovskites with halide anions – Cs_2TeX_6 (X=Cl, Br, I). DFT-simulated spectra, using both PBEsol and HSE06 functionals, were fitted to experimental data using a least squares refinement method. Several parameters were optimised and evaluated in this way, including the spectral broadening and photoionization cross-section correction weightings. Additional theoretical corrections were also investigated in the Cs_2TeX_6 series, namely the inclusion of vdW and SOC effects. The effect of using different cross-section values were mainly consistent across both materials, with the modified YL* values providing the best agreement. In metals, the optimised Gaussian component of the spectral broadening is close to the nominal instrumental resolution of 0.4 eV. Optimised Gaussian broadening is significantly larger for the halide perovskites than the instrumental resolution (~1.2 eV) and was found to be material specific. Overall, across the materials studied, the DFT-simulated spectra largely reproduce the experimental data well when using the optimised spectral broadening and photoionization cross-section parameters and allows the evaluation of these parameters. However, it is possible that higher levels of theory would produce even better agreement, which could be an avenue of future work.

In **Part III**, the topic of spectral broadening is investigated by the effect of both charging and vibrational broadening contributions to core and VB line shapes as a function of temperature. This work comprises three case studies, encompassing a range of different materials: **i)** alkali halides, MX (M = Na, Cs; X = F, I), **ii)** bismuth oxy halides, BiOX (X = Cl, Br, I) and **iii)** a series of pure/niobium-doped strontium titanate single crystals, $SrTi_{(1-x)}Nb_xO_3$ (x = 0, 0.05, 0.5, 0.7). These materials were investigated using the VB fitting method, developed in **Part I**, in which the DFT-simulated

spectrum is fitted to the experimental data via the optimization of several parameters. The optimised Gaussian component at different temperatures was used to model the extent of vibrational broadening in the VB.

The temperature dependent behaviour varied between the different classes of materials and was found to be influenced by the size of the substituent ions, the band gap and conductivities of the materials, and other temperature induced changes in the surface structure. For the MX materials, the spectral broadening was found to arise from an interplay of increasing vibrational broadening due to thermal effects, with increasing vibrational amplitude for lighter ions, and increasing charging effects due to larger band gap materials with reduced conductivities. In BiOX materials, no charging effects were observed due to the higher conductivities seen in these materials, and the spectral broadening was found to depend solely on the size of the halide anion substituent. Again, the vibrational broadening increased with increasing temperature, with larger broadening seen for lighter halide substituents. For STO and Nb-doped STO compounds, the FWHM of core levels and the optimised Gaussian broadening in the VB was found to increase roughly linearly with √T, in agreement with theoretical phonon broadening. Although no charging effects in the form of spectral broadening were observed, charging was evidenced in the uncorrected BEs, and was found to depend on both the temperature and the Nb doping level of the samples. Charging effects decreased with increasing temperatures and increasing Nb doping, due to higher conductivities. Notably, the optimised VB Gaussian broadening in the Nb-STO series has a similar magnitude to the broadening exhibited in the O 1s spectra. As the valence DOS is mainly located on the O site, this could explain the similar temperature-dependent broadening behaviour. It is therefore possible that broadening the O pDOS more than the Sr and Ti pDOS could be justified in an alternative broadening optimisation method and would be an interesting topic for future research.

In **Part IV**, the methodology of refining DFT-simulated spectra for the analysis of VB XPS spectra used in **Parts II-III** is extended to the modelling of mixed phase systems. This is applied to the quantitative mapping of mixed phase TiO_2 surfaces, using DFT-simulated spectra derived from PBEsol DOS. Similarly to the case of STO in **Part III**, the YL and YL* photoionization cross-section values were not found to well reproduce the experimental VB structure, and were thus optimised further. A large contribution from the Ti p component was found necessary to reproduce the XPS VB, which was also the case for STO. As was found for all other non-metallic materials studied in **Parts II-III**, the optimised Gaussian broadening was much larger than the nominal experimental resolution. Spectra simulated for low index surfaces of anatase using a slab/vacuum model did not show significant differences to the bulk structure calculations after application of optimised broadening and cross-section parameters.

The mixed-phase XPS/DFT fitting model was applied to mapping the surface phase fraction on the mixed-phase films, with clear identification of the rutile-rich regions. Use of an empirical method, where experimental VB were used as the reference spectra, resulted in close agreement to the compositions predicted by the DFT model. Spatially resolved photocatalytic activity was measured using photocatalytic reduction of a resazurin-based *smart ink*, which highlighted the same rutile-rich areas as evidenced by XPS and DFT analysis. Therefore, a clear connection was established between the XPS/DFT determined phase fraction and the experimentally determined photocatalytic activity, allowing large scale mapping using the two complementary techniques. This could be extended to include pixel-by-pixel analysis, combined with a smaller x-ray spot size, to obtain higher spatial resolution. The activity was also suspected to arise from additional factors other than the composition alone, such as film thickness and morphology, and ink thickness, which could form the basis of future investigations.

In **Part V**, an *operando* electrochemical XPS cell was designed and developed for the Thermo Fisher Nexsa G2 spectrometer, where XPS and electrochemistry techniques were performed in tandem. Optimised data acquisition methods were utilised for CV and XPS techniques, where a CV scan rate of 2 mVs^{-1} and fast snapshot XPS spectra collected at 10 s per core-level were able to monitor real-time electrochemical changes at the WE/IL interface. Initially, the IL electrolyte [BMIM][TFSI] was studied in a simple 3-electrode cell on a glass slide, using an Al WE, Pt RE and Pt CE. Decomposition of the [BMIM][TFSI] IL electrolyte was observed via a change in composition after CA measurements, and before and after CV measurements. New peaks appeared in F 1*s* and S 2*p* spectra, which can be attributed to this decomposition and formation of SEI species. Non-Faradaic behaviour was observed at positive potentials, which coincided with the increased decomposition of the IL. The capacitive current is suggested to arise from the build-up of charge and could also be influenced by the asymmetric SA of the WE and RE.

The [BMIM][TFSI]/NaTFSI system was studied using a second, more developed cell, in which a larger volume of IL was used (~ 30 μL) in a 3D printed basin, using the same electrode materials detailed above. The increased depth and volume of the IL meant that a much larger SA of the CE was in contact with the electrolyte, and a smaller relative SA of the WE. The BE shifts of the IL and Na species measured at the WE/IL interface exhibited a ~ -1.0 eV/V shift, and the shape of the *operando* CV displayed expected reduction characteristics on cycling from 0.0 to -2.5 V. During cycling, the appearance of new spectral features in the F 1*s* and Na 1*s* spectra is attributed to the formation of SEI species at the surface of the electrode. Future work on *operando* measurements could include more advanced WE materials with relevant applications in Na ion batteries, and a range of different IL electrolytes to evaluate compatibility and stability.

Author Contributions

Part III

Mark Isaacs helped with temperature dependent XPS experiments.

Part IV

Joe Willis helped with getting started on DFT calculations.

Raul Quesada-Cabrera synthesised the thin film samples and assisted with photocatalysis measurements and analysis.

Part V

Ionic liquids were synthesised by Yutong Shen and Avishek Dey.

The [BMIM][TFSI]/NaTFSI *operando* XPS measurements were performed with Tim Nunney and Avishek Dey at Thermo Fisher Scientific.

Appendix A

PXRD data, refinement, and figure for Cs_2TeX_6 compounds by Yuhan Liu

List of Figures

List of Tables

Table D1 Measured binding energies of the ILs in this study in four different environments.

Table D2. Estimated errors for the fitted BE and FWHM C 1s, N 1s, and F 1s BE peak parameters for the series of ionic liquids.

Table D3. Estimated errors for the fitted BE and FWHM C 1s, N 1s, F 1s and O 1s BE peak parameters for the preliminary glass cell measurements.

Table D4. Estimated errors for the fitted FWHM F 1s BE peak parameter during various *in-situ* and *operando* measurements.

Appendix A

Table A1. The experimental binding energies tabulated by Trzhaskovskaya and Yarzhemsky A(TY),[90] for the elements Cu, Ag and Au. In the case of orbitals that exhibit spin-orbit splitting, the lower binding energy peak is reported. Orbitals with binding energies $> \sim 10$ eV (indicated by the shaded rows) were modified using the 'ratio' method. This involves multiplying together a cross-section value for the element of interest, with the ratio of two cross-section values for the next heaviest element with appropriate filled orbitals. The orbitals used in the 'ratio' method calculation, and the input values from Yeh and Lindau (YL),[84] are detailed in the following rows. The output of the 'ratio' method calculation (the modified YL* value) is listed in **Table 2.2** in **Part II**.

	Cu		Ag		Au	
Experimental Binding Energy (TY) / eV	4s	1.2	5s	8.0	6s	9.0
	3p$_{3/2}$	**72.8**	**4p$_{3/2}$**	**55.9**	**5p$_{3/2}$**	**56.9**
	3d$_{5/2}$	1.5	4d$_{5/2}$	3.1	5d$_{5/2}$	1.8
Ratio method calculation	$Cu\ 4p \cong Cu\ 4s \times \dfrac{Ge\ 4p}{Ge\ 4s}$		$Ag\ 5p \cong Ag\ 5s \times \dfrac{Sn\ 5p}{Sn\ 5s}$		$Au\ 6p \cong Au\ 6s \times \dfrac{Tl\ 6p}{Tl\ 6s}$	
Ratio method input values (YL)	$Cu\ 4p \cong$ 2.70E-04 x 1.33E-04		$Ag\ 5p \cong$ 2.90E-04 x 1.86E-04		$Au\ 6p \cong$ 2.90E-04 x 1.34E-04	

Table A2. The experimental binding energies tabulated by Trzhaskovskaya and Yarzhemsky (TY),[90] for the elements Cs,Te, Cl, Br and I. In the case of orbitals that exhibit spin-orbit splitting, the lower binding energy peak is reported. Orbitals with binding energies > ~ 10 eV (indicated by the shaded rows) were modified using the 'ratio' method. This involves multiplying together a cross-section value for the element of interest, with the ratio of two cross-section values for the next heaviest element with appropriate filled orbitals. The orbitals used in the 'ratio' method calculation, and the input values from Yeh and Lindau (YL),[84] are detailed in the following rows. The output of the 'ratio' method calculation (the modified YL* value) is listed in **Table 2.5** in **Part II**. Note that although the Cs 6*s* binding energy is within the VB region, there is no YL value for Cs 6*s*, therefore it is also estimated.

	Cs		Te		Cl		Br		I	
Experimental Binding Energy (TY)	6s	4.0	**5s**	**11.6**	**3s**	**17.5**	**4s**	**27.3**	**5s**	**13.6**
	5p₃/₂	**11.4**	5p₃/₂	2.0	3p₃/₂	6.7	4p₃/₂	4.6	5p₃/₂	2.9
	4d₅/₂	**76.5**	**4d₅/₂**	**39.2**			**3d₅/₂**	**69.0**	**4d₅/₂**	**48.9**
Ratio method calculation	$Cs\,6s$ $\cong Cs\,5s$ $\times \dfrac{La\,6s}{La\,5s}$		$Te\,6s$ $\cong Te\,5s$ $\times \dfrac{Ba\,6s}{Ba\,5s}$		$Cl\,4s$ $\cong Cl\,3s$ $\times \dfrac{Ca\,4s}{Ca\,3s}$		$Br\,5s$ $\cong Br\,4s$ $\times \dfrac{Sr\,5s}{Sr\,4s}$		$I\,6s$ $\cong I\,5s$ $\times \dfrac{Ba\,6s}{Ba\,5s}$	
	$Cs\,6p$ $\cong Cs\,5p$ $\times \dfrac{Tl\,6p}{Tl\,5p}$									
	$Cs\,5d$ $\cong Cs\,5s$ $\times \dfrac{La\,5d}{La\,5s}$		$Te\,5d$ $\cong Te\,5s$ $\times \dfrac{La\,5d}{La\,5s}$				$Br\,4d$ $\cong Br\,4s$ $\times \dfrac{Y\,4d}{Y\,4s}$		$I\,5d$ $\cong I\,5s \times \dfrac{La\,5d}{La\,5s}$	
Ratio method input values (YL)	$Cs\,6s \cong$ 1.250E-03 x 8.79E-02		$Te\,6s \cong$ 8.500E-04 x 7.931E-02		$Cl\,4s \cong$ 1.25E-03 x 6.596E-02		$Br\,5s \cong$ 1.25E-03 x 7.692E-02		$I\,6s \cong$ 9.500E-04 x 7.931E-02	
	$Cs\,6p \cong$ 9.667E-04 x 4.85E-02									
	$Cs\,5d \cong$ 1.250E-03 x 4.606E-01		$Te\,5d \cong$ 8.500E-04 x 4.606E-01				$Br\,4d \cong$ 1.25E-03 x 2.000E-01		$I\,5d \cong$ 9.500E-04 x 4.606E-01	
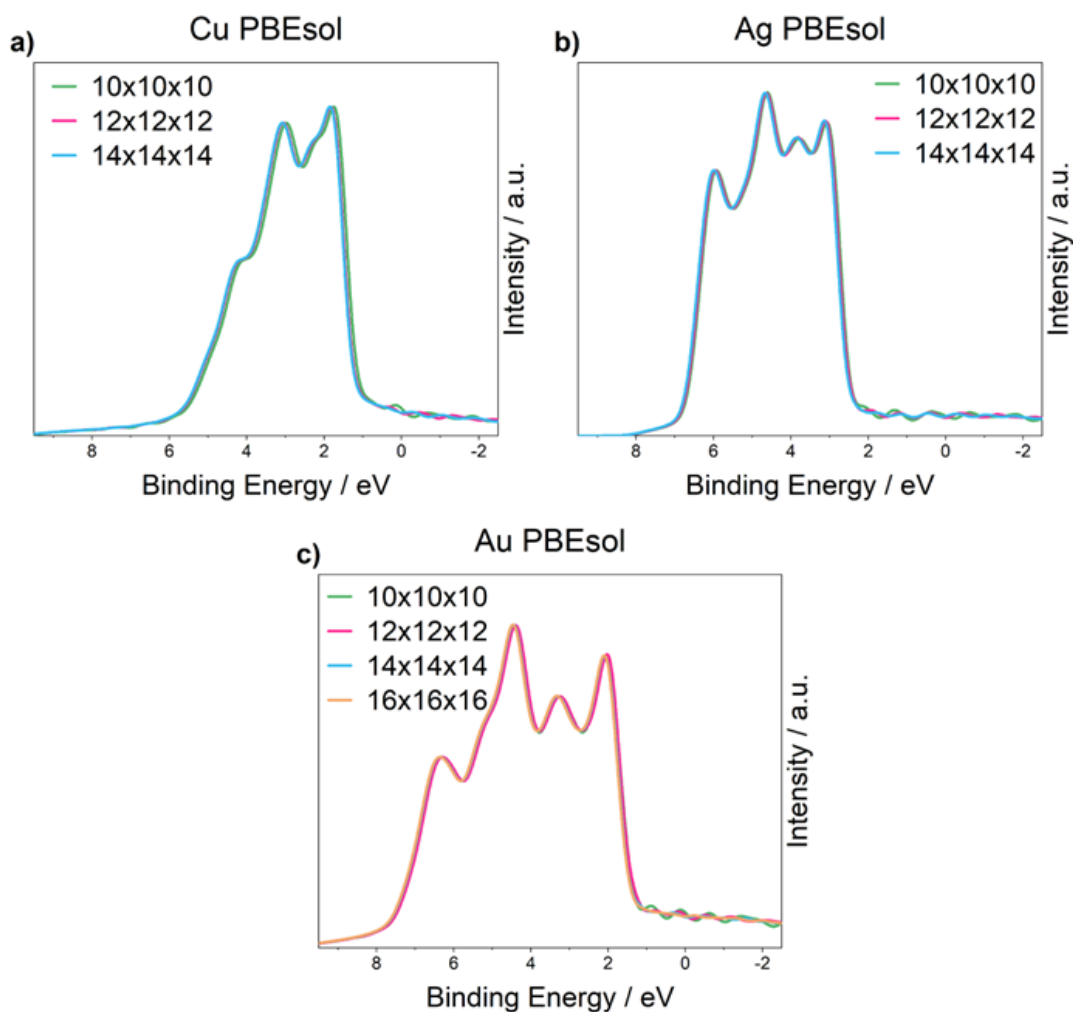
Figure A1. Convergence of the k-point density with respect to the appearance of the broadened valence density of states for the metals **a)** Cu, **b)** Ag and **c)** Au. All electronic structure calculations were performed using PBEsol following geometry optimisation.

Table A3. Elemental quantification from XPS survey spectra for the selected materials Cs_2TeX_6, X = Cl, Br, I, showing small concentrations of impurities.

Sample Identifier	Name	Position	FWHM / eV	Raw Area	%At Conc
Cs_2TeCl_6	O 1s	532.06	3.29	138401.4	10.17
	C 1s	285.29	2.98	180958.7	34.67
	Cl 2p	199.02	3.19	475970.3	38.70
	Cs 3d	724.32	2.29	1714021	10.51
	Te 3d	576.64	2.30	720076	5.21
	Sn 3d	487.63	2.22	64430.15	0.54
	I 3d	619.18	2.17	29234.46	0.20
Cs_2TeBr_6	O 1s	532.53	3.00	174943.5	12.33
	C 1s	285.35	2.82	215695	39.64
	Cs 3d	724.41	2.28	1733918	10.20
	Br 3p	182.43	3.15	929000.8	32.73
	Te 3d	576.23	2.38	583978.9	4.05
	I 3d	619.51	2.39	92383.51	0.60
	Sn 3d	487.9	2.44	54690.16	0.44
Cs_2TeI_6	O 1s	532.49	2.90	155590.9	17.97
	C 1s	285.4	2.74	163692.8	49.30
	I 3d	619.2	2.35	1841934	19.58
	Cs 3d	724.53	2.24	914686.2	8.82
	Te 3d	575.32	2.49	343317.6	3.90
	Sn 3d	487.76	2.35	33399.81	0.44
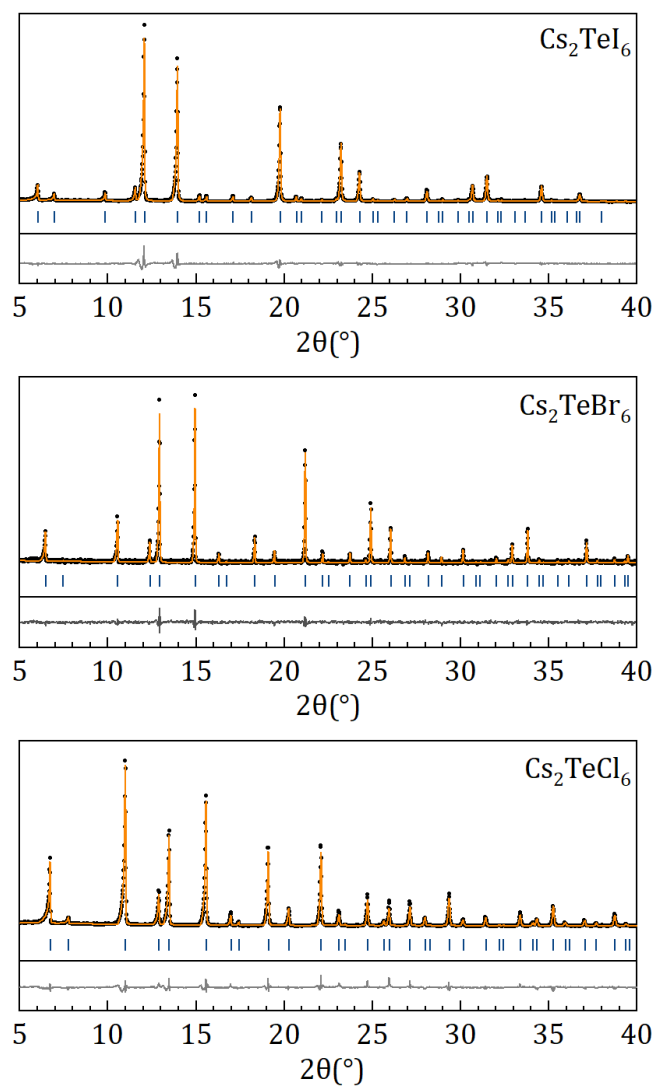
Figure A2. PXRD data collected for Cs_2TeX_6 (X = Cl, Br, I) samples synthesised via the same method used in this work. Sample synthesis, data collection, refinement, and figure by Yuhan Liu.
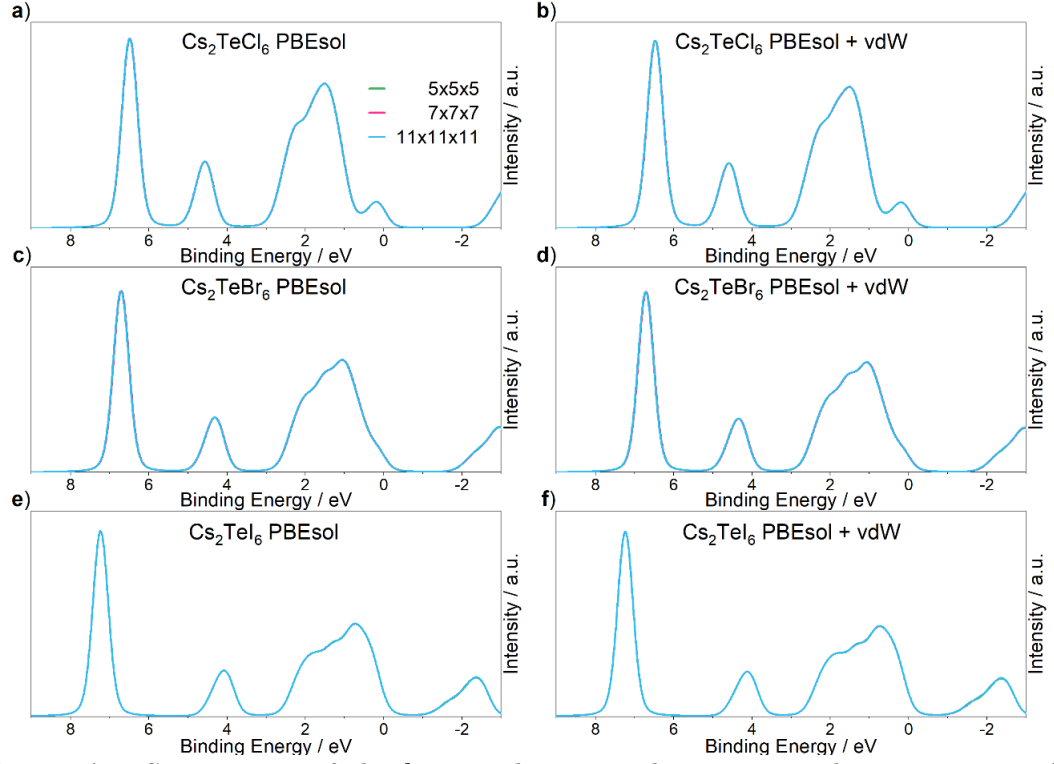
Figure A3. Convergence of the k-point density with respect to the appearance of the broadened valence density of states for the materials Cs_2TeX_6, **(a,b)** X = Cl, **(c,d)** X = Br, **(e,f)** X = I. The electronic structure calculations were performed on the optimised geometries obtained by PBEsol (left column) and PBEsol + vdW (right column).

Figure A4. Convergence of the k-point density with respect to the appearance of the broadened valence density of states for the materials Cs_2TeX_6, **(a,b)** X = Cl, **(c,d)** X = Br, **(e,f)** X = I. The electronic structure calculations were performed on the optimised geometries obtained by HSE06 (left column) and HSE06 + vdW (right column).
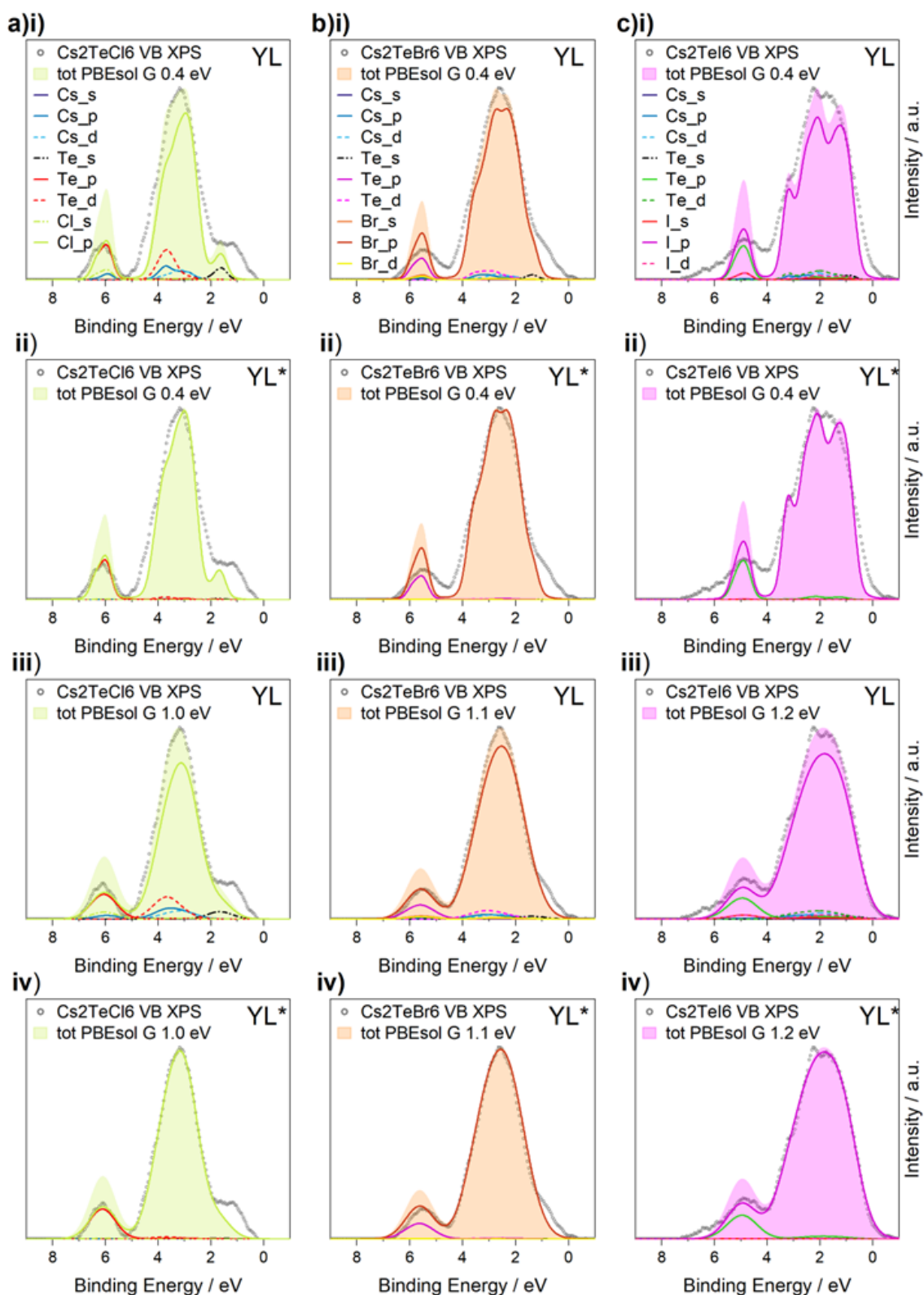
Figure A5. VB XPS spectra for the series of Cs_2TeX_6 compounds **(a-c)** X = Cl, Br, I, fitted with PBEsol DFT simulated spectra. The calculated DOS broadened by the nominal instrumental resolution of 0.4 eV and corrected by **i)** YL cross-sections, **ii)** modified YL cross-sections (YL*). The Gaussian component of the broadening optimised for **iii)** YL and **iv)** YL*

Appendix B

Table B1. The experimental binding energies tabulated by Trzhaskovskaya and Yarzhemsky (TY),[90] for the elements Na, Cs, F and I. In the case of orbitals that exhibit spin-orbit splitting, the lower binding energy peak is reported. Orbitals with binding energies > ~ 10 eV (indicated by the shaded rows) were modified using the 'ratio' method. This involves multiplying together a cross-section value for the element of interest, with the ratio of two cross-section values for the next heaviest element with appropriate filled orbitals. The orbitals used in the 'ratio' method calculation, and the input values from Yeh and Lindau (YL),[84] are detailed in the following rows. The output of the 'ratio' method calculation (the modified YL* value) is listed in **Table 3.2** in **Part III**.

|	Na		Cs		F		I	
Experimental Binding Energy (TY)	3s	0.7	6s	4.0	**2s**	**34.0**	**5s**	**13.6**
	2p₃/₂	**31.0**	**5p₃/₂**	**11.4**	2p₃/₂	8.7	5p₃/₂	2.9
			4d₅/₂	**76.5**			**4d₅/₂**	**48.9**
Ratio method calculation			$Cs\ 6s \cong Cs\ 5s \times \dfrac{La\ 6s}{La\ 5s}$		$F\ 3s \cong F\ 2s \times \dfrac{Na\ 3s}{Na\ 2s}$		$I\ 6s \cong I\ 5s \times \dfrac{Ba\ 6s}{Ba\ 5s}$	
	$Na\ 3p \cong Na\ 2p \times \dfrac{Al\ 3p}{Al\ 2p}$		$Cs\ 6p \cong Cs\ 5p \times \dfrac{Tl\ 6p}{Tl\ 5p}$					
			$Cs\ 5d \cong Cs\ 5s \times \dfrac{La\ 5d}{La\ 5s}$				$I\ 5d \cong I\ 5s \times \dfrac{La\ 5d}{La\ 5s}$	
Ratio method input values (YL)			$Cs\ 6s \cong$ 1.250E-03 x 8.79E-02		$F\ 3s \cong$ 1.400E-03 x 3.344E-02		$I\ 6s \cong$ 9.500E-04 x 7.931E-02	
	$Na\ 3p \cong$ 4.167E-04 x 4.917E-02		$Cs\ 6p \cong$ 9.667E-04 x 4.85E-02					
			$Cs\ 5d \cong$ 1.250E-03 x 4.606E-01				$I\ 5d \cong$ 9.500E-04 x 4.606E-01	
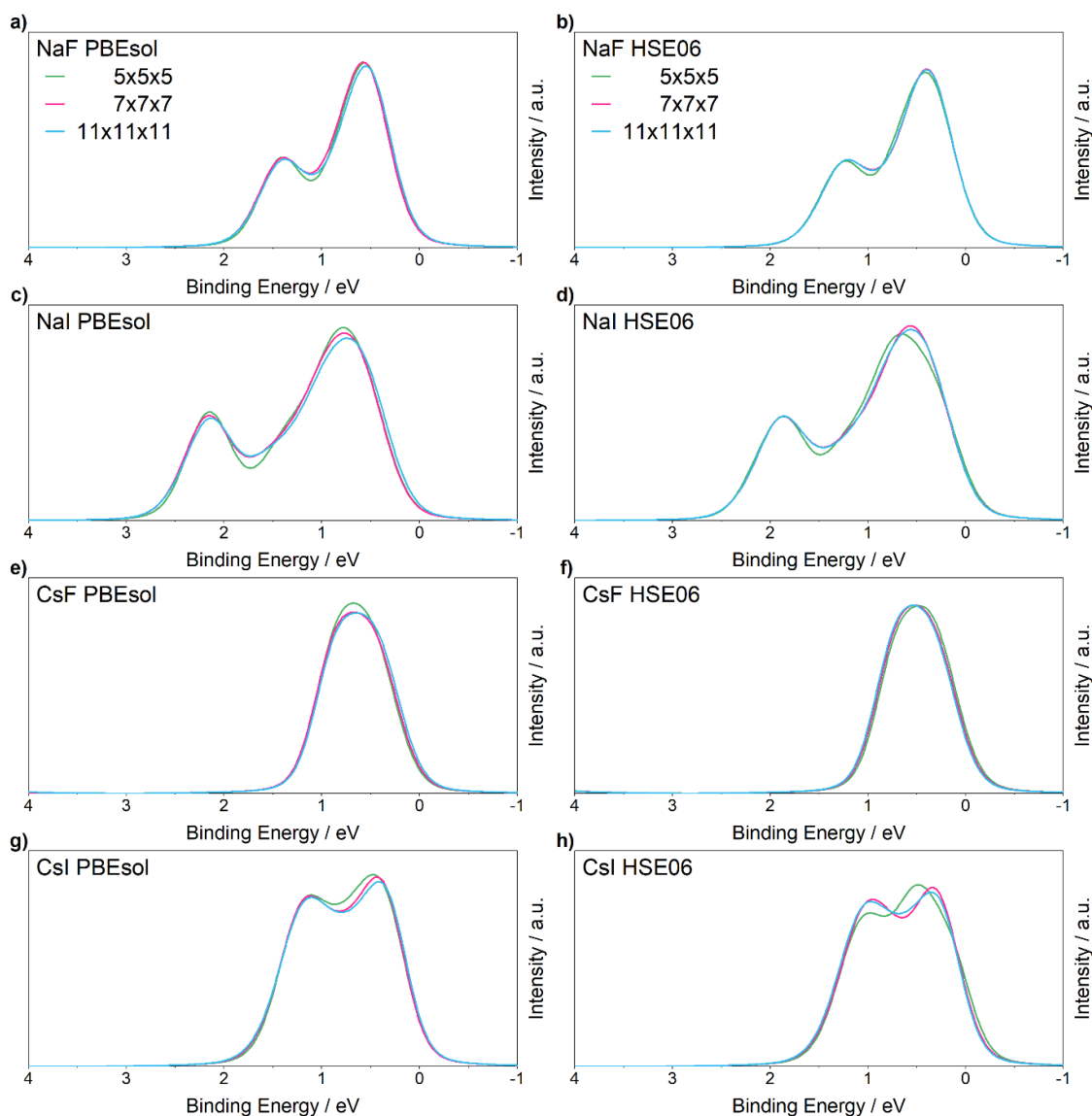
Figure B1. Convergence of the k-point density with respect to the appearance of the broadened valence density of states for the materials **a,b)** NaF **c,d)** NaI **e,f)** CsF and **g,h)** CsI. The electronic structure calculations were performed using PBEsol (left column) and HSE06 (right column) functionals.
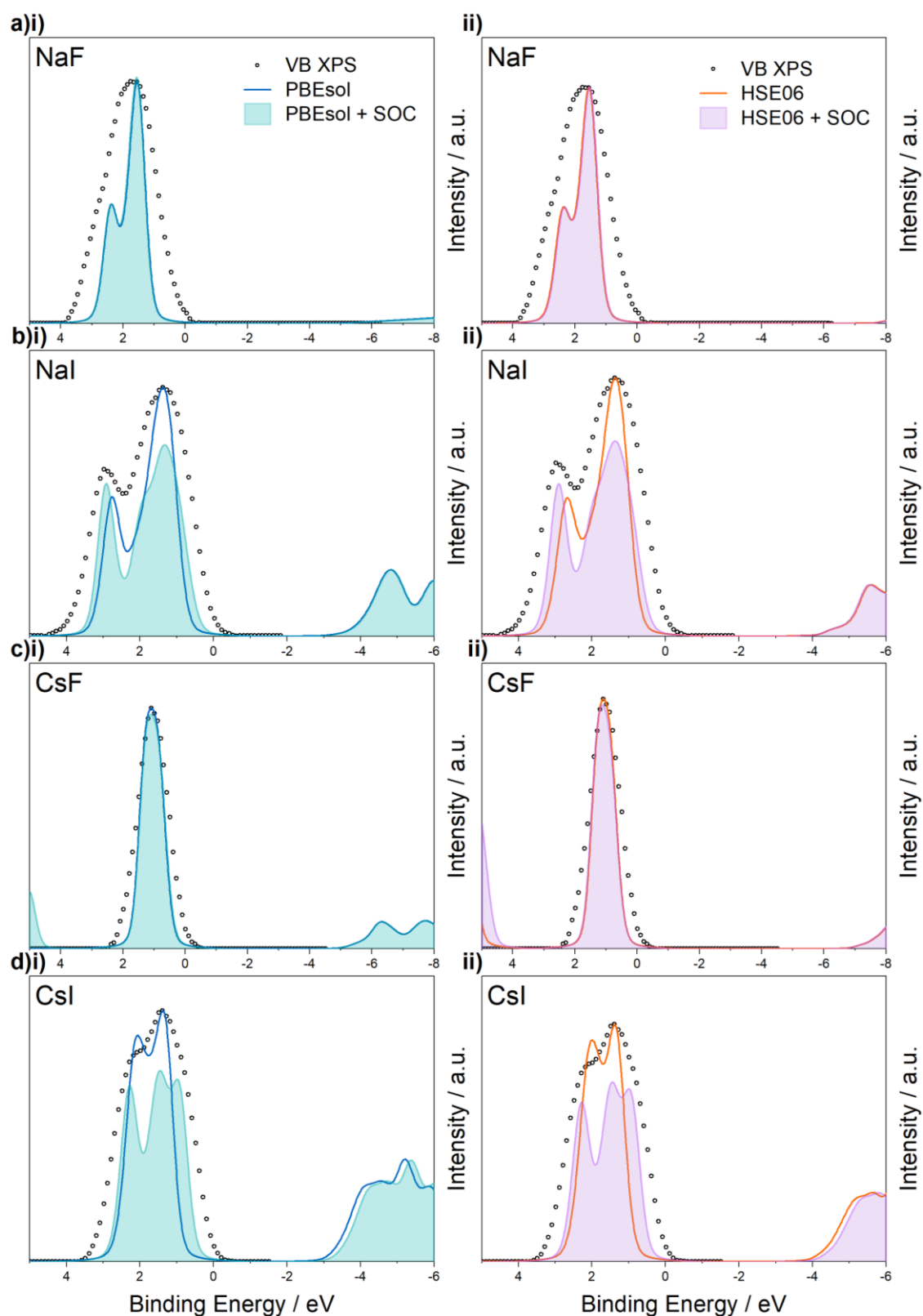
Figure B2. VB XPS spectra for the series of MX compounds **a)** NaF, **b)** NaI, **c)** CsF, and **d)** CsI, together with DFT calculated DOS using **i)** PBEsol and **ii)** HSE06 functionals with and without including SOC effects. The experimental VB is normalised to the VB spectral maximum of plain **i)** PBEsol and **ii)** HSE06 and shifted to align with the theoretical DOS, which are broadened by the nominal instrumental resolution of 0.4 eV. The SOC DOS are also shifted slightly for comparison with the XPS VB. The calculated bandgap is smaller using PBEsol than HSE06. Inclusion of SOC narrows the bandgap.

Table B2. Estimated errors for the fitted FWHM peak parameters in the temperature dependent core level XPS data for the series of MX compounds (M = Na, Cs; X = F, I). The errors have been estimated via Monte Carlo simulations using CasaXPS software. In this approach, the software simulates multiple (200) measurements by adding synthetic noise to the peak model, and then evaluating the stability of the model to give an estimate of the errors associated with the fitted peak parameters.The errors are given in eV to 1 s.f.

Temp / °C	NaF (F)	NaI (I)	CsF (F)	CsI (I)
-115	0.02	0.009	0.02	0.005
-60	0.02	0.007	0.02	0.005
20	0.008	0.01	0.01	0.003
100	0.01	0.005	0.03	0.005
180	0.008	0.009	0.02	

Temp / °C	NaF (Na)	NaI (Na)	CsF (Cs)	CsI (Cs)
-115	0.01	0.02	0.005	0.005
-60	0.01	0.02	0.005	0.005
20	0.007	0.03	0.004	0.004
100	0.01	0.02	0.006	0.006
180	0.009	0.02	0.007	0.004

Table B3. The experimental binding energies tabulated by Trzhaskovskaya and Yarzhemsky (TY),[90] for the elements Bi, O, Cl, Br, and I. In the case of orbitals that exhibit spin-orbit splitting, the lower binding energy peak is reported. Orbitals with binding energies > ~ 10 eV (indicated by the shaded rows) were modified using the 'ratio' method. This involves multiplying together a cross-section value for the element of interest, with the ratio of two cross-section values for the next heaviest element with appropriate filled orbitals. The orbitals used in the 'ratio' method calculation, and the input values from Yeh and Lindau (YL),[84] are detailed in the following rows. The output of the 'ratio' method calculation (the modified YL* value) is listed in **Table 3.6** in **Part III**.

|	Bi	O	Cl	Br	I
Experimental Binding Energy (TY)	6s　　7.5	**2s　　23.7**	**3s　　17.5**	**4s　　27.3**	**5s　　13.6**
	$6p_{3/2}$　　0.2	$2p_{3/2}$　　7.4	$3p_{3/2}$　　6.7	$4p_{3/2}$　　4.6	$5p_{3/2}$　　2.9
	$5d_{5/2}$　24.4			**$3d_{5/2}$　69.0**	**$4d_{5/2}$　48.9**
Ratio method calculation		$O\ 3s$ $\cong O\ 2s$ $\times \dfrac{Na\ 3s}{Na\ 2s}$	$Cl\ 4s$ $\cong Cl\ 3s$ $\times \dfrac{Ca\ 4s}{Ca\ 3s}$	$Br\ 5s$ $\cong Br\ 4s$ $\times \dfrac{Sr\ 5s}{Sr\ 4s}$	$I\ 6s$ $\cong I\ 5s$ $\times \dfrac{Ba\ 6s}{Ba\ 5s}$
	$Bi\ 6d$ $\cong Bi\ 6s$ $\times \dfrac{Ac\ 6d}{Ac\ 6s}$			$Br\ 4d$ $\cong Br\ 4s$ $\times \dfrac{Y\ 4d}{Y\ 4s}$	$I\ 5d$ $\cong I\ 5s \times$ $\dfrac{La\ 5d}{La\ 5s}$
Ratio method input values (YL)		$O\ 3s \cong$ 9.50E-04 x 3.34E-02	$Cl\ 4s \cong$ 1.25E-03 x 6.596E-02	$Br\ 5s \cong$ 1.25E-03 x 7.692E-02	$I\ 6s \cong$ 9.500E-04 x 7.931E-02
	$Bi\ 6d \cong$ 6.50E-04 x 5.333E-01			$Br\ 4d \cong$ 1.25E-03 x 2.000E-01	$I\ 5d \cong$ 9.500E-04 x 4.606E-01
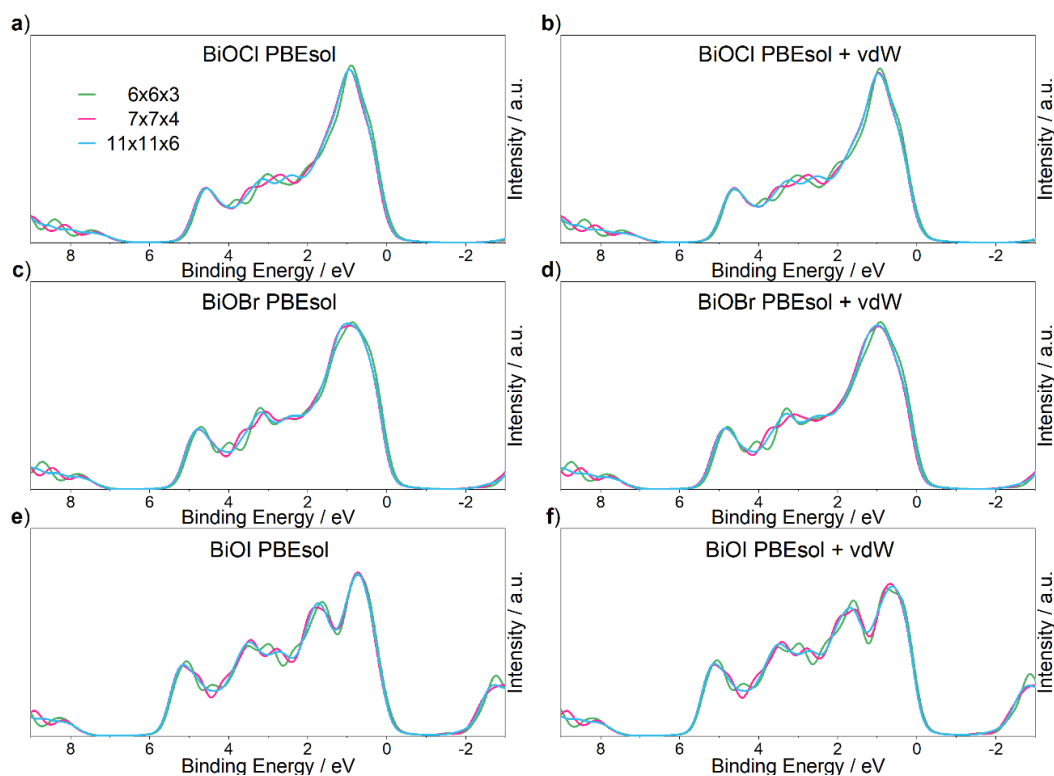
Figure B3. Convergence of the k-point density with respect to the appearance of the broadened valence density of states for the materials BiOX, **(a,b)** X = Cl, **(c,d)** X = Br, **(e,f)** X = I. The electronic structure calculations were performed on the optimised geometries obtained by PBEsol (left column) and PBEsol + vdW (right column).
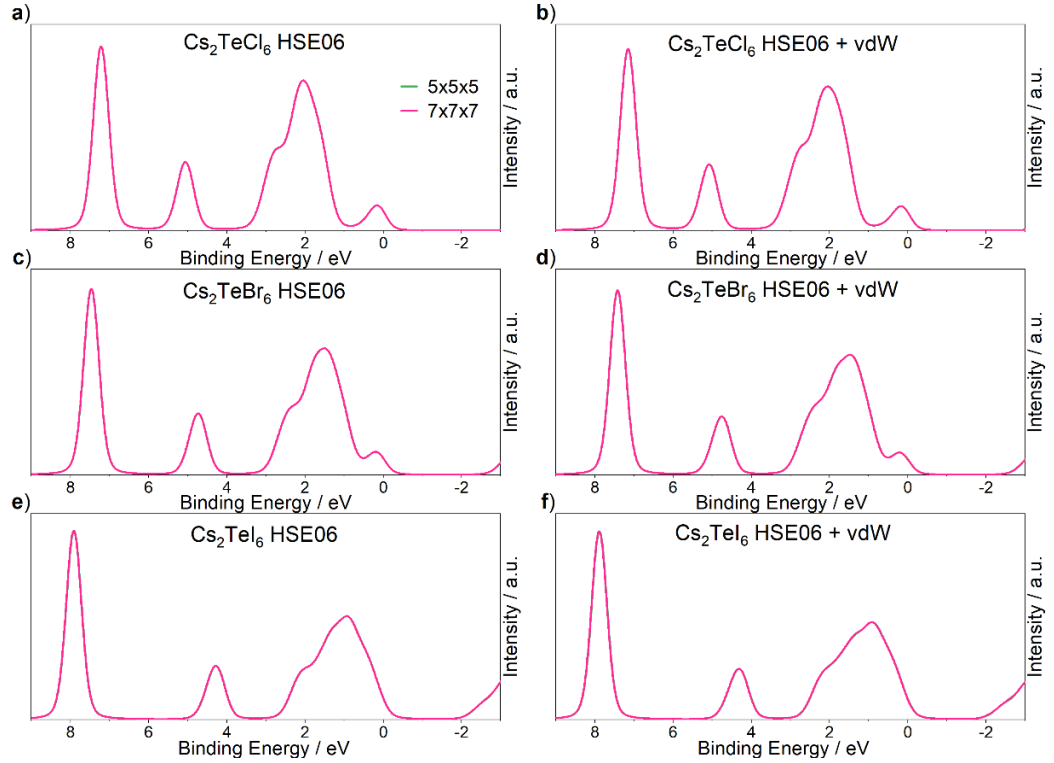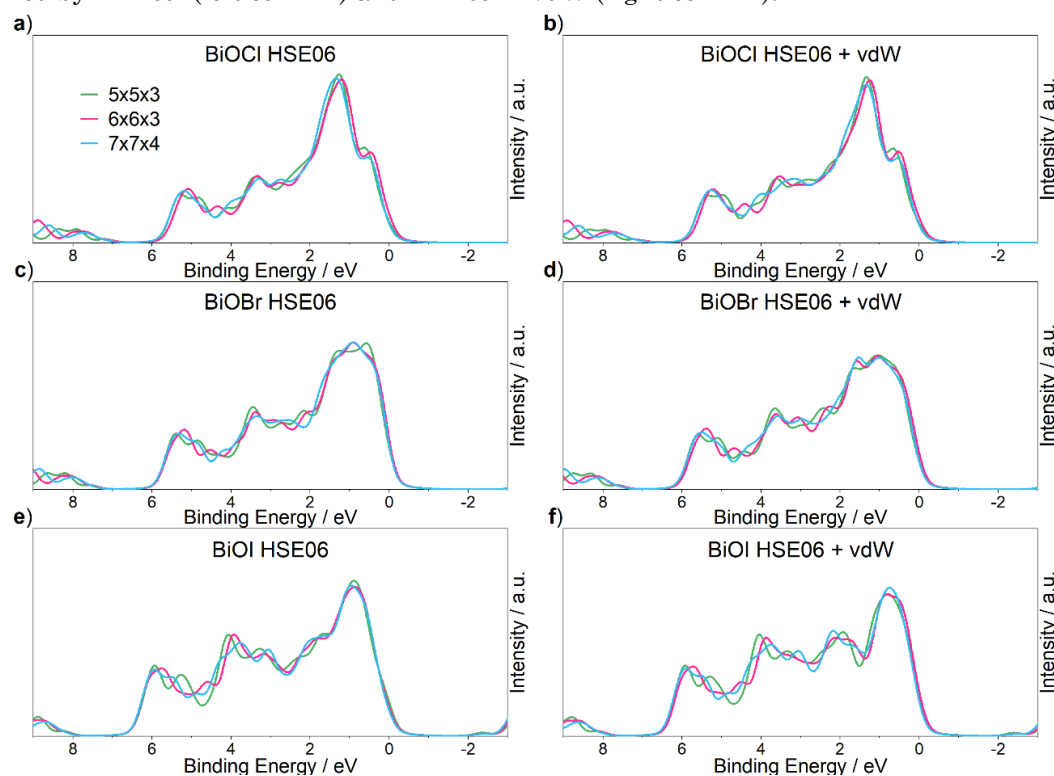

Figure B4. Convergence of the k-point density with respect to the appearance of the broadened valence density of states for the materials BiOX, **(a,b)** X = Cl, **(c,d)** X = Br, **(e,f)** X = I. The electronic structure calculations were performed on the optimised geometries obtained by HSE06 (left column) and HSE06 + vdW (right column).
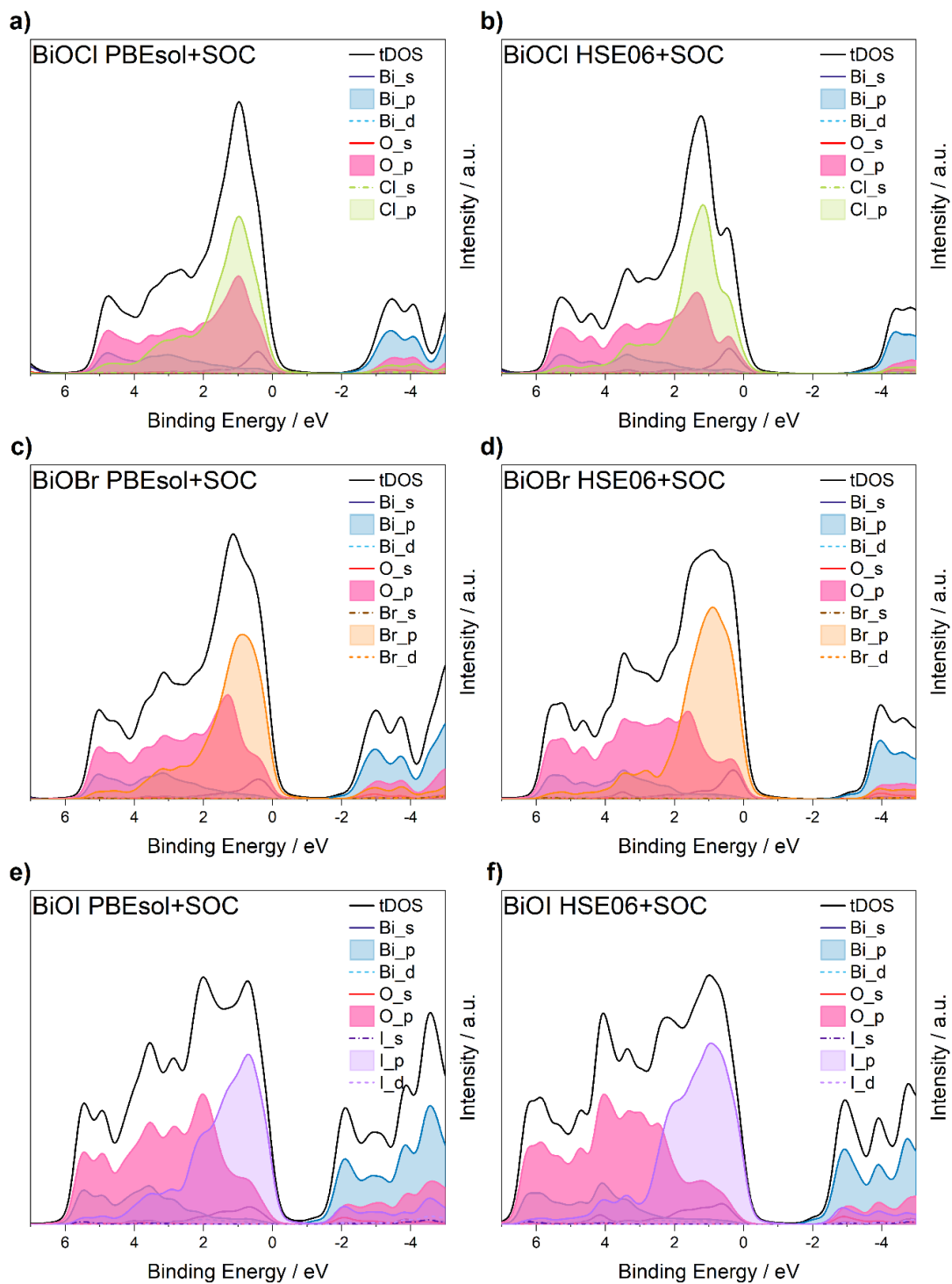
Figure B5. Orbital projected DOS (pDOS) for the materials BiOX, **(a,b)** X = Cl, **(c,d)** X = Br, **(e,f)** X = I. The electronic structure calculations were performed on the optimised geometries obtained by PBEsol + SOC (left column) and HSE06 + SOC (right column).

Table B4. Estimated errors for the fitted BE and FWHM peak parameters in the temperature dependent core level XPS data for the series of BiOX compounds (X = Cl, Br, I). The errors have been estimated via Monte Carlo simulations using CasaXPS software. In this approach, the software simulates multiple (200) measurements by adding synthetic noise to the peak model, and then evaluating the stability of the model to give an estimate of the errors associated with the fitted peak parameters. The errors are given in eV to 1 s.f.

Temp / °C	BiOCl Bi 4f FWHM	BiOBr Bi 4f FWHM	BiOI Bi 4f FWHM
-115	0.005	0.005	0.007
-60	0.005	0.007	0.007
20	0.006	0.006	0.005
100	0.008	0.01	0.01
180	0.007	0.008	0.005

Temp / °C	BiOCl Cl 2p FWHM	BiOBr Br 3d FWHM	BiOI I 3d FWHM
-115	0.04	0.02	0.01
-60	0.03	0.02	0.02
20	0.05	0.04	0.009
100	0.05	0.1	0.02
180	0.05	0.04	0.01

Temp / °C	BiOCl Bi 4f BE	BiOBr Bi 4f BE	BiOI Bi 4f BE
-115	0.003	0.003	0.004
-60	0.003	0.004	0.004
20	0.003	0.004	0.003
100	0.005	0.007	0.006
180	0.004	0.004	0.003
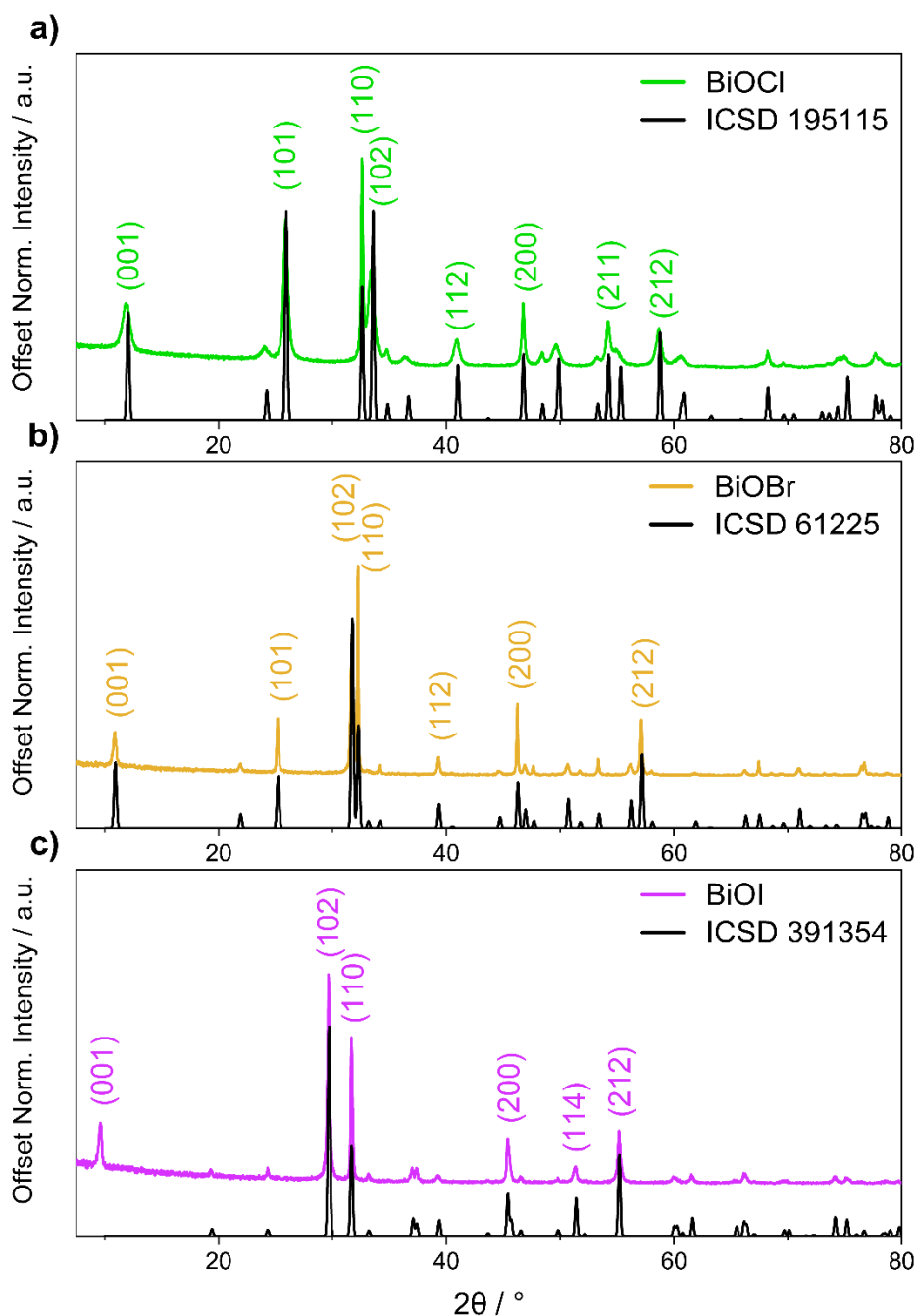
Figure B6. PXRD patterns for the BiOX compounds synthesised in this work, X = **a)** Cl, **b)** Br, and **c)** I. The diffraction peaks can be well indexed to the pure tetragonal BiOCl, BiOBr and BiOI phases,[155] and are in good agreement with reference patterns ICSD 195115,[156] 61225,[157] and 391354,[158] respectively. Note that the BiOI reference pattern begins after 2θ = 10°, therefore the (001) signal is absent.

Table B5. The experimental binding energies tabulated by Trzhaskovskaya and Yarzhemsky (TY),[90] for the elements Sr, Ti and O. Orbitals with binding energies > ~ 10 eV (indicated by the shaded rows) were modified using the 'ratio' method. This involves multiplying together a cross-section value for the element of interest, with the ratio of two cross-section values for the next heaviest element with appropriate filled orbitals. The orbitals used in the 'ratio' method calculation, and the input values from Yeh and Lindau (YL),[84] are detailed in the following rows. The output of the 'ratio' method calculation (the modified YL* value) is listed in **Table 3.9** in **Part III**.

	Sr		Ti		O	
Experimental Binding Energy (TY)	5s	5.0	4s	1.6	**2s**	**23.7**
	4p$_{3/2}$	**19.5**	**3p$_{3/2}$**	**32.2**	2p$_{3/2}$	7.4
	3d$_{5/2}$	**133.1**	3d$_{3/2}$	3.7		
Ratio method calculation					$O\,3s \cong O\,2s \times \dfrac{Na\,3s}{Na\,2s}$	
	$Sr\,5p \cong Sr\,5s \times \dfrac{Sn\,5p}{Sn\,5s}$		$Ti\,4p \cong Ti\,4s \times \dfrac{Ge\,4p}{Ge\,4s}$			
	$Sr\,4d \cong Sr\,4s \times \dfrac{Y\,4d}{Y\,4s}$					
Ratio method input values (YL)					$O\,3s \cong$ 9.50E-04 x 3.34E-02	
	$Sr\,5p \cong$ 1.500E-04 x 6.417E-01		$Ti\,4p \cong$ 2.500E-04 x 4.933E-01			
	$Sr\,4d \cong$ 1.950E-03 x 2.000E-01					
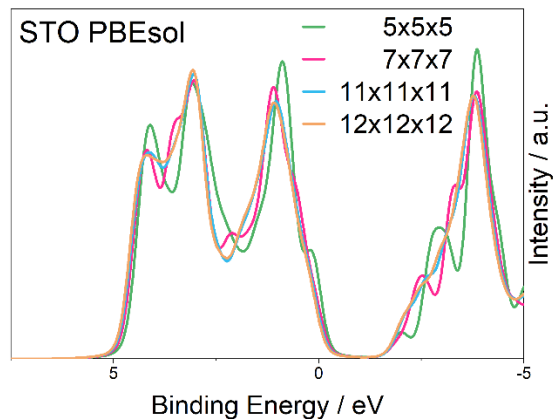
Figure B7. Convergence of the k-point density with respect to the appearance of the broadened valence density of states for STO. The electronic structure calculations were performed using PBEsol.
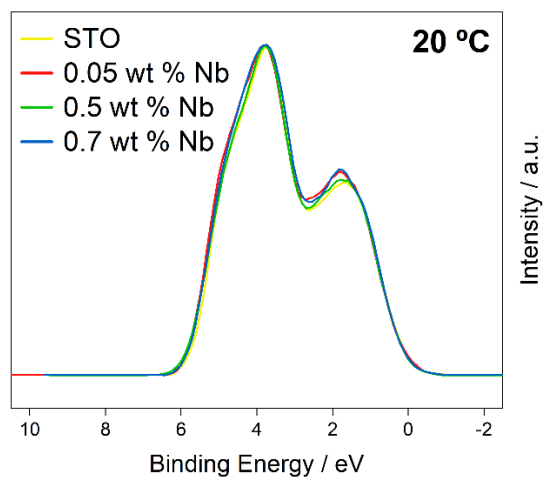
Figure B8. VB XPS spectra for the series of pure/niobium-doped strontium titanate single crystals, $SrTi_{(1-x)}Nb_xO_3$ (x = 0, 0.05, 0.08, 0.5) at RT, showing that the appearance of the experimental VB does not vary significantly with the Nb doping concentrations investigated.

Table B6. The RSS for various weightings of the YL* cross-section correction for the simulated STO spectrum. The RSS was calculated for Gaussian broadenings of 0.9 − 1.1 eV, showing a minimum at 1.0 eV, corresponding to the optimised weightings of each orbital component displayed in the table.

Orbital	YL* cross section	multiplier			
		Gaussian 0.8 eV	Gaussian 0.9 eV	Gaussian 1.0 eV	Gaussian 1.1 eV
Sr 5s	1.500E-04	7	7	1	1
Sr 5p	9.63E-05	1	1	10	10
Sr 4d	3.90E-04	1	1	2	1
Ti 4s	2.500E-04	2	2	3	1
Ti 4p	1.23E-04	6	7	10	9
Ti 3d	8.500E-05	1	1	3	4
O 3s	3.18E-05	1	1	1	1
O 2p	6.00E-05	1	1	2	2
	RSS	**0.10**	**0.06**	**0.05**	**0.06**

Table B7. Estimated errors for the fitted BE and FWHM C 1*s* peak parameters in the temperature dependent core level XPS data for the series of pure/niobium-doped strontium titanate single crystals, SrTi$_{(1-x)}$Nb$_x$O$_3$ (x = 0, 0.05, 0.08, 0.5). The errors have been estimated via Monte Carlo simulations using CasaXPS software. In this approach, the software simulates multiple (200) measurements by adding synthetic noise to the peak model, and then evaluating the stability of the model to give an estimate of the errors associated with the fitted peak parameters. The errors are given in eV to 1 s.f.

Temp / °C	STO C 1*s* BE	0.05 % Nb-STO C 1*s* BE	0.5 % Nb-STO C 1*s* BE	0.7 % Nb-STO C 1*s* BE
20	0.005	0.004	0.006	0.005
40	0.005	0.005	0.006	0.005
80	0.006	0.007	0.007	0.005
120	0.006	0.01	0.009	0.008
180	0.006	0.006	0.007	0.005
240	0.006	0.007	0.009	0.008
300	0.007	0.005	0.006	0.005
400	0.009	0.004	0.005	0.003
500	0.006	0.005	0.005	0.004
600	0.009	0.010	0.008	0.007
700	0.01	0.012	0.009	0.009

Temp / °C	STO C 1*s* FWHM	0.05 % Nb-STO C 1*s* FWHM	0.5 % Nb-STO C 1*s* FWHM	0.7 % Nb-STO C 1*s* FWHM
20	0.01	0.01	0.01	0.01
40	0.01	0.01	0.01	0.01
80	0.01	0.02	0.01	0.01
120	0.01	0.03	0.02	0.02
180	0.01	0.01	0.01	0.01
240	0.01	0.02	0.02	0.02
300	0.02	0.01	0.02	0.02
400	0.02	0.01	0.02	0.01
500	0.01	0.01	0.03	0.01
600	0.02	0.02	0.04	0.04
700	0.02	0.03	0.05	0.05

Table B8. Estimated errors for the fitted BE and FWHM Sr $3d_{5/2}$ BE peak parameters in the temperature dependent core level XPS data for the series of pure/niobium-doped strontium titanate single crystals, $SrTi_{(1-x)}Nb_xO_3$ (x = 0, 0.05, 0.08, 0.5). The errors have been estimated via Monte Carlo simulations using CasaXPS software. In this approach, the software simulates multiple (200) measurements by adding synthetic noise to the peak model, and then evaluating the stability of the model to give an estimate of the errors associated with the fitted peak parameters. The errors are given in eV to 1 s.f.

Temp / °C	STO Sr $3d_{5/2}$ BE	0.05 % Nb-STO Sr $3d_{5/2}$ BE	0.5 % Nb-STO Sr $3d_{5/2}$ BE	0.7 % Nb-STO Sr $3d_{5/2}$ BE
20	0.0009	0.0009	0.0009	0.0009
40	0.0008	0.0008		0.0009
80	0.0009	0.0009	0.0009	0.0009
120	0.0009	0.002	0.001	0.001
180	0.0009	0.001		0.001
240	0.0008	0.001	0.002	0.001
300	0.0009	0.001	0.0009	0.001
400	0.001	0.0008	0.0009	0.0008
500		0.0009	0.0009	0.0009
600	0.0009	0.0009	0.0009	0.0008
700	0.0008	0.0009	0.0009	0.001

Temp / °C	STO Sr 3d$_{5/2}$ FWHM	0.05 % Nb-STO Sr 3d$_{5/2}$ FWHM	0.5 % Nb-STO Sr 3d$_{5/2}$ FWHM	0.7 % Nb-STO Sr 3d$_{5/2}$ FWHM
20	0.001	0.001	0.001	0.001
40	0.001	0.002		0.002
80	0.001	0.002	0.001	0.001
120	0.001	0.003	0.002	0.002
180	0.001	0.002		0.002
240	0.002	0.002	0.002	0.002
300	0.002	0.002	0.002	0.002
400	0.002	0.001	0.001	0.001
500		0.001	0.001	0.001
600	0.001	0.001	0.001	0.001
700	0.001	0.001	0.002	0.002

Table B9. Estimated errors for the fitted BE and FWHM Ti $2p_{3/2}$ peak parameters in the temperature dependent core level XPS data for the series of pure/niobium-doped strontium titanate single crystals, SrTi$_{(1-x)}$Nb$_x$O$_3$ (x = 0, 0.05, 0.08, 0.5). The errors have been estimated via Monte Carlo simulations using CasaXPS software. In this approach, the software simulates multiple (200) measurements by adding synthetic noise to the peak model, and then evaluating the stability of the model to give an estimate of the errors associated with the fitted peak parameters. The errors are given in eV to 1 s.f.

Temp / °C	STO Ti $2p_{3/2}$ BE	0.05 % Nb-STO Ti $2p_{3/2}$ BE	0.5 % Nb-STO Ti $2p_{3/2}$ BE	0.7 % Nb-STO Ti $2p_{3/2}$ BE
20	0.002	0.001	0.001	0.002
40	0.001	0.002	0.002	0.002
80	0.001	0.002	0.001	0.002
120	0.001	0.003	0.002	0.002
180	0.001	0.002	0.002	0.002
240	0.001	0.002	0.002	0.002
300	0.002	0.002	0.002	0.002
400	0.002	0.002	0.002	0.002
500	0.002	0.002	0.002	0.002
600	0.002	0.002	0.002	0.002
700	0.001	0.002	0.002	0.002

Temp / °C	STO Ti $2p_{3/2}$ FWHM	0.05 % Nb-STO Ti $2p_{3/2}$ FWHM	0.5 % Nb-STO Ti $2p_{3/2}$ FWHM	0.7 % Nb-STO Ti $2p_{3/2}$ FWHM
20	0.003	0.003	0.003	0.003
40	0.003	0.003	0.004	0.004
80	0.003	0.005	0.003	0.004
120	0.003	0.006	0.005	0.005
180	0.004	0.005	0.003	0.004
240	0.003	0.006	0.005	0.005
300	0.004	0.004	0.003	0.004
400	0.004	0.004	0.004	0.004
500	0.003	0.004	0.004	0.004
600	0.003	0.003	0.004	0.003
700	0.003	0.004	0.004	0.004

Table B10. Estimated errors for the fitted BE and FWHM O 1*s* peak parameters in the temperature dependent core level XPS data for the series of pure/niobium-doped strontium titanate single crystals, $SrTi_{(1-x)}Nb_xO_3$ (x = 0, 0.05, 0.08, 0.5). The errors have been estimated via Monte Carlo simulations using CasaXPS software. In this approach, the software simulates multiple (200) measurements by adding synthetic noise to the peak model, and then evaluating the stability of the model to give an estimate of the errors associated with the fitted peak parameters. The errors are given in eV to 1 s.f.

Temp / °C	STO O 1*s* BE	0.05 % Nb-STO O 1*s* BE	0.5 % Nb-STO O 1*s* BE	0.7 % Nb-STO O 1*s* BE
20	0.002	0.002	0.002	0.002
40	0.002	0.002	0.002	0.002
80	0.002	0.003	0.002	0.002
120	0.002	0.003	0.003	0.003
180	0.002	0.003	0.002	0.002
240	0.002	0.003	0.003	0.003
300	0.002	0.003	0.002	0.002
400	0.002	0.002	0.002	0.002
500		0.002	0.002	0.002
600	0.002	0.002	0.002	0.002
700	0.002	0.002	0.002	0.002
Temp / °C	STO O 1*s* FWHM	0.05 % Nb-STO O 1*s* FWHM	0.5 % Nb-STO O 1*s* FWHM	0.7 % Nb-STO O 1*s* FWHM
20	0.003	0.004	0.004	0.004
40	0.004	0.004	0.006	0.005
80	0.004	0.007	0.004	0.005
120	0.004	0.008	0.005	0.006
180	0.005	0.007	0.004	0.005
240	0.005	0.007	0.006	0.006
300	0.005	0.006	0.006	0.005
400	0.006	0.004	0.005	0.005
500		0.004	0.004	0.004
600	0.004	0.004	0.004	0.004
700	0.004	0.005	0.005	0.004

Table B11. Estimated errors for the fitted BE and FWHM Sr $3d_{5/2}$ and Ti $2p_{3/2}$ BE peak parameters in the varied FG current core level XPS data for the series of pure/niobium-doped strontium titanate single crystals, $SrTi_{(1-x)}Nb_xO_3$ (x = 0, 0.05, 0.08, 0.5). The errors have been estimated via Monte Carlo simulations using CasaXPS software. In this approach, the software simulates multiple (200) measurements by adding synthetic noise to the peak model, and then evaluating the stability of the model to give an estimate of the errors associated with the fitted peak parameters. The errors are given in eV to 1 s.f.

FG Current / μA	STO Sr $3d_{5/2}$ BE	0.05 % Nb-STO Sr $3d_{5/2}$ BE	0.5 % Nb-STO Sr $3d_{5/2}$ BE	0.7 % Nb-STO Sr $3d_{5/2}$ BE
0	0.003	0.003	0.002	0.003
50	0.002	0.002	0.002	0.002
75	0.002	0.002	0.002	0.002
100	0.002	0.002	0.002	0.003
FG Current / μA	**STO Sr 3d$_{5/2}$ FWHM**	**0.05 % Nb-STO Sr 3d$_{5/2}$ FWHM**	**0.5 % Nb-STO Sr 3d$_{5/2}$ FWHM**	**0.7 % Nb-STO Sr 3d$_{5/2}$ FWHM**
0	0.005	0.004	0.004	0.004
50	0.004	0.003	0.004	0.004
75	0.004	0.004	0.004	0.004
100	0.004	0.003	0.004	0.004
FG Current / μA	**STO Ti 2$p_{3/2}$ BE**	**0.05 % Nb-STO Ti 2$p_{3/2}$ BE**	**0.5 % Nb-STO Ti 2$p_{3/2}$ BE**	**0.7 % Nb-STO Ti 2$p_{3/2}$ BE**
0	0.003	0.004	0.003	0.004
50	0.003	0.004	0.003	0.004
75	0.003	0.003	0.003	0.003
100	0.003	0.003	0.003	0.003
FG Current / μA	**STO Ti 2$p_{3/2}$ FWHM**	**0.05 % Nb-STO Ti 2$p_{3/2}$ FWHM**	**0.5 % Nb-STO Ti 2$p_{3/2}$ FWHM**	**0.7 % Nb-STO Ti 2$p_{3/2}$ FWHM**
0	0.008	0.009	0.007	0.008
50	0.007	0.008	0.007	0.008
75	0.007	0.007	0.007	0.006
100	0.006	0.008	0.007	0.006
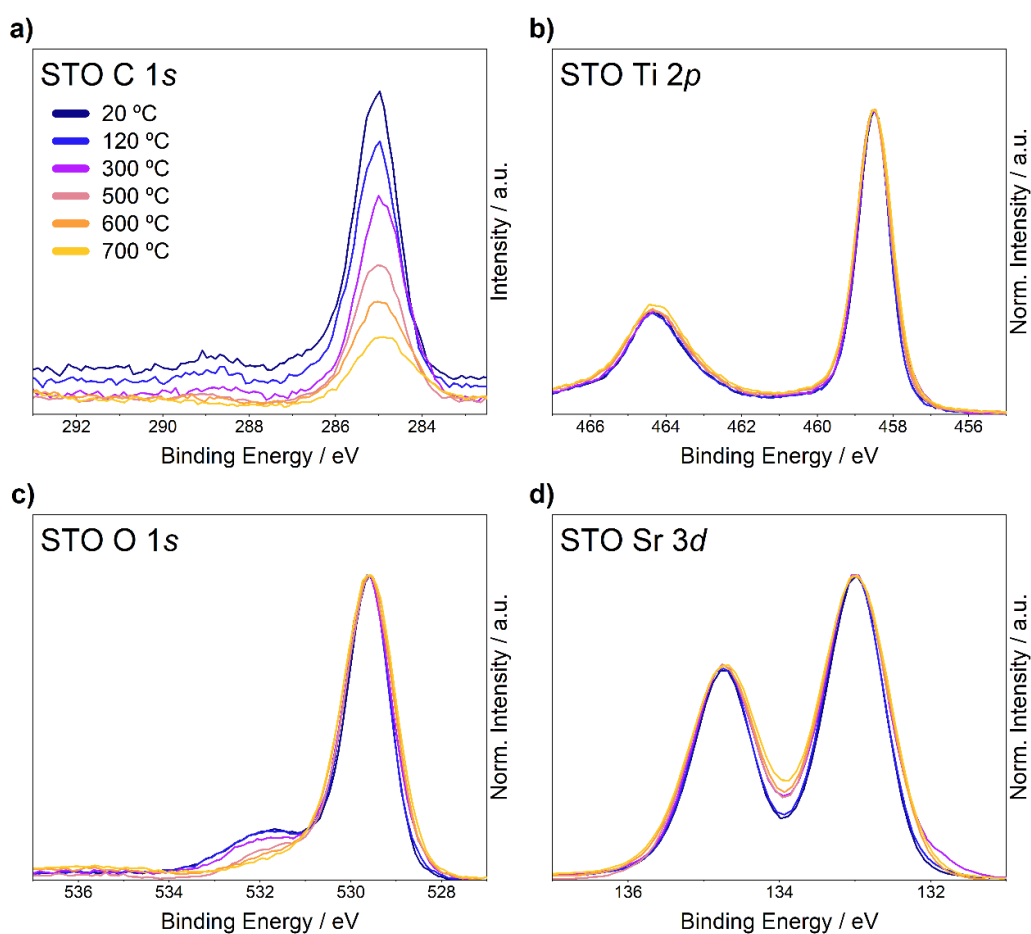
Figure B9. The variation with temperature of the core levels of the STO sample: **a)** C 1*s* showing both the C 1*s* and Sr 3*p* ½ peaks, **b)** the Ti 2*p* peak, **c)** the O 1*s* peak and **d)** the Sr 3*d* peak. All spectra have been normalised and overlayed at the BE for charge corrected undoped STO at RT for clarity, except for the C 1*s* region, which is not normalised to show the decreasing carbon contamination with the increasing temperature.
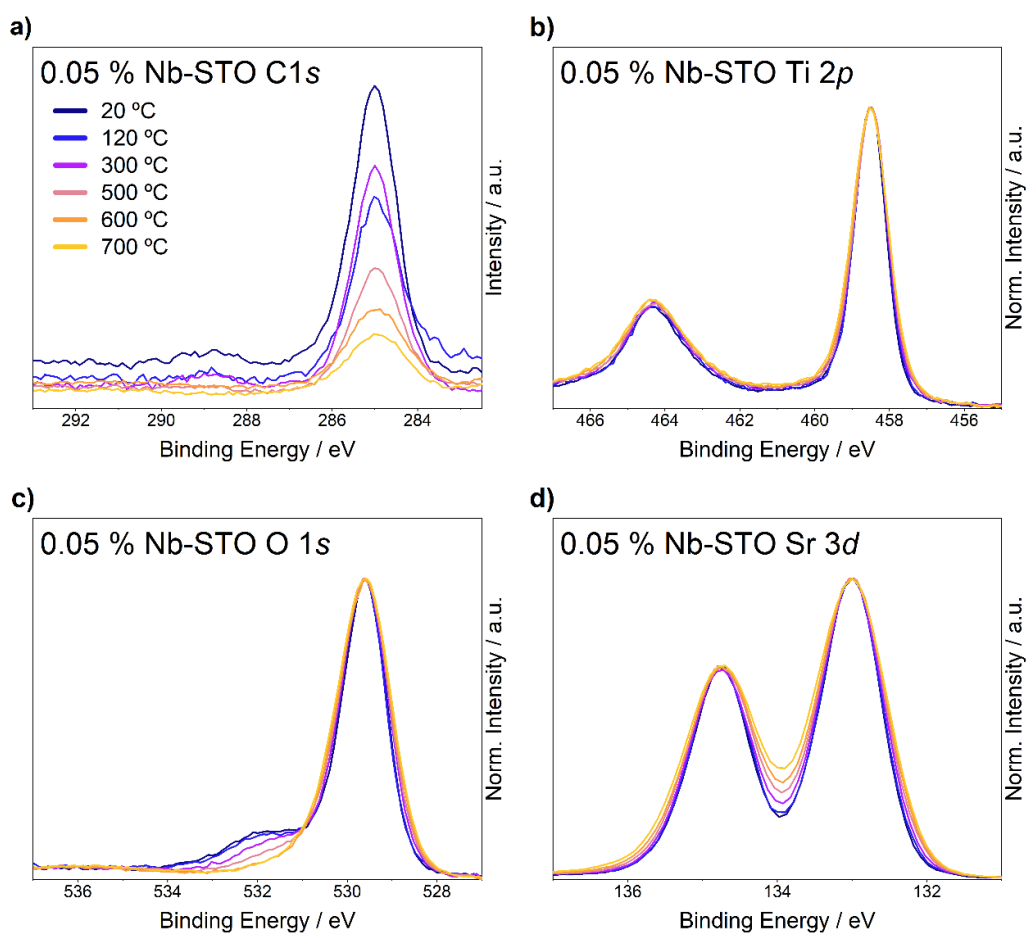
Figure B10. The variation with temperature of the core levels of the 0.05 wt % Nb-STO sample: **a)** C 1s showing both the C 1s and Sr 3p ½ peaks, **b)** the Ti 2p peak, **c)** the O 1s peak and **d)** the Sr 3d peak. All spectra have been normalised and overlayed at the BE for charge corrected undoped STO at RT for clarity, except for the C 1s region, which is not normalised to show the decreasing carbon contamination with the increasing temperature.
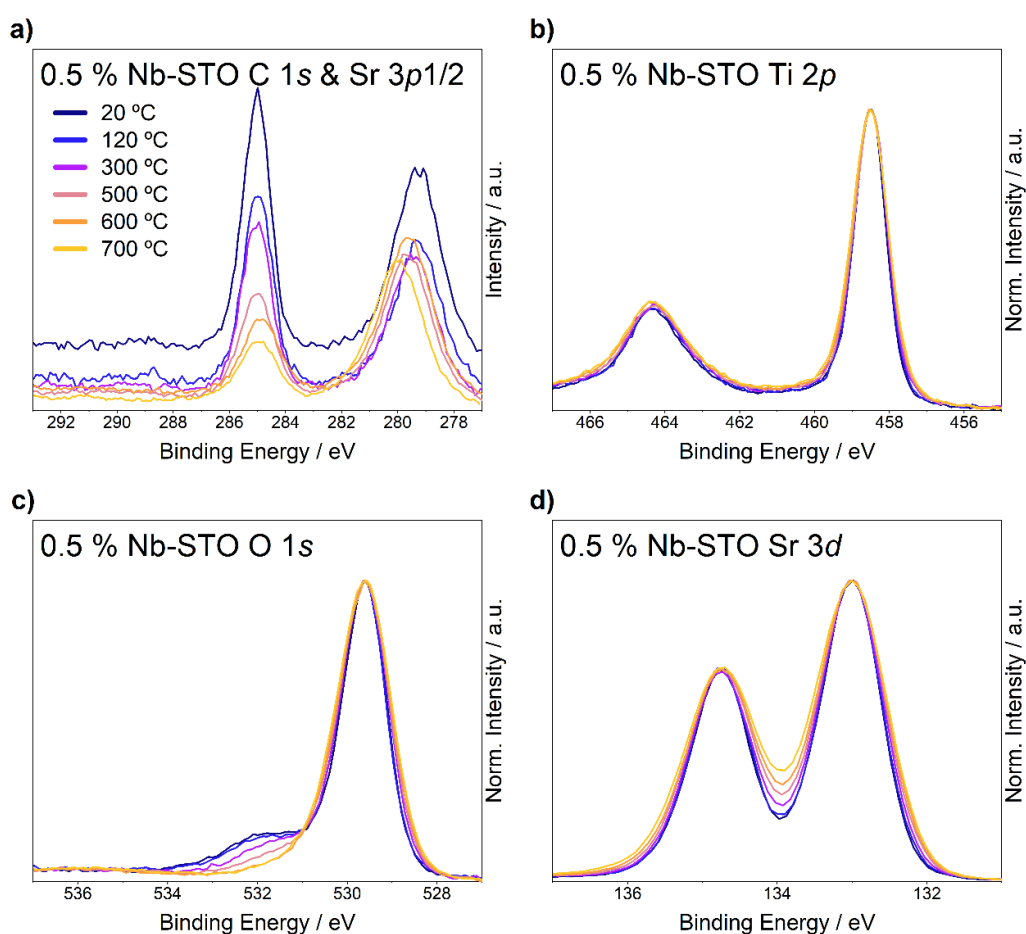
Figure B11. The variation with temperature of the core levels of the 0.5 wt % Nb-STO sample: **a)** C 1*s* showing both the C 1*s* and Sr 3*p* ½ peaks, **b)** the Ti 2*p* peak, **c)** the O 1*s* peak and **d)** the Sr 3*d* peak. All spectra have been normalised and overlayed at the BE for charge corrected undoped STO at RT for clarity, except for the C 1*s* region, which is not normalised to show the decreasing carbon contamination with the increasing temperature.

Appendix C
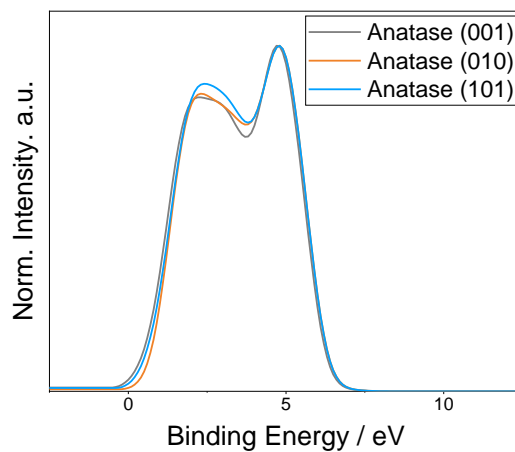
Figure C1. The DFT-simulated VB spectra for different slab unit cells of anatase, corresponding to different low index surface terminations, (001), (010) and (101), showing remarkably similar features.
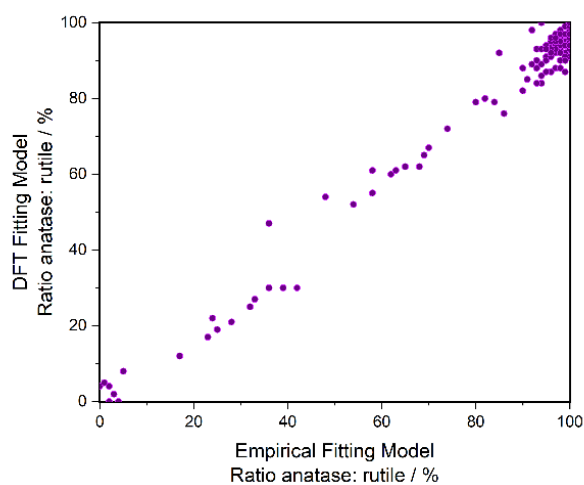
Figure C2. Correlation of the compositions of the mixed phase TiO_2 samples, as determined by the DFT fitting model and the Empirical fitting model.
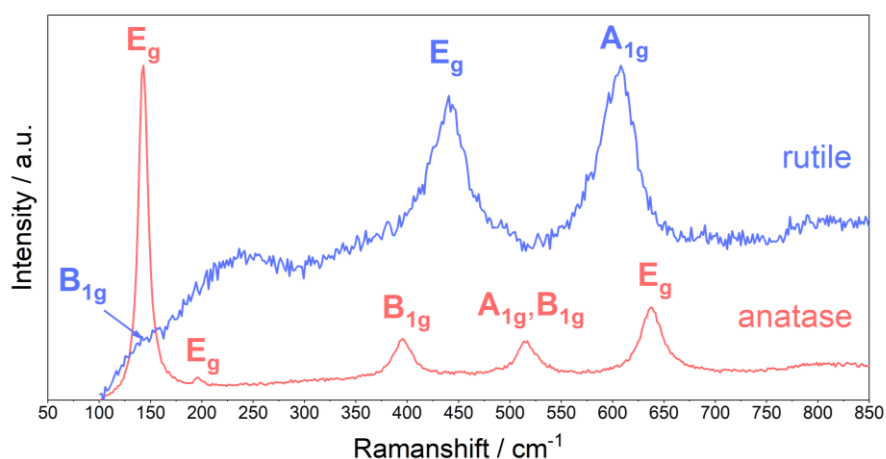
Figure C3. Raman spectra recorded on the anatase (red line) and rutile (blue line) single phase thin films. The assigned modes confirm the presence of the anatase and rutile phases.[185]
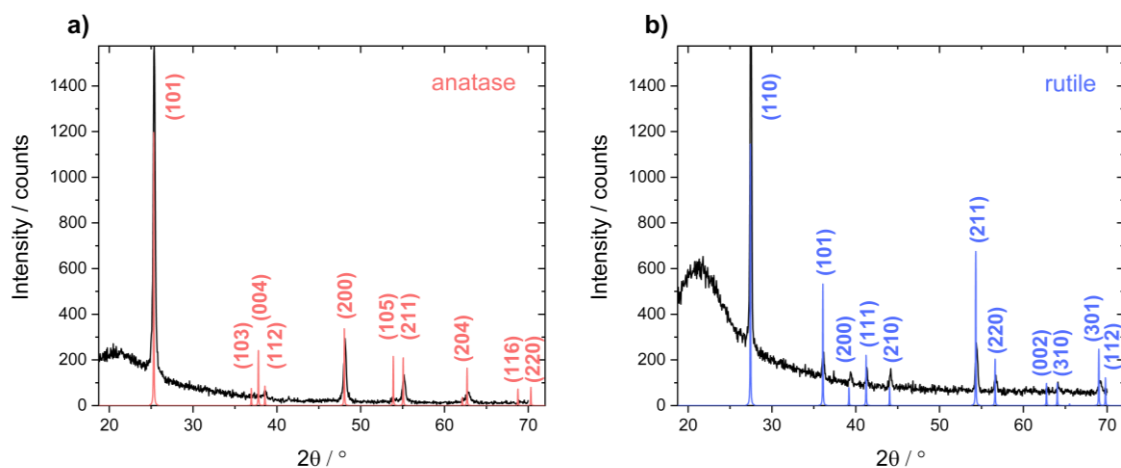
Figure C4. XRD data recorded on the **a)** anatase and **b)** rutile single phase films. The peaks are in agreement with reference patterns recorded on pure phase nanopowders.

Appendix D

Table D1. Measured binding energies of the ILs in this study in four different environments along with reference values determined via an internal calibration method with the imidazolium nitrogen,[236] and the difference from the reference value (Δ_{BE}^{ref}).

		Binding Energy / eV					Δ_{BE}^{ref} / eV			
		Ref.[236]	Cu FG OFF	Cu FG ON	Glass FG OFF	Glass FG ON	Cu FG OFF	Cu FG ON	Glass FG OFF	Glass FG ON
C 1s	$C_2H_5MIm.BF_4$	285.3	285.7	285.9	303.3	283.9	0.39	0.58	17.97	-1.36
	$C_4H_9MIm.BF_4$	285.1	285.7	285.9	301.3	284.1	0.55	0.80	16.17	-1.05
	$C_{10}H_{21}MIm.BF_4$	285.0	285.7	285.8	297.7	284.6	0.67	0.83	12.71	-0.44
	$C_4H_9MIm.PF_6$	285.2	285.7	285.8	303.9	284.3	0.46	0.58	18.70	-0.90
N 1s	$C_2H_5MIm.BF_4$	402.0	402.5	402.6	419.5	400.6	0.45	0.63	17.51	-1.36
	$C_4H_9MIm.BF_4$	402.0	402.5	402.6	417.8	400.8	0.45	0.64	15.77	-1.21
	$C_{10}H_{21}MIm.BF_4$	402.0	402.5	402.6	414.4	401.3	0.46	0.63	12.43	-0.68
	$C_4H_9MIm.PF_6$	402.1	402.7	402.7	420.6	401.2	0.62	0.55	18.45	-0.95
F 1s	$C_2H_5MIm.BF_4$	686.0	686.6	686.8	703.5	684.8	0.55	0.75	17.49	-1.23
	$C_4H_9MIm.BF_4$	686.0	686.5	686.7	701.7	684.9	0.51	0.72	15.68	-1.11
	$C_{10}H_{21}MIm.BF_4$	686.0	686.6	686.7	698.2	685.4	0.57	0.74	12.22	-0.61
	$C_4H_9MIm.PF_6$	686.7	687.4	687.3	704.8	685.8	0.65	0.59	18.13	-0.95

Table D2. Estimated errors for the fitted BE and FWHM C 1s, N 1s, and F 1s BE peak parameters under various XPS measurement conditions data for the series ionic liquids. The errors have been estimated via Monte Carlo simulations using CasaXPS software. In this approach, the software simulates multiple (200) measurements by adding synthetic noise to the peak model, and then evaluating the stability of the model to give an estimate of the errors associated with the fitted peak parameters. The errors are given in eV to 1 s.f.

XPS Measurement	[C$_2$H$_5$MIm][BF$_4$] C 1s BE	[C$_4$H$_9$MIm][BF$_4$] C 1s BE	[C$_{10}$H$_{21}$MIm][BF$_4$] C 1s BE	[C$_4$H$_9$MIm][PF$_6$] C 1s BE
Cu FG OFF	0.007	0.006	0.003	0.007
Cu FG ON	0.008	0.006	0.003	0.006
Glass FG OFF	0.02	0.007	0.004	0.006
Glass FG ON	0.008	0.007	0.004	0.007
XPS Measurement	**[C$_2$H$_5$MIm][BF$_4$] C 1s FWHM**	**[C$_4$H$_9$MIm][BF$_4$] C 1s FWHM**	**[C$_{10}$H$_{21}$MIm][BF$_4$] C 1s FWHM**	**[C$_4$H$_9$MIm][PF$_6$] C 1s FWHM**
Cu FG OFF	0.01	0.01	0.006	0.01
Cu FG ON	0.01	0.01	0.007	0.01
Glass FG OFF	0.03	0.01	0.004	0.01
Glass FG ON	0.02	0.01	0.008	0.01
XPS Measurement	**[C$_2$H$_5$MIm][BF$_4$] N 1s BE**	**[C$_4$H$_9$MIm][BF$_4$] N 1s BE**	**[C$_{10}$H$_{21}$MIm][BF$_4$] N 1s BE**	**[C$_4$H$_9$MIm][PF$_6$] N 1s BE**
Cu FG OFF	0.007	0.006	0.008	0.005
Cu FG ON	0.006	0.006	0.02	0.005
Glass FG OFF	0.007	0.007	0.007	0.03
Glass FG ON	0.007	0.008	0.008	0.020
XPS Measurement	**[C$_2$H$_5$MIm][BF$_4$] N 1s FWHM**	**[C$_4$H$_9$MIm][BF$_4$] N 1s FWHM**	**[C$_{10}$H$_{21}$MIm][BF$_4$] N 1s FWHM**	**[C$_4$H$_9$MIm][PF$_6$] N 1s FWHM**
Cu FG OFF	0.01	0.01	0.02	0.01
Cu FG ON	0.01	0.01	0.02	0.01
Glass FG OFF	0.02	0.02	0.02	0.03
Glass FG ON	0.01	0.02	0.02	0.02
XPS Measurement	**[C$_2$H$_5$MIm][BF$_4$] F 1s BE**	**[C$_4$H$_9$MIm][BF$_4$] F 1s BE**	**[C$_{10}$H$_{21}$MIm][BF$_4$] F 1s BE**	**[C$_4$H$_9$MIm][PF$_6$] F 1s BE**
Cu FG OFF	0.005	0.005	0.007	0.002
Cu FG ON	0.005	0.005	0.008	0.002
Glass FG OFF	0.005	0.006	0.007	0.001
Glass FG ON	0.005	0.007	0.007	0.001
XPS Measurement	**[C$_2$H$_5$MIm][BF$_4$] F 1s FWHM**	**[C$_4$H$_9$MIm][BF$_4$] F 1s FWHM**	**[C$_{10}$H$_{21}$MIm][BF$_4$] F 1s FWHM**	**[C$_4$H$_9$MIm][PF$_6$] F 1s FWHM**
Cu FG OFF	0.01	0.01	0.02	0.003
Cu FG ON	0.01	0.01	0.02	0.003
Glass FG OFF	0.01	0.01	0.02	0.003
Glass FG ON	0.01	0.01	0.02	0.003

Table D3. Estimated errors for the fitted BE and FWHM C 1s, N 1s, F 1s and O 1s BE peak parameters at various scanning positions during preliminary measurements on the electrochemical XPS glass cell. The errors have been estimated via Monte Carlo simulations using CasaXPS software. In this approach, the software simulates multiple (200) measurements by adding synthetic noise to the peak model, and then evaluating the stability of the model to give an estimate of the errors associated with the fitted peak parameters. The errors are given in eV to 1 s.f.

FWHM	IL Electrolyte Centre	Line Scan Position 0	Line Scan Position 21
C 1s (CF$_3$)	0.004	0.03	0.07
F 1s	0.002	0.01	0.02
N 1s cation	0.003	0.02	0.06
N 1s anion	0.007	0.05	0.1
O 1s	0.002	0.01	0.02
BE	IL Electrolyte Centre	Line Scan Position 0	Line Scan Position 21
C 1s (CF$_3$)	0.002	0.01	0.03
F 1s	0.001	0.004	0.01
N 1s cation	0.001	0.01	0.02
N 1s anion	0.002	0.02	0.04
O 1s	0.001	0.005	0.01

Table D4. Estimated errors for the fitted FWHM F 1*s* BE peak parameter at different potentials during various *in-situ* and *operando* measurements using the electrochemical XPS glass cell. The different measurements are summarised in the column headings. The errors have been estimated via Monte Carlo simulations using CasaXPS software. In this approach, the software simulates multiple (200) measurements by adding synthetic noise to the peak model, and then evaluating the stability of the model to give an estimate of the errors associated with the fitted peak parameters. The errors are given in eV to 1 s.f.

CA IL Chronoamperometry measurements at the ionic liquid centre		CA WE Chronoamperometry measurements at the working electrode/electrolyte interface		CV IL Cyclic voltammetry measurements at the ionic liquid centre		CV WE Cyclic voltammetry measurements at the working electrode/electrolyte interface	
Potential / V	F 1*s* FWHM	Potential / V	F 1*s* FWHM	Potential / V	F 1*s* FWHM	Potential / V	F 1*s* FWHM
-1.0	0.005	-1.0	0.008	0.59	0.005	0.70	0.01
-0.8	0.004	-0.8	0.007	0.37	0.005	0.48	0.01
-0.6	0.004	-0.6	0.007	0.15	0.005	0.26	0.009
-0.4	0.005	-0.4	0.006	-0.07	0.005	0.04	0.009
-0.2	0.005	-0.2	0.007	-0.28	0.004	-0.17	0.009
0.0	0.005	0.0	0.007	-0.50	0.005	-0.39	0.01
0.2	0.005	0.2	0.02	-0.72	0.004	-0.61	0.009
0.4	0.005	0.4	0.01	-0.94	0.004	-0.83	0.009
0.6	0.005	0.6	0.009	-0.85	0.004	-0.96	0.009
0.8	0.004	0.8	0.009	-0.63	0.004	-0.74	0.01
0.8	0.004	0.8	0.009	-0.41	0.004	-0.52	0.01
1.0	0.005	1.0	0.009	-0.19	0.005	-0.30	0.01
0.0	0.004	0.0	0.01	0.02	0.005	-0.09	0.008
				0.24	0.005	0.13	0.01
				0.46	0.004	0.35	0.01
				0.68	0.005	0.57	0.01
						0.79	0.01

Figure D1. The XPS F 1s, N 1s and O 1s regions of the imidazolium ILs **a-c)** [C$_2$H$_5$MIm][BF$_4$] **d-f)** [C$_4$H$_9$MIm][BF$_4$] **g-i)** [C$_{10}$H$_{21}$MIm][BF$_4$] and **j-l)** [C$_4$H$_9$MIm][PF6]. There is contamination present in [C$_2$H$_5$MIm][BF$_4$] and [C$_4$H$_9$MIm][BF$_4$] which is evident in the C 1s region (main work) but also supported by the strong oxygen signals in **(c)** and **(f)**. There also seems to be some fluorine impurity in [C$_4$H$_9$MIm][BF$_4$] **(d)**.
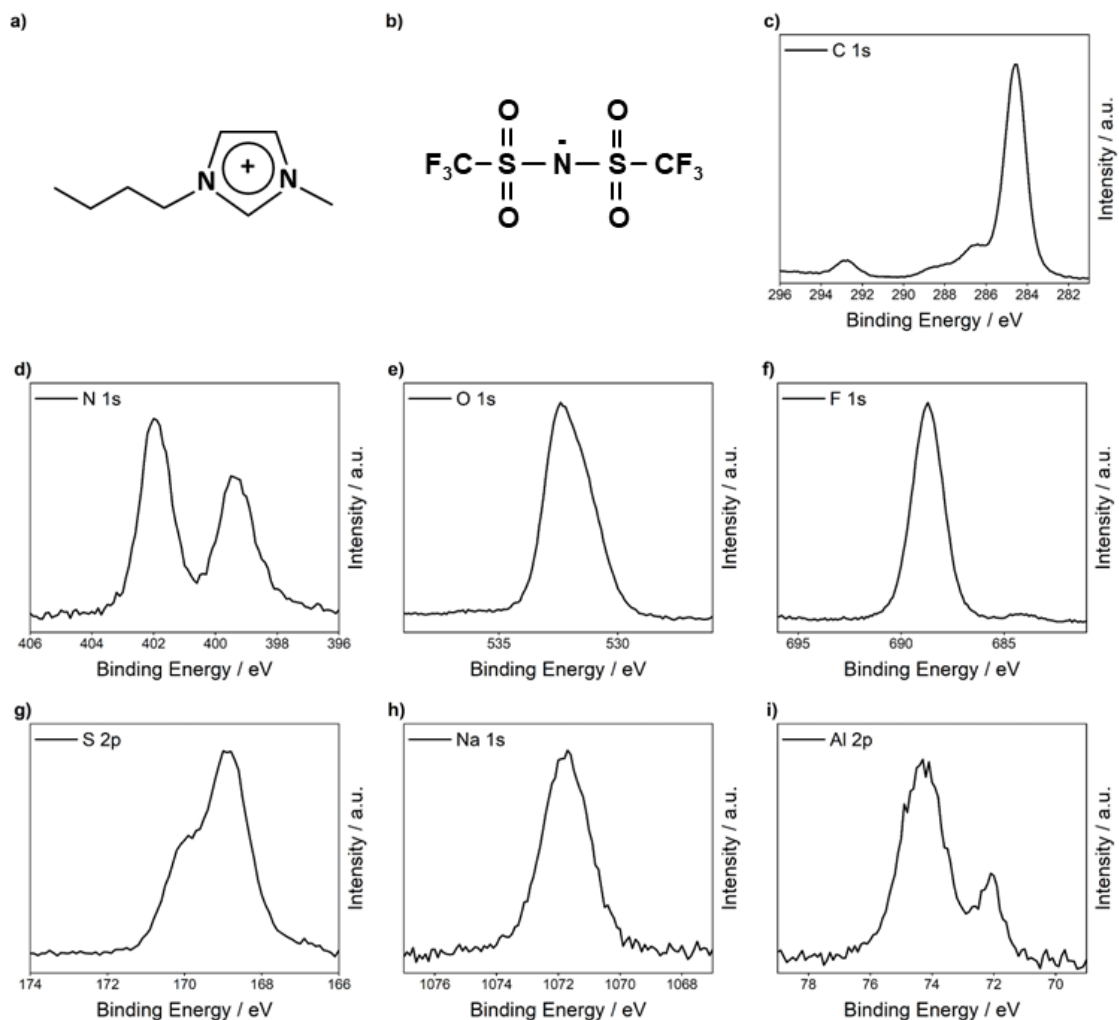
Figure D2a) The structure of the [BMIm] cation and **b)** the [TFSI] anion of the IL electrolyte. All species are clearly identified in the high resolution XPS spectra taken at the WE/IL interface. **c)** C 1*s*, **d)** N 1*s*, **e)** O 1*s*, **f)** F 1*s*, **g)** S 2*p*, **h)** Na 1*s*, and **d)** Al 2*p*.
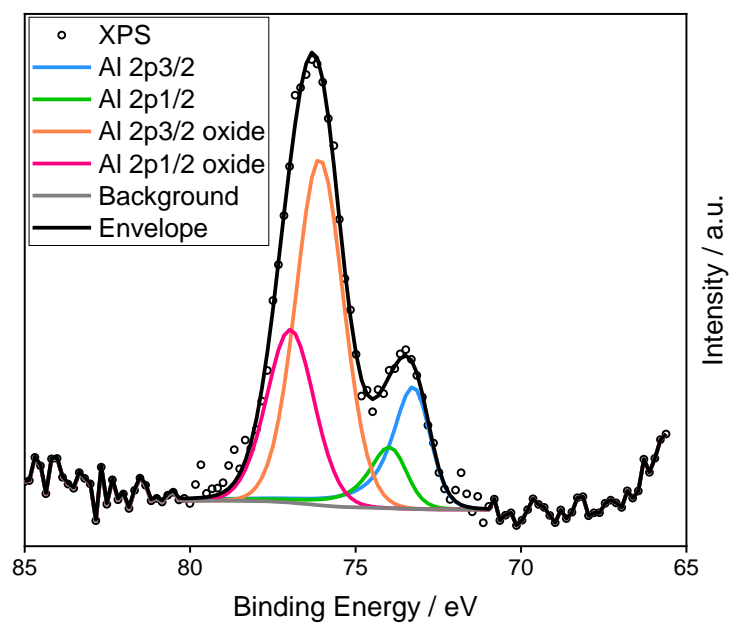
Figure D3. Fitting of the Al $2p$ region into metallic and oxide components. The oxide component is modelled using a GL(30) lineshape, and the metallic line shape used was ST(33)LA(1,1.3,165). The metallic line shape was taken from a previously reported model.[254] The Na $2s$ core-level is just visible at the low BE limit.

REFERENCES

1. R. Lee, R. Quesada-Cabrera, J. Willis, A. Iqbal, I. P. Parkin, D. O. Scanlon and R. G. Palgrave, *ACS Applied Materials & Interfaces*, 2023, **15**, 39956-39965.
2. M. A. Isaacs, J. Davies-Jones, P. R. Davies, S. Guan, R. Lee, D. J. Morgan and R. Palgrave, *Materials Chemistry Frontiers*, 2021, **5**, 7931-7963.
3. M. A. Isaacs, C. Drivas, R. Lee, R. Palgrave, C. M. A. Parlett and D. J. Morgan, *Applied Surface Science Advances*, 2023, **18**, 100469.
4. R. Arrigo, L. Ban, T. Bartels-Rausch, P. R. Davies, S. Eyley, W. Flavell, G. Galli, S. Guan, S. Hall, G. Held, J. Kahk, R. Lee, R. Lindsay, J. Lischner, K. Lovelock, A. Nilsson, D. Payne, O. Renault, A. Shard and S. Suzer, *Faraday Discussions*, 2022, **236**, 412-428.
5. A. Ruiz-Gonzalez, J. L. Huang, C. Xun, R. Chhabra, R. Lee, H. Yizhong, A. Davenport, B. Li, R. Palgrave and K. L. Choy, *Applied Materials Today*, 2022, **29**, 101600.
6. J. G. Jenkin, R. C. G. Leckey and J. Liesegang, *Journal of Electron Spectroscopy and Related Phenomena*, 1977, **12**, 1-35.
7. J. G. Jenkin, J. D. Riley, J. Liesegang and R. C. G. Leckey, *Journal of Electron Spectroscopy and Related Phenomena*, 1978, **14**, 477-485.
8. A. Einstein, *Annalen Der Physik*, 1905, **17**, 132-148.
9. S. Hagström, C. Nordling and K. Siegbahn, *Physics Letters*, 1964, **9**, 235-236.
10. J. Hedman, P. F. Heden, C. Nordling and K. Siegbahn, *Physics Letters A*, 1969, **A 29**, 178.
11. R. Nordberg, R. G. Albridge, T. Bergmark, U. Ericson, A. Fahlman, K. Hamrin, J. Hedman, G. Johansson, C. Nordling, K. Siegbahn and B. Lindberg, *Nature*, 1967, **214**, 481-+.
12. K. Siegbahn, C. Nordling and A. Fahlman, *ESCA, Atomic, Molecular and Solid State Structure Studied by Means of Electron Spectroscopy*, Almqvist & Wiksells, Uppsala, 1967.
13. K. Siegbahn, *Philosophical Transactions of the Royal Society of London. Series A, Mathematical and Physical Sciences*, 1970, **268**, 33-57.
14. H. Kuzmany, *Solid-State Spectroscopy: An Introduction, Second Edition*, 2009, 1-554.
15. S. Hüfner and T. W. Huber, *Photoelectron Spectroscopy: Principles and Applications*, Springer, 2003.
16. S. Suga and A. Sekiyama, *Photoelectron Spectroscopy: Bulk and Surface Electronic Structures*, Springer Berlin Heidelberg, 2013.
17. C. S. Fadley, *Nuclear Instruments & Methods*, 2009, **601**, 8-31.
18. C. S. Fadley, *Journal of Electron Spectroscopy and Related Phenomena*, 2010, **178-179**, 2-32.
19. F. Reinert and S. Hufner, *New Journal of Physics*, 2005, **7**.
20. C. J. Powell and A. Jablonski, *Nuclear Instruments and Methods in Physics Research Section A: Accelerators, Spectrometers, Detectors and Associated Equipment*, 2009, **601**, 54-65.
21. J. F. Moulder and J. Chastain, *Handbook of X-ray Photoelectron Spectroscopy: A Reference Book of Standard Spectra for Identification and Interpretation of XPS Data*, Physical Electronics Division, Perkin-Elmer Corporation, 1992.
22. B. V. Crist, *Handbook of Monochromatic XPS Spectra, Semiconductors*, Wiley, 2000.
23. M. P. Seah and W. A. Dench, *Surface and Interface Analysis*, 1979, **1**, 2-11.
24. P. Swift, *Surface and Interface Analysis*, 1982, **4**, 47-51.
25. G. Greczynski and L. Hultman, *Progress in Materials Science*, 2020, **107**, 100591.
26. D. J. Hnatowich, 1971, **42**, 4883.
27. I. Bertoti, *Surface & Coatings Technology*, 2002, **151**, 194-203.
28. A. Pélisson-Schecker, H. J. Hug and J. Patscheider, *Surface and Interface Analysis*, 2012, **44**, 29-36.

29.   D. R. Baer, K. Artyushkova, H. Cohen, C. D. Easton, M. Engelhard, T. R. Gengenbach, G. Greczynski, P. Mack, D. J. Morgan and A. Roberts, *Journal of Vacuum Science & Technology A*, 2020, **38**, 031204.
30.   M. C. Biesinger, *Applied Surface Science*, 2022, **597**, 153681.
31.   P. A. Cox, *The Electronic Structure and Chemistry of Solids*, Oxford University Press, 1987.
32.   M. Malvestuto, M. Pedio, S. Nannarone, G. Pavia, G. Scarel, M. Fanciulli and F. Boscherini, *Journal of Applied Physics*, 2007, **101**, 074104.
33.   D. Koh, S. K. Banerjee, C. Locke, S. E. Saddow, J. Brockman, M. Kuhn and S. W. King, *Journal of Vacuum Science & Technology B*, 2020, **38**, 041206.
34.   F. R. McFeely, S. P. Kowalczyk, L. Ley, R. G. Cavell, R. A. Pollak and D. A. Shirley, *Physical Review B*, 1974, **9**, 5268-5278.
35.   S. Kono, H. Kodama, K. Ichikawa, T. Yoshikawa, T. Abukawa and A. Sawabe, *Japanese Journal of Applied Physics*, 2014, **53**, 05FP03.
36.   J. R. Waldrop and R. W. Grant, *Applied Physics Letters*, 1990, **56**, 557-559.
37.   E. A. Kraut, R. W. Grant, J. R. Waldrop and S. P. Kowalczyk, *Physical Review Letters*, 1980, **44**, 1620-1623.
38.   E. A. Kraut, R. W. Grant, J. R. Waldrop and S. P. Kowalczyk, *Physical Review B*, 1983, **28**, 1965-1977.
39.   P. Reddy, I. Bryan, Z. Bryan, W. Guo, L. Hussey, R. Collazo and Z. Sitar, *Journal of Applied Physics*, 2014, **116**, 123701.
40.   E. T. Yu, E. T. Croke, T. C. McGill and R. H. Miles, *Applied Physics Letters*, 1990, **56**, 569-571.
41.   R. Puthenkovilakam and J. P. Chang, *Applied Physics Letters*, 2004, **84**, 1353-1355.
42.   L. A. H. Jones, Z. Xing, J. E. N. Swallow, H. Shiel, T. J. Featherstone, M. J. Smiles, N. Fleck, P. K. Thakur, T.-L. Lee, L. J. Hardwick, D. O. Scanlon, A. Regoutz, T. D. Veal and V. R. Dhanak, *The Journal of Physical Chemistry C*, 2022, **126**, 21022-21033.
43.   S. A. Chambers, T. Droubay, T. C. Kaspar, M. Gutowski and M. van Schilfgaarde, *Surface Science*, 2004, **554**, 81-89.
44.   S. A. Chambers and T. J. Irwin, *Physical Review B*, 1988, **38**, 7484-7492.
45.   S. A. Chambers, Y. Liang, Z. Yu, R. Droopad, J. Ramdani and K. Eisenbeiser, *Applied Physics Letters*, 2000, **77**, 1662-1664.
46.   J. R. Chelikowsky and M. L. Cohen, *Physical Review B*, 1976, **14**, 556-582.
47.   S. A. Chambers, T. Droubay, T. C. Kaspar and M. Gutowski, *Journal of Vacuum Science & Technology B: Microelectronics and Nanometer Structures*, 2004, **22**, 2205.
48.   J. Endres, D. A. Egger, M. Kulbak, R. A. Kerner, L. Zhao, S. H. Silver, G. Hodes, B. P. Rand, D. Cahen, L. Kronik and A. Kahn, *The Journal of Physical Chemistry Letters*, 2016, **7**, 2722-2729.
49.   B. Philippe, T. J. Jacobsson, J.-P. Correa-Baena, N. K. Jena, A. Banerjee, S. Chakraborty, U. B. Cappel, R. Ahuja, A. Hagfeldt, M. Odelius and H. Rensmo, *The Journal of Physical Chemistry C*, 2017, **121**, 26655-26666.
50.   E. Schrödinger, *Physical Review*, 1926, **28**, 1049-1070.
51.   A. R. Leach, *Molecular Modelling : Principles and Applications*, Prentice Hall, Harlow, England, 2nd edn., 2001.
52.   P. Hohenberg and W. Kohn, *Physical Review*, 1964, **136**, B864-B871.
53.   W. Kohn and L. J. Sham, *Physical Review*, 1965, **140**, A1133-A1138.
54.   J. P. Perdew, K. Burke and M. Ernzerhof, *Physical Review Letters*, 1996, **77**, 3865-3868.
55.   L. Vega and F. Viñes, *Journal of Computational Chemistry*, 2020, **41**, 2598-2603.
56.   J. P. Perdew, A. Ruzsinszky, G. I. Csonka, O. A. Vydrov, G. E. Scuseria, L. A. Constantin, X. Zhou and K. Burke, *Physical Review Letters*, 2008, **100**, 136406.

57. J. Heyd, G. Scuseria and M. Ernzerhof, *Journal of Chemical Physics*, 2003, **118**, 8207-8215.
58. S. Grimme, *Journal of Computational Chemistry*, 2004, **25**, 1463-1473.
59. M. Bagheri and P. Blaha, *Journal of Electron Spectroscopy and Related Phenomena*, 2019, **230**, 1-9.
60. T. J. Whittles, L. A. Burton, J. M. Skelton, A. Walsh, T. D. Veal and V. R. Dhanak, *Chemistry of Materials*, 2016, **28**, 3718-3726.
61. P. D. C. King, T. D. Veal, F. Fuchs, C. Y. Wang, D. J. Payne, A. Bourlange, H. Zhang, G. R. Bell, V. Cimalla, O. Ambacher, R. G. Egdell, F. Bechstedt and C. F. McConville, *Physical Review B*, 2009, **79**.
62. J. Swallow, C. Vorwerk, P. Mazzolini, P. Vogt, O. Bierwagen, A. Karg, M. Eickhoff, J. Schormann, M. Wagner, J. Roberts, P. Chalker, M. Smiles, P. Murgatroyd, S. Razek, Z. Lebens-Higgins, L. Piper, L. Jones, P. Thakur, T. Lee, J. Varley, J. Furthmuller, C. Draxl, T. Veal and A. Regoutz, *Chemistry of Materials*, 2020, **32**, 8460-8470.
63. P. D. C. King, T. D. Veal, C. F. McConville, F. Fuchs, J. Furthmüller, F. Bechstedt, J. Schörmann, D. J. As, K. Lischka, H. Lu and W. J. Schaff, *Physical Review B*, 2008, **77**.
64. P. D. C. King, T. D. Veal, A. Schleife, J. Zúñiga-Pérez, B. Martel, P. H. Jefferson, F. Fuchs, V. Muñoz-Sanjosé, F. Bechstedt and C. F. Mcconville, *Physical Review B*, 2009, **79**, 205205.
65. J. J. Mudd, T.-L. Lee, V. Muñoz-Sanjosé, J. Zúñiga-Pérez, D. J. Payne, R. G. Egdell and C. F. McConville, *Physical Review B*, 2014, **89**, 165305.
66. C. Kalha, L. E. Ratcliff, J. J. G. Moreno, S. Mohr, M. Mantsinen, N. K. Fernando, P. K. Thakur, T.-L. Lee, H.-H. Tseng, T. S. Nunney, J. M. Kahk, J. Lischner and A. Regoutz, *Physical Review B*, 2022, **105**.
67. J. M. Kahk, C. G. Poll, F. E. Oropeza, J. M. Ablett, D. Geolin, J. P. Rueff, S. Agrestini, Y. Utsumi, K. D. Tsuei, Y. F. Liao, F. Borgatti, G. Panaccione, A. Regoutz, R. G. Egdell, B. J. Morgan, D. O. Scanlon and D. J. Payne, *Physical Review Letters*, 2014, **112**.
68. J. P. Allen, N. M. Galea, G. W. Watson, R. G. Palgrave, J. M. Kahk, D. J. Payne, M. D. M. Robinson, G. Field, A. Regoutz and R. G. Egdell, *The Journal of Physical Chemistry C*, 2014, **118**, 25330-25339.
69. D. J. Payne, R. G. Egdell, D. S. L. Law, P. A. Glans, T. Learmonth, K. E. Smith, J. H. Guo, A. Walsh and G. W. Watson, *Journal of Materials Chemistry*, 2007, **17**, 267-277.
70. L.-Å. Näslund, M.-H. Mikkelä, E. Kokkonen and M. Magnuson, *2D Materials*, 2021, **8**, 045026.
71. C. J. Krajewska, S. R. Kavanagh, L. Zhang, D. J. Kubicki, K. Dey, K. Gałkowski, C. P. Grey, S. D. Stranks, A. Walsh, D. O. Scanlon and R. G. Palgrave, *Chemical Science*, 2021, **12**, 14686-14699.
72. A. Abfalterer, J. Shamsi, D. J. Kubicki, C. N. Savory, J. Xiao, G. Divitini, W. Li, S. Macpherson, K. Gałkowski, J. L. MacManus-Driscoll, D. O. Scanlon and S. D. Stranks, *ACS Materials Letters*, 2020, **2**, 1644-1652.
73. M. Parvizian, A. Duràn Balsa, R. Pokratath, C. Kalha, S. Lee, D. Van Den Eynden, M. Ibáñez, A. Regoutz and J. De Roo, *Angewandte Chemie International Edition*, 2022, **61**, e202207013.
74. A. J. Jackson, A. M. Ganose, A. Regoutz, R. G., Egdell and D. O. Scanlon, *Journal of Open Source Software*, 2018, 773.
75. C. J. Nelin, P. S. Bagus, M. A. Brown, M. Sterrer and H.-J. Freund, *Angewandte Chemie International Edition*, 2011, **50**, 10174-10177.
76. D. M. Riffe, G. K. Wertheim and P. H. Citrin, *Physical Review Letters*, 1991, **67**, 116-119.
77. U. Gelius, S. Svensson, H. Siegbahn, E. Basilier, A. Faxalv and K. Siegbahn, *Chemical Physics Letters*, 1974, **28**, 1-7.
78. T. Wolfram and S. Ellialtioğlu, *Physical Review B*, 1979, **19**, 43-46.

79. C. S. Fadley and D. A. Shirley, *Journal of research of the National Bureau of Standards. Section A, Physics and chemistry*, 1970, **74A**, 543-558.

80. J. J. Joyce, J. M. Wills, T. Durakiewicz, M. T. Butterfield, E. Guziewicz, J. L. Sarrao, L. A. Morales, A. J. Arko and O. Eriksson, *Phys Rev Lett*, 2003, **91**, 176401.

81. S. Thiess, T. L. Lee, F. Bottin and J. Zegenhagen, *Solid State Communications*, 2010, **150**, 553-556.

82. S. K. V. Farahani, T. D. Veal, J. J. Mudd, D. O. Scanlon, G. W. Watson, O. Bierwagen, M. E. White, J. S. Speck and C. F. McConville, *Physical Review B*, 2014, **90**, 155413.

83. J. H. Scofield, *Theoretical photoionization cross sections from 1 to 1500 keV.*, Office of Scientific and Technical Information (OSTI), Lawrence Livermore Laboratory, 1973.

84. J. J. Yeh and I. Lindau, *Atomic Data and Nuclear Data Tables*, 1985, **32**, 1-155.

85. G. Panaccione, G. Cautero, M. Cautero, A. Fondacaro, M. Grioni, P. Lacovig, G. Monaco, F. Offi, G. Paolicelli, M. Sacchi, N. Stojic, G. Stefani, R. Tommasini and P. Torelli, *Journal of Physics-Condensed Matter*, 2005, **17**, 2671-2679.

86. Y. Dou, R. G. Egdell, D. S. L. Law, N. M. Harrison and B. G. Searle, *Journal of Physics-Condensed Matter*, 1998, **10**, 8447-8458.

87. A. Walsh, G. W. Watson, D. J. Payne, R. G. Edgell, J. Guo, P.-A. Glans, T. Learmonth and K. E. Smith, *Physical Review B*, 2006, **73**, 235104.

88. C. A. Mizzi, P. Koirala and L. D. Marks, *Physical Review Materials*, 2018, **2**, 025001.

89. J. C. Woicik, E. J. Nelson, L. Kronik, M. Jain, J. R. Chelikowsky, D. Heskett, L. E. Berman and G. S. Herman, *Physical Review Letters*, 2002, **89**, 077401.

90. M. B. Trzhaskovskaya and V. G. Yarzhemsky, *Atomic Data and Nuclear Data Tables*, 2018, **119**, 99-174.

91. J. S. O. Evans and I. R. Evans, *Journal of Chemical Education*, 2021, **98**, 495-505.

92. D. A. Shirley, *Physical Review B*, 1972, **5**, 4709-4714.

93. Jouaiti, *Journal of electron spectroscopy and related phenomena*, 1992, **59**, 327.

94. M. H. Engelhard, D. R. Baer, A. Herrera-Gomez and P. M. A. Sherwood, *Journal of Vacuum Science & Technology A*, 2020, **38**, 063203.

95. N. Christensen and B. Seraphin, *Physical Review B-Solid State*, 1971, **4**, 3321.

96. M. Ramchandani, *Journal of Physics Part C Solid State Physics*, 1970, **3**, S1.

97. N. Fairley, V. Fernandez, M. Richard-Plouet, C. Guillot-Deudon, J. Walton, E. Smith, D. Flahaut, M. Greiner, M. Biesinger, S. Tougaard, D. Morgan and J. Baltrusaitis, *Applied Surface Science Advances*, 2021, **5**, 100112.

98. G. Kresse and J. Furthmuller, *Physical Review B*, 1996, **54**, 11169-11186.

99. A. M. Ganose, C. N. Savory and D. O. Scanlon, *The Journal of Physical Chemistry Letters*, 2015, **6**, 4594-4598.

100. D. O. Scanlon, P. D. C. King, R. P. Singh, A. De La Torre, S. M. Walker, G. Balakrishnan, F. Baumberger and C. R. A. Catlow, *Advanced Materials*, 2012, **24**, 2154-2158.

101. S. Budi, W. A. Adi, Yusmaniar, Z. Fairuza, I. Basori and A. A. Umar, *International Journal of Electrochemical Science*, 2022, **17**, 1-12.

102. Y. S. Chen, Y. L. Wei, P. M. Chang and L. J. Ye, *Journal of Alloys and Compounds*, 2011, **509**, 5381-5387.

103. L. P. Salamakha, E. Bauer, S. I. Mudryi, A. P. Goncalves, M. Almeida and H. Noel, *Journal of Alloys and Compounds*, 2009, **479**, 184-188.

104. P. Steiner, S. Hufner, A. J. Freeman and D. S. Wang, *Solid State Communications*, 1982, **44**, 619-622.

105. M. M. Lee, J. Teuscher, T. Miyasaka, T. N. Murakami and H. J. Snaith, *Science*, 2012, **338**, 643-647.

106. J. Burschka, N. Pellet, S.-J. Moon, R. Humphry-Baker, P. Gao, M. K. Nazeeruddin and M. Grätzel, *Nature*, 2013, **499**, 316-319.

107. M. Liu, M. B. Johnston and H. J. Snaith, *Nature*, 2013, **501**, 395-398.

108. B. Hailegnaw, S. Kirmayer, E. Edri, G. Hodes and D. Cahen, *Journal of Physical Chemistry Letters*, 2015, **6**, 1543-1547.
109. G. P. Nagabhushana, R. Shivaramaiah and A. Navrotsky, *Proceedings of the National Academy of Sciences of the United States of America*, 2016, **113**, 7717-7721.
110. A. H. Slavney, T. Hu, A. M. Lindenberg and H. I. Karunadasa, *Journal of the American Chemical Society*, 2016, **138**, 2138-2141.
111. E. T. McClure, M. R. Ball, W. Windl and P. M. Woodward, *Chemistry of Materials*, 2016, **28**, 1348-1354.
112. B. Lee, C. C. Stoumpos, N. Zhou, F. Hao, C. Malliakas, C.-Y. Yeh, T. J. Marks, M. G. Kanatzidis and R. P. H. Chang, *Journal of the American Chemical Society*, 2014, **136**, 15379-15385.
113. A. E. Maughan, A. M. Ganose, D. O. Scanlon and J. R. Neilson, *Chemistry of Materials*, 2019, **31**, 1184-1195.
114. M. C. Folgueras, J. Jin, M. Gao, L. N. Quan, J. A. Steele, S. Srivastava, M. B. Ross, R. Zhang, F. Seeler, K. Schierle-Arndt, M. Asta and P. Yang, *The Journal of Physical Chemistry C*, 2021, **125**, 25126-25139.
115. C. Pi, X. Yu, W. Chen, L. Yang, C. Wang, Z. Liu, Y. Wang, J. Qiu, B. Liu and X. Xu, *Materials Advances*, 2021, **2**, 1043-1049.
116. J. Zhang, S. Li, P. Yang, W. Liu and Y. Liao, *Journal of Materials Science*, 2018, **53**, 4378-4386.
117. M. K. Bahl, R. L. Watson and K. J. Irgolic, *Journal of Chemical Physics*, 1977, **66**, 5526-5535.
118. G. Engel, *Naturwissenschaften*, 1933, **21**, 704.
119. A. K. Das and A. D. Brown, *Canadian Journal of Chemistry*, 1966, **8**, 939-943.
120. L. M. Manojlovic, *Bulletin of the Boris Kidric Institute of Nuclear Sciences*, 1956, **6**, 149-152.
121. S. R. Kavanagh, C. N. Savory, S. M. Liga, G. Konstantatos, A. Walsh and D. O. Scanlon, *The Journal of Physical Chemistry Letters*, 2022, **13**, 10965-10975.
122. Y. Cai, W. Xie, H. Ding, Y. Chen, K. Thirumal, L. H. Wong, N. Mathews, S. G. Mhaisalkar, M. Sherburne and M. Asta, *Chemistry of Materials*, 2017, **29**, 7740-7749.
123. A. E. Maughan, A. M. Ganose, M. M. Bordelon, E. M. Miller, D. O. Scanlon and J. R. Neilson, *Journal of the American Chemical Society*, 2016, **138**, 8453-8464.
124. W. Chen and A. Pasquarello, *Physical Review B*, 2014, **90**, 165133.
125. J. P. Perdew and M. Levy, *Physical Review Letters*, 1983, **51**, 1884-1887.
126. L. J. Sham and M. Schlüter, *Physical Review Letters*, 1983, **51**, 1888-1891.
127. P. Mori-Sánchez, A. J. Cohen and W. Yang, *Physical Review Letters*, 2008, **100**, 146401.
128. E. Y. Peresh, V. I. Sidei, N. I. Gaborets, O. V. Zubaka, I. P. Stercho and I. E. Barchii, *Inorganic Materials*, 2014, **50**, 101-106.
129. J. Heyd, J. E. Peralta, G. E. Scuseria and R. L. Martin, *The Journal of Chemical Physics*, 2005, **123**, 174101.
130. J. Yang, T. Zhu and S. Liu, *Physical Review B*, 2022, **106**, 195159.
131. X. Diao, Y. Diao, Y. Tang, G. Zhao, Q. Gu, Y. Xie, Y. Shi, P. Zhu and L. Zhang, *Scientific Reports*, 2022, **12**, 1-16.
132. J. Liu, H. Zhang, Y. Li and Z. Liu, *The Journal of Physical Chemistry B*, 2018, **122**, 10600-10606.
133. P. H. Citrin, P. Eisenberger and D. R. Hamann, *Physical Review Letters*, 1974, **33**, 965-969.
134. P. H. Citrin and T. D. Thomas, *The Journal of Chemical Physics*, 1972, **57**, 4446-4461.
135. M. Iwan and C. Kunz, *Physics Letters*, 1977, **60A**, 345-347.
136. J. J. Markham, *Reviews of Modern Physics*, 1959, **31**, 956-989.
137. I. S. Messaoudi, A. Zaoui and M. Ferhat, *physica status solidi (b)*, 2015, **252**, 490-495.

138. D. Lewis, R. J. Cole and P. Weightman, *Journal of Physics: Condensed Matter*, 1999, **11**, 8431-8436.
139. R. J. Cole and P. Weightman, *Journal of Physics-Condensed Matter*, 1998, **10**, 5679-5695.
140. A. W. Newton, S. Haines, P. Weightman and R. J. Cole, *Journal of Electron Spectroscopy and Related Phenomena*, 2004, **136**, 235-238.
141. S. Krischok, M. Eremtchenko, M. Himmerlich, P. Lorenz, J. Uhlig, A. Neumann, R. Öttking, W. J. D. Beenken, O. Höfft, S. Bahr, V. Kempter and J. A. Schaefer, *The Journal of Physical Chemistry B*, 2007, **111**, 4801-4806.
142. E. F. Smith, F. J. M. Rutten, I. J. Villar-Garcia, D. Briggs and P. Licence, *Langmuir*, 2006, **22**, 9386-9392.
143. Y. Shirako, Y. G. Shi, A. Aimi, D. Mori, H. Kojitani, K. Yamaura, Y. Inaguma and M. Akaogi, *Journal of Solid State Chemistry*, 2012, **191**, 167-174.
144. H. E. Swanson, E. Posnjak and R. W. G. Wyckoff, *National Bureau of Standards Circular (U. S.)*, 1955, **4**, 31-32.
145. E. Posnjak and R. W. G. Wyckoff, *Journal of the Washington Academy of Sciences*, 1922, **12**, 248-251.
146. C. R. Gopikrishnan, D. Jose and A. Datta, *AIP Advances*, 2012, **2**, 012131.
147. A. E. Gheribi, J. A. Torres and P. Chartrand, *Solar Energy Materials and Solar Cells*, 2014, **126**, 11-25.
148. F. C. Brown, C. Gähwiller, H. Fujita, A. B. Kunz, W. Scheifley and N. Carrera, *Physical Review B*, 1970, **2**, 2126-2138.
149. A. M. Ganose, M. Cuff, K. T. Butler, A. Walsh and D. O. Scanlon, *Chemistry of Materials*, 2016, **28**, 1980-1984.
150. K. Zhang, C. Liu, F. Huang, C. Zheng and W. Wang, *Applied catalysis.*, 2006, **68**, 125.
151. J. Zhang, F. J. Shi, J. Lin, D. F. Chen, J. M. Gao, Z. X. Huang, X. X. Ding and C. C. Tang, *Chemistry of Materials*, 2008, **20**, 2937-2941.
152. X. Zhang, Z. Ai, F. Jia and L. Zhang, *Journal of physical chemistry.*, 2008, **112**, 747.
153. J.-X. Zhang and Z.-Y. Zhao, *Inorganic Chemistry*, 2023, **62**, 8397-8406.
154. Y. Li, H. Jiang, X. Wang, X. Hong and B. Liang, *RSC Advances*, 2021, **11**, 26855-26875.
155. Y. Long, Q. Han, Z. Yang, Y. Ai, S. Sun, Y. Wang, Q. Liang and M. Ding, *Journal of Materials Chemistry A*, 2018, **6**, 13005-13011.
156. A. Biswas, R. Das, C. Dey, R. Banerjee and P. Poddar, *Crystal growth & design.*, 2014, **14**, 236.
157. J. Ketterer and V. Kraemer, *Acta crystallographica .* 1986, **42**, 1098.
158. E. Keller and V. Krämer, *Zeitschrift Fur Naturforschung Section B-a Journal of Chemical Sciences*, 2005, **60**, 1255-1263.
159. D. S. Bhachu, S. J. A. Moniz, S. Sathasivam, D. O. Scanlon, A. Walsh, S. M. Bawaked, M. Mokhtar, A. Y. Obaid, I. P. Parkin, J. Tang and C. J. Carmalt, *Chemical Science*, 2016, **7**, 4832-4841.
160. W. L. Huang and Q. Zhu, *Journal of Computational Chemistry*, 2009, **30**, 183-190.
161. H. Lim, C. Song, M. Seo, D. Kim, M. Jung, H. Kang, S. Kim, K.-J. Lee, Y. Yu, G. Kim, K.-J. Kim and B. S. Mun, *Journal of Materials Chemistry C*, 2021, **9**, 13094-13102.
162. M. S. MartíN González, M. H. Aguirre, E. Morán, M. Á. Alario-Franco, V. Perez-Dieste, J. Avila and M. C. Asensio, *Solid State Sciences*, 2000, **2**, 519-524.
163. Z. Zhang, P. Qian, X. Yang, B. Wu, H. L. Cai, F. M. Zhang and X. S. Wu, *Scientific Reports*, 2022, **12**, 2499.
164. C. M. Culbertson, A. T. Flak, M. Yatskin, P. H.-Y. Cheong, D. P. Cann and M. R. Dolgos, *Scientific Reports*, 2020, **10**, 1-10.

165. S. Astley, D. Hu, K. Hazeldine, J. Ash, R. E. Cross, S. Cooil, W. Allen, Martin, J. Evans, K. James, F. Venturini, D. C. Grinter, P. Ferrer, R. Arrigo, G. Held, G. T. Williams and D. A. Evans, *Faraday Discussions*, 2022, **236**, 191-204.

166. N. Sarin, M. Mishra, G. Gupta, M. Arora and V. Luthra, *physica status solidi (b)*, 2018, **255**, 1700683.

167. M. Andrä, H. Bluhm, R. Dittmann, C. M. Schneider, R. Waser, D. N. Mueller and F. Gunkel, *Physical Review Materials*, 2019, **3**, 044604.

168. S. A. Chambers, Y. Comes, S. R. Spurgeon and P. V. Sushko, *Applied Physics Letters*, 2017, **110**, 082104.

169. L. E. Alexander, *Advances in X-ray Analysis*, 1976, **20**, 1-13.

170. D. L. Bish and S. A. Howard, *J Journal of Applied Crystallography*, 1988, **21**, 86-91.

171. R. Hill and C. J. J. o. A. C. Howard, 1987, **20**, 467-474.

172. F. J. Humphreys, *Journal of Materials Science*, 2001, **36**, 3833-3854.

173. H. Rietveld, *Journal of Applied Crystallography*, 1969, **2**, 65.

174. A. C. Breeson, G. Sankar, G. K. L. Goh and R. G. Palgrave, *Physical Chemistry Chemical Physics*, 2016, **18**, 24722-24728.

175. A. C. Breeson, G. Sankar, G. K. L. Goh and R. G. Palgrave, *Applied Surface Science*, 2017, **423**, 205-209.

176. D. N. G. Krishna, R. P. George and J. Philip, *Thin Solid Films*, 2019, **681**, 58-68.

177. D. N. G. Krishna, C. Anushree, R. P. George and J. Philip, *Applied Surface Science*, 2018, **462**, 932-943.

178. D. A. H. Hanaor and C. C. Sorrell, *Journal of Materials Science*, 2011, **46**, 855-874.

179. J. He, Y.-E. Du, Y. Bai, J. An, X. Cai, Y. Chen, P. Wang, X. Yang and Q. Feng, *Molecules*, 2019, **24**, 2996.

180. Y. K. Kho, A. Iwase, W. Y. Teoh, L. Mädler, A. Kudo and R. Amal, *The Journal of Physical Chemistry C*, 2010, **114**, 2821-2829.

181. R. Quesada-Cabrera, C. Sotelo-Vazquez, J. C. Bear, J. A. Darr and I. P. Parkin, *Advanced Materials Interfaces*, 2014, **1**, 1400069.

182. R. Su, R. Bechstein, L. Sø, R. T. Vang, M. Sillassen, B. Esbjörnsson, A. Palmqvist and F. Besenbacher, *The Journal of Physical Chemistry C*, 2011, **115**, 24287-24292.

183. R. Asahi, Y. Taga, W. Mannstadt and A. J. Freeman, *Physical Review B*, 2000, **61**, 7459-7465.

184. P. I. Sorantin and K. Schwarz, *Inorganic Chemistry*, 1992, **31**, 567-576.

185. A. R. Zanatta, *AIP Advances*, 2017, **7**, 075201.

186. OriginLab Corporation, OriginLab, https://www.originlab.com/, (accessed 26 11 2021).

187. A. Mills, J. Wang, S. Lee and M. Simonsen, *Chemical Communications*, 2005, 2721-2723.

188. ISO 21066:2018, Fine ceramics (advanced ceramics, advanced technical ceramics) - Qualitative and semiquantitative assessment of the photocatalytic activities of surfaces by the reduction of resazurin in a deposited ink film, https://www.iso.org/standard/69815.html).

189. K. Brlec, D. Davies and D. Scanlon, *Journal of Open Source Software*, 2021, **6**, 3171.

190. D. O. Scanlon, C. W. Dunnill, J. Buckeridge, S. A. Shevlin, A. J. Logsdail, S. M. Woodley, C. R. A. Catlow, M. J. Powell, R. G. Palgrave, I. P. Parkin, G. W. Watson, T. W. Keal, P. Sherwood, A. Walsh and A. A. Sokol, *Nature Materials*, 2013, **12**, 798-801.

191. J. Buckeridge, K. T. Butler, C. R. A. Catlow, A. J. Logsdail, D. O. Scanlon, S. A. Shevlin, S. M. Woodley, A. A. Sokol and A. Walsh, *Chemistry of Materials*, 2015, **27**, 3844-3851.

192. M. T. Greiner and Z.-H. Lu, *NPG Asia Materials*, 2013, **5**, e55-e55.

193. T. Ohsaka, F. Izumi and Y. Fujiki, *Journal of Raman Spectroscopy*, 1978, **7**, 321-324.

194. S. P. S. Porto, P. A. Fleury and T. C. Damen, *Physical Review*, 1967, **154**, 522-526.

195. J. Zhang, P. Zhou, J. Liu and J. Yu, *Phys. Chem. Chem. Phys.*, 2014, **16**, 20382-20386.

196. T. Luttrell, S. Halpegamage, J. Tao, A. Kramer, E. Sutter and M. Batzill, *Scientific Reports*, 2015, **4**, 4043.
197. A. F. Silva, *Trends in Interfacial Electrochemistry*, Springer Netherlands, 2012.
198. T. Torimoto, T. Tsuda, K.-I. Okazaki and S. Kuwabata, *Advanced Materials*, 2010, **22**, 1196-1221.
199. K. R. J. Lovelock, I. J. Villar-Garcia, F. Maier, H.-P. SteinrüCk and P. Licence, *Chemical Reviews*, 2010, **110**, 5158-5190.
200. A. Foelske-Schmitz, in *Encyclopedia of Interfacial Chemistry: Surface Science and Electrochemistry*, ed. K. Wandelt, Elsevier, 2018, pp. 591 - 606.
201. N. Andreu, D. Flahaut, R. Dedryvère, M. Minvielle, H. Martinez and D. Gonbeau, *ACS Applied Materials & Interfaces*, 2015, **7**, 6629-6636.
202. N. Yabuuchi and T. Ohzuku, *Journal of Power Sources*, 2003, **119-121**, 171-174.
203. S.-Y. Yang, X.-Y. Wang, Z.-L. Liu, Q.-Q. Chen, X.-K. Yang and Q.-L. Wei, *The Chinese Journal of Nonferrous Metals*, 2011, **21**, 1995-2001.
204. H. Kobayashi, Y. Arachi, S. Emura, H. Kageyama, K. Tatsumi and T. Kamiyama, *Journal of Power Sources*, 2005, **146**, 640-644.
205. M. Ma, N. A. Chernova, B. H. Toby, P. Y. Zavalij and M. S. Whittingham, *Journal of Power Sources*, 2007, **165**, 517-534.
206. Y. Bentaleb, I. Saadoune, K. Maher, L. Saadi, K. Fujimoto and S. Ito, *Journal of Power Sources*, 2010, **195**, 1510-1515.
207. S. Oh, J. K. Lee, D. Byun, W. I. Cho and B. Won Cho, *Journal of Power Sources*, 2004, **132**, 249-255.
208. Y. Oh, D. Ahn, S. Nam and B. Park, *Journal of Solid State Electrochemistry*, 2010, **14**, 1235-1240.
209. Y. Huang, J. Chen, F. Cheng, W. Wan, W. Liu, H. Zhou and X. Zhang, *Journal of Power Sources*, 2010, **195**, 8267-8274.
210. E. Yeager, W. E. Ogrady, M. Y. C. Woo and P. Hagans, *Journal of the Electrochemical Society*, 1978, **125**, 348-349.
211. R. O. Ansell, T. Dickinson, A. F. Povey and P. M. A. Sherwood, *Journal of Electroanalytical Chemistry*, 1979, **98**, 69-77.
212. R. O. Ansell, T. Dickinson, A. F. Povey and P. M. A. Sherwood, *Journal of Electroanalytical Chemistry*, 1979, **98**, 79-89.
213. H. Neff, W. Foditsch and R. Kotz, *Journal of Electron Spectroscopy and Related Phenomena*, 1984, **33**, 171-174.
214. W. N. Hansen, C. L. Wang and T. W. Humpherys, *Journal of Electroanalytical Chemistry*, 1978, **93**, 87-98.
215. W. N. Hansen, C. L. Wang and T. W. Humphryes, *Journal of Electroanalytical Chemistry*, 1978, **90**, 137-141.
216. W. N. Hansen, D. M. Kolb, D. L. Rath and R. Wille, *Journal of Electroanalytical Chemistry*, 1980, **110**, 369-373.
217. D. M. Kolb, D. L. Rath, R. Wille and W. N. Hansen, *Berichte Der Bunsen-Gesellschaft-Physical Chemistry Chemical Physics*, 1983, **87**, 1108-1113.
218. E. R. Kötz, H. Neff and K. Müller, *Journal of Electroanalytical Chemistry and Interfacial Electrochemistry*, 1986, **215**, 331-344.
219. S. Wenzel, T. Leichtweiss, D. Krüger, J. Sann and J. Janek, *Solid State Ionics*, 2015, **278**, 98-105.
220. H. Huo, M. Jiang, B. Mogwitz, J. Sann, Y. Yusim, T. T. Zuo, Y. Moryson, P. Minnmann, F. H. Richter, C. Veer Singh and J. Janek, *Angewandte Chemie International Edition*, 2023, **62**, e202218044.
221. R. Wibowo, L. Aldous, R. M. J. Jacobs, N. S. A. Manan and R. G. Compton, *Chemical Physics Letters*, 2011, **517**, 103-107.

222. Z. Liu, O. Höfft, A. S. Gödde and F. Endres, *The Journal of Physical Chemistry C*, 2021, **125**, 26793-26800.
223. D. Weingarth, A. Foelske-Schmitz, A. Wokaun and R. Kötz, *Electrochemistry Communications*, 2011, **13**, 619-622.
224. A. Benayad, J. E. Morales-Ugarte, C. C. Santini and R. Bouchet, *Journal of Physical Chemistry A*, 2021, **125**, 1069-1081.
225. J.-J. Velasco-Vélez, L. J. Falling, D. Bernsmeier, M. J. Sear, P. C. J. Clark, T.-S. Chan, E. Stotz, M. Hävecker, R. Kraehnert, A. Knop-Gericke, C.-H. Chuang, D. E. Starr, M. Favaro and R. V. Mom, *Journal of Physics D: Applied Physics*, 2021, **54**, 124003.
226. B. O. Shalom, M. A. Andrés, Y. Yu, A. R. Head and B. Eren, *Electrochemistry Communications*, 2022, **142**.
227. M. Favaro, B. Jeong, P. N. Ross, J. Yano, Z. Hussain, Z. Liu and E. J. Crumlin, *Nature Communications*, 2016, **7**, 12695.
228. J. Dupont, *Journal of the Brazilian Chemical Society*, 2004, **15**, 341-350.
229. Y. Chauvin, L. Mussmann and H. Olivier, *Angewandte Chemie International Edition in English*, 1996, **34**, 2698-2700.
230. P. A. Z. Suarez, J. E. L. Dullius, S. Einloft, R. F. DeSouza and J. Dupont, *Polyhedron*, 1996, **15**, 1217-1219.
231. P. Bonhôte, A.-P. Dias, N. Papageorgiou, K. Kalyanasundaram and M. Grätzel, *Inorganic Chemistry*, 1996, **35**, 1168-1178.
232. N. Subasree and J. A. Selvi, *Heliyon*, 2020, **6**, e03498.
233. V. Lockett, R. Sedev, C. Bassell and J. Ralston, *Physical Chemistry Chemical Physics*, 2008, **10**, 1330.
234. S. Caporali, U. Bardi and A. Lavacchi, *Journal of Electron Spectroscopy and Related Phenomena*, 2006, **151**, 4-8.
235. E. F. Smith, I. J. Villar Garcia, D. Briggs and P. Licence, *Chemical Communications*, 2005, 5633.
236. I. J. Villar-Garcia, E. F. Smith, A. W. Taylor, F. Qiu, K. R. J. Lovelock, R. G. Jones and P. Licence, *Phys. Chem. Chem. Phys.*, 2011, **13**, 2797-2808.
237. G. Beamson, D. T. Clark, J. Kendrick and D. Briggs, *Journal of Electron Spectroscopy and Related Phenomena*, 1991, **57**, 79-90.
238. D. Briggs and N. Fairley, *Surface and Interface Analysis*, 2002, **33**, 283-290.
239. A. Foelske-Schmitz and M. Sauer, *Journal of Electron Spectroscopy and Related Phenomena*, 2018, **224**, 51-58.
240. A. Foelske and M. Sauer, *Electrochimica Acta*, 2019, **319**, 456-461.
241. M. D. Hanwell, D. E. Curtis, D. C. Lonie, T. Vandermeersch, E. Zurek and G. R. Hutchison, *Journal of Cheminformatics*, 2012, **4**, 17.
242. S. Zhao, Y. Ren, W. Lu, J. Wang and W. Yin, *Physical Chemistry Chemical Physics*, 2012, **14**, 13444.
243. T. Ikari, A. Keppler, M. Reinmoller, W. J. D. Beenken, S. Krischok, M. Marschewski, W. Maus-Friedrichs, O. Hofft and F. Endres, *e-Journal of Surface Science and Nanotechnology*, 2010, **8**, 241-245.
244. I. Kuusik, M. Berholts, J. Kruusma, V. Kisand, A. Tõnisoo, E. Lust and E. Nõmmiste, *RSC Advances*, 2018, **8**, 30298-30304.
245. I. Kuusik, M. Berholts, J. Kruusma, A. Tõnisoo, E. Lust, E. Nõmmiste and V. Kisand, *RSC Advances*, 2019, **9**, 33140-33146.
246. S. Rangan, J. Viereck and R. A. Bartynski, *The Journal of Physical Chemistry B*, 2020, **124**, 7909-7917.
247. N. Tapia-Ruiz, A. R. Armstrong, H. Alptekin, M. A. Amores, H. T. Au, J. Barker, R. Boston, W. R. Brant, J. M. Brittain, Y. Chen, M. Chhowalla, Y. S. Choi, S. I. R. Costa, M. C. Ribadeneyra, S. A. Cussen, E. J. Cussen, W. I. F. David, A. V. Desai, S. A. M. Dickson, E. I.

Eweka, J. D. Forero-Saboya, C. P. Grey, J. M. Griffin, P. Gross, X. Hua, J. T. S. Irvine, P. Johansson, M. O. Jones, M. Karlsmo, E. Kendrick, E. Kim, O. V. Kolosov, Z. N. Li, S. F. L. Mertens, R. Mogensen, L. Monconduit, R. E. Morris, A. J. Naylor, S. Nikman, C. A. O'Keefe, D. M. C. Ould, R. G. Palgrave, P. Poizot, A. Ponrouch, S. Renault, E. M. Reynolds, A. Rudola, R. Sayers, D. O. Scanlon, S. Sen, V. R. Seymour, B. Silvan, M. T. Sougrati, L. Stievano, G. S. Stone, C. I. Thomas, M. M. Titirici, J. C. Tong, T. J. Wood, D. S. Wright and R. Younesi, *Journal of Physics-Energy*, 2021, **3**.

248.   K. M. Abraham, *ACS Energy Letters*, 2020, **5**, 3544-3547.

249.   B. L. Ellis and L. F. Nazar, *Current Opinion in Solid State & Materials Science*, 2012, **16**, 168.

250.   W. C. Zhang, J. Lu and Z. P. Guo, *Materials Today*, 2021, **50**, 400-417.

251.   P. Aydogan Gokturk and S. Suzer, *The Journal of Physical Chemistry C*, 2021, **125**, 9453-9460.

252.   Autodesk Inc., AutoCAD 3D Software, https://www.autodesk.co.uk/products/autocad/, (accessed 10 January 2023).

253.   ThermoFisher, Increased Throughput Using Snapshot Spectra; Application Note:31009, https://tools.thermofisher.com/content/sfs/brochures/D16066~.pdf, (accessed 24 November 2023).

254.   G. H. Major, N. Fairley, P. M. A. Sherwood, M. R. Linford, J. Terry, V. Fernandez and K. Artyushkova, *Journal of Vacuum Science & Technology A: Vacuum, Surfaces, and Films*, 2020, **38**, 061203.